Evaluation of Nondestructive Test Methods for Concrete Bridge Deck Condition Assessment

by

Zachary W. Coleman

A thesis submitted to the Graduate Faculty of
Auburn University
in partial fulfillment of the
requirements for the Degree of
Master of Science

Auburn, Alabama
August 7th, 2021

Keywords: ground-penetrating radar, impact echo, infrared thermography, half-cell corrosion potential, electrical resistivity, deterioration

Approved by

Anton K. Schindler, Chair, Mountain Spirit Professor of Civil Engineering
Robert W. Barnes, Brasfield & Gorrie Associate Professor of Civil Engineering
Mary L. Hughes, Lecturer of Civil Engineering

Abstract

To facilitate locating subsurface concrete bridge deck defects and determining their corresponding severity, departments of transportation are switching to nondestructive test (NDT) methods. However, the difficulty in consistently locating defects with any one method has inspired investigations of the accuracy of each NDT method in detecting different defects. Accordingly, this project aims to assess the accuracy of nondestructive technologies available to the Alabama Department of Transportation (ALDOT) to evaluate the in-place condition of concrete bridge decks. To accomplish this, 20 laboratory specimens and an 18 ft by 31 ft bridge were fabricated with simulated defects representative of those found in a typical in-service deteriorated bridge decks. Ground-penetrating radar, impact-echo, infrared thermography, half-cell corrosion potential, and electrical resistivity technologies were used to locate delaminations, corrosion, deterioration, voids, cracks, and poorly constructed concrete. Recommendations for the use of each NDT method in identifying different concrete subsurface defects were developed.

Dedicated to Mom and Dad.

If you're going through Hell,

keep going.

- Winston Churchill

Acknowledgements

First and foremost, I want to thank God for guiding me to where I stand today. Through His divine providence, He has gifted me with countless blessings and challenges that have all served to make me the man I am today. Without Him, nothing is possible. I also want to express my gratitude to His blessed mother, Mary, for being a comfort and source of wisdom to me through the years.

From the other side of the country, I want to thank Mom and Dad for being endlessly committed to my personal development. The determination to see things through, even when I was most miserable, which they have instilled in me has helped me press on through the good times and bad. I also need to extend my thanks to my loving siblings, Sam, Morgan, Troy, and Montana who have been my best friends and supporters all my life. No talk of endless support would be complete without recognition of my soon-to-be beloved Madeline Skye Coleman. Her love and encouragement have been invaluable to me, even from 786 miles away.

Down in the most beautiful village in the world, I want to give special thanks to Dr. Schindler. Since the day I began working for him, Dr. Schindler has been committed not only to the success of our research, but also my professional development. His resolute belief in my abilities, outside-of-the-box ideas, and at times unusual methods has instilled within me greater confidence in my own abilities as a researcher, educator, and professional. Reflecting on the ways in which I have grown between the first time I set foot in Harbert Center and the last time I closed the door to my office, many of those

growths are the direct result of Dr. Schindler's guidance. I could not have asked for a better advisor during my time at Auburn.

I would like to also thank Dr. Barnes for serving on my committee and further enabling me to be passionate about the world's greatest material, concrete! Learning from Dr. Barnes in several of his concrete design classes has been incredibly useful towards building a future predicated in concrete research. I am grateful for his guidance in refining the work of this thesis.

Even after graduating from Lafayette College, my friend and mentor, Dr. David Mante, has continued to be instrumental in the fostering of my love for concrete and the further development of myself. Without him, I never would have become so confident that I could tackle any problem or challenge thrown at me, whether that be teaching myself about electromagnetic wave propagation, building a reinforced concrete bridge, or repairing that spalled drywall in my bathroom. To him I must say — thank you for continuing to give me an ideal standard to aspire to as a future teacher and mentor.

The work of this thesis would not have been possible without the aid of fellow graduate assistant Christian Jetzel and lab manager Rob Crosby. The impressive hands-on knowledge which they both share has surely facilitated a higher quality of experimental procedures beyond that which I previously knew how to develop. Thanks are also due to the wonderful lab assistants that I have had the pleasure of working with on my Auburn journey, William Bloodworth and Melanie Monaghan. The two have gone above and beyond just being an extra set of hands, taking an active interest in the topic at hand and helping me work through frustrating roadblocks in our research.

Last (but certainly not least), I want to extend my most sincere regards to my third committee member, Dr. Hughes — there are no words that I could choose to adequately describe the undeniably positive impact that she has had on my life. Along with her husband, Carl, she has treated me like a lifelong friend from the first day I met her. Together, the two of them have given me invaluable technical, professional, and emotional guidance — most importantly, they gave me a home away from home, even before I committed to Auburn for graduate school. The two of them are not only the highest personifications of the Auburn creed, but also, to quote a dear friend of mine "the closest things I have ever seen to angels on Earth." To them I must say — thank you for the love, care, football games, trips to church, meals, sagacious advice, and banana pudding. Like countless others, you have touched my life in a tremendous way.

Table of Contents

List of Tables

List of Figures

List of Abbreviations

NDT	Nondestructive test
GPR	Ground-penetrating radar
HCP	Half-cell corrosion potential
IRT	Infrared thermography
ER	Electrical resistivity
IE	Impact echo
DOT	Department of Transportation
ALDOT	Alabama Department of Transportation
ROC	Receiver operator characteristic

Chapter 1: Introduction

1.1 Background on Use of NDT Methods in Monitoring Concrete Bridge Decks

Nondestructive test (NDT) methods are predominantly non-invasive techniques used to determine concrete material properties and evaluate the condition of concrete elements used in buildings and infrastructure (ACI Committee 228 2013). As opposed to traditional methods of concrete quality assurance that rely on discrete testing of samples during construction, NDT methods offer the advantage of a rapid estimation of the in-place hardened properties of concrete as well as a condition assessment of the associated element.

To facilitate assessing the condition of their bridge infrastructure, Departments of Transportation (DOTs) are switching to NDT methods. The bridge deck is often the most deteriorated element of a concrete bridge and is thus the focus of many DOT nondestructive evaluations. These assessments are chiefly aimed at identifying subsurface defects (for example corrosion, delaminations, honeycombing) that, if left unrepaired, could lead to the premature removal of the bridge from service and/or the structural failure of the deck (Gucunski et al. 2013).

1.2 Justification of Research

The Federal Highway Administration (FHWA) reported that, in 2005, the price of repairing and/or replacing deteriorating highway bridges in the United States was approximately $100 billion (Lemieux 2005). Accordingly, early identification of defects in concrete bridge decks could allow for the reduction in this total cost, the extension of the life cycles

of bridge decks, and the promotion of the structural integrity of the affected decks. NDT methods have become increasingly viable means of achieving these goals.

Despite the growing prominence of NDT methods in bridge deck evaluations, there is still much uncertainty regarding (1) which types of defects each NDT method is capable of detecting, (2) how to interpret NDT data for defect identification, and (3) what is the most efficient, cost-effective, and accurate way to profile deck deterioration. These uncertainties, coupled with unrealistic expectations and improper use of NDT methods, have inhibited a more widespread, successful implementation of nondestructive evaluations of concrete bridge decks.

Sharing many of the previously mentioned frustrations with NDT methods, the Alabama Department of Transportation (ALDOT) has had limited success accurately assessing the condition of the state's concrete bridge decks in nondestructive evaluations. This problem is further exacerbated by the lack of a local testing facility for ALDOT employees to develop hands-on training with NDT technologies. To facilitate more accurate condition assessments of Alabama's concrete bridge decks, the Auburn University Highway Research Center (AUHRC) is investigating the capabilities of NDT technologies available to ALDOT in identifying different forms of concrete bridge deck deterioration.

1.3 Research Objectives

The primary objective of this project is to determine the most feasible and accurate means for ALDOT to accurately profile concrete bridge deck deterioration, using their available NDT technologies. In support of a robust testing facility for ALDOT employees to develop hands-on NDT training, a secondary objective of this research is to design and construct a

concrete test bridge with simulated defects in the deck. Topics of particular interest in this study include:

- The ability of each NDT method to accurately detect different subsurface bridge deck defects; and
- The degree to which the true condition of decks correlates with the predicted condition determined in accordance with current data analysis specifications and recommendations.

1.4 Research Approach

To accomplish the objectives of this project, the scope of supporting tasks was subdivided into two phases. The results of the two phases of experimental procedures are presented in this thesis.

Phase one of this project constituted the laboratory evaluation of the capability of NDT methods to accurately locate different types of concrete bridge deck defects. Towards this aim, 20 concrete specimens were constructed, each fabricated with a plausible deck defect. A review of the theory of operation of each NDT method along with literature describing previously used techniques of fabricating representative defects was implemented to best engineer corrosion, delaminations, honeycombing, voids, and cracks into the laboratory specimens. With knowledge of the location and severity of the fabricated defects, the laboratory specimens were evaluated using ground-penetrating radar (GPR), infrared thermography (IRT), impact echo (IE), half-cell corrosion potential (HCP), and electrical resistivity (ER) methods. Post-processing of NDT data for each specimen using available prediction criteria and statistical analyses allowed for an assessment of how

accurately each NDT method was in detecting different defects. A forensic analysis of the specimens using coring facilitated confirmation that defects were simulated in their correct locations and to their desired severity.

The second phase of this project relied on the results of phase one to determine which laboratory defect details should be implemented in the design and construction of the deteriorated concrete bridge. Key considerations in the bridge design included (1) spatial accommodation of ALDOT NDT methods attached to a truck, (2) obscurity of defect locations to facilitate better NDT operator training, and (3) the structural integrity of the bridge under factored loading. Nondestructive evaluation of the bridge by AUHRC employees allowed for further validation of the capability of each NDT method in detecting different modes of bridge deck deterioration.

1.5 Thesis Organization

This thesis is organized as described in this subsection. Chapter 1 introduces readers to nondestructive testing of bridge decks as well as presents the justification, objectives, and approach of the research conducted in this study. Chapter 2 provides a cursory introduction to the five NDT methods implemented in this study and the physical principles governing their operation. Chapter 3 synthesizes a literature review of the capabilities of the five foregoing NDT methods when use uniquely and cooperatively with one another in evaluations of bridge decks. Chapter 4 discusses the experimental approach to investigating the defect-detection capabilities of the five NDT methods in a laboratory setting (phase one), presents the results of experimental testing and analysis of laboratory data, and offers conclusions. Chapter 5 discusses the experimental approach towards developing/constructing a full-scale bridge deck with simulated defects for further NDT

method validation (phase two). Results of nondestructive testing of the deck and corresponding conclusions are also presented. Lastly, overall conclusions developed from both project phases and recommendations for how best to implement the five investigated NDT methods in evaluations of in-service bridge decks are presented in Chapter 6. Opportunities for future studies in this field are also mentioned.

Chapter 2: Background

2.1 Introduction

The purpose of this chapter is to provide background on the theory of operation of the NDT technologies used in this study and the forms of reinforced concrete bridge deck deterioration which they aim to detect. A rigorous discussion on the mechanics of each NDT method is not included in this thesis, as a thorough understanding of the behavior of each method is sufficient to predict the qualitative response of a tested concrete element.

2.2 Mechanisms of Reinforced Concrete Bridge Deck Deterioration

While reinforced concrete structures can be susceptible to many deteriorations or defects resulting from environmental conditions and poor construction, those of chief concern to DOTs when evaluating bridge decks are corrosion, delaminations, vertical cracking, large voids, honeycombing, and concrete deterioration. A brief discussion on the mechanisms of each of the foregoing defects is presented in this section.

Corrosion of embedded reinforcing steel in concrete can threaten the durability, life cycle, and structural integrity of a reinforced concrete element. Corrosion is an electrochemical process that requires the presence of iron, oxygen, water, and an electron transferring mechanism (anode and cathode pair) to occur. Under normal, ambient conditions, reinforcing steel would be immediately subjected to corrosion. However, the hydration of portland cement creates a highly alkaline pore solution, which allows for the formation of a thin passivating layer on the surface of reinforcing steel, protecting it from

corrosion. Calcium hydroxides formed during hydration allow for the pH of the concrete pore solution to be approximately between 12 and 13 (Emmons 1993).

However, this passivating layer can be destroyed or destabilized by either a reduction in pH or the presence of significant amounts of chloride ions respectively (Mehta and Monteiro 2013). While concretes typically have a small amount of chlorides present in their mixtures, the most harmful source of chlorides in concrete come from deicing chemicals (road salt) or marine environments. Accordingly, high paste porosity and cracking can facilitate the ingress of chlorides into the concrete and accelerate the onset of corrosion. Reduction in the pH of the concrete pore solution can result from acid attack, carbonation, or the pozzolanic reaction. Carbonation occurs when carbon dioxide from the environment neutralizes the highly alkaline pore solution, effectively destroying the passivating layer once the depth of carbonation reaches that of the embedded reinforcement (COST 509 1997). Furthermore, supplementary cementing materials (SCMs) such as fly ash, slag cement, or silica fume can react with calcium hydroxides in the pore solution to produce calcium silicate hydrates, reducing the pH of the pore solution (Kosmatka and Wilson 2011).

With the passivating layer removed, available moisture and oxygen facilitate electron transfer between anodic and cathodic regions among reinforcing steel. Embedded reinforcing steel can corrode uniformly, as numerous micro-cells are established along the reinforcement. Alternatively, localized steel depassivation can result in macro-cell corrosion in which a substantial corrosion pit forms at a concentrated anode. Regardless, the products of the subsequent corrosion reaction occupy more volume than the metallic reactants as the corrosion process propagates, causing substantial internal expansive

stresses around the reinforcing steel (Mehta and Monteiro 2013). The resulting circumferential tensile stresses in the concrete surrounding the reinforcement can lead to delaminations and vertical cracking. By reducing the net area of embedded reinforcement, corrosion can threaten the structural integrity of a concrete element, especially in prestressed applications in which prestressing strands are much smaller than traditional, non-prestressed steel reinforcement. Other factors such as the number of wetting/drying cycles, the water-cement ratio, and the use of chemical accelerators can affect the risk of corrosion (ACI Committee 222 2001). Corrosion of embedded reinforcing steel and corresponding damage to concrete can be seen in Figure 2-1.

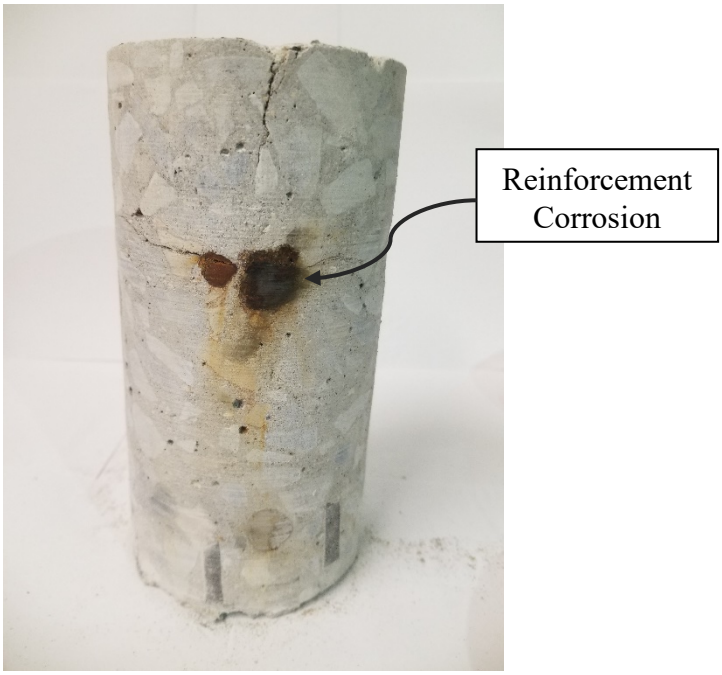

Figure 2-1: Corrosion of Steel Reinforcement

In concrete bridge decks, many delaminations and vertical cracks may be caused by the expansive forces of corrosion. However, some delaminations may be stress-induced from traffic loading. For those caused by corrosion, delaminations are horizontal cracks

which exist on the same plane as the reinforcing steel. As the corrosion process continues, delaminations can propagate towards the surface and cause spalling. For this reason, it is advantageous to identify delaminations and corrosion as soon as possible. Like delaminations, vertical cracking can be caused by mechanisms other than corrosion. Plastic shrinkage, concrete deterioration, drying shrinkage, thermal effects, and loading can cause the concrete surface to crack, increasing concrete permeability and further heightening the risk of durability concerns (Mehta and Monteiro 2013). Typical corrosion-induced delaminations and vertical cracks from a concrete deck can be observed in Figure 2-2.

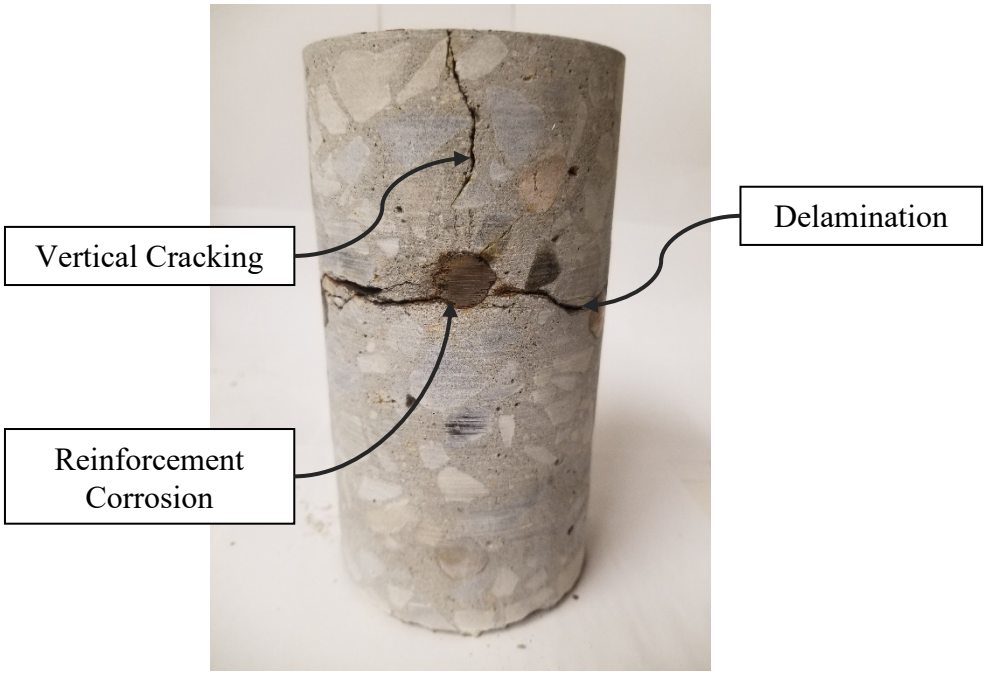

Figure 2-2: Corrosion-Induced Delamination and Vertical Cracking in Concrete

An in-place reinforced concrete bridge deck can also contain defects caused by poor-construction practices that lead to the presence of excessively large voids and honeycombing in the deck. Large voids may be present in hardened concrete from

improper consolidation practices. Furthermore, when contaminated aggregates are mixed into concrete, the fine sediment attached to the aggregates may break free and combine to create clay balls which cause voids in concrete. Honeycombing occurs when concrete is inadequately consolidated, resulting in voids between nearby coarse aggregate (ACI 2018), giving the loosely connected network of aggregate the appearance of honeycombs. Honeycombing can be caused in reinforced concrete elements by many factors including (1) highly congested reinforcement, (2) low concrete workability, (3) insufficient cover to formed surfaces, (4) improper consolidation of fresh concrete, (5) leaking at joints, and (6) segregation during placement (Emmons 1993). Honeycombing can be observed in the side of the concrete slab, shown in Figure 2-3.

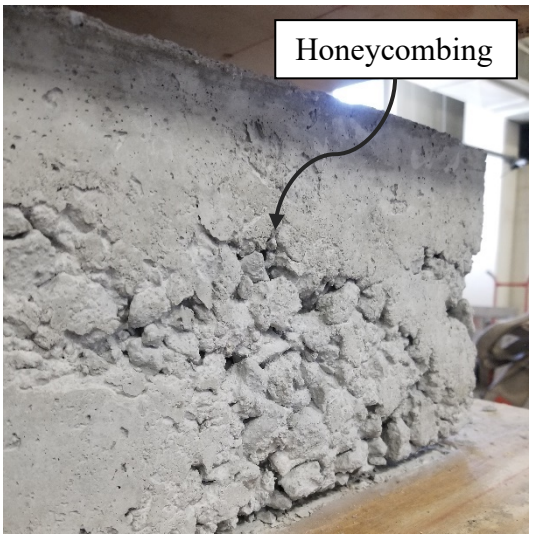

Figure 2-3: Honeycombing in a Concrete Slab

In addition to the foregoing defects, a bridge deck can also be distressed by concrete deterioration. An in-place bridge deck may become degraded through many freeze/thaw cycles, alkali aggregate reactivity, abrasion, acid attack, or other deterioration mechanisms.

Such deterioration can lead to a progressively increasing network of microcracking within the concrete deck, reducing its structural integrity and durability.

2.3 Background Principles of NDT Technologies

The objective of this section is to present the fundamental behavioral characteristics of the NDT technologies used in this study. GPR, IRT, and IE all rely on the response of a concrete element to induced waves aimed at assessing the condition of the element. HCP and ER take advantage of the electrochemical activity of a bridge deck under induced current to assess the risk and rate of corrosion of embedded metallic reinforcement.

2.3.1 Ground-Penetrating Radar

GPR employs electromagnetic waves to image embedded objects and abnormalities in a subsurface. A typical GPR system consists of either a ground-coupled or air-coupled antenna connected to a data acquisition system. There are a variety of antennas with different central frequencies commercially available. Selection of the proper antenna for a given project is largely governed by the size of object that one desires an electromagnetic wave to respond to. Antennas with high frequencies have short wavelengths; as such, the radar waves which they emit exhibit high scattered scattering losses (Jol 2008). Accordingly, low frequency antennas (for example 50 MHz) transmit waves with large wavelengths that allow a wave to penetrate deeply with less scattering loss but with low resolution (Jol 2008). Conversely, the transmitted waves of a high frequency antenna (for example 2600 MHz) have a much shorter wavelength, allowing for a high-resolution wave with a low depth of penetration. GPR scans of concrete bridge decks benefit from the use of high frequency antennas, since the needed penetration depth is low and high resolution is advantageous to image smaller anomalies.

The three most important electrical material properties in a GPR evaluation are the magnetic permeability (μ), the dielectric permittivity (ε) and the electrical conductivity (σ). Since concrete is practically a non-magnetic material (Davis et al. 2003), its magnetic permeability does not significantly affect GPR waves. The dielectric permittivity affects the resistance of a material to an electrical field and subsequently the ability of that material to hold an electric charge (Jol 2008). Within GPR applications, it is convenient to express the dielectric permittivity as a relative dielectric constant (κ), which is simply the ratio of the dielectric permittivity of a material to that of a vacuum. Moreover, the electrical conductivity describes the ability of a material to carry a current (Jol 2008). In concrete, electrical charges may be passed via electrolysis of the ionic pore solution. Attenuation (i.e. energy absorption) of an electromagnetic wave is heavily influenced by the electrical conductivity of the medium. Materials with a high electrical conductivity can greatly attenuate electromagnetic waves, not allowing them to penetrate very far into the medium. Furthermore, conductivity of a material is equal to the inverse of its electrical resistivity after reinforcement depassivation (COST 509 1997). Accordingly, many of the factors affecting concrete electrical resistivity also affect its electrical conductivity. For comparison purposes, the relative dielectric constants and static conductivity (the real static representation of conductivity in GPR waves) of various materials are given in Table 2.1.

Table 2-1: Relative Dielectric Constants of Various Materials (Jol 2008)

Material	Relative Dielectric Constant (κ)	Static Conductivity (σ_s) (mS/m)
Air	1	0
Concrete — dry	4–10	1–10
Concrete — wet	10–20	100–1000
Freshwater	78 (25°C)–88	0.1–10

As the GPR antenna passes along a surface, it transmits an electromagnetic wave into the medium. When the electromagnetic wave encounters the interface of two materials of differing relative dielectric constants, part of the energy from that wave passes through while the rest of the wave is reflected to the antenna, which also acts as a receiver. The time it takes for the incident wave leave the antenna, be reflected off a medium, and subsequently return to the antenna is called the two-way travel time. The magnitude of the measured signal amplitude can be approximated by the reflection coefficient, for low-loss materials with high GPR frequencies using Equation 2.1 (Mehta and Monteiro 2013).

$$R = \frac{\sqrt{\kappa_1} - \sqrt{\kappa_2}}{\sqrt{\kappa_1} + \sqrt{\kappa_2}} \tag{2.1}$$

where

R = the reflection coefficient;

κ_1 = the relative dielectric constant of the first material the wave passes through; and

κ_2 = the relative dielectric constant of the 2nd material the waves passes through.

From this equation, one may observe that the most prominent signals reflected to the receiver are those that occur at the interface of two materials with a high dielectric contrast. The relative dielectric contrast of steel mathematically approaches infinity, making the dielectric contrast between reinforcing steel and concrete practically infinite. Thus, the signal reflected by reinforcing steel can be the most pronounced reflection observed in a concrete bridge deck. GPR data collected perpendicular to the direction of the reinforcing steel are imaged as hyperbolas in the resulting “cross-sectional views”, or

B-scans, of the deck, such as that in Figure 2-4. If the GPR antenna is positioned directly above a steel reinforcement and oriented such that it is pushed parallel to the reinforcement, a straight line is observed at the level of the reinforcement in a B-scan. The horizontal black and white lines shown at the top of the radar profile in Figure 2-4 corresponding to the direct air and direct ground waves. The direct air wave is the first wave that arrives at the receiver, immediately travelling through the air from the transmitter. Moreover, the direct ground wave is the second wave to arrive at the receiver, leaving the transmitter, travelling along the concrete surface, and returning to the receiver.

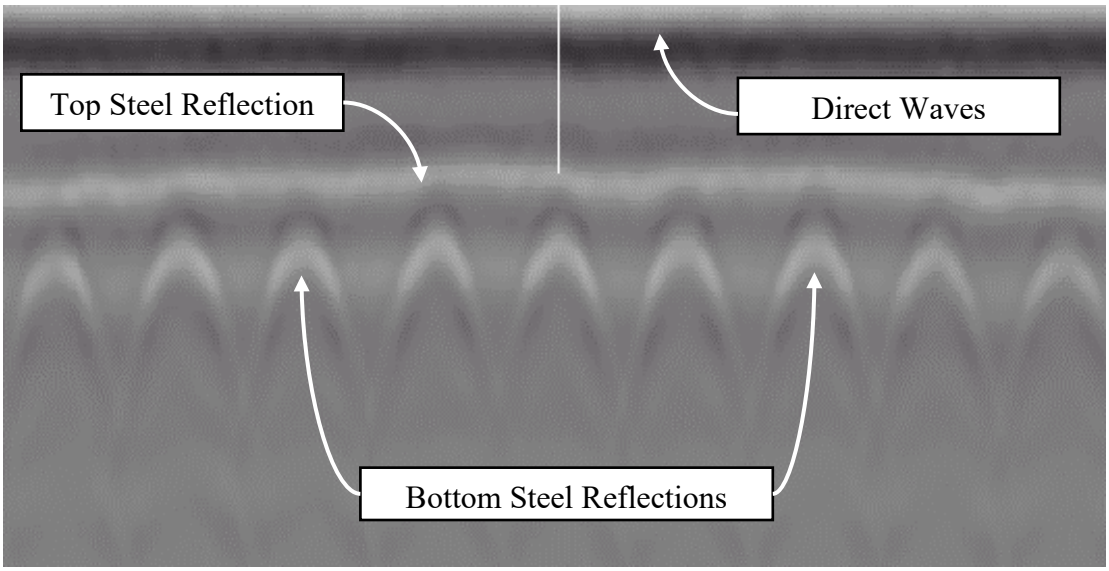

Figure 2-4: GPR Scan of a Concrete Bridge Deck

GPR is a compelling NDT method to many DOTs because it allows for a rapid evaluation of the condition of a reinforced concrete bridge deck. It is not necessary to alter the wearing surface of the deck as one would have to when using other NDT methods such as ground-coupled IE. Additionally, ground-coupled measurements can be collected by pushing a cart with an antenna affixed to the bottom, or an antenna may be attached to a

vehicle for air-coupled measurements at high speeds. Accordingly, much research conducted in the recent decades has focused on how best to correlate the results of GPR surveys with the true state of deterioration of bridge decks. A laboratory GPR survey of a fabricated concrete slab with a hand cart can be seen in Figure 2-5.

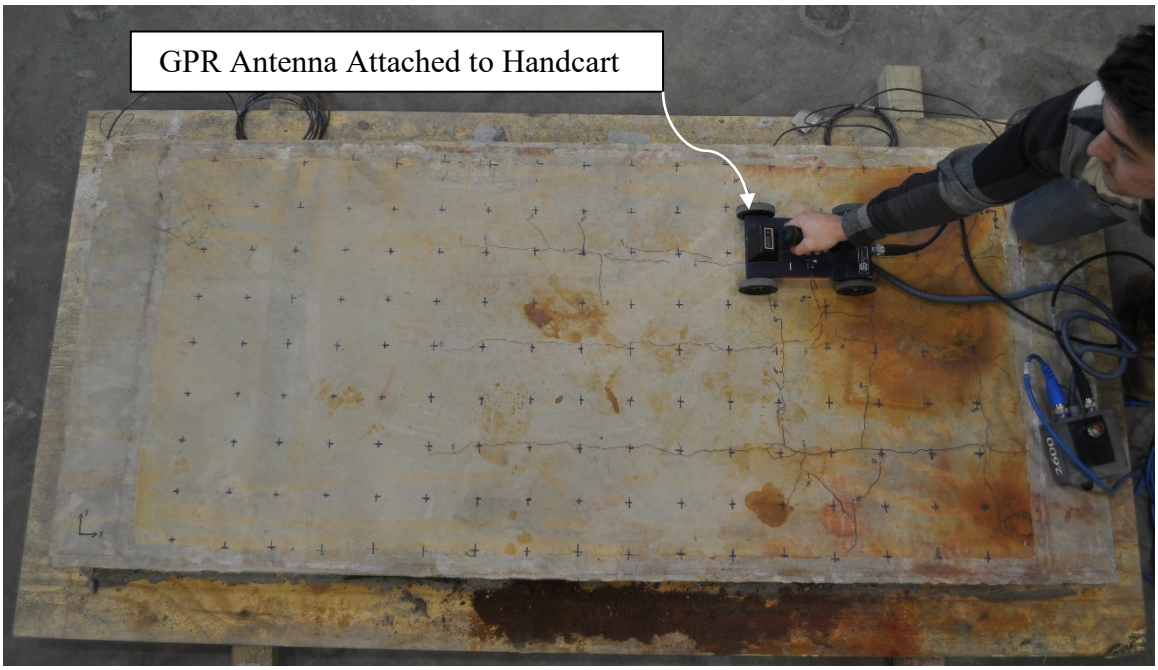

Figure 2-5: GPR Evaluation of Deteriorated Laboratory Specimen

2.3.2 Impact Echo

The IE method is one form of nondestructive stress wave propagation methods that aims to locate differences in elastic properties that are indicative of flaws in a tested element. To nondestructively evaluate a structure using stress waves, a harmless impact force is applied to the surface of an element, resulting in longitudinal (P) and transverse (S) body waves as well as surface (R) waves. In the IE method, these body waves propagate in compression and shear throughout the medium, reflecting off geometric boundaries and subsurface irregularities back towards the surface. Within concrete bridge decks, these

irregularities can be caused by delaminations, voids, honeycombing, and other internal defects. Reflected waves cause displacements at the surface, which are recorded using a displacement transducer. Waves continue to reflect off the surface, internal flaws, and the other exterior sides, creating a transient resonance condition that allows for the detection of defects (Sansalone 1997). Impact-echo testing can be conducted using either "ground-coupled" or "air-coupled" technologies. In ground-coupled impact echo testing, the transducer is in contact with the surface of the tested element, thus coupling the system with the ground. Conversely, in air-coupled impact echo evaluations, rather than using a displacement transducer, a microphone is suspended slightly over the tested surface to records acoustic waves associated with leaky surface waves generated by impact. As ground-coupled impact-echo testing has historically been slow given the need to ensure good contact between the transducer and concrete via grounding down the abrasive surface, air-coupled impact echo has been receiving more attention as a faster testing procedure.

After testing, recorded data are processed into the frequency domain using a Fast Fourier Transform, and the following equation, reported by Sansalone (1997), is used to estimate the depth from which the wave was reflected:

$$T = \frac{\beta C_p}{2 f_p} \tag{2.2}$$

where

T = the depth to the reflecting interface, units of length;

β = factor for the cross-sectional geometry of the tested element, 0.96 for a slab;

C_p = the velocity of the P wave in concrete, units of length per time; and

f_p = the frequency of the first transient mode, units of frequency.

To accurately estimate the depth to a defect, one must confidently know the depth of the tested element to calibrate the P wave velocity. Once that has been determined, measurements may be taken at any point on the slab, peak frequencies can be identified, and the depth to the peak reflections may be calculated using Equation 2.2. A schematic illustrating the IE method can be seen in Figure 2-6.

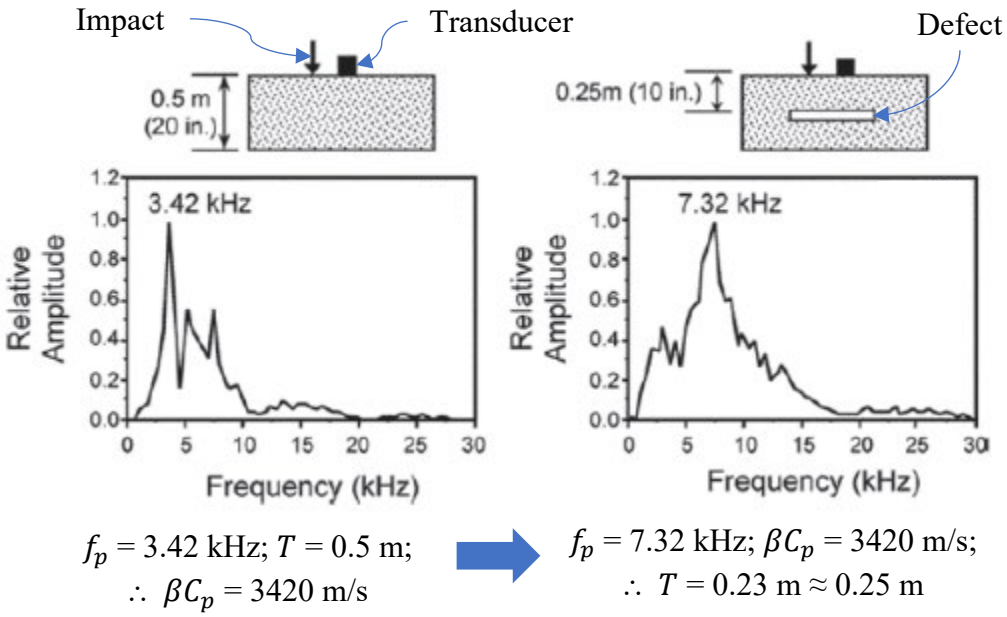

Figure 2-6: Validation of IE Method on Concrete Slabs (Adapted from ACI Committee 228 2013)

An IE evaluation of a laboratory specimen suspected to be heavily delaminated from corrosion can be seen in Figure 2-7. For this particular evaluation, both the source of impact and the transducer were housed in the same handheld testing apparatus. Surface

displacements resulting from impact and accompanying frequency spectra were displayed on the shown data acquisition system.

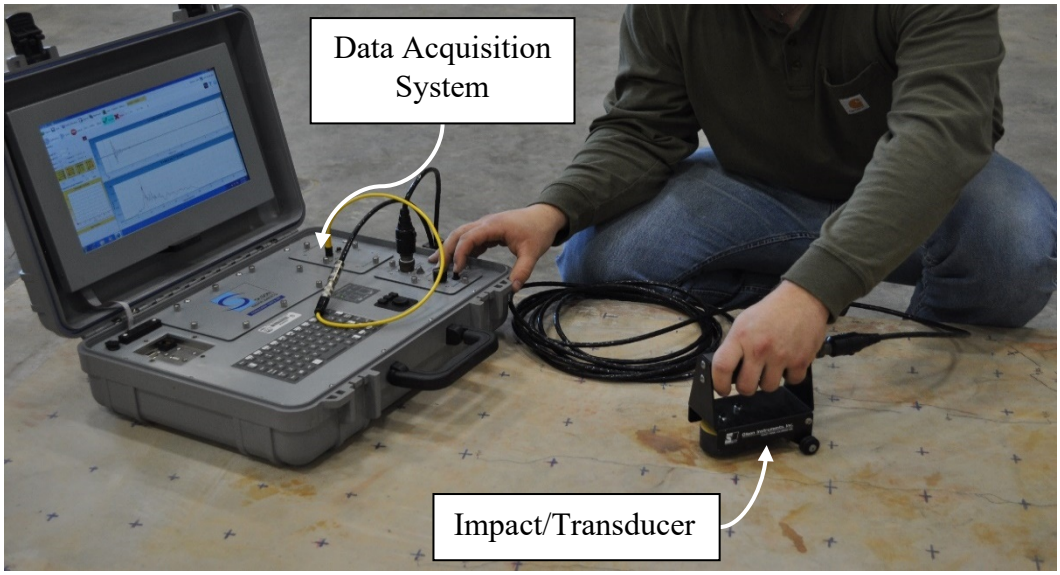

Figure 2-7: IE Evaluation of Deteriorated Laboratory Specimen

The IE method has chiefly been used in concrete bridge deck condition assessments to determine the location and extent of shallow delaminations, cracks, voids, honeycombing, and surface-opening cracks (Sansalone 1997). Despite the accuracy with which IE can identify many of these defects, concrete bridge deck deterioration evaluation with this method can suffer from several limitations. Adequately mapping the extents of a defect can require many closely spaced testing points. Additionally, the abrasive surface of the concrete deck may need to be ground down to allow for sufficient contact with the impacting instrument. These restrictions cause the IE method to be relatively slow in comparison with other methods that do not suffer from these limitations, such as GPR and IRT.

2.3.3 Infrared Thermography

Infrared thermography relies on thermal anomalies in electromagnetic radiation to detect defects in a concrete element. Any object with a temperature above absolute zero will radiate heat to its surroundings through electromagnetic waves. In this NDT method, an infrared camera is used to measure the surface radiation of an object to develop its surface temperature profile. The emissivity of a material quantifies how effectively it can radiate heat. Strictly speaking, the emissivity of a material is a surface property that is defined as the ratio of the energy that can be radiated by a material compared to that of a perfect blackbody (Malhotra and Carino 2003). Accordingly, surfaces that are dark and rough have a higher emissivity than smooth, shiny surfaces. Concrete has a high emissivity, allowing IRT to be an effective technique in imaging irregular radiation that can be caused by subsurface abnormalities.

As in all materials, within a concrete bridge deck, thermal energy can be transferred from warmer to cooler areas through conduction, convection, and radiation. The conductive resistance of concrete is significantly less than that of either convection or radiation such that conduction dominates heat transfer in concrete (Malhotra and Carino 2003). Under uniform heating, a concrete bridge deck can exhibit localized temperature differences (hot/cold spots) that are indicative of voids and delaminations. Air-filled voids and delaminations reduce the localized conductivity of the deck such that the surface temperatures recorded over these defects are irregular because of poor conduction. Thus, conductive heat flow in the vicinity of the defects is relatively slow in comparison to that in sound portions of concrete, creating “hot spots” when the deck is heating during the day

and “cold spots” during the evening when it is cooling. This behavior is illustrated in Figure 2-8.

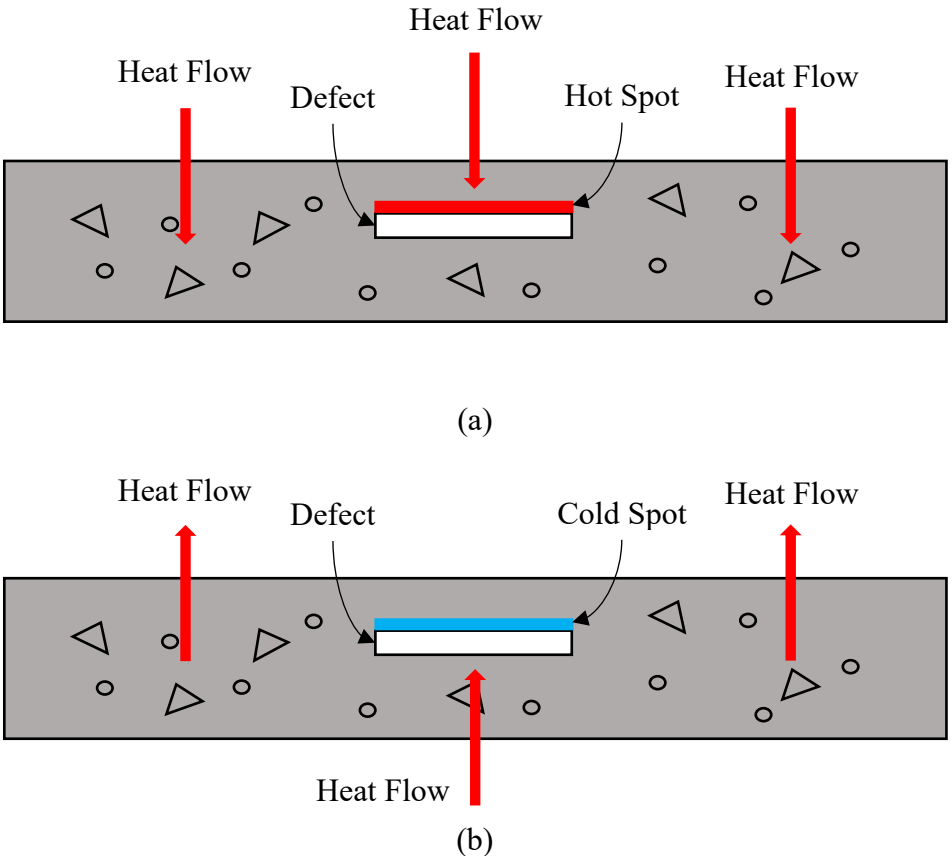

Figure 2-8: Effect of Defects on Deck Temperature Distribution during (a) Heating and (b) Cooling (Adapted from ACI Committee 228 2013)

An infrared camera with sufficient precision is used to image the surface thermal profile of a bridge deck in an IRT evaluation. Similar to GPR, IRT is an appealing NDT method to DOTs for evaluating concrete bridge decks because a thermal camera can be attached to a vehicle, allowing for a relatively rapid condition assessment. Additionally, no alteration of the deck wearing surface is required to perform the evaluation. Nonetheless, environmental factors such as surface cooling through convection from wind

and sporadic cloud coverage can inhibit accurate condition assessment with IRT. An IRT evaluation of a laboratory concrete specimen with a novel cart can be seen in Figure 2-9.

Figure 2-9: IRT Evaluation of Deteriorated Laboratory Specimen

2.3.4 Half-Cell Corrosion Potential

When assessing whether embedded reinforcement is actively corroding or passive, the half-cell corrosion potential method is implemented. In the HCP method, the potential difference between two half-cells is measured using a high impedance voltmeter. Within each half-cell, an electrode is submerged in an electrolyte solution, allowing for a redox reaction to occur which creates a potential difference between the anode and cathode in the half-cell. In this method, a reference electrode with a stable and reproducible potential, typically a copper-copper sulfate (CSE) electrode, is used in the half-cell that is touched to the concrete surface at locations of interest (ASTM C876 2015), as illustrated in Figure 2-10. The other half-cell is the concrete bridge deck, in which the reinforcing steel acts as

the electrode and the pore solution (filled with Cl^- and SO_4^- anions) is the electrolyte (Gucunski et al. 2013).

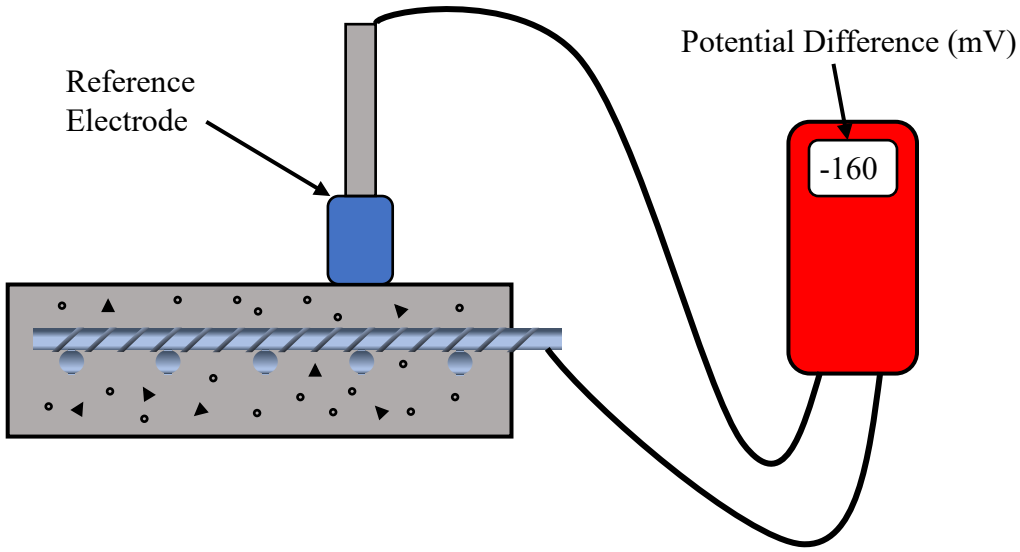

Figure 2-10: HCP Experimental Setup

To measure the potential difference between the two half-cells, the reference electrode is connected to the negative lead of a voltmeter and the positive lead is connected to the reinforcement mat or a piece of metal that is known to be in contact with the reinforcement. The circuit is complete once the reference electrode touches the surface of the deck. By moving the reference electrode to different locations along the surface of the deck, spatial electric potential difference measurements may be recorded to produce a contour map which can identify areas of probable corrosion. Half-cell potential measurements can be collected on a point-by-point basis (as illustrated in Figure 2-10) or using a rolling wheel electrode, such as that used in the evaluation shown in Figure 2-11. Interpreting half-cell corrosion potentials has become a rather debated topic. Accordingly, it will be discussed in the literature reviewed presented in Chapter 3 of this document.

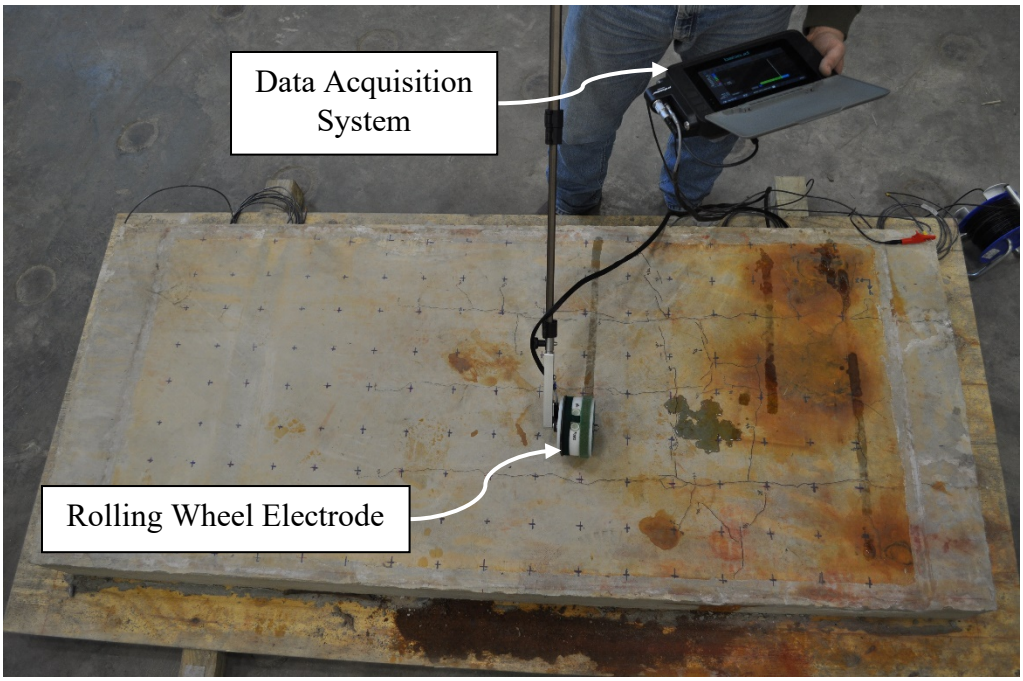

Figure 2-11: HCP Evaluation of Corroded Laboratory Specimen

The HCP method suffers from several limitations that can skew the ability of these potential thresholds to characterize the corroded state of the reinforcement mat. Within evaluations of concrete bridge decks, the sensitivity of the half-cell potential measurement to the moisture content of concrete is a primary concern. The higher the degree of saturation of the concrete, the more negative the potentials (Vassie 1978). ASTM C876 (2015) acknowledges the effect of moisture on the HCP method, noting that elements without sufficient moisture (such as in arid environments) can raise the concrete resistivity substantially, precluding an accurate assessment of reinforcement corrosion with this method. Furthermore, in certain saturated environments that preclude oxygen from reaching embedded reinforcement, measured potential differences may be extremely negative, falsely indicating active reinforcement corrosion where it cannot exist (since oxygen is not available). Additionally, Mehta and Monteiro (2013) note that

microcracking around reinforcing steel can lead to localized corrosion which changes the concrete resistivity, thus affecting the potential measurement. Stray currents leaking into a reinforced concrete element may also affect half-cell potential measurements (ASTM C876 2015).

2.3.5 Electrical Resistivity

Whereas one may only obtain a probability of active reinforcement corrosion from the HCP method, the electrical resistivity (ER) method (sometimes referred to as surface resistivity in literature) offers an estimation of the rate of corrosion of reinforcement, which is particularly important to DOTs planning bridge deck repairs. Since the ionic pore solution of concrete serves as the transport mechanism for corrosion current among anode/cathode pairs in reinforcing steel (Gucunksi et al. 2013), the electrical resistivity of concrete influences how quickly the current can travel—the lower the resistivity, the faster the current. Accordingly, the ER method aims to accurately measure concrete resistivity at discrete locations to estimate the rate of corrosion of reinforcing steel. Before the corrosion process begins, resistivity measurements can be collected to assess the resistance of a saturated concrete specimen to fluid transport (ACI Committee 228 2013).

Classical resistance used in Ohm's Law is not a material property; rather, it is dependent on the geometric properties of the measured object as well as the material resistivity (Mehta and Monteiro 2013). It is inconvenient to use the resistance as an indication of corrosion activity; thus, manipulations of Ohm's Law and the relationship between resistance and material resistivity allow for an estimation of material resistivity based on electrical current and potential difference. A common technique for measuring concrete resistivity with the ER method is the Wenner technique. Implementing the

Wenner technique in a four-probe resistivity instrument, a current is induced and measured between two outer probes when in contact with the concrete surface, as illustrated in Figure 2-12. A voltmeter measures the potential difference between the two inner probes.

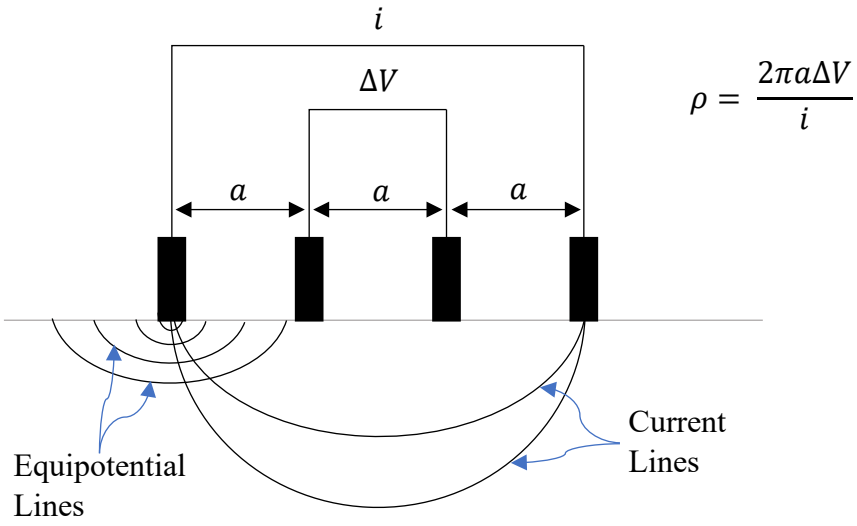

Figure 2-12: Measurement of Concrete Resistivity Using the Wenner Technique (Adapted from Broomfield and Millard 2002)

Using the potential difference and current measured with the instrument, the material resistivity can be calculated as follows (Mehta and Monteiro 2013):

$$\rho = \frac{2\pi a \Delta V}{i} \tag{2.3}$$

where

ρ = the material resistivity, Ω·m;

a = the spacing between instrument probes, m;

ΔV = the measured potential difference between the inner probes, V; and

i = the current measured between the outer probes, A.

An ER evaluation of a concrete specimen distressed from corrosion can be seen in Figure 2-13.

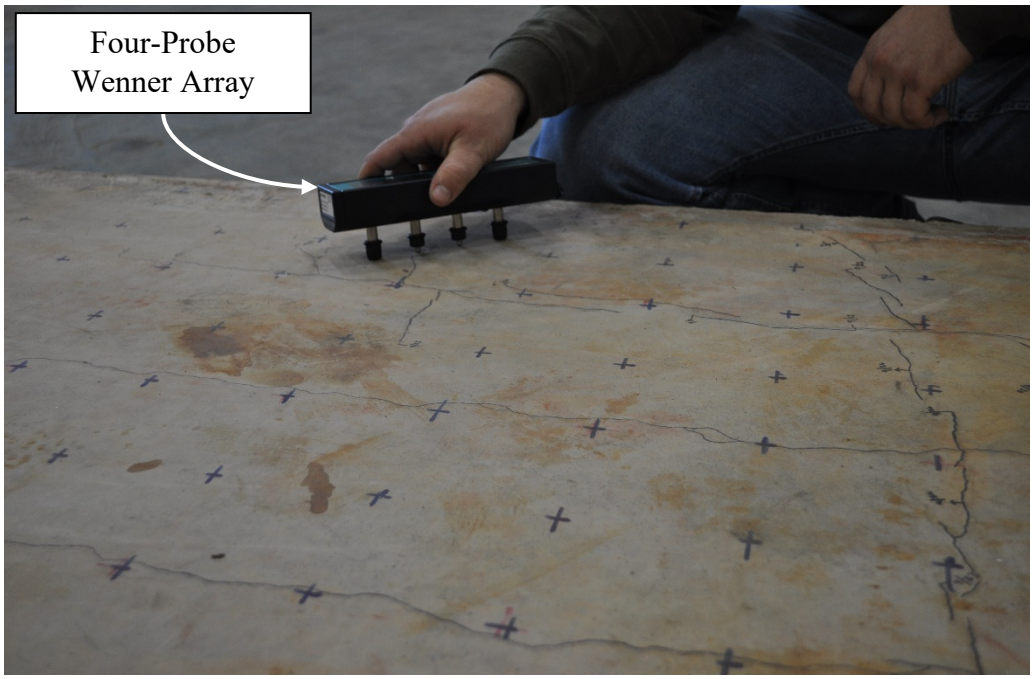

Figure 2-13: ER Evaluation of Deteriorated Laboratory Specimen

Correlation between concrete electrical resistivity and corrosion rate of reinforcing steel is empirically developed from experimental work. There is currently no ASTM specification pertaining to the in-place measurement of concrete electrical resistivity as an indication of the rate of corrosion. Literature concerning resistivity measurements in concrete elements offer guidance on the selection of threshold values to signify corrosion rates, which will be elaborated upon in Chapter 3 of this document.

Aside from uncertainty regarding the best threshold values to use to identify corrosion rates, the ER method has several other limitations that can worsen the accuracy of field measurements. Gowers and Millard (1999) showed that (1) the geometry of the element, (2) poor electrical contact, (3) concrete inhomogeneity, (4) the presence of reinforcing steel, (5) surface layers of differing resistivities, and (6) ambient environmental conditions can affect Wenner resistivity readings of concrete elements. Difficulty in precisely determining the effects of these factors in the field preclude standardization of threshold resistivity values corresponding to rates of corrosion. Additionally, the ER method is disadvantageous from a speed perspective, as it requires wetting of the concrete surface and discrete tests between reinforcing steel to produce spatial contour maps of concrete electrical resistivity.

2.4 Synthesis of NDT Technologies to Assess Bridge Deck Condition

Concrete bridge decks are often distressed by more than one type of defect. Thus, depending on the appropriateness of any one NDT method in identifying different defects, DOTs may rely on a multi-technique approach to evaluate the condition of a bridge deck. For example, the HCP method may allow for accurate mapping of active reinforcement corrosion; nonetheless, the IE method may be better suited in identifying delaminations resulting from corrosion. Additionally, several NDT methods are often used in conjunction with one another to allow for greater confidence in the accuracy of produced spatial contour plots of deterioration. It is for this reason that the ER and HCP methods are often cooperatively implemented in concrete bridge deck corrosion inspections.

Chapter 3: Previous NDT Studies for Concrete Bridge Deck Condition Assessment

3.1 Introduction

The purpose of this chapter is to review studies pertaining to the state-of-the-art development and implementation of NDT methods in most effectively assessing the condition of concrete bridge decks. As DOTs often use a multi-technique approach to nondestructively evaluate bridge decks, researchers have investigated which NDT technologies are most beneficial when used independently or in conjunction with others. Several such studies are presented in the following sections. While these studies may also explore other NDT technologies apart from those elaborated upon in Chapter 2, conclusions regarding those technologies will be omitted from this chapter to facilitate a more pointed discussion of technologies explored in this thesis. Despite the widespread usage of NDT technologies by DOTs, there still exists uncertainty regarding the effectiveness of each NDT method in identifying different concrete defects. Accordingly, previous work aiming to explore the capabilities of the GPR, IE, IRT, HCP, and ER methods are summarized.

3.2 Previous Multi-Method NDT Research

A compelling argument proposed by many academics and other NDT operators is that no individual NDT method is capable of accurately identifying and characterizing all major forms of bridge deck deterioration (e.g. Gucunski et al. 2013). Accordingly, researchers have investigated the effectiveness of different NDT methods used in conjunction with one another in developing more accurate profiles of reinforced concrete bridge deck deterioration.

3.2.1 Kee et al. (2012)

Kee et al. (2012) performed a nondestructive evaluation of a fabricated 8 ft x 20 ft reinforced concrete bridge deck containing simulated delaminations and vertical cracks in El Paso, Texas. Thin (1–2 mm) foam and 12 mil polyester were used to simulate shallow (2.5 in.) and deep (6 in.) delaminations in the bridge deck while inserted cardboard was used to mimic vertical cracks in the deck. The deck was tested with novel air-coupled IE systems developed independently from one another by the University of Illinois and the University of Texas. The specimen was also evaluated with a commercially available, stationary IRT camera. Several noteworthy phenomena investigated by the authors included the effect of test grid spacing on the ability of air-coupled IE system to accurately detect delaminations and the influence of the time of testing with respect to sunrise on IRT measurements. Compelling conclusions from this study included the following: (1) air-coupled IE allows for a generally consistent and rapid nondestructive evaluation for frequency responses less than 5 kHz, (2) the effect of deep delaminations on the peak frequency observed using air-coupled IE does not appear to be consistent, (3) delamination defects smaller than twice the grid spacing are difficult to detect with air-coupled IE, (4) unlike air-coupled IE, IRT can accurately image the extent of shallow delaminations, and (5) overnight bridge deck cooling allows for the detection of both shallow and deep delaminations with IRT (Kee et al. 2012). The authors (2012) recommended the deployment of IE to identify the location of delaminations followed by IRT testing to determine the extent of those delaminations.

3.2.2 Gucunski et al. (2013)

As part of the Second Strategic Highway Research Program (SHRP 2), Gucunski et al. (2013) investigated the utility of NDT technologies in condition assessments of in-service bridge decks and representative laboratory specimens. Among those NDT methods included were GPR, IE, IRT, HCP, and ER. Through participation from ten teams in collecting/processing data, the overall utility of each NDT method was graded considering its 1) accuracy/precision, 2) speed, 3) ease of use, and 4) cost, in decreasing order of importance. Noteworthy conclusions from this study included: (1) no single NDT method is capable of detecting all prominent types of bridge deck deterioration (delamination, corrosion, vertical cracking, and concrete degradation), (2) IE, GPR, and IRT exhibit a fair-to-good level of accuracy in detecting/characterizing delaminations, (3) HCP, ER, and GPR exhibit a fair-to-good ability to detect corrosion and characterize its environment, (4) IE and GPR are generally successful in locating/characterizing concrete deterioration, and (5) IE, HCP, GPR, IRT, and ER were all graded as top technologies in the detection and characterization of bridge deck deterioration (Gucunski et al. 2013). If a DOT aims to obtain an overall condition assessment of a concrete bridge deck, the authors recommend the implementation of GPR.

3.2.3 Pailes and Gucunski (2015)

Pailes and Gucunski (2015) believed that the most complete assessment of a deteriorating bridge deck could be obtained through the use of multiple NDT methods. To facilitate a better understanding of the interdependent relationship among NDT data collected from various technologies in a multi-method evaluation, Pailes and Gucunski (2015) surveyed twelve bridge decks in the United States using ER, HCP, GPR, and IE. NDT evaluations

were conducted in both 2009 and 2011 to investigate potential changes in NDT data caused by time-dependent progression of bridge deck deterioration. Data collected from each method were also compared spatially with one another to identify the level of agreement in methods aiming to locate the same type of deterioration. Pailes and Gucunski (2015) concluded the following: (1) locations of deterioration identified using ER and HCP correlate well with zones of GPR signal attenuation, (2) ER/HCP and ER/GPR show strong agreement in spatial deterioration, (3) ER, HCP, and GPR measurements are highly repeatable over different years, (4) areas of low electrical resistivity serve as activation sites for future corrosion, and (5) a resistivity threshold less than 40 kΩ-cm creates an environment conducive to active reinforcement corrosion.

3.2.4 Meng et al. (2020)

Meng et al. (2020) aimed to evaluate the influence of different types of overlays on nondestructive corrosion evaluations using ER, HCP, and GPR. Seven 120 in. by 40 in. by 8 in. reinforced concrete specimens were constructed with simulated defects, each having a different overlay—asphalt with a liquid membrane, asphalt with a sheet membrane, asphalt without a membrane, silica fume-modified concrete, latex-modified concrete, epoxy polymer concrete, and polyester polymer concrete. The NDT methods were employed before artificial corrosion of reinforcement, after corrosion but before installation of the overlay, and after installation of the overlay. The three NDT methods confirmed that initially, no corrosion/corrosive environment existed; however, after accelerated corroding processes were implemented, the specimens exhibited active reinforcement corrosion and corrosive environments. NDT surveys collected after construction of the overlays allowed Meng et al. (2020) to conclude the following: (1) the

high resistivity of overlays precludes an accurate assessment of the rate of corrosion in reinforced concrete decks using ER, (2) the use of silica fume-modified concrete, asphalt with a liquid membrane, and polyester polymer as overlays may worsen the accuracy of GPR measurements in identifying corrosive environments, (3) the use of asphalt with a sheet membrane, asphalt without a membrane, latex-modified concrete, and epoxy polymer concrete as overlays does not preclude accurate detection of corrosive environments with GPR, (4) the epoxy polymer concrete, silica-fume modified concrete, and three asphalt overlays cause HCP measurements indicative of active reinforcement corrosion to be higher than -350 mV (the other two overlays did not affect this threshold), and (5) debonding between the overlays and concrete deck may not affect GPR and HCP measurements, unless the debonding thickness is large.

3.2 Previous Ground-Penetrating Radar Research

The development of GPR as a primary tool in nondestructive evaluations of concrete infrastructure has received great attention in the academic community, because of the technology's potential for rapid and cost-efficient deployment. Recent studies in exploring this potential for GPR implementation have aimed to (1) confidently determine which forms of bridge deck deterioration GPR is most effective in identifying and (2) develop new post-processing techniques to improve the accuracy of the method.

3.2.1 Scott, Rezaizadeh, and Moore (2001)

Scott, Rezaizadeh, and Moore (2001) conducted a phenomenology study, evaluating the capability of the HERMES GPR system to detect corrosion-induced delaminations, in continuation of research funded by the Federal Highway Administration (FHWA). Air gaps of controlled thickness were created in laboratory specimens by strategically cracking

the specimen or offsetting plates with shims. Regarding the HERMES GPR system, Scott, Rezaizadeh, and Moore (2001) concluded that, while the GPR system is capable of detecting air gaps on the order of 1.3 cm in thickness, it is not able to identify gaps of thicknesses comparable to that typical of corrosion-induced delaminations.

3.2.2 Barnes and Trottier (2004)

To evaluate the ability of GPR to estimate necessary deck repair quantities in supplement to traditional visual inspections, Barnes and Trottier (2004) conducted nondestructive evaluations of 24 in-service bridge decks. In conjunction with GPR measurements, both chain-dragging and HCP surveys were performed to serve as ground-truth bases off which to compare the accuracy of GPR in detecting delaminations and active reinforcement corrosion, respectively. In particular, the authors were interested in investigating the performance of GPR in identifying deterioration ranges in which visual inspection was typically least effective—10 to 50% of the deck area. Noteworthy conclusions from this study included: (1) within the range of 10 to 50% deterioration, the differences between the percentage of deteriorated deck between the GPR and chain drag surveys is insignificant; however, (2) there is little agreement in the locations of deterioration within this range, (3) on decks with less than 10% or greater than 50% deterioration, GPR surveys exhibit significant deviations in predicted quantities of repairs from that measured using chain dragging, and (4) precursors to deterioration which chiefly affect GPR measurements such as moisture and high concentration of chloride ions might partially explain substantial discrepancies between GPR surveys and ground-truth profiles (Barnes and Trottier 2004).

3.2.3 Barnes, Trottier, and Forgeron (2008)

In pursuit of providing a more accurate estimate of the area of corrosion-induced damage in a bridge deck using GPR, Barnes, Trottier and Forgeron (2008) conducted a study exploring the effect of variations in cover depth to the reinforcing steel on signal reflection amplitudes of the top layer of reinforcement. HCP and chain-dragging surveys were performed on six in-service bridge decks in Canada to serve as ground-truth bases off which to compare the accuracy of GPR surveys. The GPR datasets were post-processed using least-squares regression analysis of the 90^{th} percentile signal amplitudes to facilitate quantification of the effect of cover variations on signal amplitudes. By removing the effect of cover variation from the amplitude datasets, the authors hypothesized that the remaining scatter in amplitude values was chiefly caused by differences in moisture and chloride content within the cover layer. Barnes, Trottier, and Forgeron (2008) concluded that (1) for exposed reinforced concrete bridge decks, variations in cover depth can have a tangible effect on the ability to accurately interpret GPR data and (2) removal of the effects of cover variation in GPR surveys can allow for improved spatial correlation and damage quantity estimation to that reported in chain drag and HCP surveys.

3.2.4 Martino et al. (2015)

To facilitate the development of a universal GPR threshold that distinguishes between corroded and non-corroded reinforcing steel, Martino et al. (2015) analyzed GPR and HCP data previously recorded for a bridge deck removed from service, 17 artificially corroded slabs, and one in-service bridge deck. While ASTM C876 (2015) only provides a 90% probability that a location classified as corroded or non-corroded is not a false positive, the HCP surveys of these concrete specimens were still used as ground truth bases off which

to calibrate the GPR threshold for corrosion. A receiver operating characteristic (ROC) analysis was applied to the aforementioned concrete specimens separately to determine the optimal GPR threshold that allowed for maximum agreement between the GPR survey and its respective HCP survey. Martino et al. (2015) observed that optimal thresholds of -1.88 dB, -1.51 dB, and -1.76 dB for the removed bridge deck, laboratory slabs, and in-service bridge decks respectively resulted in between 70.59–91.11% agreement between GPR data and ground truth information.

The authors postulated that the average of the three GPR thresholds, -1.72 dB, may be an useful universal threshold to distinguish between corroded and non-corroded concrete (Martino et al. 2015). Applying this threshold to the three case studies resulted in a 91.11%, 70.59%, and 75.00% percentage agreement respectively, in order. The authors also concluded that ROC analysis can be used to accurately correlate GPR to HCP surveys to determine a GPR threshold that serves as the boundary of corroded and non-corroded areas (Martino et al. 2015).

3.2.5 Hong et al. (2017)

Hong et al. (2017) aimed to validate a new method for periodic monitoring of corrosion within reinforced concrete elements using GPR. The proposed method relied on aligning GPR images with a transformation matrix and normalizing the energy intensities recorded by the surveys for direct comparison with one another. Visual discrepancies between two spatial maps of energy distribution were hypothesized to be the result of corrosion of steel reinforcement. To validate this methodology, a portion of a 10 m by 4 m by 30 cm reinforced concrete slab located at BAM (Federal Institute for Material Research and Testing) in Berlin, Germany, was artificially corroded in select locations. GPR and HCP

surveys were conducted before and after artificial corrosion to observe the effect that the process had on respective measurements. The HCP surveys were used as ground truth bases off which to compare the accuracy of GPR measurements. After post-processing the GPR surveys with the aforementioned alignment/normalization method, Hong et al. (2017) visually inspected the differences in energy intensity between the two resulting maps and concluded the following: (1) the proposed post-processing method for GPR images allows for the discernment of changes in signal intensity among GPR images representative of different times, (2) HCP surveys confirm that the unchanged area in GPR signal intensity correspond with non-corroded areas, and (3) HCP surveys confirm that areas in which GPR signal intensity significantly decrease correspond with areas having a high risk of active reinforcement corrosion.

3.2.6 Sultan and Washer (2018)

In response to decades of confusion regarding whether GPR had the ability to directly detect delaminations in concrete bridge decks, Sultan and Washer (2018) conducted reliability analyses of three GPR datasets. GPR evaluations were performed on a laboratory mock-up specimen with simulated delaminations, an abandoned bridge deck with a low chloride concentration, and an in-service deck with high chloride concentration. Reliability analyses were performed on the depth-uncorrected amplitude datasets as the cover variation was negligible, per cover meter measurements. Analyses of the GPR surveys from the mock-up specimen and abandoned bridge deck respectively yielded 0.508 and 0.475 probabilities of correctly distinguishing between sound concrete and delaminated concrete, in accordance with ASTM D6087-08 (2015) testing specifications. The in-service bridge with high chloride concentration exhibited little improvement in

correctly identifying delaminated concrete, with a probability of 0.67 (i.e. one out of every three conclusions would be incorrect). Based on these findings, Sultan and Washer (2018) concluded the following: (1) in accordance with ASTM testing procedures for detecting bridge deck deterioration, GPR is incapable of distinguishing the difference between delaminated and sound concrete, and (2) the increase in probability of accurate delamination discernment with increased chloride levels suggests that GPR responds to the presence of a corrosive environment, rather than actual damage.

3.2.7 Wong and Poon (2018)

To support further implementation of GPR in evaluations aimed at identifying corrosion-induced delaminations, Wong and Poon (2018) conducted accelerated corrosion via impressed current on steel reinforcement in a test specimen. The specimen was cast in portions, joined at a vertical cold joint. One portion was prepared using 4% saline water to facilitate chloride-induced corrosion while the other portion was prepared using tap water. Reinforcement reflection amplitude and wave velocity analyses were used to compare the respective responses of GPR over the two portions. Little change in wave velocity was observed between the two portions; however, substantial differences in reflection amplitude were noticed. Wong and Poon (2018) hypothesized that this difference was due to (1) backscattering from surface crack air interfaces developed from accelerated corrosion, and/or (2) the presence of rust particles which reduced the dielectric contrast at wave reflection. It was concluded that GPR amplitude analysis facilitated effective identification of corrosion within reinforced concrete elements, and changes in amplitude were likely caused by surface cracking (Wong and Poon 2018).

3.3 Previous Impact-Echo Research

The IE method was developed to address the need to reliably locate delaminations of varying depths in concrete elements. Since its validation by Sansalone (1989), the IE method has been generally well-accepted as being capable of accurately locating delaminations. A desirable feature of impact echo in locating subsurface defects is that only one side of a structure needs to be accessed, unlike other prominent methods such as ultrasonic pulse velocity. However, in comparison with more rapid NDT methods such as GPR and IRT, discrete testing with the IE method can be slow and cumbersome. This weakness of the IE method has inspired studies aimed at developing rapid, air-coupled IE methods that do not sacrifice its accuracy in delamination detection.

3.3.1 Sansalone and Carino (1989)

Sansalone and Carino (1989) developed the IE method as an alternative means of identifying delaminated zones of concrete. Difficulties associated with traditional acoustic-impact methods such as operator subjectivity in interpreting results were precluded in the IE method by the consistent impact which the technology imparted on a concrete surface. In this study, a mock-up slab with embedded plastic sheeting to simulate delaminations was tested along with two asphalt-covered specimens that were distressed by corrosion. The results of the IE testing on the corroded specimens were verified by drilling inspection holes at the locations of the delaminations. For the mock-up slab, the locations and dimensions of the simulated delaminations were accurately determined using the IE method. Additionally, the depth and location of delaminations reported using the IE method agreed well with manual verification from inspection holes. Several important conclusions from this study included: (1) the IE method is a valid alternative method to

sounding for locating delaminations in concrete specimens, regardless of whether there exists an asphalt overlay or not, and (2) for shallow delaminations, the contact time for the impact must be shorter than for deeper delaminations to excite a high-frequency response at the shallow depth (Sansalone and Carino 1989).

3.3.2 Cheng and Sansalone (1993)

To understand the behavior of a delaminated plate subject to an impact load and further validate the IE method, Cheng and Sansalone (1993) conducted experimental studies and a numerical analysis of delaminated concrete plates. The authors hoped to understand the influence of the depth of delamination, the position of the impact relative to the plane of the delamination, and the size of the delamination on the response measured with the IE method. This investigation was complemented with the validation of the IE method on an in-service bridge deck with the help of the New York State Department of Transportation (NYSDOT). Hammer sounding was performed on the same bridge to serve as a ground truth basis from which to compare the results of IE testing; the two were in excellent agreement. Important conclusions from this study included the following: (1) the impact response of concrete plates with shallow delaminations excites at least one flexural mode of vibration above the delamination, allowing for the difference in behavior observed between shallow and deep delaminations, (2) the elastic properties of the concrete in conjunction with the depth, dimensions, and location of the delamination with respect to the impact influence the impact response of the plate, and (3) the IE method provides a valid alternative to hammer sounding to locate concrete delaminations, especially since the latter can only identify shallow delaminations (Cheng and Sansalone 1993).

3.3.3 Cheng and Sansalone (1995)

To further validate the utility of impact echo in nondestructive evaluations of concrete elements, Cheng and Sansalone (1995) conducted numerical and experimental studies aimed at determining the minimum delamination thickness that could be detected using impact echo. Impact-echo testing was conducted over delaminations created in two specimens by mechanical jacking and expansive cement. The results were used in nonlinear fracture analysis modeling to determine that 0.025 mm is about the average minimum delamination thickness which can be detected through impact-echo testing (Cheng and Sansalone 1995).

3.3.4 Tawhed and Gassman (2002)

Using two damaged concrete bridge decks removed from service, Tawhed and Gassman (2002) conducted impact-echo testing of the decks to assess the ability of impact echo to locate internal damage. One slab was statically loaded to failure; corresponding impact-echo measurements were recorded before and after loading. Moreover, the other slab was dynamically loaded to failure using cyclic loading. Additionally, impact-echo testing was conducted after each cycle of the dynamic load testing. Tawhed and Gassman (2002) observed significant reductions in compression wave (P-wave) velocities in locations of the decks that became progressively damaged during loading. Accordingly, they concluded that impact echo could be used to assess the quality of concrete in a structure during its service life by monitoring variations in compression wave velocity (2002). Significant reductions in compression wave velocity might then warrant the removal of the damaged element from service.

3.3.5 Zhu and Popovics (2007)

In this study, the results from testing of concrete slabs containing artificial delaminations and voids using a novel air-couple IE system were presented. Testing was conducted over both metal and rigid plastic ducts with simulated grouting voids to assess the capability of air-coupled impact echo system to detect voids. From their testing, Zhu and Popovics noted that (1) air-coupled IE can be used to detect both shallow (60 mm) and deep (200 mm) delaminations, (2) with progressively closer spacing, air-coupled IE can be used to accurately determine the areal extent of shallow but not deep delaminations, (3) comparative analysis of frequencies measured from thin-walled metal ducts can allow for differentiation of zones of full, partial, or zero grouting, and (4) the filling condition of a rigid plastic duct could not be determined from the air-coupled IE testing.

3.3.3 Guthrie et al. (2019)

Under the funding of the Utah Department of Transportation (UDOT) and the U.S. Army Dugway Proving Ground, Guthrie et al. (2019) developed an automated, air-coupled IE testing device to rapidly locate concrete bridge deck delaminations. The device was utilized along with chain dragging (as a ground truth) on a concrete bridge deck in Northern Utah. The eleven-span bridge had a total length of 434 m, requiring four man-hours to scan the bridge with the air-coupled IE device and more than 30 man-hours to do so with chain dragging. In parallel with a visual analysis of the two datasets, a quantitative analysis was used to develop a universal threshold of relative energy of echoes to discern between delaminated and sound concrete. This value was empirically determined to equate the average areas of delaminations in concrete between the two methods. Ten of thirteen inspection borings confirmed the presence of delaminations that were predicted by both

NDT methods. Noteworthy conclusions from this work included: (1) the air-coupled impact-echo system was capable of scanning the bridge deck seven times faster than traditional chain dragging, (2) spatial plots of delaminations produced from chain dragging and visual inspection of IE data correlated well with one another, (3) the threshold value of 1.415×10^{-5} allowed for ten of the thirteen test sections to estimate delaminated areas within 3 percentage points of one another, and (4) the developed air-coupled IE device may not be well-suited to locate deep delaminations (Guthrie et al. 2019).

3.4 Previous Infrared Thermography Research

The use of IRT as a means of nondestructively evaluating concrete bridge decks has been under investigation for several decades because, like GPR, it has the potential to allow for a rapid evaluation of bridge decks without removal/modification of the wearing surface. Past studies have chiefly focused on the capacity of IRT to image subsurface delaminations, voids, and honeycombing. In addition to evaluating the capacity of IRT to detect the foregoing defects, past studies have explored the influence of the time of testing relative to sunrise/sunset and ambient conditions (e.g. cloud coverage and wind velocity) on IRT evaluations.

3.4.1 Cheng, Cheng, and Chiang (2008)

With partial funding from the National Science Council, Cheng, Cheng, and Chiang (2008) investigated the ability of IRT to image subsurface voids and honeycombing of varying depths/dimensions in concrete slabs and elements with tile bonded to concrete. Mock-up specimens with simulated voids and honeycombing were constructed to be heated with halogen lamps supplying 2000 watts of power. Honeycombing was simulated within the specimens by filling the voids that extended from the termination of cover to the bottom of

the specimen with coarse aggregate. Each specimen was heated for five minutes with the system of halogen lamps, and the surface temperature profile was measured using a NEC TH7102 infrared camera, capable of detecting temperature differences on the order of 0.08°C. Noteworthy conclusions pertaining to the use of IRT on concrete slabs included: (1) heating sources can be used to create surface temperature differentials detectable with IRT, (2) the smaller the depth of subsurface defect, the more quickly the peak temperature under heating is reached, (3) the larger the area of the defect, the greater the surface temperature differential recorded, and (4) IRT provides little quantifiable information regarding the depth of a defect (Cheng, Cheng, and Chiang 2008). Accordingly, Cheng, Cheng, and Chiang (2008) recommended the use of an elastic wave method such as IE to determine the depth of a defect identified using the IRT method.

3.4.2 Washer, Fenwick, and Bolleni (2010)

Under the funding of the Montana, Texas, and New York DOTs, Washer, Fenwick, and Bolleni (2010) investigated the effects of direct solar loading on the detection of subsurface defects using IRT. A 2.4 m by 2.4 m concrete block with a thickness of 0.9 m was constructed with Styrofoam sheets simulating internal defects. The 13 mm thick, 300 mm by 300 mm sheets were placed at varying depths to explore the effect of defect depth on the time of maximum thermal contrast and the value of that contrast. A FLIR S65 thermal camera with a sensitivity of 0.08°C imaged the block every ten minutes while a weather station was used to record the average ambient temperature, wind speed, relative humidity, and solar loading. After several months of imaging, the resulting data were analyzed to correlate total and maximum solar loading with the thermal contrast of each defect. Washer, Fenwick, and Bolleni (2010) observed that: (1) the optimum time of day to image

subsurface defects varied between 5.67 hours after sunrise for a 25-mm-deep defect to about 9 hours after sunrise for a 127-mm-deep defect, (2) total solar loading energy correlated better ($R^2 = 0.75$) to maximum thermal contrast than maximum solar loading ($R^2 = 0.55$), and (3) on some days, a positive thermal contrast (hot spot) may not exist.

3.4.3 Vaghefi et al. (2013)

As part of the *Bridge Construction Assessment Using Remote Sensors* program, Vaghefi et al. (2013) investigated the use of a three-dimensional optical bridge evaluation system (3DOBs) in parallel with IRT to respectively evaluate the surface and subsurface conditions of a concrete bridge deck. In support of this objective, an automated post-processing method was developed to calculate the delaminated area of a bridge deck, based on the number of pixels associated with temperatures larger than a threshold value input by the user. The 3DOBs system and a FLIR SC640 thermal camera were respectively attached to a moving truck and push-cart to facilitate relatively rapid evaluation of the Mannsiding Road Bridge in Michigan. A chain dragging survey was conducted to initially serve as a ground truth basis off which to compare the IRT survey. However, stark discrepancies in total delaminated area as reported with chain dragging between two surveys performed within three years of one another compelled the authors to retrieve cores of the deck to evaluate the accuracy of IRT. Of the ten cores, seven showed visible damage while only four of those cores were shown as delaminated from infrared imaging. Two of the delaminated cores that were not detected using IRT were defected at depths of 3 in. or deeper. However, a different core which was delaminated at 3 in. was detected using IRT. Vaghefi et al. (2013) concluded that: (1) the use of 3DOBs and IRT allows for faster bridge

inspection that one would obtain with traditional methods and (2) IRT is a well-established tool in nondestructively evaluating concrete bridge decks.

3.4.4 Raja et al. (2020)

Raja et al. (2020) sought to investigate the influence of ambient environmental conditions and delamination characteristics (size, depth, thickness, etc…) on thermal imaging through experimental processes and numerical analyses. Two mock-up specimens with delaminations simulated by 5 mm thick Styrofoam were heated by four 500 W halogen lamps and imaged with a FLIR 1050sc infrared camera, while being cooled at several wind speeds supplied by a fan. The heat flux on the slab surface was recorded for both sixty minutes of heating and cooling to facilitate the development of a correlation between thermal loading and thermal contrast of the surface. A numerical model was calibrated to the results of the experimental studies, and parametric studies were then performed to explore the influence of the rate of heat flux on the thermal contrast of the surface. From the experimental methods and numerical analyses, Raja et al. (2020) concluded the follow: (1) an increase in wind velocity corresponds with a decrease in thermal contrast with deeper delaminations being more severely affected, (2) the thermal contrast increases with the total heat input but can also be affected by the heat flux rate/duration and the geometries of the delamination, (3) a minimum thermal contrast of 0.5°C proposed by ASTM D4788-03 (2013) is a safe threshold for detecting delaminations in concrete elements, (4) there exists a linear relationship ($R^2 = 0.99$) between the square of the delamination depth and total heat input required to generate a 1°C thermal contrast, (5) the smaller a delamination is, the higher the total heat input required under a constant low heat flux (this effect diminishes as the delamination area increases), and (6) a total heat input of 0.68 kW-h/m^2

from the sun can generate a thermal contrast of 1°C for delaminations up to 63 mm below the surface.

3.5 Previous Half-Cell Corrosion Potential Research

The use of half-cell potential measurements in identifying active reinforcement corrosion in reinforced concrete elements has been implemented substantially since the approach was monumentally validated in the late 60's and early 70's by the Highway Research Board (e.g. Stratfull 1973; Spellman and Stratfull 1973). The results of these studies are referenced in the currently approved ASTM C876 (2015) specification concerning the interpretation of half-cell potentials as an indication of the probability of active reinforcement corrosion. Using what ASTM C876 (2015) terms the "numeric magnitude technique" one would directly interpret potential measurements obtained using a copper/copper sulfate electrode as shown in Table 3-1, provided that:

1. The carbonation front has not arrived at the level of the embedded steel;
2. Unless shielded from drying since casting, indoor concrete has been frequently wetted;
3. Neither the moisture nor oxygen content of outdoor reinforced concrete are highly variable; and
4. Numeric magnitude criteria are not used to evaluate changes in corrosion activity over time in a rehabilitated structure should the rehabilitation effort have caused the moisture content, oxygen content, or both at the level of embedded steel to change over time.

Table 3-1: ASTM Thresholds for Corrosion Probability in HCP Measurements (ASTM C876 2015)

Measured Potential (mV – CSE)	Probability of Corrosion
> -200	Less than 10%
-200 to -350	Uncertain
< -350	Greater than 90%

Given the many factors that can affect half-cell potential measurements, the effectiveness of applying the results from the early Highway Research Board has been debated. Those that reject the use of the ASTM C876 (2015) criteria or other such thresholds may be proponents of other techniques of potential interpretation, such as the "potential difference technique" (ASTM C876 2015) in which the rate of change of potentials is used as an indicator of corrosion activity.

3.5.1 Elsener et al. (1990)

Synthesizing the results of half-cell corrosion potential testing of various distinctive reinforced concrete elements, Elsener at al. (1990) aimed to demonstrate that a fixed threshold serving to identify active corrosion (e.g. -350 mV) does not exist. The authors (1990) first offered and explained the following factors which they claimed affect half-cell potentials:

1. Concrete cover depth: as the cover depth increases, potentials over actively corroding and passive steel become less distinguishable. Accordingly, smaller zones of active reinforcement corrosion become more difficult to identify;
2. Concrete resistivity: the varying moisture content and ionic concentration of concrete pore solution can cause measured half-cell potentials to fluctuate;

3. High resistive surface layers: corrosion macrocell currents avoid highly resistive surface layers, causing half-cell potentials measured over such layers to be more positive;
4. Polarization effects: saturated elements may exhibit extremely negative potentials even if oxygen access is restricted in the element (e.g. underwater concrete). These potentials are not linked to active reinforcement corrosion.

Given the many factors that affect half-cell potentials, Elsener et al. (1990) argued that fixed thresholds cannot be used to distinguish passive steel from active corrosion. The authors presented how half-cell potentials from various case studies would be interpreted using the ASTM C876 numeric magnitude thresholds (shown in Table 3-1). From a HCP evaluation of the Cugniertobel II bridge deck, active reinforcement corrosion was located in areas with measured potentials more negative than -300 mV CSE. More than 70% of the active corrosion locations would not have been detected had the ASTM criteria been used. Furthermore, from an HCP evaluation of the Morbio bridge deck, passive zones with measured potentials around 0 mV CSE were recorded. Potentials of some locations of active reinforcement corrosion were more positive than -200 mV CSE. Moreover, implementation of the ASTM criteria for potential interpretation would have resulted in none of the active corrosion sites being identified. Given the lack of accuracy of the ASTM fixed criteria, Elsener et al. (1990) recommended that potential readings measured on bridge decks be treated statistically to distinguish zones of active corrosion from those of passive reinforcement.

3.5.2 Clemeña (1992)

To reconcile debate concerning the applicability of fixed ASTM criteria in discerning between active corrosion and passive reinforcement given half-cell potentials, Clemeña (1992) undertook an experimental investigation funded by the Federal Highway Administration. The top reinforcement mat of three reinforced concrete slabs with differing cover depth (1 in., 2 in., and 3 in.) were subjected to accelerated chloride-induced corrosion. The three slabs were cured outdoors for at least 60 days before half-cell potentials were measured. To evaluate the appropriateness of the fixed ASTM criteria, each location where a potential was measured was classified as sound or defective in accordance with the following rule—if there was a transverse crack, delamination, or spall within 6 in. of the test location, the corresponding potential was classified as defective. Otherwise, it was classified as sound. Using this classification scheme, the following classifications were developed:

- Virtually 100% of potentials more positive than -150 mV were collected at sound locations;
- 100% of potentials more negative than -450 mV were associated with a defect;
- Only 28–85% of potentials between -301 mV and -350 mV actually corresponded with a defect; and
- Of potentials between -351 mV and -400 mV, 70–100% were collected over defects.

Based on these results, Clemeña (1992) concluded that the numeric magnitude technique and corresponding interpretation criteria offered by ASTM could result in imprecise indications of the condition of embedded reinforcement in bridge decks.

3.5.3 RILEM TC 154 (2003)

To facilitate appropriate application and interpretation of half-cell potentials in reinforced concrete structures, RILEM TC 154 (2003) compiled technical recommendations discussed hereinafter. In this document, factors affecting half-cell potentials were considered. Since the IR drop in potential difference measurements is influenced by concrete, the cover depth was identified as a factor affecting half-cell potentials. Furthermore, it was noted that temperature does not practically affect potentials measurements on site when using the (1) copper/copper sulfate sat., (2) calomel (Hg / Hg_2Cl_2) KCl sat., and (3) silver chloride (Ag / AgCl) KCl sat reference electrodes (RILEM TC 154 2003). Additionally, concrete resistivity was identified as having a pronounced effect on half-cell potentials measurements (RILEM TC 154 2003). Given the many factors that RILEM TC 154 (2003) noted can affect half-cell potential measurements, they claimed that numerical magnitude techniques using either the van Daveer Criteria or ASTM C876 absolute criteria should not be used to assess the state of corrosion in embedded steel reinforcing.

3.5.4 Yodsudjai and Pattarakittam (2016)

In this study, Yodsudjai and Pattarakittam (2016) sought to investigate the influence of concrete cover, chloride content, compressive strength, and moisture content on the HCP measurements in reinforced concrete specimens. Twenty-one 300 mm by 300 mm by 100 mm and three 300 mm by 300 mm by 125 mm concrete slabs were fabricated with three levels of cover (25, 50, 100 mm), three chloride content levels (0.6, 1.2, and 1.8% by weight of cement content) and two different compressive strengths (17.65 and 20.69 MPa). After the specimens had cured for 28 days, their corrosion levels were monitored weekly with

HCP measurements performed during alternating wetting and drying cycles. Analysis of the HCP survey from each specimen allowed for the formulation of the following noteworthy conclusions: (1) increases in the moisture content and chloride content correspond with more negative HCP values, (2) increases in the compressive strength make HCP values more positive, (3) concrete cover affects the HCP measurements, but the relationship between the two is inconclusive, (4) HCP surveys were much more sensitive in the dry state to variation caused by the foregoing parameters than when specimens were tested in the wet condition, and (5) the level of corrosion increased as HCP values became more negative (Yodsudjai and Pattarakittam 2016).

3.6 Previous Electrical Resistivity Research

While half-cell measurements can be an excellent NDT method for identifying active corrosion of embedded reinforcement in bridge decks, they cannot provide an estimate of the rate of corrosion (ACI Committee 228 2013). Knowledge of the corrosion current rate is important to bridge owners who need to assess the urgency of needed repairs. Measuring the in situ corrosion rate of bridge decks using a linear polarization method can be slow and cumbersome in comparison with other NDT methods. As the electrical resistivity (ER) test can be performed relatively quickly, and electrical resistivity is intuitively linked to the corrosion rate via electrolytic current flow, studies have been conducted investigating how ER testing might be used in lieu of the linear polarization method on bridge decks. Accordingly, the factors that affect concrete electrical resistivity have been explored. Using the ER method as an indication of the risk of corrosion has also been investigated.

3.6.1 Feliú et al. (1996)

In part to assess the effectiveness of various NDT methods in measuring the in situ rates of corrosion, Feliú et al. (1996) conducted testing on both laboratory specimens and in-service structures. A portable device using a galvanostatic pulse was implemented to measure the corrosion rates of the foregoing concrete elements. Furthermore, electrical resistivity of the same elements was measured, allowing for a comparison of corrosion current and resistivity. When the measured corrosion rate was plotted against the measured electrical resistivity, as provided in Figure 3-1, a clear correlation could be observed between the two parameters. Generally, it appeared that the corrosion current was a linear function of the electrical resistivity.

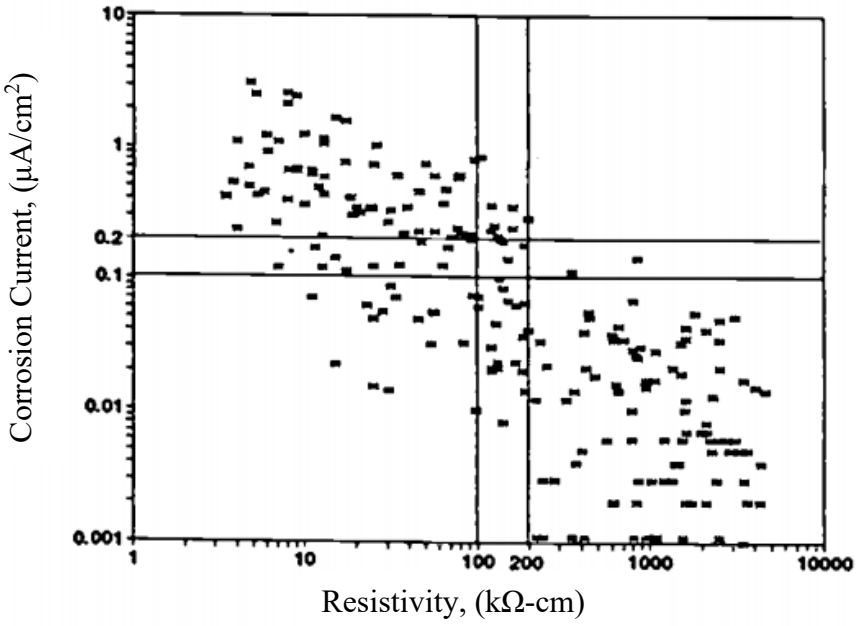

Figure 3-1: Correlation Between Corrosion Current and Electrical Resistivity (Adapted from Feliú et al. 1996)

From that data, the authors offered guidance on using resistivity measurements as indicators of the risk of corrosion. Both the numerical criteria which they offered and the corresponding interpretations are provided in Table 3-2.

Table 3-2: Resistivity Criteria Regarding Risk of Corrosion (Feliú et al. 1996)

Resistivity (kΩ-cm)	Corrosion Risk
>100–200	Negligeable corrosion. Too dry concrete
50–100	Low corrosion rate
10–50	Moderate to high corrosion when steel is active
<10	Resistivity is not the controlling parameter of corrosion rate

3.6.2 Gowers and Millard (1999)

As the industry had increasingly moved towards the use of the Wenner technique in measuring electrical resistivity concrete, Gowers and Millard (1999) synthesized the results of studies aimed at identifying sources of error in resistivity measurements obtained using the Wenner technique. Based on the results of various experimental and numerical investigations, the authors (1999) identified the following five factors as inducing error in the measured Wenner resistivity, in comparison to the true resistivity:

1. Concrete geometry: measured resistivity using the Wenner technique assumes the test element is of semi-infinite volume. Thus, provided that the spacing of electrodes in the Wenner probe, a, is substantially smaller than the dimensions of the test element, no significant error measurement error exists;
2. Concrete heterogeneity: aggregate particles have a very high resistivity in comparison with the hydrated cement paste. Accordingly, if the electrode spacing is too small, an aggregate particle below an electrode may increase measurement scatter;

3. Surface layers of different resistivity than the bulk concrete: a surface layer of distinct resistivity from the underlying bulk concrete can distort the applied field of current. In particular, low resistivity layers (e.g. filled with excessive chloride ions) were found to have a more perturbing effect than high resistivity layers (e.g. carbonated concrete).
4. The presence of steel reinforcement: since steel is a more effective conductor of electricity than concrete, it has the potential to skew resistivity measurements. While a resistivity measurement taken directly over and parallel to a steel reinforcing bar can significantly affect the measurement, readings taken orthogonal to or isolated from reinforcing do not influence the corresponding readings.
5. Changes in ambient environmental conditions: while no clear correlation was observed between measured resistivity and the air relative humidity or occurrence of rainfall, it was noted that a 1°C increase in air temperature corresponded with a -0.33 kΩ-cm decrease in measured resistivity, per Figure 3-2.

Given the influence of surface layers on the accuracy of measured resistivity, Gowers and Millard (1999) recommended that resistivity be measured using the Wenner technique no earlier than 24 h after a rainfall event has occurred. Furthermore, they noted that a correction of +1 kΩ-cm per 3°C increase in air temperature be applied to compare measured resistivities from the Wenner probe.

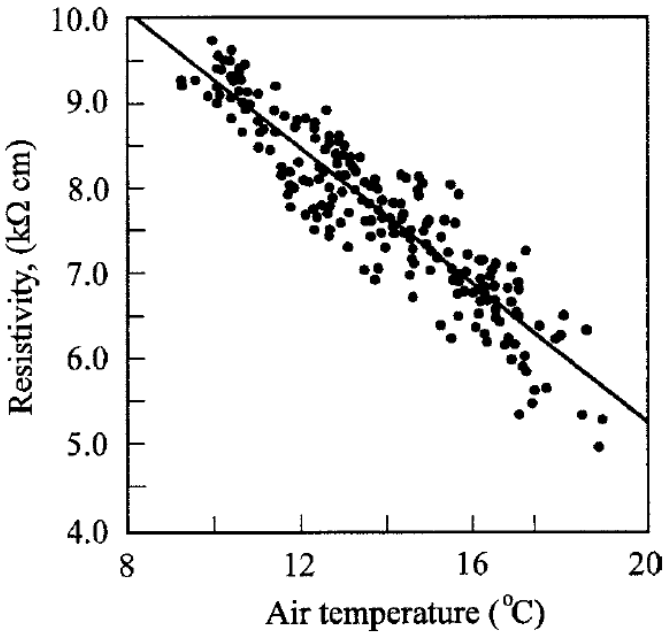

Figure 3-2: Linear Relationship Between Measured Resistivity and Air Temperature (Gowers and Millard 1999)

3.6.3 Polder (2001)

In consultation with RILEM TC 154, Polder (2001) described factors affecting concrete resistivity and provided guidelines for interpreting measurements for various exposures and concrete compositions. Polder (2001) noted that the resistivity of concrete is related to the susceptibility of chloride ion penetration. Furthermore, as current in concrete is carried through the pore solution, parameters influencing concrete pores were identified. The author (2001) noted that:

- Increased moisture content and wider pores (caused by a higher water-cement ratio) cause lower resistivity; and

- Lower water-cement ratios, longer curing periods, lower moisture contents, carbonation, and the reaction of pozzolanic minerals such as blast furnace slag, fly ash, and silica fume result in increased concrete resistivity.

Additionally, the inverse relationship between resistivity and temperature was identified and attributed to the influence of temperature on ion behavior in the concrete pore solution. Polder (2001) noted that interpreting resistivity measurements as indicators of the rate of corrosion needs further investigation. However, the following criteria from COST 509 (1997) were referenced when assessing the risk of corrosion with resistivity for ordinary portland cement concretes at 20°C:

- A resistivity less than 10 kΩ-cm is indicative of a high risk of corrosion;
- A resistivity of 10–50 kΩ-cm is indicative of a moderate risk of corrosion;
- A resistivity of 50–100 kΩ-cm is indicative of a low risk of corrosion; and
- A resistivity greater than 100 kΩ-cm is indicative of a negligible risk of corrosion.

3.6.4 Broomfield and Millard (2002)

Drawing on past work seeking to establish a correlation between corrosion rate and concrete resistivity (Langford and Broomfield 1987), Broomfield and Millard (2002) proposed the following as ways of interpreting threshold resistivity (kΩ-cm) values:

- A resistivity greater than 20 kΩ-cm is indicative of a low corrosion rate;
- A resistivity of 10–20 kΩ-cm is indicative of a low to moderate corrosion rate;
- A resistivity of 5–10 kΩ-cm is indicative of a high corrosion rate; and
- A resistivity less than 5 kΩ-cm is indicative of a very high corrosion rate.

As a word of caution when using these threshold values, the authors (2002) noted that these thresholds are only applicable after embedded reinforcement is depassivated; i.e. corrosion is active. Accordingly, a location in which resistivity measurements are to be collected should first be confirmed to be actively corroding via HCP testing.

3.6.5 Nadelman and Kurtis (2014)

Nadelman and Kurtis (2014) observed that both the electrical resistivity and permeability of concrete are, in part, governed by the tortuosity of the pore network. A more tortuous pore network presents a complex path for electrons to flow through; thus, increasing electrical resistivity (Nadelman and Kurtis 2014). Furthermore, a tortuous pore network would inhibit the permeation of fluids (Nadelman and Kurtis 2014). As the tortuosity of the pore network is linked to concrete microstructure, the authors aimed to investigate how mixture proportions affected the tortuosity and resistivity of concrete. Resistivity measurements for concrete specimens from six distinct mixture proportions were recorded for 56 days. The mixture proportions were selected to identify how varying water-cement ratio, supplementary cementing materials (SCMs), and cement type affected resistivity. From this study, Nadelman and Kurtis (2014) concluded that 1) an increased water-cement ratio or replacement of portland cement with less-reactive limestone fillers results in lower concrete resistivity, and 2) the pozzolanic reaction from SCMs can be observed from resistivity development curves by relative increases in the rate of change of electrical resistivity.

3.6.6 Yoon and Chang (2020)

To further investigate the influence of chloride ions on resistivity measurements from carbonated and non-carbonated concrete, Yoon and Change (2020) constructed laboratory

specimens with differing water-cement ratios, chloride ion contents, and degrees of carbonation. Distinct from the primary objectives of the study, it was observed that, among saturated concrete specimens, that with the lowest water-cement ratio had the highest electrical resistivity towards the end of the experimental period (> 300 days). Furthermore, while studying the influence of pore water on concrete electrical resistivity, Yoon and Change (2020) observed a substantial change in resistivity as tested concrete specimens dried. From their dataset, an abrupt decrease in the ratio of air-dried to saturated concrete resistivity was noticed when the pore network was 30-45% filled with water. Nonetheless, the resistivity of air-dried concrete relative to a saturated specimen was fairly constant beyond pore network moisture contents greater than the foregoing range. Accordingly, the authors (2020) concluded that the ratio of air-dried to saturated concrete resistivities is quite sensitive to the moisture content of the pore network.

Concerning the influence of chloride ions on resistivity measurements of carbonated and non-carbonated concrete, Yoon and Change (2020) concluded that:

1. An increased chloride ion concentration corresponds to reduced concrete resistivity;
2. The influence of chloride ions is low at early concrete maturities since chloride ions are being actively absorbed and the concrete microstructure is developing significantly;
3. Concrete resistivity generally increases in proportion to chloride ion concentration and depth of carbonation.

3.7 Comments on Previous NDT Literature

The concise review of the foregoing NDT studies reflects that nondestructive testing has received an increasing amount of interest as a means of evaluating the condition of civil infrastructure. Accordingly, a substantial effort has been developing in understanding the capabilities of each NDT method and determining how best to implement them to facilitate rapid, yet accurate evaluations of concrete elements. Through reflection of the aforementioned studies, the following comments are offered:

- The use of NDT methods in evaluating reinforced concrete bridge decks is a relatively new, developing field that has the potential to be a valuable tool to DOTs in prolonging the life cycle of civil infrastructure;
- No single NDT method is capable of accurately detecting all major defects in bridge decks, warranting the deployment of multi-method nondestructive evaluations;
- Confusion regarding how best to interpret and post-process NDT data begs the development of more thorough guidance and standards pertaining to the discernment of defective concrete from sound concrete;
- Environmental conditions, mixture proportions, geometry of elements, and human interaction with the bridge deck can all influence NDT data, heightening difficulties in developing universal thresholds applicable to all concrete bridge decks that serve to identify defective zones of the deck; and

- NDT literature published in the last several decades reflects the uncertainty that still exists with regards to the capacity of each NDT method in detecting different forms of concrete bridge deck defects.

Chapter 4: Phase 1—Experimental Testing of Laboratory Specimens

4.1 Chapter Objectives and Outline

The primary objective of Phase 1 of this project was to evaluate the effectiveness of the five aforementioned NDT methods in detecting simulated defects in 20 laboratory specimens representative of in-service bridge decks. In support of this goal, six of the twenty specimens were tested in both the air-dried and moist conditions to determine the influence of moisture content on NDT measurements.

Methods of simulating different forms of bridge deck defects in each specimen are first discussed. The experimental methodology of each NDT method is then described and accompanied by a discussion of the data analysis methods and post-processing algorithms implemented in this study. Subsequently, data retrieved from each NDT method is presented, and the results of the processed data are discussed. Conclusions regarding the capabilities of each NDT method and the factors that affect them are developed.

4.2 Laboratory Specimen Design

Twenty 3 ft by 7 ft reinforced concrete specimens were fabricated to evaluate which types of defects the NDT methods used in this study could identify. Each specimen was named in accordance with the primary defect simulated in the specimen. Abbreviations used in the specimen names can be found in Table 4-1. Discussions regarding the design and fabrication of each specimen are included in the following subsections, grouping specimens of similar simulated defects. The control specimen (Specimen CTRL) is included within the discussion of the deterioration specimens.

Table 4-1: Laboratory Specimen Abbreviation Guide

Abbreviation	Simulated Defect
CTRL	Control (No Defects)
C	Corrosion
CR	Vertical Cracking
DE	Deterioration
DL	Delamination
PC	Poor Construction
V	Voids

4.2.1 Corrosion Specimen Fabrication

Test Specimens C1 and C2 were constructed to evaluate the capability of NDT methods to detect corrosion of embedded reinforcement and the corresponding damage induced on the surrounding concrete. A conceptual drawing of the plan view of those two specimens can be observed in Figure 4-1. Only ¾ in. of cover was provided in Specimen C1 in an effort to create corrosion-induced vertical cracks, as it was hypothesized that expansive corrosive stresses would sooner be relieved through vertical cracking than horizontal delaminations for such a shallow cover. In contrast, Specimen C2 was constructed with 2 in. of cover to the topmost reinforcement to primarily cause corrosion-induced delaminations rather than vertical cracks.

Per Figure 4-1, the upper reinforcement mat in Specimens C1 and C2 was corroded by ponding a portion of the slab surface in a 3% NaCl solution and impressing current into the reinforcement, as similarly accomplished in previous research (Almusallam et al. 1996; Jayaprakash et al. 2012; Guo et al. 2015). The top reinforcement mat was cut into thirds to create three zones of differing levels of corrosion. A 12V battery was used to corrode

Zones 2 and 3; the cuts in the reinforcement mats mitigated flow of current between adjacent zones.

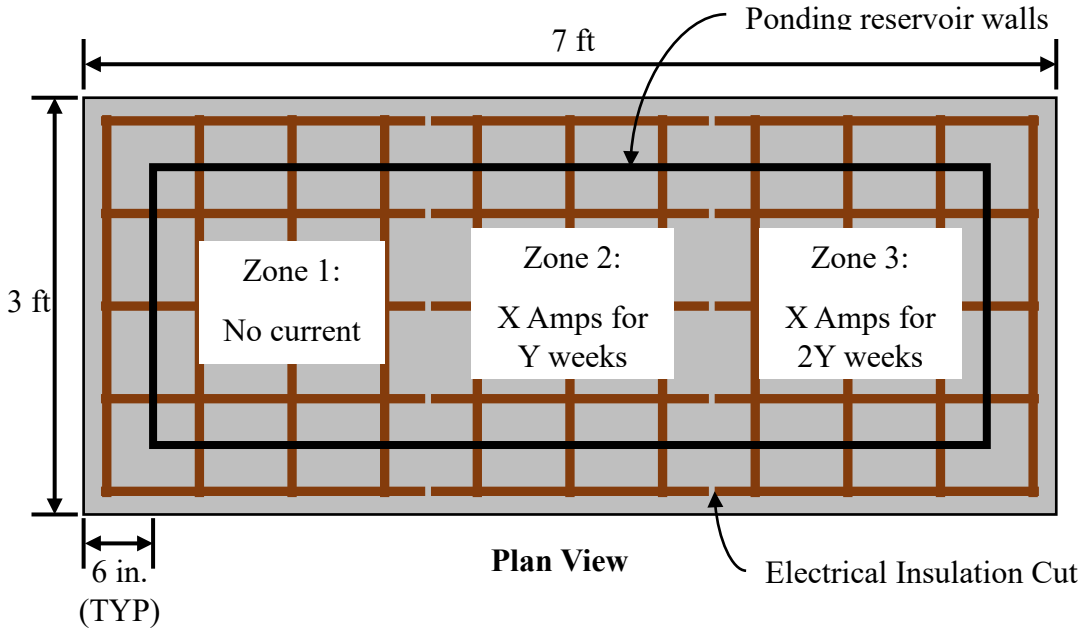

Figure 4-1: Conceptual Plan View of Specimens C1 and C2

For both corrosion specimens, the NaCl solution was ponded on the slab surface for seven days prior to application of current, which began 35 days after placement of concrete. It was hypothesized that current in Zones 2 and 3 would pull chloride ions in the cover layer to the reinforcement, removing the passivating layer and accelerating the rate of corrosion. For Specimen C1, current was impressed through Zones 2 and 3 for approximately 7 and 14 days respectively. It was hypothesized that current would need to be applied over a longer duration in Specimen C2 than Specimen C1 since the cover layer of the former was greater than that of the latter. For this reason, in Specimen C2, current was impressed through Zones 2 and 3 for approximately 14 and 27 days respectively. For both specimens, the effects of this accelerated corrosion method was evidenced through

substantial surface staining from corrosion products traveling upwards through the cover layer, as seen in Figure 4-2. The location and quantity of corrosion products corresponded well with the hypothesized zones of corrosion.

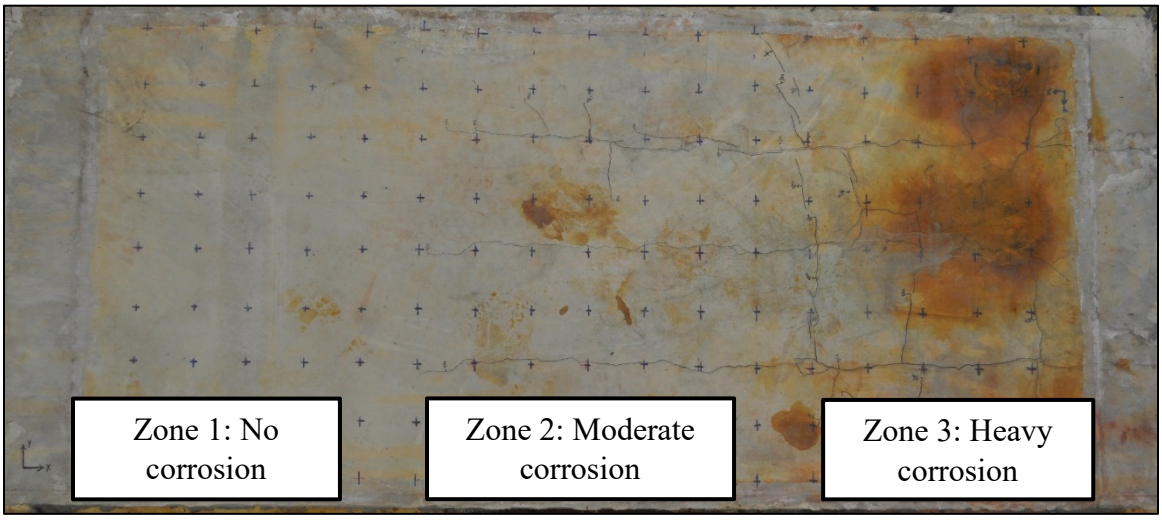

Figure 4-2: Plan View of Specimen C2 after Accelerated Corrosion.

4.2.2 Cracked Specimen Fabrication

Specimen CR1 was designed to simulate vertical cracks of varying thicknesses, extents, and depths that might occur in an in-service bridge deck. In accordance with similar vertical crack simulation implemented by Lin et al. (2018), partial depth cracks of varying thickness were simulated using plastic sheeting, as can be observed in Figure 4-3. Furthermore, a partial depth crack spanning the width of the specimen was simulated by casting the right and left portions of the slab separately and forming the two together using a cold joint. The top of the contact interface of the two portions was poorly prepared to replicate cracking damage while the lower part was made to bond well together.

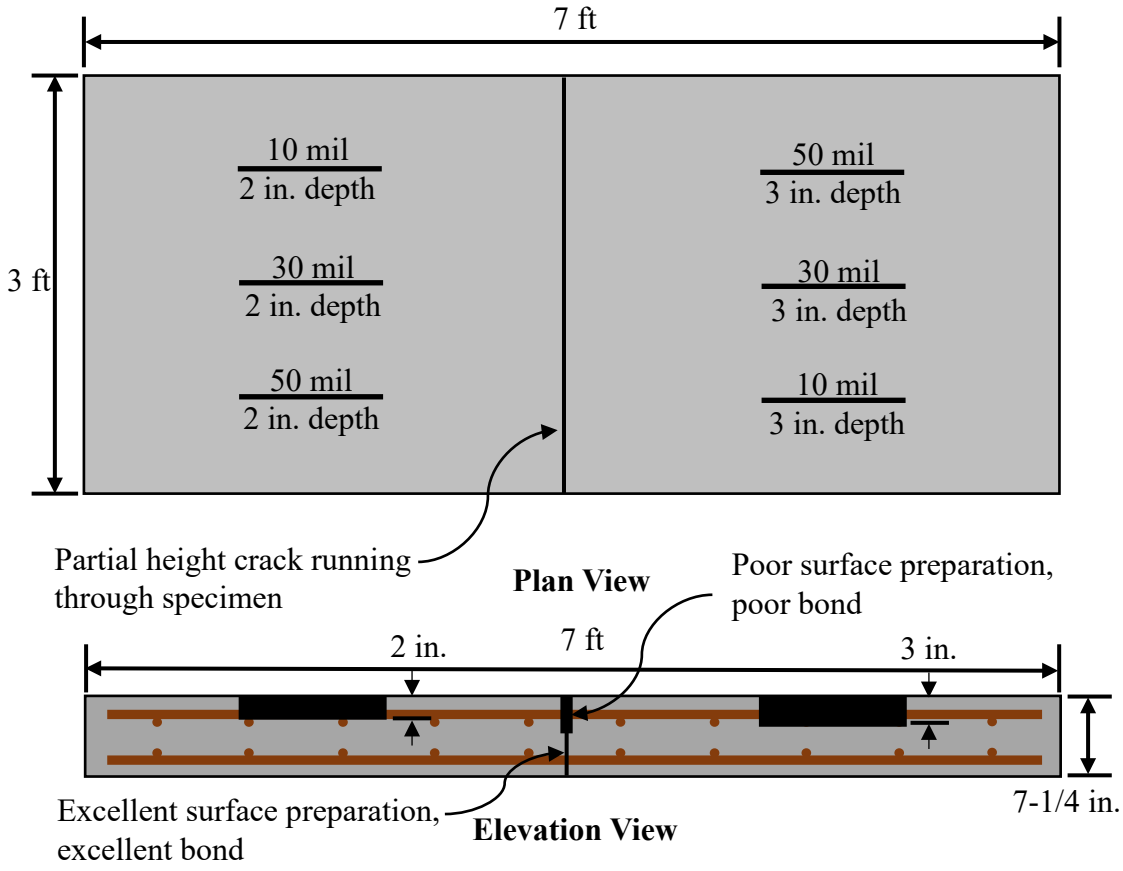

Figure 4-3: Conceptual Views of Specimen CR1

4.2.3 Deterioration Specimen Fabrication

Test Specimen CTRL and Specimens DE2–5 were fabricated to evaluate the capability of the NDT methods to detect concrete deterioration in bridge decks. For each specimen, a 1 ft by 5 ft miniature slab with simulated deterioration was placed in the specimen formwork and surrounded by sound, properly consolidated concrete, as can be observed in Figure 4-4. This approach to defect simulation was inspired by past studies in which defects were introduced in a small portion of concrete which was later surrounded with sound concrete (Lin et al. 2018, Stefan et al. 2018). Moreover, for all specimens, 2

in. of cover to the topmost reinforcement was provided to be representative of a typical Alabama bridge deck.

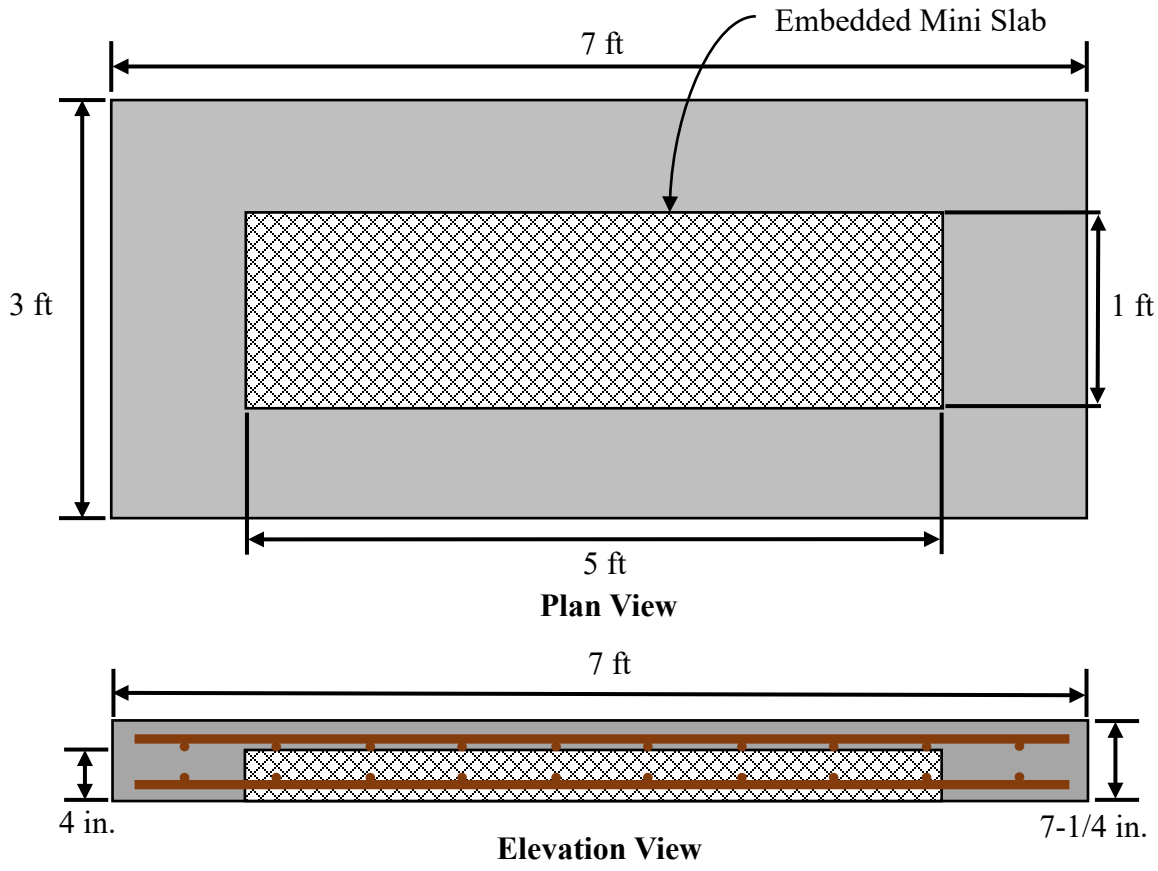

Figure 4-4: Conceptual Views of CTRL and DE Specimens

Unlike the DE specimens, Specimen CTRL was not deliberately fabricated with any defects. Nonetheless, this specimen was still built by casting concrete around a hardened 1 ft by 5 ft miniature slab. Rather, that miniature slab contained no simulated defects and was made using the same mixture proportions as the surrounding concrete. Accordingly, this specimen was built as a control to evaluate whether any given NDT method responded to the presence of the cold joint between the miniature slab and the

surrounding concrete, rather than the defects simulated in the miniature slabs of the DE specimens. Thus, if an NDT method indicated that there was a defect at the location of the miniature slab in the control specimen, it would make it difficult to claim that the NDT method responded to a simulated defect in a DE specimen. As with all miniature slabs fabricated for this study, the surface of the miniature slab of the control specimen was intentionally roughened to allow for improved bond with the surrounding concrete to be placed, as can be seen in Figure 4-5.

Figure 4-5: Miniature Slab for Test Specimen CTRL

Several different approaches were implemented to simulate deterioration in Specimens DE2–5. Deterioration in Specimen DE2 was simulated by adding a high dosage of air-entraining admixture to the concrete in the miniature slab, increasing its air content. It was hypothesized that a high air content in the miniature slab relative to the surrounding sound concrete would mimic the increased porosity of concrete caused by progressive deterioration. To replicate a more severe state of concrete deterioration, the miniature slab

of Specimen DE3 was constructed using concrete with a high degree of honeycombing, as can be observed in Figure 4-6.

Figure 4-6: Miniature Slab for Test Specimen DE3

A different method for simulating concrete deterioration was implemented for Specimens DE4–5. For these specimens, anti-cracking fibers added to the miniature slabs were used to replicate microcracking networks caused by deterioration mechanisms, similar to previous work by Ham et al. (2016). To simulate varying degrees of deterioration, different dosages of anti-cracking fibers were added to the two specimens. In Specimen DE4, a 12 pcy dosage of fibers was added to the miniature slab of while a more moderate dosage of 6 pcy was added to the miniature slab of Specimen DE5.

4.2.4 Delamination Specimen Fabrication

Test Specimens DL1–8 were constructed with simulated delaminations of varying size, thickness, depth, and degree of bond to be representative of the many types of delaminations that one may encounter in an in-service bridge deck. Specimens DL1–2

were fabricated with 4 in. by 8 in. plastic and foam sheets of varying thicknesses, as shown in Figure 4-7, to determine what is the thinnest detectable delamination for each NDT method.

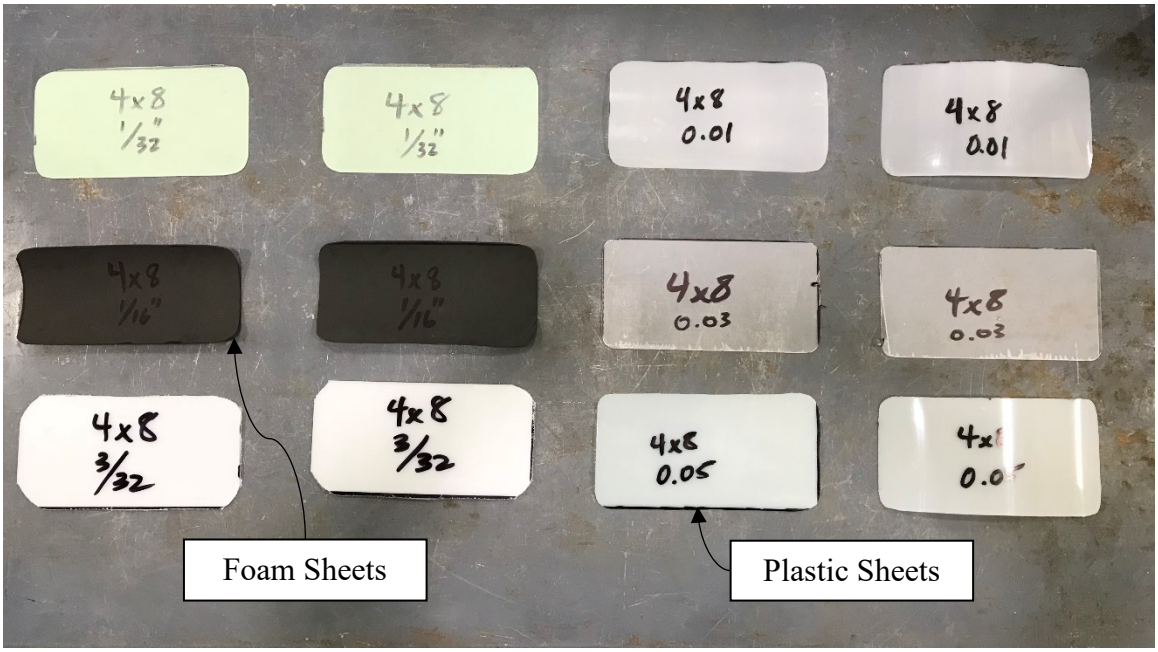

Figure 4-7: Plastic and Foam Inserts for Delamination Simulation

The choice to use plastic and foam sheets as artificial delaminations in these specimens was made in accordance with previous studies in which these defect simulation techniques had been implemented (Cheng and Sansalone 1993; Sansalone and Carino 1989). To investigate the influence of delamination depth on detectability, sheets were pinched within the upper reinforcement mat in Specimen DL1 (as shown in Figure 4-8) and within the lower reinforcement mat in Specimen DL2 (as shown in Figure 4-9). For the purposes of this thesis, delaminations at the level of the upper reinforcement mat are termed “shallow delaminations” while those at the level of the bottom reinforcement mat

are termed “deep delaminations”. As can be observed in Figure 4-8, the depth to the shallow delaminations in Specimen DL1 was approximately 2-5/8 in.

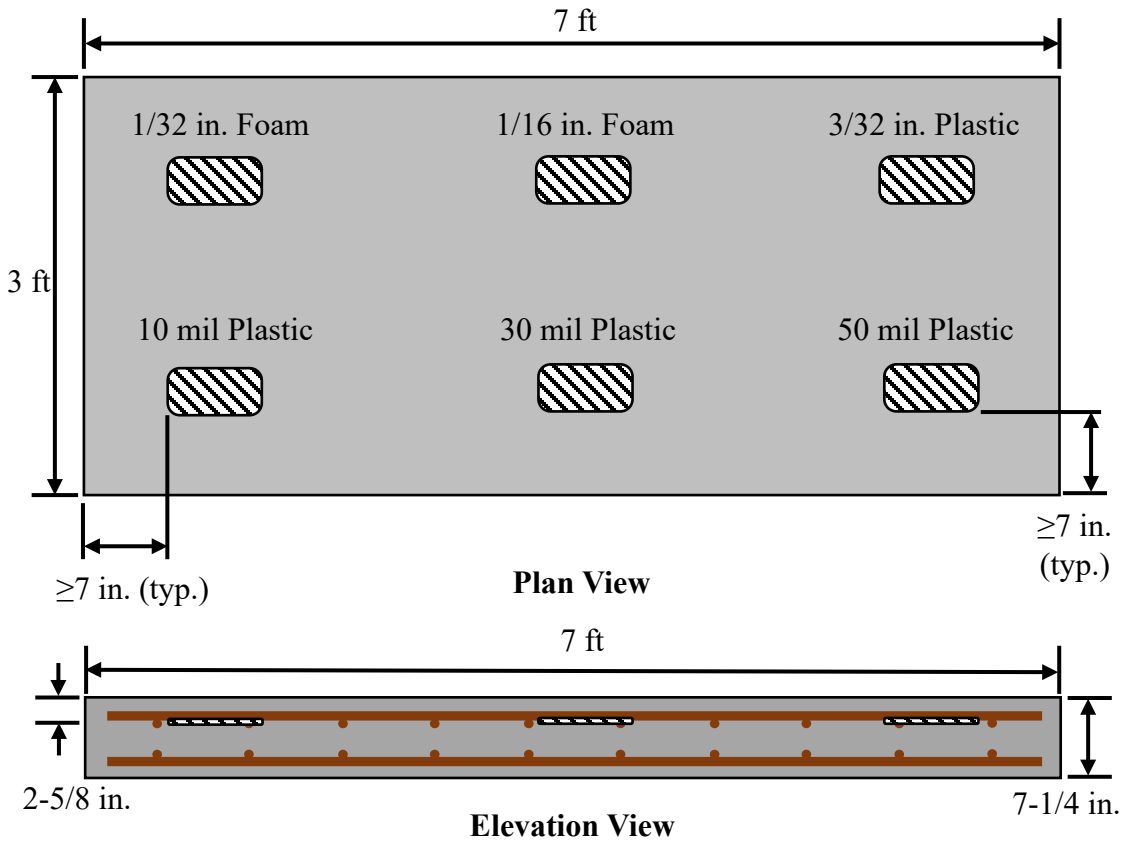

Figure 4-8: Conceptual Views of Specimen DL1

Delaminations placed in Specimen DL2, shown in Figure 4-9, were of the same in-plane dimensions and thicknesses as those from Specimen DL1. The two sets of delaminations differed only in depth; the deep delaminations in Specimen DL2 were placed 10-3/8 in. below the top surface rather than 2-5/8 in.

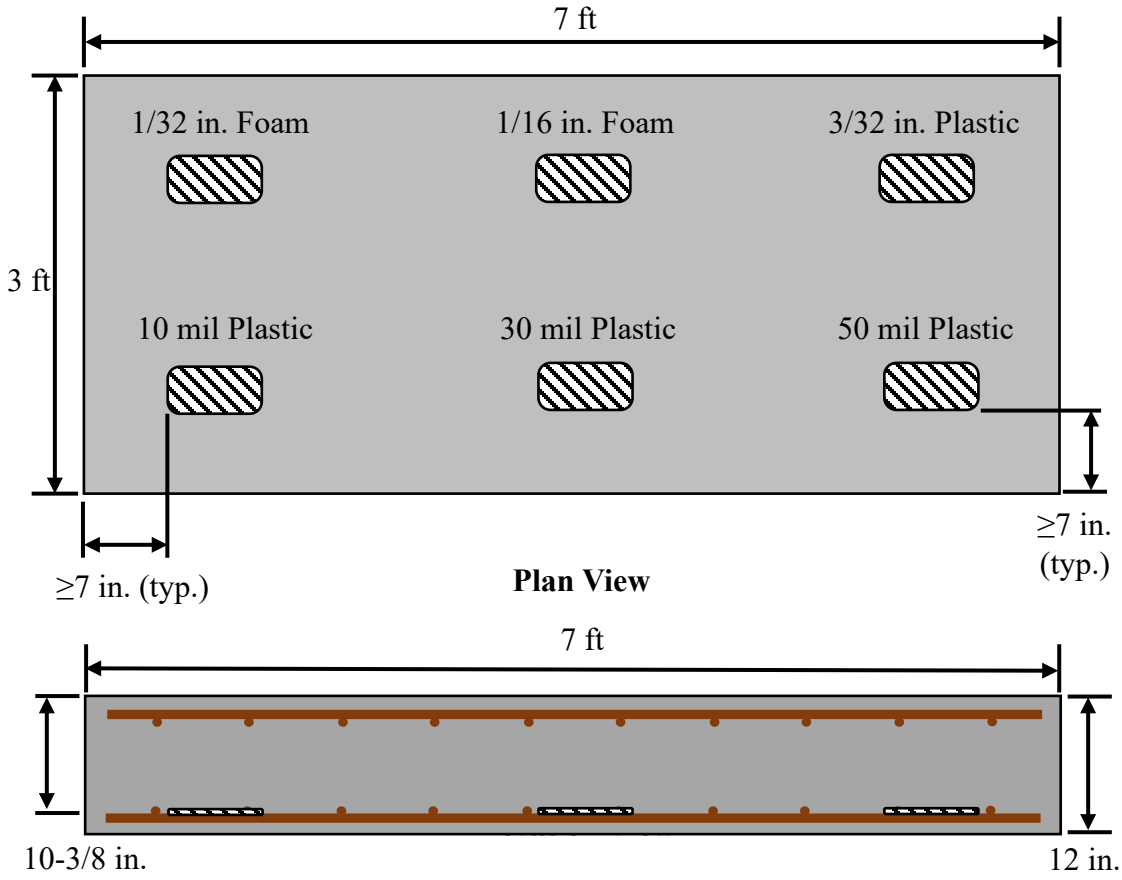

Figure 4-9: Conceptual Views of Specimen DL2

To investigate the capability of the NDT methods to detect real delaminations rather than gaps caused by inserted sheets, Specimens DL3–4 were fabricated. Sand and oil layers were placed within the specimens to cause real delaminations in a manner adapted from Lin and Sansalone (1996). As can be observed in conceptual views of Specimen DL3, shown in Figure 4-10, the sand and oil layers were placed distinctly from one another to allow for an investigation of which delaminating technique was more effective. For both specimens, the 1 ft 6 in. by 3 ft layers of sand and oil were placed at the level of the steel reinforcement to cause large delaminations. The two specimens were identical in all ways

except that Specimen DL3 had shallow delaminations in a 7-1/4 in. thick slab while Specimen DL4 had deep delaminations in a 12 in. thick slab.

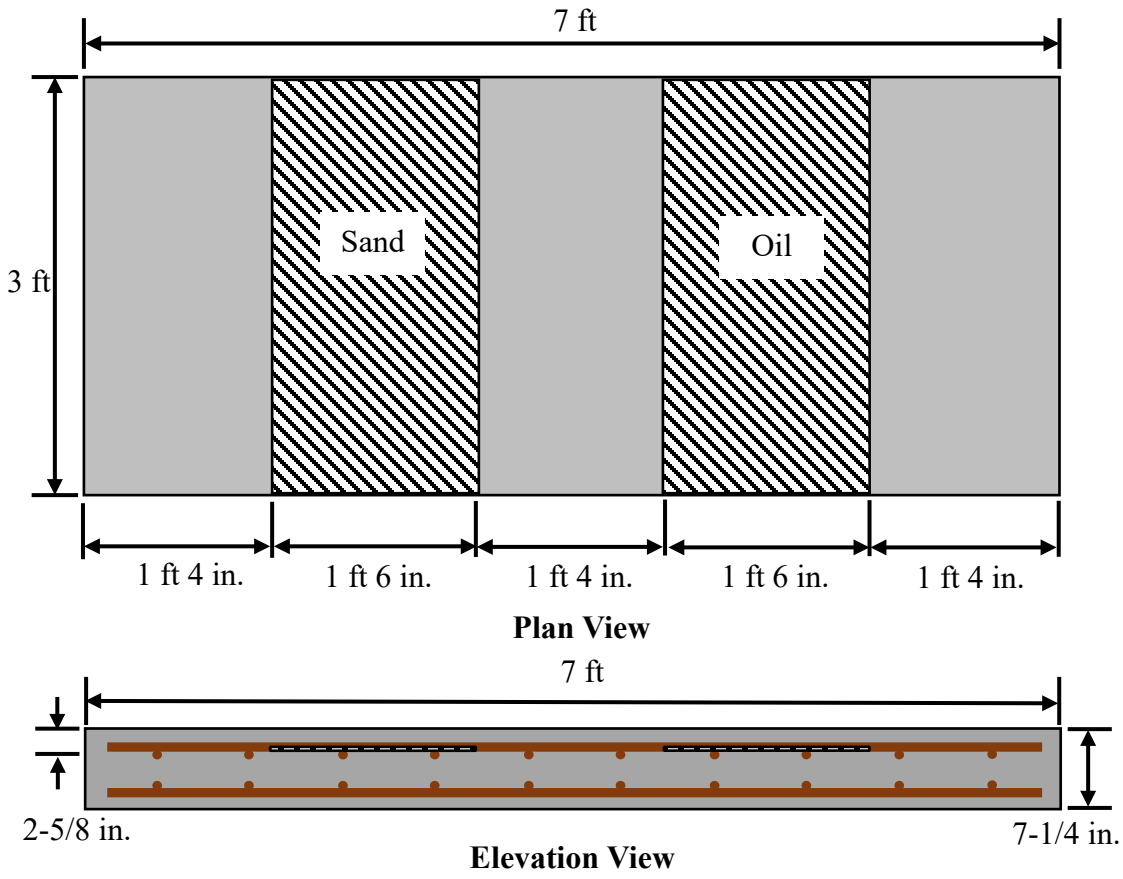

Figure 4-10: Conceptual Views of Specimen DL3

The two specimens were constructed by first placing a lift of concrete into the formwork up to the top reinforcement mat at which the sand and oil layers were being placed, as can be observed in Figure 4-11. After the layers had been placed, the second lift was placed on top of the first.

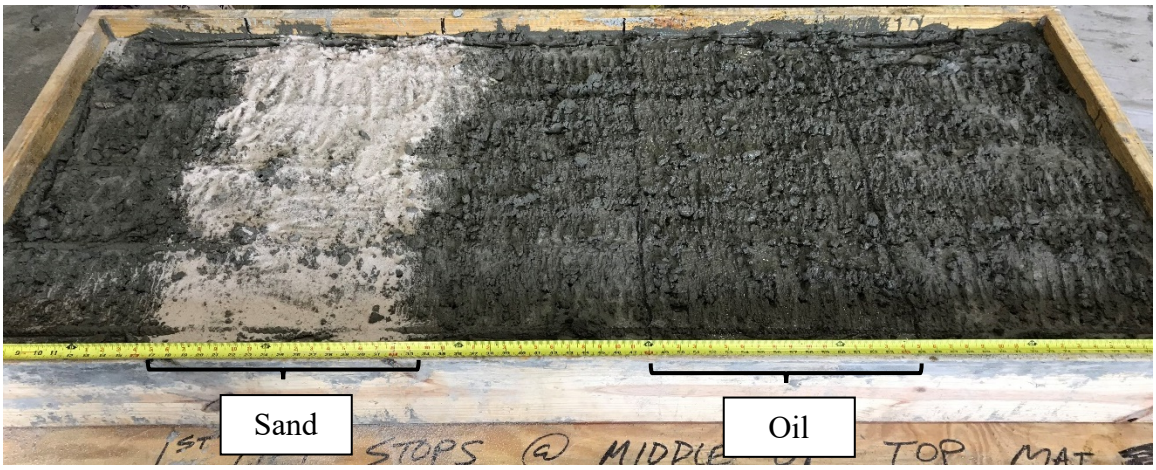

Figure 4-11: Sand and Oil Delamination Simulation

Apart from delamination depth and thickness, it was expected that the in-plane dimensions of a delamination would affect its detectability using NDT methods. To explore this notion, Specimens DL5 and DL6 were fabricated, respectively containing shallow and deep delaminations of varying areal extent. Shallow delaminations were placed in Specimen DL5, as can be observed in Figure 4-12, while deep delaminations were simulated in Specimen DL6. As in Specimens DL1–2, delaminations were simulated using plastic inserts that were pinched between perpendicular reinforcement in the top and bottom mats. Analogous to the relationship of Specimens DL2 and DL4 to DL1 and DL3 respectively, Specimen DL6 was the "deep counterpart" to Specimen DL5.

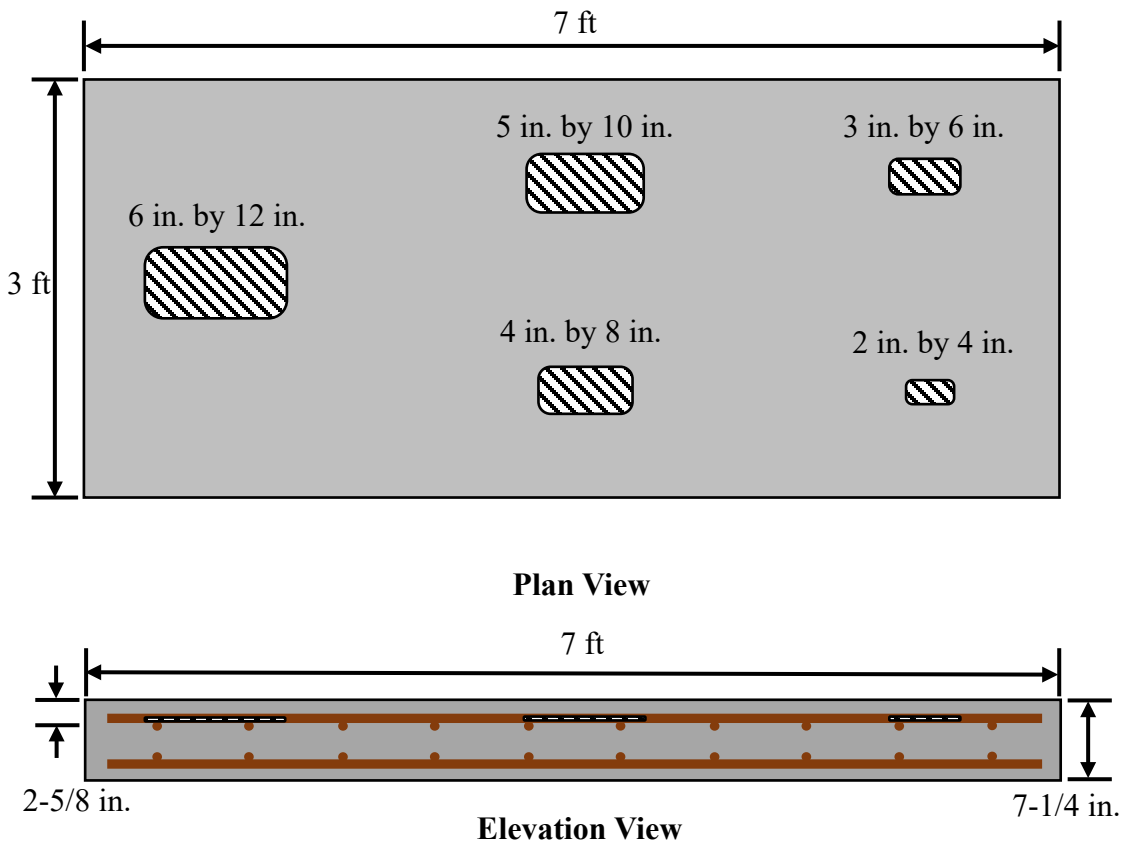

Figure 4-12: Conceptual Views of Specimen DL5

Lastly, Specimens DL7–8 were constructed to investigate the influence of unbonded fraction of area on delamination detectability. Inspired by work performed by Lin and Sansalone (1996), partially bonded delaminations were simulated in these two specimens using plastic inserts with checkerboard cuts to allow for concrete above and below the cuts to bond together, causing the partially bonded delaminations, as can be observed in Figure 4-13. Note that 'U' refers to the fraction of unbonded area (solid plastic) and 't' refers to the thickness of the plastic inserts.

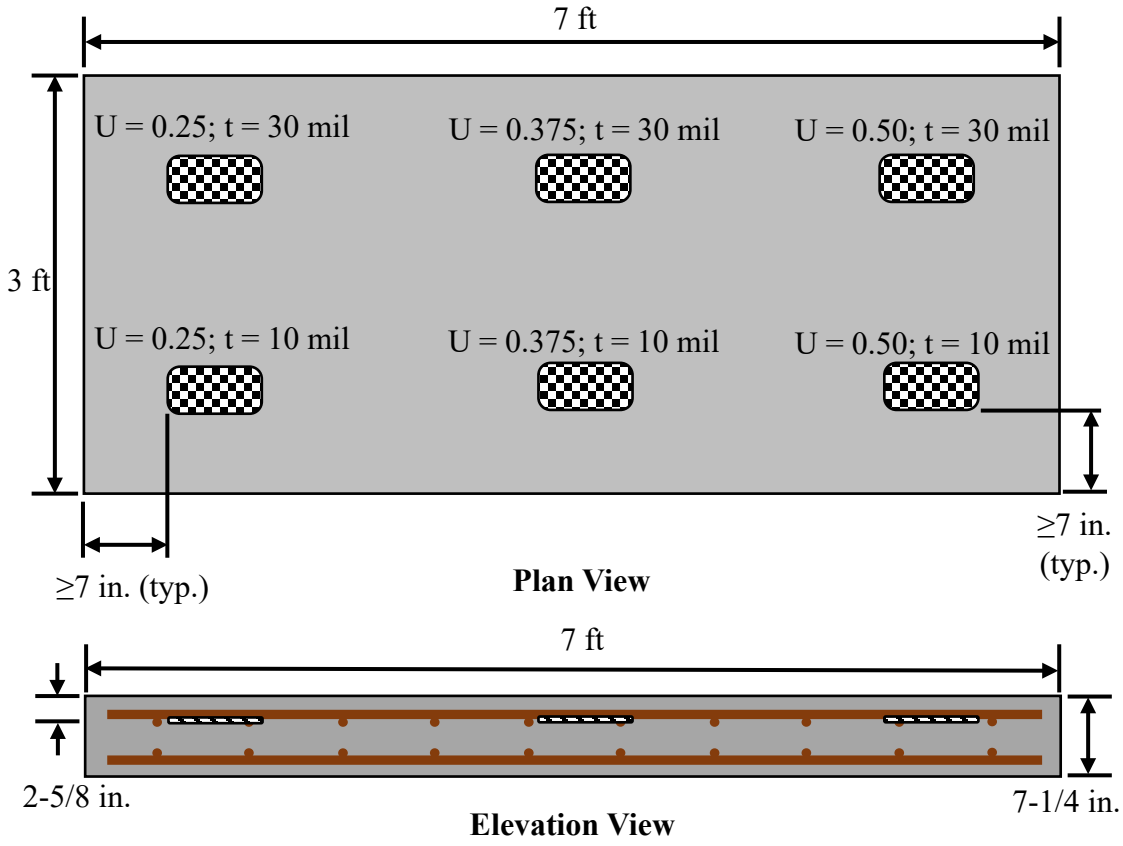

Figure 4-13: Conceptual View of Specimen DL7

In both specimens, plastic inserts were also of varying thickness to explore the interdependence of delamination thickness and fraction of unbonded area on detectability. The thicknesses and unbonded fractions of the partially bonded delaminations in Specimen DL8, shown in Figure 4-14, were greater than those of Specimen DL7 as it was hypothesized that the greater depth to the deep delaminations would greatly attenuate incident NDT waves, thus requiring more severe defects to be detected.

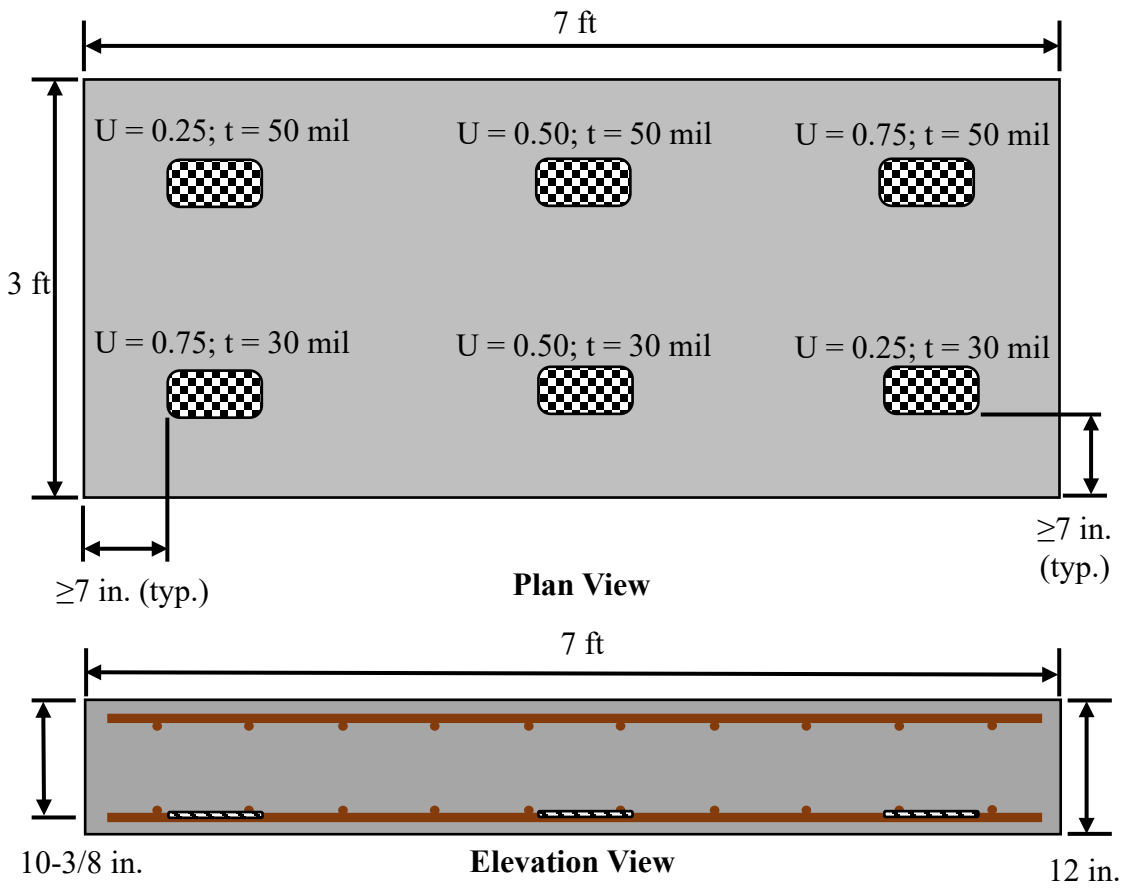

Figure 4-14: Conceptual Views of Specimen DL8

4.2.5 Poor-Construction Specimen Fabrication

Test Specimens PC1–2 were constructed to assess the ability of NDT methods to locate poorly constructed concrete in bridge decks. Just as with the deterioration specimens, poorly constructed concrete was simulated in Specimens PC1–2 by casting sound concrete around a 1 ft by 5 ft miniature slab of defective concrete. The miniature slab for Specimen PC1 was created using a low-strength concrete (water/cement ratio = 0.6) with respect to the surrounding sound concrete. Accordingly, this specimen aimed to represent an in-service bridge deck in which a portion of the deck has a lower compressive strength than the rest of the deck due to poor-construction practices such as adding extra water to the

concrete on site. Test Specimen PC2 was designed to simulate a different poor-construction practice commonly found on construction sites, undervibration of concrete. Such construction practices may result in a high content of entrapped air or even honeycombing within the poorly constructed concrete. Thus, the concrete of the miniature slab was flawed by poorly consolidating it.

4.2.6 Void Specimen Fabrication

Test Specimens V1 and V2 were fabricated to evaluate the ability of NDT methods to identify voids in concrete bridge decks. Such voids can be the result of poor-construction practices and may be filled with either water or air. Similarly, voids in concrete may be the result of the use of unclean aggregates in concrete mixtures. During mixing, particulates on the aggregates are freed and agglomerate, forming balls of sediment. Such agglomerates can cause voids in concrete if placed in the bridge deck. Accordingly, the void specimens were built to be representative of these types of voids that may be found in a concrete bridge deck. Voids of diameters ranging between 1/2 in. to 2-1/2 in. were simulated in both Specimens V1 and V2, as can be observed in Figure 4-15. Furthermore, voids were placed on both the top and bottom reinforcement mats to explore the influence of depth on void detectability.

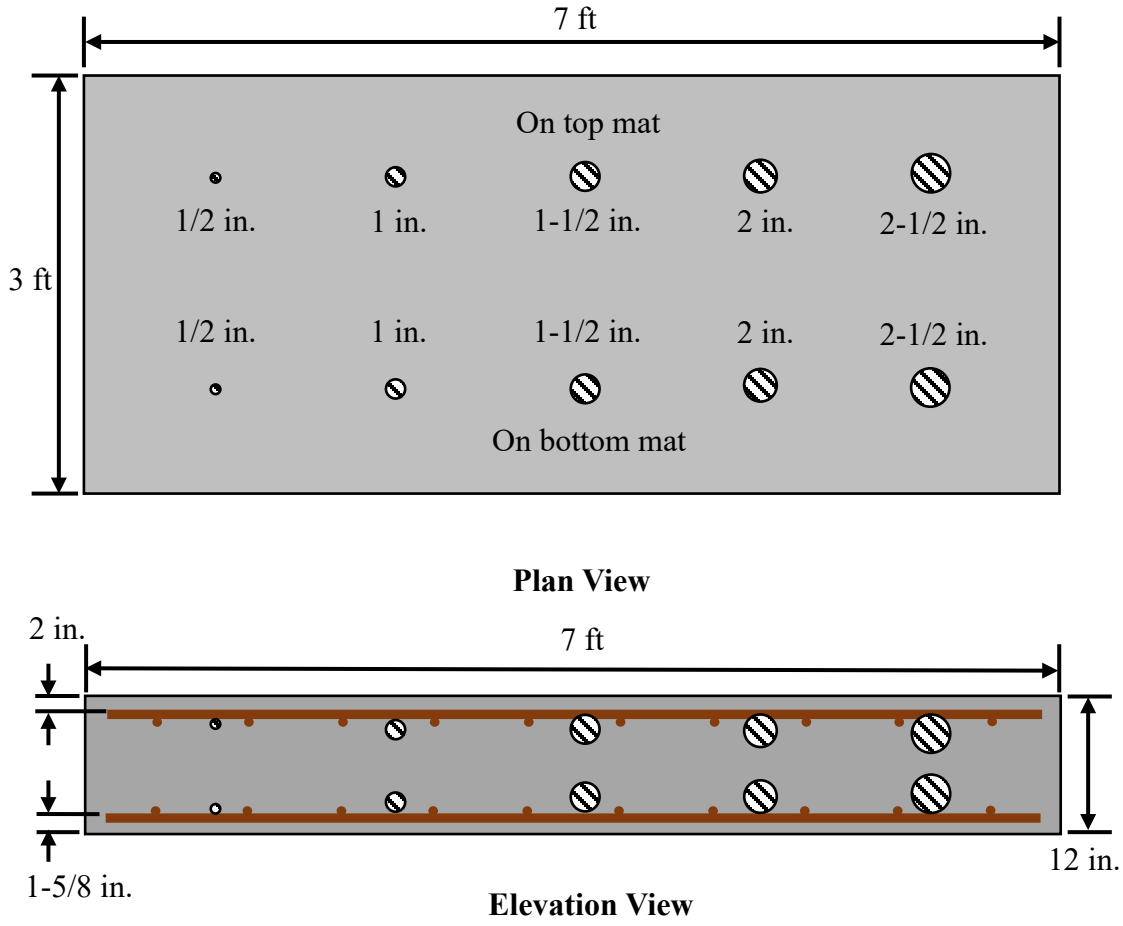

Figure 4-15: Conceptual Views of Void Specimens

In Specimen V1, voids were placed in the concrete by filling balloons with water and tying them to the reinforcement mats, as can be observed in Figure 4-16. To simulate clays balls in concrete, plastic bags were loosely filled with clay and placed in Specimen V2 as shown in Figure 4-17. As in Specimen V1, the bags were tied to the top and bottom reinforcement mats to keep them in place during concrete placement.

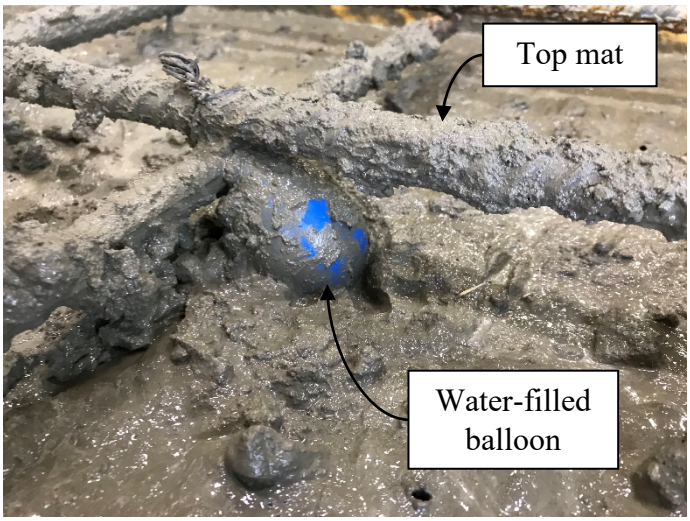

Figure 4-16: Void Installation in Specimen V1

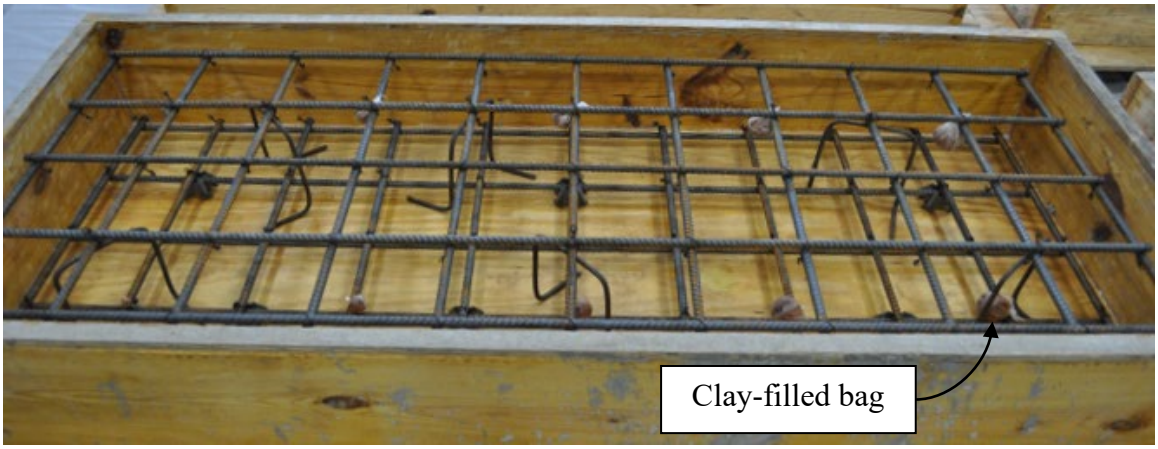

Figure 4-17: Clay Void Installation in Specimen V2

4.3 Laboratory Experimental Methodology

A 4 in. by 4 in. grid was marked on each specimen to facilitate discrete testing for the production of spatial contours maps of measurements from each NDT method. The origin of the grid was offset six inches in both directions from the southwest corner of the specimens. This location for the grid origin allowed for grid lines to alternate between

being directly over reinforcing steel or directly between two pieces of reinforcement. Before evaluating several specimens in a moist condition, the specimen surfaces were prepared to the saturated surface dry condition to prevent surface ponding from influencing the accuracy of collected measurements.

4.3.1 Ground-Penetrating Radar Data Collection

GPR data was collected in accordance with ASTM D6087 (2015) by collecting wave reflections perpendicular to the top layer of reinforcing steel. Additionally, wave reflections were recorded while the GPR antenna was oriented perpendicular to the bottom layer of reinforcing steel in the top mat to investigate whether measured reflections of the bottom layer of reinforcing steel correlate better with zones of simulated defects than do reflections of the top layer. For the laboratory specimens, the top layer of reinforcing steel corresponded with the longitudinal reinforcement while the bottom layer corresponded with the transverse reinforcement.

A GSSI SIR 2000 data acquisition unit was used in conjunction with a GSSI 2600 MHz high resolution antenna to collect GPR data. The data acquisition system configuration settings that were approved by an ALDOT GPR technician are summarized in Table 4-2.

Table 4-2: SIR 2000 Configuration Settings

Samples per Scan	Scans per Second	Scans per Inch
512	200	36

Data were collected in both directions along the 4 in. by 4 in. grid, allowing for the collection of wave reflection amplitudes both along reinforcement and directly between

reinforcement for both the top and bottom reinforcement layer of the top mat. The significance of collecting GPR data in this manner will be expounded upon in Section 4.4.1.

In accordance with the GSSI BridgeScan Handbook (2017), to obtain the reinforcement reflections from the top mat of the laboratory specimens, the GPR inspection passes were analyzed in RADAN 7. A time-zero correction algorithm was first implemented to remove the direct air wave and direct ground wave from each two-dimensional line scan. Then, a migration function was performed to focus the hyperbolas associated with the reinforcement into singular dots to facilitate ease of data sampling. The dielectric constant (which is directly related to the wave velocity) of each laboratory specimen was estimated through iteration, ensuring that the top mat of reinforcement was at the appropriate depth from the top surface in line scans, based on estimated cover quantities. The dielectric constant and corresponding wave velocity for each specimen tested in the air-dried and moist states can be found in Table 4-3. Note that many values for specimens tested in the moist state are listed as n/a since only six specimens were tested in both moisture states. The dielectric constants observed in Table 4-3 are generally in good agreement with that reported for concrete of varying moisture content by Jol (2008). With the concrete dielectric constant and wave velocity known, an auto-picking tool was then used to select the peak amplitude reflection from each migrated piece of reinforcing steel; a manual selection tool was used when the auto-picking tool failed to select the correct reflections. The foregoing methodology was used to select the peak reflections collected from the transverse (top reinforcement) and longitudinal (bottom reinforcement) datasets separately. The spatial coordinates, reflection amplitude (expressed in decibels), and the two-way travel time for each reflection were exported for later post-processing.

Table 4-3: Air-Dried and Moist Specimen Dielectric Constants and Wave Velocities

	Air-Dried		Moist	
Specimen ID	**Dielectric Constant**	**Wave Velocity (in/ns)**	**Dielectric Constant**	**Wave Velocity (in/ns)**
CTRL	6	4.82	n/a	n/a
CR1	6.5	4.63	n/a	n/a
C1	12	3.41	15	3.05
C2	12	3.41	10	3.73
DE2	9	3.93	n/a	n/a
DE3	7.5	4.31	8	4.17
DE4	6.5	4.63	n/a	n/a
DE5	6.5	4.63	n/a	n/a
DL1	8	4.17	22	2.52
DL2	10	3.73	n/a	n/a
DL3	7	4.46	8	4.17
DL4	10	3.73	n/a	n/a
DL5	7	4.46	n/a	n/a
DL6	7	4.46	n/a	n/a
DL7	7	4.46	9	3.93
DL8	8	4.17	n/a	n/a
PC1	6	4.82	n/a	n/a
PC2	9	3.93	n/a	n/a
V1	6	4.82	n/a	n/a
V2	6.5	4.63	n/a	n/a

n/a: Not available

4.3.2 Impact-Echo Data Collection

The Olson Instruments Impact Echo system was used to evaluate the laboratory specimens using the impact-echo method. An impact-echo test head was used to induce the impacting force and measure the resulting surface displacement. Data were recorded, analyzed, and displayed on the Olson Freedom Data PC using the built in WinIE data analysis program. Discrete measurements were taken at every point on the 4 in. by 4 in. grid overlaid on the specimens, allowing for a total of 133 measurements per slab for the production of spatial contour maps of specimen condition.

Before beginning IE testing, basic parameters were input on the Freedom Data PC, largely in accordance with the default settings prescribed in the Freedom Data PC system reference manual (Olson Instruments Inc., 2015). Those settings are summarized in Table 4-4 .

Table 4-4: Freedom Data PC Basic Parameters

Time/Point (µs)	Points/Record	# of Records	Trigger Level (Volts)	Trigger Delay (µs)
10	1024	3	-0.5	1/10

Time per point is a measure of how often displacement data are recorded; in this case, every 10 microseconds. Points per record dictates the number of measurements recorded in a given waveform. Three records per data point was selected to mitigate the effects of outlying waveforms. Effectively, at a given grid point, the surface was impacted three times, three separate waveforms were recorded, and the results were grouped together (note that the operator had the option to remove waveforms that were thought to be poor before they were grouped together). The system trigger level determines the minimum voltage required to begin data acquisition while the trigger delay specifies how soon after an operator presses the impact button that the system begins recording measurements.

After establishing the foregoing basic parameters, the concrete compression wave velocity needed to be determined for each slab to allow for accurate estimates of target depths associated with the dominant frequency of a given impact. The compression wave velocity for each specimen tested in the air-dried state can be found in Table 4-5.

Table 4-5: Impact-Echo Specimen Wave Velocity

Specimen ID	Compression Wave Velocity (ft/s)
CTRL	13,390
C1	12,600
C2	12,640
DE2	13,870
DE3	13,020
DE4	13,800
DE5	13,350
DL1	13,420
DL2	13,680
DL3	14,550
DL4	13,780
DL5	13,660
DL6	14,460
DL7	13,090
DL8	14,440
PC1	13,980
PC2	13,680
V1	14,290
V2	15,670

To determine the values in Table 4-5, the testing head was placed over a location in which there were known to be no simulated defects, and the surface was impacted until the measured waveform reflected a single, dominant mode associated with the bottom of the specimen. Since the depth of each specimen was known, the compression wave velocity could be determined through iteration by matching the depth reported by the Freedom Data PC to the known depth of slab. These compression wave velocities were generally in the range of expected velocities reported by Popovics and Rose (1994.) With the concrete wave velocity of each specimen known, data were collected on each specimen over the 133

grid points. An auto-picking tool was used to select the dominant frequency excited during testing which was used to estimate the depth of response, as can be seen in Figure 4-18.

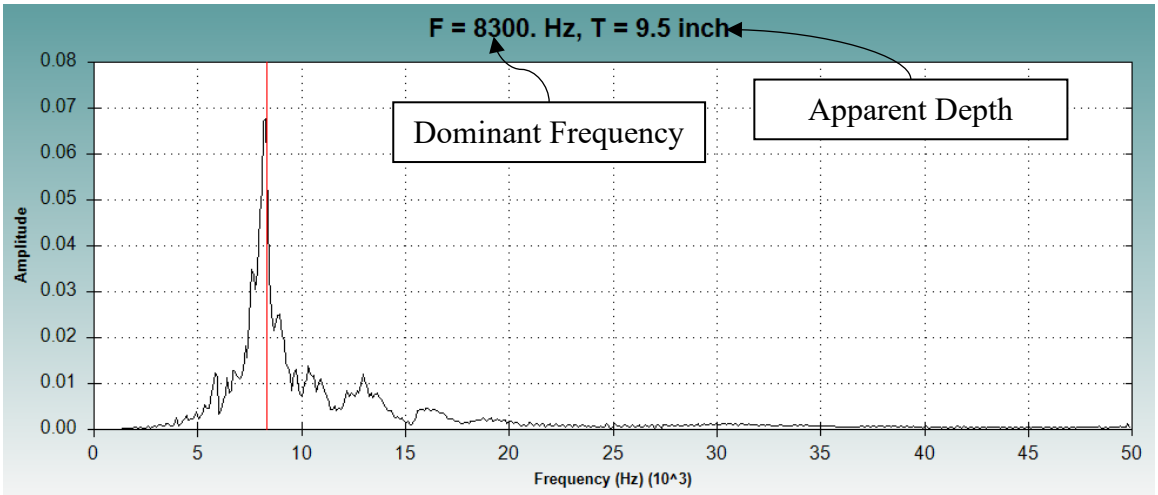

Figure 4-18: Typical Frequency Response Data from an Impact-Echo Test

4.3.3 Infrared Thermography Data Collection

To evaluate the capability of the infrared thermography method to detect defects in reinforced concrete bridge decks, two infrared cameras were used. Shown in Figure 4-19, a FLIR E60 handheld infrared camera was used to capture discrete thermal images of test specimens while continuous thermal profiles of the specimens were collected using a MOBA MTPS-100.

It was expected that both cameras would be capable of identifying surface temperature differentials typical of concrete bridge deck defects. As ASTM D4788 (2013) recommends using a thermal sensor with a minimum resolution of 0.2°C, the FLIR E60 possessed a sufficient resolution of about 0.05°C at 30°C (FLIR 2014) to fulfill ASTM guidance. With a thermal resolution of 0.1°C (MOBA 2014), the MTPS-100 also fulfilled the foregoing ASTM recommendation. Additionally, the FLIR E60 and MTPS-100 can

measure object temperatures in the range of -20°C to +120°C and 0°C to 280°C respectively which both cover the scope of typical surface temperatures of bridge decks.

Figure 4-19: MOBA MTPS-100 and FLIR E60 Thermal Cameras (Left to Right)

On sunny days with low cloud coverage, test specimens were placed outdoors in a location unaffected by shadows during testing hours. Insulation was strapped to the edges of the specimens to mitigate heat flux losses to make thermal evaluation of the specimens more representative of that of an in-place bridge deck. Once the specimens were exposed to sunlight, they were scanned using the two thermal cameras every 15 minutes to investigate how long the specimens need be exposed to sunlight before defects were clearly distinguishable from sound concrete. The location selected to conduct IRT testing was free of shadows from nearby trees, buildings etc. Furthermore, four to five hours of direct sunlight could uniformly cover a tested specimen, starting at about 11:00 AM. Heat flux sensors were adhered to specimens initially to validate that heat fluxes into the specimens were relatively uniform. With the FLIR E60, discrete thermal images were captured at the East/West ends of a specimen and at its center. One such thermal image and its corresponding photograph can be observed in Figure 4-20.

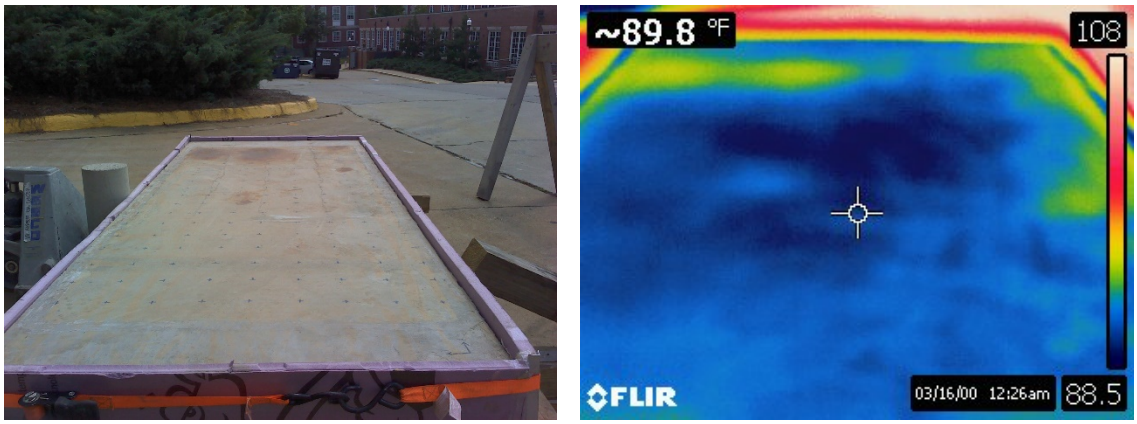

Figure 4-20: Photograph and Thermal Image (Left to Right) of Test Specimen from FLIR E60

The MOBA MTPS-100 was used cooperatively with the FLIR E60 to provide greater confidence in results from thermal imaging and to evaluate the performance of the continuous thermal profile sensor in accurately discerning between sound and defective concrete. While thermal cameras like the MTPS-100 are typically used in asphalt paving, it was hypothesized that the sensor could also be used for concrete bridge deck deterioration mapping. The PAVE-IR Scan software (MOBA 2014) settings were modified to make the thermal camera collect surface temperature measurements on a grid approximately 4 in. by 4 in. The camera was affixed to a wooden frame and slowly pushed along the test specimens as measurements were being collected. The temperature measurements and corresponding spatial coordinates were exported to a data analysis program after testing to present the data on a spatial contour plot.

4.3.4 Half-cell Corrosion Potential Data Collection

Half-cell potential measurements were collected using the Proceq Corrosion module for the Profometer. The reference electrode prescribed in the Profometer manual (Proceq SA,

2017) was a copper-copper sulfate electrode which was housed in a rolling wheel to facilitate continuous data measurement along a given direction. The wheel was saturated for an hour, and the specified copper sulfate solution was then added to the wheel.

After preparing the reference electrode, the ground cable from the Profometer was connected to a laboratory specimen via electrical cables attached to the reinforcement mats during fabrication to facilitate half-cell measurements. As Specimens C1 and C2 were the only two corroded specimens, the half-cell corrosion potential method was only applied to them. Because the top reinforcement mats in the corroded specimens were cut into thirds to produce different levels of corrosion, the ground cable was moved to the section of the mat being tested during half-cell measurements. Readings were taken by rolling the wheel over the steel reinforcement, collecting a potential difference reading every four inches along the survey lines. Measurements were collected in the transverse direction to collect a more robust dataset of potential difference measurements (since within the overlaid gird, there were nine pieces of reinforcement in the transverse direction and five pieces in the longitudinal direction).

Both half-cell potential and electrical resistivity measurements were collected twice each week for a month to evaluate the effects of time on measurements, both during and after rapid corrosion from impressed current. The dates in which measurements were collected along with the corresponding total length of accelerated corrosion per zone are provided in Table 4-6.

Table 4-6: Dates of Corrosion Method Measurements and Corresponding Length of Accelerated Corrosion

Date (M, D, Y)	Specimen C1 Corrosion Length (Days)		Specimen C2 Corrosion Length (Days)	
	Zone 2	Zone 3	Zone 2	Zone 3
09/12/19	6.90	8.85	8.85	8.85
09/16/19	-	11.85	11.85	11.85
09/19/19	-	13.90	13.90	13.90
09/23/19	-	-	-	16.88
09/26/19	-	-	-	18.96
09/30/19	-	-	-	21.96
10/03/19	-	-	-	23.96
10/07/19	-	-	-	27.00

Furthermore, approximately five months after accelerated corrosion was terminated, Specimens C1 and C2 were moistened for three months (as will be described in Section 4.3.6) and half-cell potential measurements were collected. Afterwards, the specimens were allowed to air-dry for one month and measurements were taken again. When collecting measurements in the air-dried state, the specimen surfaces were premoistened for varying times in accordance with Proceq (2017) recommendations in order to investigate the influence of pre-moistening time on half-cell measurements.

4.3.5 Electrical Resistivity Data Collection

Concrete electrical resistivity was measured using the Proceq Resipod which operates on the principle of a Wenner probe (Proceq SA 2017). The four probes of the Resipod were pressed into a shallow container of water to fill its reservoirs before each measurement of concrete resistivity (this would help facilitate good connection between the test instrument and the concrete). The concrete surface was wetted to allow for an accurate resistivity

measurement (since current flows within the ionic pore fluid of concrete). As with the half-cell corrosion potential method, the electrical resistivity method was only employed on Specimens C1 and C2. Electrical resistivity was measured twice each week, for a month to evaluate the effects of time on measurements, as with the HCP method.

Measurements were taken by positioning the instrument diagonally between two intersections of reinforcing steel. Since steel conducts electricity much more easily than concrete, positioning the instrument such that was parallel to it could preclude an accurate measurement of concrete resistivity. Subsequently, resistivity was measured diagonally five times within the confines of four pieces of reinforcement, each time moving the instrument slightly. The median of the five measurements was selected as the concrete resistivity to remove the effects of outliers. The center of the instrument was used as the spatial location corresponding to measured resistivity, to be used in graphical presentation of resistivity measurements. Data collection with the Wenner probe is illustrated in Figure 4-21.

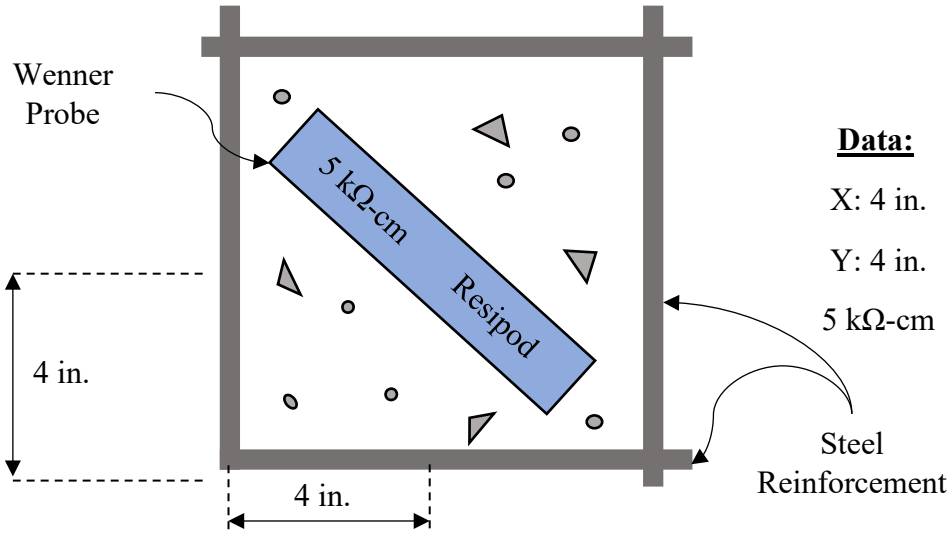

Figure 4-21: Concrete Electrical Resistivity Measurement Using the Proceq Resipod

4.3.6 Test Specimen Ponding Program

To evaluate the effects of moisture content on NDT measurements, six test specimens were selected to be moistened. Specimens C1, C2, DL1, DL3, DL7, and DE3 were selected as they were hypothesized to exhibit defects that could potentially affect NDT measurements differently when moistened. A PVC manifold was constructed that spanned among the six specimens. Soaker hoses were connected to the manifold and laid over each specimen. The hoses were then covered by saturated burlap and plastic sheeting, to mitigate evaporative losses. The soaker hoses were activated every 48 hours for three months before any NDT methods were used on the specimens. It was assumed that, at this time, the specimens were in a fairly moist state. This method of moistening the specimens can be seen in Figure 4-22.

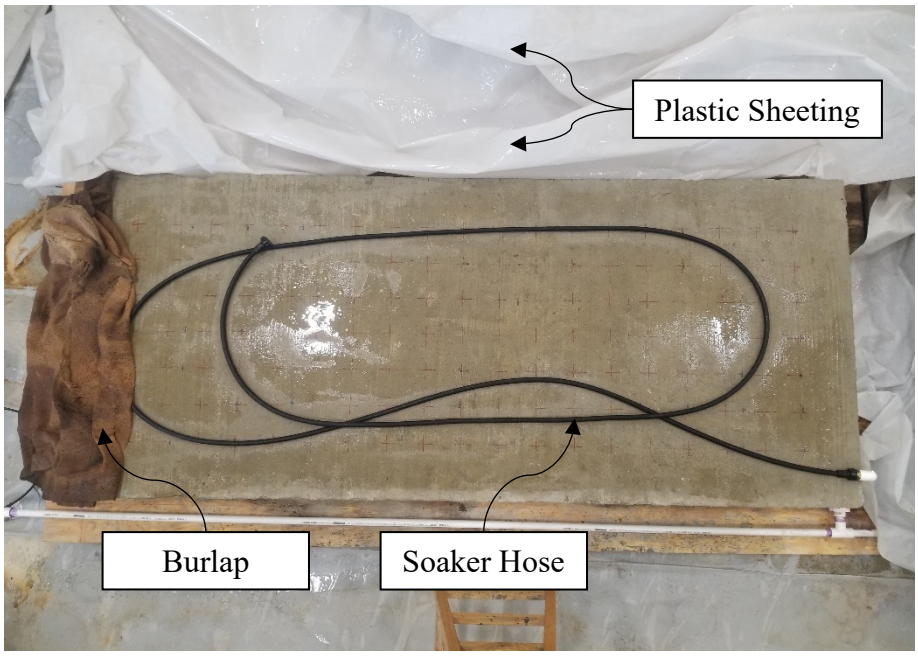

Figure 4-22: Ponding Program for Laboratory Specimens

4.4 Analytical Methodology

Analytical analyses of NDT methods aimed to answer questions regarding (1) the capability of each method to respond to different simulated defects, (2) the interdependency of different NDT methods, (3) the effect of moisture content on NDT data, and (4) how best to collect/process NDT data to maximize correlation with the true condition of a given concrete element. Much of this effort was concentrated on the investigation of GPR, given the high potential for rapid deployment and potential uncertainties associated with this technology.

4.4.1 Effect of Grid Location and Inspection Direction on GPR Data

Given the present degree of skepticism regarding the accuracy of GPR measurements, GPR technicians may collect data both respectively perpendicular to the top and bottom reinforcing layers of the upper reinforcement mat in a reinforced concrete bridge deck. Consistency between the two perpendicular inspections may give GPR operators a greater sense of confidence regarding whether GPR data correspond to the true condition of a bridge deck. Nonetheless, as ASTM D6087 (2015) testing specifications primarily prescribe collecting ground-coupled GPR data perpendicular to the top lay of the top mat, it is unclear if data collected perpendicular to the bottom layer and processed in a manner similar to that prescribed by ASTM will allow for accurate deterioration mapping of bridge decks. Furthermore, ASTM D6087 (2015) recommends collecting air-launched GPR data parallel to the flow of traffic, regardless of the direction of the top layer of reinforcing steel.

Accordingly, one potential factor that could preclude direct implementation of the ASTM methodology when GPR data are collected perpendicular to the bottom steel layer is the location of the GPR antenna with respect to the top layer. It was hypothesized that,

at the intersection of reinforcement spanning in perpendicular directions, the position of the top layer directly over the bottom layer may cause incident GPR waves to be partially reflected by the top layer before reaching the bottom layer. If a GPR evaluation consisted of passes both over the intersections of perpendicular reinforcement and between intersections, wave amplitudes collected over intersections may be significantly less than those collected between intersections. This phenomenon was hypothesized to occur when targeting bottom reinforcement reflections at intersections, as illustrated in Figure 4-23(a). It was unclear whether a similar effect would be observed when targeting top reinforcement reflections at intersections, shown in Figure 4-23(b).

Nonetheless, it was hypothesized that inspection passes performed perpendicular to the bottom steel in the top mat may allow for the detection of defects at greater depths than could be detected by performing passes perpendicular to the top steel. As the concept of detecting defects with GPR is predicated on the argument that GPR waves are attenuated by the defects, data sampling at the bottom steel may allow for the detection of defects between the top and bottom steel in the upper mat. The ability to detect defects in this depth range may be significant, especially for corrosion induced delaminations which can originate at the level of the reinforcement.

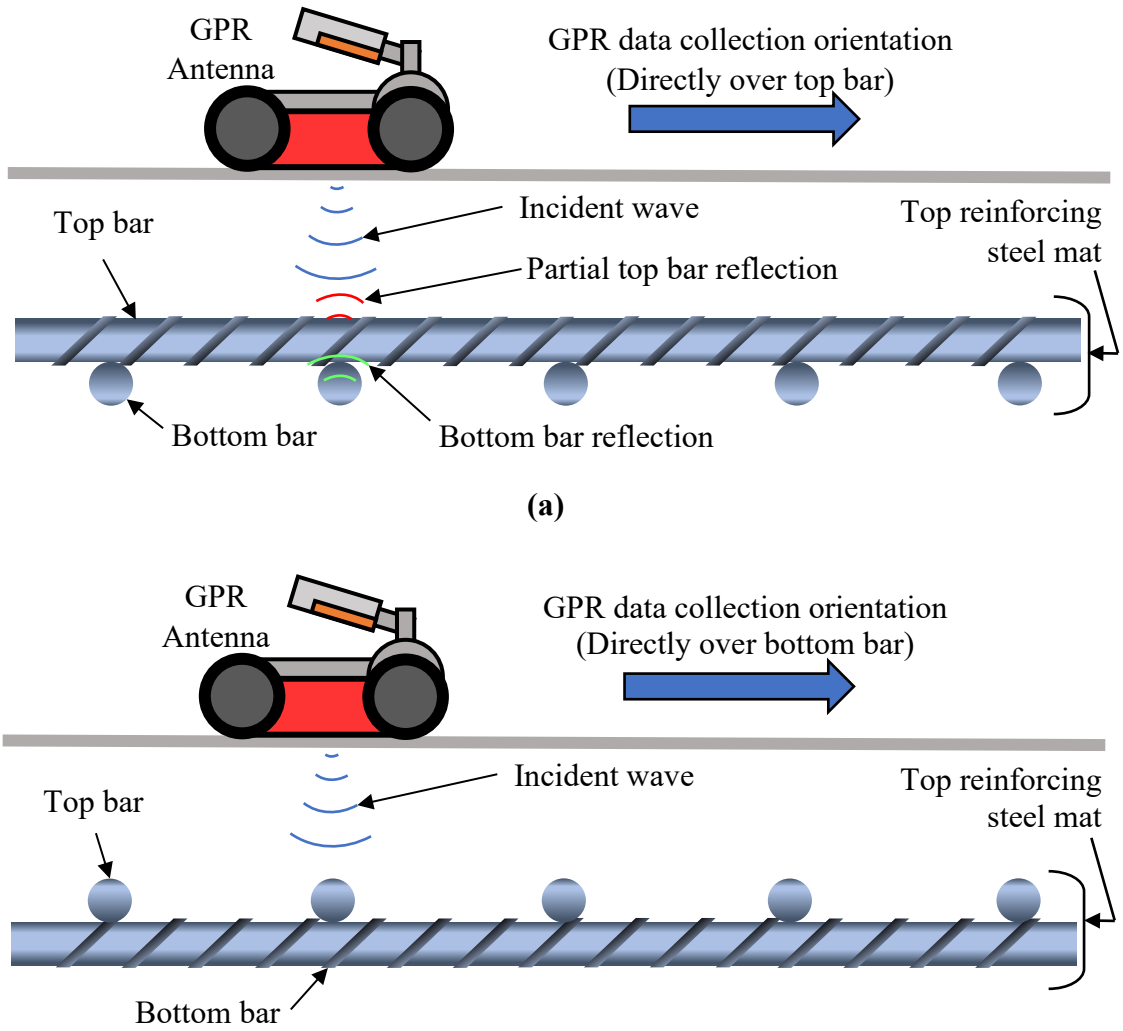

Figure 4-23: (a) Hypothesized Reinforcement Influence on GPR Data Collected Perpendicular to Bottom Bar and (b) Data Collected Perpendicular to Top Bar

To test all hypotheses regarding differences in GPR results based on the orientation of data collection and location of grid lines (whether that be directly over the intersection of reinforcement, between intersections, or a combination of the two), six subsets of the GPR dataset from each test specimen were created. The six created subsets were termed "Top Bar Passes (All)", "Top Bar Passes (Between)", "Top Bar Passes (Over)", "Bottom Bar Passes (All)", "Bottom Bar Passes (Between)", and "Bottom Bar Passes (Over)".

Accordingly, “Top Bar Passes (All)” contained all reflection amplitudes from data collected perpendicular to the top layer, “Top Bar Passes (Between)” contained all data collected perpendicular to the top layer that laid between the intersections of the bottom layer, “Top Bar Passes (Over)” contained all collected data perpendicular to the top layer directly over the intersections of the bottom steel, and similarly for the other three subsets. Figure 4-24 serves to help visualize the assignment of data to subsets, based on spatial location with respect to the top reinforcement mat.

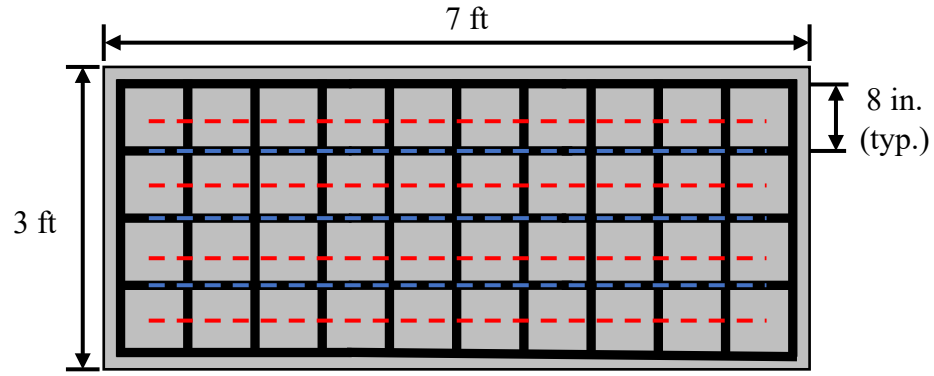

Red: Bottom Bar Passes (Between); Blue: Bottom Bar Passes (Over)

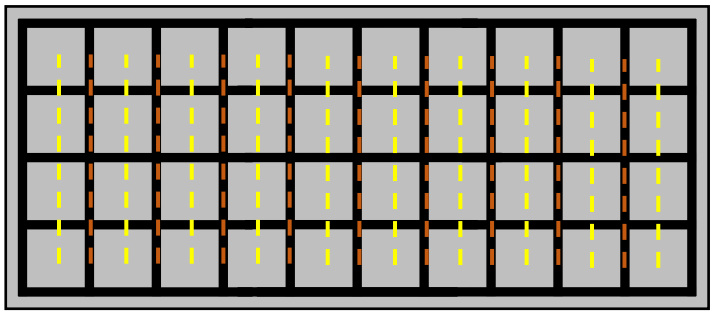

Yellow: Top Bar Passes (Between); Brown: Top Bar Passes (Over)

Figure 4-24: GPR Inspection Pass Subsets (Specimen Plan View)

Statistical hypothesis testing between relevant groups was used to investigate the influence of grid location and data-collection orientation on GPR results. If data collected over the intersection of reinforcement belonged to the same distribution of wave reflection

amplitudes as that from data collected between intersections, there would be no statistically significant difference in either means or variance between the two GPR data subsets. Alternatively, a difference in either means or variance would suggest that reflections from the two subsets do not belong to the same sample. Accordingly, the two subsets would form two different distributions that would theoretically preclude the use of a singular amplitude threshold that delineates between sound or defective concrete. Towards investigating this potential behavior, F-tests and T-tests were conducted to answer the following questions:

1. Is there a statistical difference in either means or variance of reflection amplitudes between the Bottom Bar Passes (Between) and Bottom Bar Passes (Over) groups?
2. Is there a statistical difference in either means or variance of reflection amplitudes between the Top Bar Passes (Between) and Top Bar Passes (Over) groups?

One-tailed t-tests were performed to address the first question since it was expected that means of the Bottom Bar Passes (Over) subset would be less than those of the Bottom Bar Passes (Between) subset because of the foregoing hypothesized influence of the top reinforcing steel layer. Conversely, two-tailed t-tests were performed to compare the means of the Top Bar Passes (Over) and Top Bar Passes (Between) groups, as it was hypothesized that there existed no difference in means. Conclusions to the two aforementioned questions would allow for an increased understanding of the behavior of GPR waves in reinforced concrete bridge decks and corresponding recommendations on how to establish effective gridlines and data-collection directions that maximize correlation between apparent deck condition (as reported by GPR) and the true condition of a bridge deck. Should there be a statistical difference in means or variance between datasets that

contain only passes over the intersections of reinforcement and groups that only contain passes between the intersections of reinforcements, inspection groups that contain a combination of the two foregoing groups could be error-ridden. Consistent with the foregoing numbering scheme, null and alternative hypotheses for the two statistical questions are presented below. Note that a 95% confidence interval was enforced for all hypothesis testing.

Question 1:

F-test

$$H_o: {s^2}_{BBPB} = {s^2}_{BBPO}$$

$$H_1: {s^2}_{BBPB} \neq {s^2}_{BBPO}$$

where

H_o = the null hypothesis;

H_1 = the alternative hypothesis;

${s^2}_{BBPB}$ = the variance of the Bottom Bar Passes (Between) sample, dB^2; and

${s^2}_{BBPO}$ = the variance of the Bottom Bar Passes (Over) sample, dB^2.

T-test

$$H_o: \mu_{BBPB} \geq \mu_{BBPO}$$

$$H_1: \mu_{BBPB} < \mu_{BBPO}$$

where

μ_{BBPB} = the mean of the Bottom Bar Passes (Between) sample, dB; and

μ_{BBPO} = the mean of the Bottom Bar Passes (Over) sample, dB.

Question 2:

F-test

$$H_o: {s^2}_{TBPB} = {s^2}_{TBPO}$$

$$H_1: {s^2}_{TBPB} \neq {s^2}_{TBPO}$$

where

${s^2}_{BBPB}$ = the variance of the Top Bar Passes (Between) sample, dB^2; and

${s^2}_{BBPO}$ = the variance of the Top Bar Passes (Over) sample, dB^2.

T-test

$$H_o: \mu_{TBPB} = \mu_{TBPO}$$

$$H_1: \mu_{TBPB} \neq \mu_{TBPO}$$

where

μ_{BBPB} = the mean of the Top Bar Passes (Between) sample, dB; and

μ_{BBPO} = the mean of the Top Bar Passes (Over) sample, dB.

Descriptive statistics in support of hypothesis testing of GPR data collected perpendicular to the bottom layer in the top reinforcement mat can be found in Table 4-7. For specimens in which simulated defects were exclusively located on gridlines over steel reinforcement, data points collected directly above those defects were removed from those datasets. As the purpose of the hypothesis testing was to evaluate whether grid selection influences GPR data, signal attenuation from any defects which GPR responds to could lead to a false conclusion regarding the relationship between grid lines and GPR data. Nonetheless, for specimens in which defects were indiscriminately distributed between inspection passes over and between steel reinforcement, data points were not removed.

Table 4-7: Descriptive Statistics for Air-Dried GPR Passes Collected Perpendicular to Bottom Steel in Top Mat

Specimen ID	Between Passes			Over Passes		
	n	μ (dB)	s^2 (dB^2)	n	μ (dB)	s^2 (dB^2)
CTRL	36	-17.55	1.44	27	-18.12	1.27
CR1	36	-15.48	0.91	27	-16.51	1.00
C1	36	-18.82	0.71	27	-19.85	0.49
C2	36	-24.44	1.58	27	-25.62	1.35
DE2	36	-19.90	2.91	27	-21.29	2.65
DE3	36	-18.61	2.03	27	-19.20	1.71
DE4	36	-16.62	1.47	27	-16.96	1.05
DE5	36	-18.05	2.00	27	-18.38	1.34
DL1	36	-18.86	0.53	21	-19.90	0.74
DL2	36	-24.13	4.37	21	-26.81	2.02
DL3	36	-17.26	0.31	27	-17.37	0.46
DL4	36	-24.34	3.29	27	-27.98	10.96
DL5	36	-17.89	0.52	21	-18.38	0.56
DL6	36	-19.05	0.23	21	-19.75	0.69
DL7	32	-18.14	0.34	20	-18.84	1.98
DL8	36	-18.66	0.62	21	-20.44	0.52
PC1	36	-16.94	1.91	27	-16.77	0.93
PC2	36	-18.47	2.40	27	-20.22	2.58
V1	36	-17.97	1.49	17	-19.54	0.35
V2	36	-17.00	0.36	17	-17.96	1.62

Similarly, descriptive statistics used in hypothesis testing of GPR data collected perpendicular to the top steel in the top reinforcement mat can be found in Table 4-8. As before, data points collected directly over defects in specimens in which defects were exclusively located over reinforcement were removed before conducting the hypothesis testing. This was performed to preclude a scenario in which the position/direction of the GPR antenna was falsely attributed to lead to statistically

significant differences in recorded data when, in actuality, those differences existed because of attenuating effects from the simulated defects.

Table 4-8: Descriptive Statistics for Air-Dried GPR Passes Collected Perpendicular to Top Steel in Top Mat

Specimen ID	Between Passes			Over Passes		
	n	μ (dB)	s^2 (dB^2)	n	μ (dB)	s^2 (dB^2)
CTRL	30	-14.83	0.37	27	-14.62	0.20
CR1	30	-13.23	0.17	27	-13.31	0.26
C1	30	-18.36	0.39	27	-18.79	0.59
C2	30	-19.90	1.47	27	-19.39	1.47
DE2	30	-16.92	0.35	27	-17.01	0.30
DE3	30	-15.45	0.20	27	-15.47	0.25
DE4	30	-14.50	0.18	27	-14.41	0.13
DE5	30	-15.44	0.27	27	-15.48	0.36
DL1	30	-15.77	0.38	21	-15.75	0.12
DL2	30	-18.46	0.72	21	-18.53	0.85
DL3	30	-14.27	0.18	27	-14.32	0.12
DL4	30	-18.69	0.97	27	-18.95	0.85
DL5	30	-15.10	0.23	21	-15.06	0.13
DL6	30	-15.57	0.11	21	-15.78	0.72
DL7	30	-14.73	0.18	21	-14.76	0.27
DL8	30	-15.44	0.08	21	-15.67	0.26
PC1	30	-14.21	0.56	27	-14.03	0.31
PC2	30	-15.35	0.46	27	-15.32	0.38
V1	30	-14.74	0.13	17	-14.67	0.14
V2	30	-14.67	0.13	17	-14.69	0.57

4.4.2 GPR Deterioration Mapping Using BridgeScan Recommendations

To evaluate the effectiveness of current GPR data-processing techniques towards defect detection in bridge decks, the GSSI BridgeScan (2017) methodology was applied to all six subsets of GPR data collected from the twenty specimens. Note that as an extension of ASTM D6087 (2015) testing specifications, the BridgeScan manual prescribes collecting

GPR data perpendicular to the top layer of the top mat. Thus, the BridgeScan manual is not directly applicable to the three subsets of GPR data collected perpendicular to the bottom steel in the top mat.

After processing data as discussed in Section 4.3.1, spatial coordinates and normalized reflection amplitudes were exported to a data analysis software (Microsoft Excel). The three-dimensional data were then sorted by normalized reflection amplitude from largest to smallest. The five maximum and minimum amplitude values were observed; if any of those values was drastically different than its neighboring values (e.g. -23 dB to -29 dB), then that value and its accompanying spatial coordinates were removed from the dataset. In this regard, outliers in the data were removed that were likely associated with accidentally sampled data (BridgeScan 2017).

After removing outliers, GSSI (2017) recommends calculating four threshold values and using that which best agrees with additional information available regarding the bridge deck (visual assessment, chain dragging, etc.). Two of those thresholds were calculated in accordance with what GSSI terms the "ASTM" method, in reference to ASTM D6087 testing specifications (2015). To calculate these two thresholds, 6 and 7 dB were respectively subtracted from the maximum reflection amplitude (after outlier removal). Thus, if the maximum reflection amplitude was -13 dB, GSSI (2017) would recommend considering -19 and -20 dB as candidate threshold values delineating between sound and deteriorated portions of a bridge deck. Furthermore, the remaining two thresholds were calculated in what the manual terms the "GSSI" method. To calculate these thresholds, the average of the maximum 10% of reflection amplitudes (after outlier

removal) was calculated. Then, 6 and 7 dB were respectively subtracted from the calculated average to calculate the two thresholds.

After determining which of the four thresholds would be used for deterioration mapping, the percentage of sound and deteriorated deck could be calculated. Reflections that are greater than (less negative) or equal to the threshold value are classified as sound portions of deck. The remaining reflections less than (more negative) the threshold value are classified as deteriorated portions of deck. To visualize the distribution of sound and deteriorated deck, three-dimensional contour plots such as that in Figure 4-25 could be created, mapping the deck deterioration. The in-plane dimensions of the plot are the spatial coordinates of the deck and the out-of-plane dimension is the reflection amplitude at a given location. The threshold value is used to delineate between sound portions of deck (green) and deteriorated portions of deck (red).

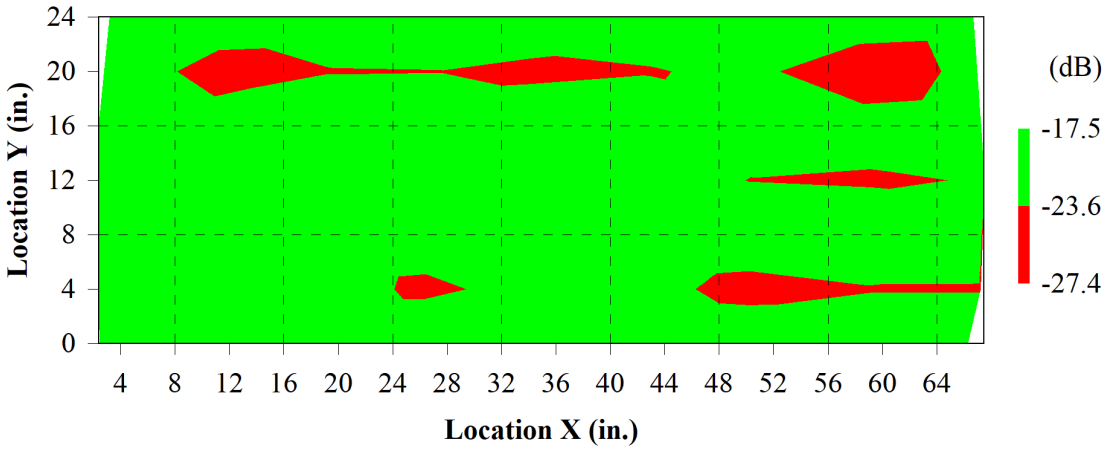

Figure 4-25: GPR Deterioration Contour Plot Made with BridgeScan Method

4.4.3 Depth Correction of GPR Data

Previous work studying how best to process GPR data to maximum correlation with the true condition of bridge decks have observed the influence of cover depth variations on

GPR data (Barnes et al. 2008; Dinh et al. 2020; and Pashoutani and Zhu 2020). The basis of such theories regarding the relationship between cover depth variations and GPR data is that differences in cover depth cause differential signal attenuation throughout the cover layer which is evidenced in two-way travel times. Accordingly, as defect detection with GPR is predicated on the theory that defects cause top mat reflections to be attenuated, differences in cover layer that cause differential attenuation may be falsely attributed to the presence of a defect. This variation in cover depth can be accounted for through analysis of the two-way travel time of GPR waves, since waves that travel a longer distance at the same velocity as a wave travelling a shorter distance will take longer to return to the GPR antenna.

In this thesis, the depth-correction algorithm proposed by Barnes et al (2008) was implemented to assess whether such a technique allowed for increased correlation of GPR data with the true state of deterioration of the laboratory specimens. Given that the algorithm was tailored towards data collected perpendicular to the top steel in the top reinforcement mat, it was not applied to passes collected perpendicular to the bottom steel in the top mat. After collecting GPR data as described in 4.3.1, the two-way travel times and reflection amplitudes were exported to a data analyzation software. For specimens with significant cover depth variation, a linear relationship was observed between the normalized amplitude and the two-way travel time, as can be seen in the top layer GPR data from Specimen C2, shown in Figure 4-26.

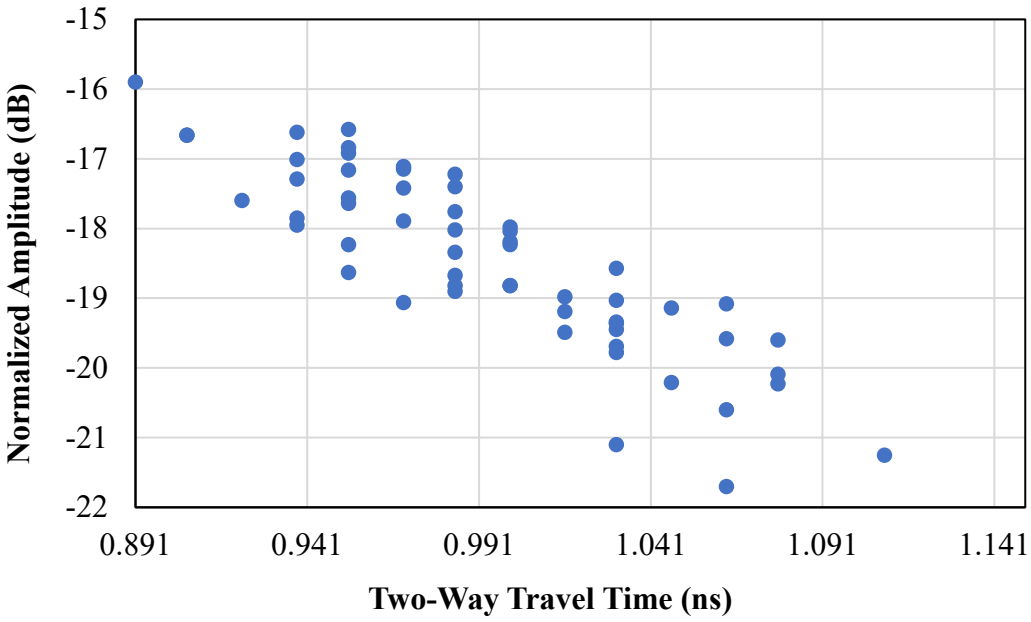

Figure 4-26: Normalized Amplitude and Two-Way Travel Time Data for Test Specimen C2

The data were separated into bins containing as close to 30 entries as possible. A linear regression was then performed on the 90th percentile from each bin. The 90th percentile was used to establish a statistical reference that was not affected by outliers (Barnes et al. 2008). The resulting best-fit line was then subtracted from the GPR data to remove the portion of that data attributed to the effects of cover depth on wave attenuation. The depth-corrected GPR data for Specimen C2 can be observed in Figure 4-27. Observe that the range of normalized amplitudes is significantly different than that from the non-depth-corrected data. The implication of this observation is that a threshold or threshold generation procedure applicable to non-depth-corrected data would not be appropriate for depth-corrected data.

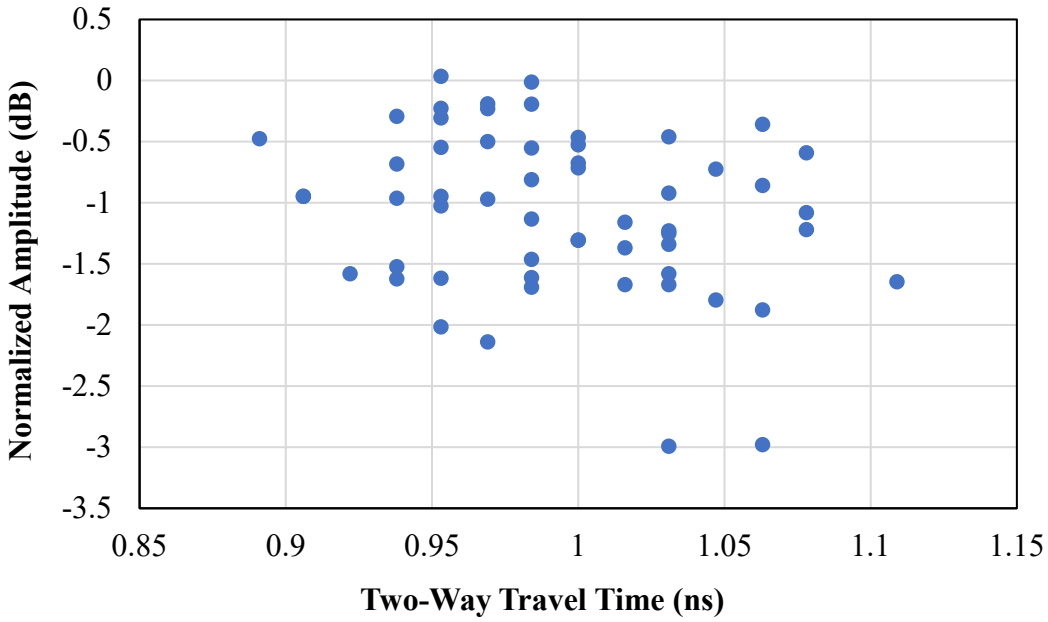

Figure 4-27: Depth-corrected GPR Data for Test Specimen C2

Spatial contour plots of the depth-corrected GPR data were then prepared. Visual comparison of the contour plots with known locations of defects in the laboratory specimens allowed for an evaluation of the capability of depth-corrected GPR data to detect different forms of concrete defects. Note that, since this depth-correction algorithm requires at least two 90th percentile values to fit a regression line to (i.e. two bins of nearly 30 entries each), the algorithm was only applied to the Top Bar Passes (All) subset of GPR data. The other two subsets from data collected perpendicular to the top steel in the top reinforcement mat did not have enough samples to perform such a regression analysis.

4.4.4 Receiver Operator Characteristic Analysis of GPR Data

In conjunction with visual assessments of spatial contour plots of NDT data, a quantitative method was needed for (1) evaluating the capability of a given NDT method in detecting a certain type of defect (e.g. delamination), and (2) quantifying the accuracy of different

thresholds/processing techniques to determine what was the most efficient way to use NDT data for concrete bridge deck evaluation. Accordingly, Receiver Operator Characteristic (ROC) analysis, an analytical tool which uses a binary classifier to sort a data point to one of four outcomes, was used on both the non-depth-corrected and depth-corrected GPR data. ROC analysis has previously been used in other analytical investigations of GPR data (Martino et al. 2015; Sultan and Washer 2018), and can be visualized using a confusion matrix, such as that shown in Figure 4-28.

Within the context of GPR data, the ROC analysis methodology demonstrated in Figure 4-28 is explained as follows. An arbitrary threshold or classifier (e.g. -16 dB) is selected to hypothesize the class of a data point as either 'Yes' or 'No'. A 'Yes' hypothesis is assigned to a data point (e.g -17 dB) that is less than (more negative) than the arbitrary threshold. In this case, the chosen threshold signals that the GPR data point corresponds to a defective point of the bridge deck. Alternatively, a 'No' hypothesis is assigned to a data point (e.g. -15 dB) that is greater than (less negative) than the arbitrary threshold. Accordingly, a 'No' hypothesized class signals that the data point corresponds to a sound point of the bridge deck.

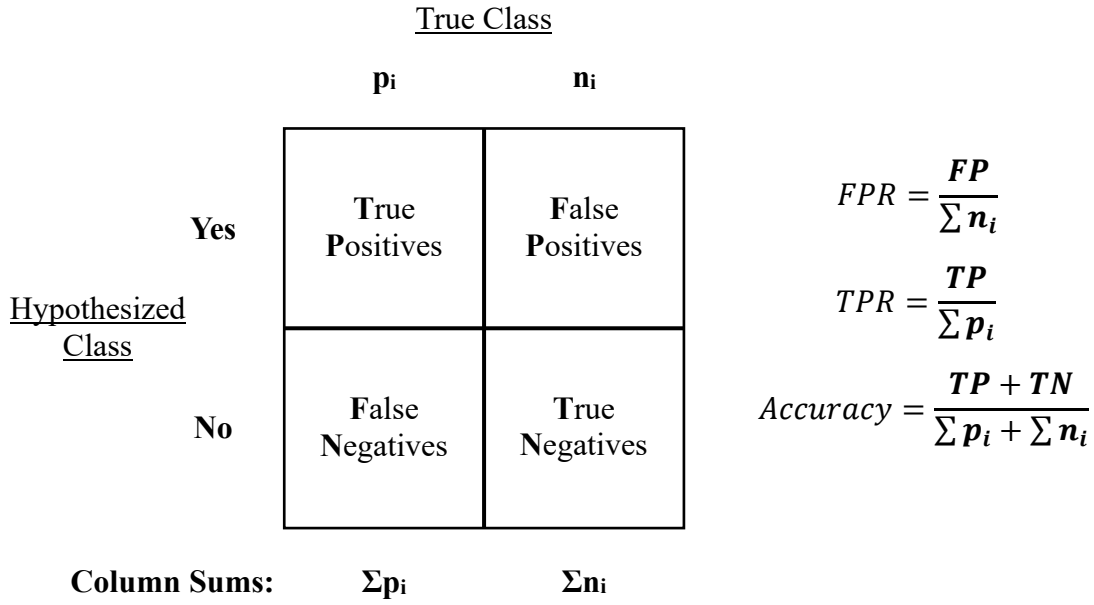

Figure 4-28: Confusion Matrix and ROC Classifier Evaluation Metrics (Adapted from Fawcett 2006)

With the hypothesized class of the data point known, the value is entered into its appropriate row of the confusion matrix and compared to the true class of the data point. For that data point, the corresponding true class is the actual condition of the bridge deck at that given point (sound or defective). The true class for a bridge deck comprises ground truth information determined through destructive coring to validate the existence of defects or through the assumption that other NDT methods (e.g. chain dragging) are 100% representative of the true condition of the deck. If the bridge deck is truly defective at that point, a positive 'p' classification is assigned to that data point. Alternatively, if the bridge deck is sound at that point, a negative 'n' classification is assigned to that data point. With the hypothesized and true class of a data point known, the data point can be mapped to one of the four outcomes on the confusion matrix.

Among the four possible outcomes shown in the confusion matrix, a 'True Positive' represents a data point in which the threshold predicted that the deck was defective at the point and ground truth information regarding the deck state (e.g. destructive coring) confirmed that it is indeed defective. Similarly, a 'True Negative' outcome represents a point on the deck which the threshold predicted was sound, and ground truth information at that point confirmed the deck was sound. Both of these outcomes represent cases in which the arbitrarily chosen threshold correctly predicts the true state of the deck. The two remaining outcomes, 'False Positive' and 'False Negative', are incorrect predictions by the threshold. A 'False Positive' is a point on the deck which the threshold signals as defective which, in fact, is actually sound. Similarly, a 'False Negative' is a point on the deck which the threshold indicates as sound yet is truly defective.

After mapping all GPR data points in a set to the four outcomes using a threshold, the threshold may be evaluated based on the false positive, true positive, and accuracy rates which can be calculated using the following equations:

$$FPR = \frac{FP}{\sum n_i} \tag{4.1}$$

where

FPR = the false positive rate of a given threshold;

FP = the number of false positives resulting from the use of a given threshold; and

$\sum n_i$ = the sum total of ground truth points that have a negative (sound) true class.

$$TPR = \frac{TP}{\sum p_i} \tag{4.2}$$

where

TPR = the true positive rate of a given threshold;

TP = the number of true positives resulting from the use of a given threshold; and

$\sum p_i$ = the sum total of ground truth points that have a positive (defective) true class.

$$Accuracy = \frac{TP + TN}{\sum p_i + \sum n_i} \tag{4.3}$$

where

$Accuracy$ = the accuracy rate of a given threshold; and

TN = the number of true negatives resulting from the use of a given threshold.

ROC analysis may be implemented for any desired number of thresholds, and the three foregoing evaluation metrics may be calculated for each threshold. A user may use the three metrics to decide which threshold is best suited for decision-making; in the case of this study, the decision is whether a given point on a bridge deck is defective or sound. If the user believes that the outcome of returning a true positive or a false positive are equally weighted, then the optimal threshold to use is that with the highest accuracy rate. Regarding nondestructive evaluations of bridge decks, this case is analogous to a bridge owner who equally weights the outcomes of correctly identifying a defective point on the deck and incorrectly claiming that a sound point on the deck is defective. If both outcomes

are not weighted equally, then some linear combination of the true and false positive rates and their respective weighting factors will be indicative of the optimal threshold. For the work performed in this study, it was assumed that the two outcomes were weighted equally, and the optimal threshold was determined as that corresponding with the highest accuracy rate.

Such a threshold was determined for the six subsets of non-depth-corrected data and depth-corrected data acquired in both the air-dried and moist states of the specimens. Thresholds were iteratively tested with ROC analysis by changing the threshold in 0.01 dB increments. For each dataset, the thresholds tested ranged between the maximum and minimum values of collected reflection amplitudes. For each point in the dataset, the hypothesized class of the point was determined in accordance with the following relationship:

$$S \geq T > D \tag{4.4}$$

where

S = a reflection amplitude corresponding with a sound point on the deck, dB;

T = the arbitrary cutoff threshold, dB; and

D = a reflection amplitude corresponding with a deteriorated point on the deck, dB.

For each dataset from a given specimen, the optimal threshold was selected as representative of the capability of GPR to detect the defect specific to the tested specimen. Additionally, the percent of deteriorated deck and percent of sound deck correctly

identified by that threshold was recorded to provide additional metrics of assessing how effectively GPR was at identifying a specific type of defect (e.g. corrosion of steel reinforcement). These two additional assessment metrics were necessary because the accuracy rate of GPR itself might not always be the best indicator of the defect detection capability of the testing method. One such example of a scenario might be a deck with a relatively small percentage of deteriorated area, e.g. 10%. If GPR testing is unable to discern the deteriorated deck from the sound deck, the optimal threshold selected from ROC analysis would result in an overall accuracy rate of 90%, since it would be most advantageous to assume the entire deck is sound (as opposed to assuming the entire deck to be deteriorated and having an overall accuracy of 10%). While the overall accuracy rate of GPR would be 90%, and 100% of the sound portions of the deck would be correctly predicted, 0% of the deteriorated deck would be correctly identified. Thus, the overall accuracy rate of GPR might then lead to the false conclusion that GPR is a good NDT method for identifying deck deterioration. Rather, if a high overall accuracy rate (e.g. 92 %) is also accompanied by high percentages of sound and deteriorated deck correctly identified, one would conclude that GPR is a good NDT method for identifying that deck deterioration.

4.4.5 Receiver Operator Characteristic Analysis of IE Data

For similar reasons discussed in the previous section, ROC analysis was also performed on the IE data collected from the air-dried and moist test specimens. The analysis procedure was modified to accommodate the different effect which defects have on IE data. Unlike the case with GPR data in which defects are expected to attenuate the wave signal and thus cause deteriorated areas to return a weaker signal than that corresponding with sound

concrete, defects may cause frequencies measured using IE testing to be less than or greater than those associated with sound concrete. Whether or not a defect causes positive or negative deviations from the frequencies of sound concrete may depend on a variety of factors including defect type and depth. Sansalone (1997) acknowledges the variable effect different defects have on IE measurements, stating that correct data interpretation often comes through pattern recognition associated with vast experience and training.

Accordingly, the ROC analysis procedure needed to be modified to account for the effects of defects which could manifest themselves on either side of the range of frequencies associated with sound concrete. To accomplish this, ROC analysis was implemented to determine the optimal pair of thresholds in accordance with the following relationship:

$$D < T_1 \leq S \leq T_2 < D \tag{4.5}$$

where

D = a frequency associated with defective concrete, Hz;

T_1 = a lower bound threshold, Hz;

S = a frequency associated with sound concrete, Hz; and

T_2 = an upper bound threshold, Hz.

The optimal pair of thresholds was determined by iteratively testing every possible pair of thresholds ranging between the minimum and maximum recorded frequency in the dataset. During each iteration, a threshold was changed by 1 Hz. As in the analysis of the GPR

data, the optimal thresholds were considered to be those that corresponded with the highest accuracy rate. The percent of sound and defective concrete correctly identified by that pair of thresholds was also calculated to provide additional metrics for assessing the capability of the IE method to detect a particular type of defect.

4.4.6 Effect of Moisture Content on NDT Data

For all NDT methods used in this study, the influence of moisture content was investigated by comparing the air-dried specimen data to the moist specimen data using spatial contour plots. Nonetheless, additional analyses were conducted on the GPR data of the six specimens tested in the air-dried and moist states to study how changes in moisture content might affect the accuracy of thresholds delineating between sound and deteriorated concrete. F-tests and paired t-tests were conducted to determine if changes in moisture content affected the variance and mean respectively of GPR data. Should an influence exist, a bridge deck may contain a range of optimal threshold values depending on its moisture content, as the notion of cutoff thresholds is predicated on an implicit assumption of how the GPR data are distributed (e.g. the "fatness" of a normal distribution). This hypothesis testing was only applied to the Transverse Passes (All) and Longitudinal Passes (All) datasets as it was assumed that moisture content was uniformly distributed throughout the test specimens such that that there was no appreciable differential moisture content between concrete above reinforcement and between it. The null and alternative hypothesis used in these analyses are presented below.

<u>F-test</u>

$$H_o: {s^2}_{AD} = {s^2}_M$$

$$H_1: {s^2}_{AD} \neq {s^2}_M$$

where

H_o = the null hypothesis;

H_1 = the alternative hypothesis;

$s^2{}_{AD}$ = the variance of an air-dried sample, dB^2; and

$s^2{}_M$ = the variance of a moist sample, dB^2.

T-test

$$H_o: \mu_{AD} = \mu_M$$

$$H_1: \mu_{AD} \neq \mu_M$$

where

μ_{AD} = the mean of an air-dried sample, dB; and

μ_M = the mean of a moist sample sample, dB.

Descriptive statistics for GPR data collected perpendicular to the top reinforcing layer in support of the foregoing hypothesis tests can be found in Table 4-9.

Table 4-9: Descriptive Statistics for GPR Passes Collected in Specimen Air-Dried and Moist States

Specimen ID	Air-Dried Data			Moist Data		
	n	μ (dB)	s^2 (dB^2)	n	μ (dB)	s^2 (dB^2)
C1	57	-18.57	0.52	57	-24.73	0.94
C2	57	-18.46	1.66	57	-19.77	2.82
DE3	57	-15.46	0.21	57	-16.20	1.34
DL1	57	-15.76	0.48	57	-15.13	0.26
DL3	57	-14.35	0.36	57	-15.24	0.22
DL7	57	-14.72	0.20	57	-16.68	0.24

4.4.7 Transformed Cumulative Probability Distribution of NDT Data

In a given dataset, each half-cell or electrical resistivity measurement, x_i, was sorted from greatest to smallest, and its corresponding cumulative probability within the dataset was calculated using Equation 4.6 (Gumbel, 1954).

$$p_i = \frac{i}{N+1} \tag{4.6}$$

where

p_i = the cumulative probability corresponding to the i[th] measurement, x_i;

i = the index value (started at 1) associated with p_i; and

N = the number of measurements in a given dataset.

Subsequently, the inverse of the standard normal cumulative distribution function, $\phi(z)$, was calculated for each cumulative probability using the approximate solution provided by Nowak and Collins (2013) in Equations 4.7 and 4.8:

$$z_i \approx \phi^{-1}(p_i) \approx -t_i + \frac{c_0 + c_1 t_i + c_2 {t_i}^2}{1 + d_1 t_i + d_2 {t_i}^2 + d_3 {t_i}^3} \; for \; p_i \leq 0.5 \tag{4.7}$$

$$z_i \approx \phi^{-1}({p_i}^*) \; for \; p_i > 0.5 \tag{4.8}$$

where

z_i = the approximate inverse of the standard normal cumulative distribution function evaluated at cumulative probability, p_i;

c_0 = 2.515517;

c_1 = 0.802853;

c_2 = 0.010328;

d_1 = 1.432788;

d_2 = 0.189269;

d_3 = 0.001308;

p_i^* = 1 - p_i; and

$t_i \approx \sqrt{-ln(p_i{}^2)}\ for\ p_i \leq 0.5$, and $\approx \sqrt{-ln(p_i{}^{*2})}\ for\ p_i > 0.5$

The resulting pairs of NDT measurements and corresponding z_i were plotted on standard linear graphs to produce the desired cumulative frequency distribution. Should the transformed distribution approximate a straight line, it could be postulated that the measurements were normally distributed (Nowak and Collins, 2013).

4.5 Results of Specimen Nondestructive Testing Program

After collecting all NDT data in accordance with the foregoing procedures, destructive cores were extracted from the twenty specimens to (1) verify that simulated defects developed as intended and (2) further establish ground truth information from which to evaluate the capabilities of each NDT method.

4.5.1 Defect Simulation Verification

In this section, cores extracted from each specimen are presented to determine whether simulated defects were fabricated as intended. Cores representative of the trends observed

in each specimen are presented in the following paragraphs; however, the remaining cores from each specimen can be observed in Appendix A.

Corrosion Specimens

As Specimens C1 and C2 were both subjected to the impressed current accelerated corrosion technique, extracted cores from these specimens were valuable towards verifying that the specimens were deteriorated to the severity expected in their three characteristic zones. It was hypothesized that, in each specimen, Zone 1 (no impressed current) would exhibit little to no corrosion. In contrast, Zone 2 (moderate duration of current) and Zone 3 (long duration of current) would be corroded with the latter being more significantly damaged from delaminations and vertical cracking. It was hypothesized that Specimen C1 would be more damaged from vertical cracking than delaminations because of its relatively small cover (3/4 in.). On the contrary, it was expected that Specimen C2 would exhibit more delaminations than vertical cracks because of its deeper cover (2 in.). Representative cores from Zones 1–3 of Specimen C1 can be found in Figure 4-29.

Figure 4-29: Extracted Cores from Zones 1–3 (Left to Right) in Specimen C1

Note that, for all cores shown in this thesis, 'X' and 'Y' refer to the spatial coordinates of the specimen where the core was extracted, with respect to the origin defined in Section 4.3. As can be observed from Figure 4-29, Zone 1 exhibited no corrosion of reinforcement while Zones 2 and 3 were both damaged from corrosion. However, the corrosion-induced damage was more severe in Zone 3, as evidenced by thicker and more expansive delaminations and vertical cracks. These observations were consistent with the intended demarcations of corrosion damage within the three zones accomplished using varying durations of impressed current and sodium-chloride ponding.

Similar observations were anticipated to be made in extracted cores from Specimen C2. As can be seen in Figure 4-30, Zone 1 of Specimen C2 showed little to no signs of corrosion, much like Zone 1 of Specimen C1. Additionally, reinforcement in Zones 2 and 3 were corroded as intended. Moreover, as in Specimen C1, the delaminations and vertical cracks observed in Zone 3 were much thicker and more expansive than those from Zone 2.

Figure 4-30: Extracted Cores from Zones 1–3 (Left to Right) in Specimen C2

Cracked Specimen

No cores were extracted from Specimen CR1 since the only simulated defects were vertical cracks which were largely visible from the surface.

Delamination Specimens

Cores were extracted from the delamination specimens to validate the presence and performance of simulated defects at their intended locations. In Specimens DL1 and DL2, plastic and foam inserts were successful in creating gaps in concrete simulating delaminations, as evidenced in cores from the two specimens shown in Figure 4-31. The shallow, foam insert in Specimen DL1 simulated a delamination while also causing a real delamination to open, spanning between the intersecting reinforcement in the core. Additionally, the deep, plastic insert in Specimen DL2 caused the concrete above and below the insert to split apart, as a real delamination would cause after core extraction.

X: 36 in., Y: 20 in.	X: 68 in., Y: 4 in.

Figure 4-31: Specimen DL1 Shallow Delamination (Left) and Specimen DL2 Deep Delamination (Right)

Cores were also extracted from Specimens DL3 and DL4 in which an effort was made to simulate extensive delaminations using sand and oil layers. Based on cores extracted at locations in which the shallow sand layer was placed in Specimen DL3, presented in Figure 4-32, the sand layer was unsuccessful in simulating delaminations. In both cores shown, it was difficult to discern a sand layer distinct from the surrounding concrete. One potential explanation for this observation was that the specimen was poorly constructed, either by inadvertently consolidating the sand layer into the surrounding concrete, not making the sand layer thick enough, or some combination of the two. The failure of this technique to simulate a delamination was also evidenced by the failure of the concrete above and below the sand layer to split apart from one another, as would occur if the layer was a real delamination. Thus, from a ground-truth perspective, the portion of Specimen DL3 within the perimeter of the shallow sand layer was not regarded as defective.

X: 12 in., Y: 8 in.

X: 28 in., Y: 4 in.

Figure 4-32: Poor Delamination Simulation using Sand Layer in Specimen DL3

Unlike the sand layer, the oil layer placed in Specimen DL3 was somewhat effective at simulating delaminations, as can be observed in Figure 4-33. The shallow oil layer could clearly be observed in the extracted cores as cracks spanning around the circumference of the cores. However, unlike the plastic, unbonded delaminations of Specimens 1–2, these oil-based delaminations did not cause the concrete above and below the delamination to come apart from one another. Accordingly, the oil layer caused partially bonded shallow delaminations in Specimen DL3. The oil layer appeared to be more adequately constructed than the sand layer, thus allowing for it to be a more effective technique for simulating delaminations.

X: 44 in., Y: 20 in.

X: 52 in., Y: 4 in.

Figure 4-33: Shallow Delamination Simulation using Oil Layer in Specimen DL3

Cores were also extracted over the sand and oil layers in Specimen DL4 to further validate whether the layers effectively simulated expansive delaminations in bridge decks. Unlike what was observed in Specimen DL3, the sand layer in Specimen DL4 appeared to effectively simulate delaminations, as can be seen in the cores shown in Figure 4-34. For both cores, the sand layer caused the concrete above and below the layer to split apart, emulating the behavior of a unbonded delamination in a bridge deck. Standing in contrast to the conclusions from Specimen DL3, this result indicated that the deep sand layer was an effective means of simulating a delamination. This apparent contradiction further reinforced the hypothesis that the effectiveness of the sand layer was sensitive to fabrication variability.

X: 16 in., Y: 8 in.	X: 20 in., Y: 16 in.

Figure 4-34: Deep Delamination Simulation using Sand Layer in Specimen DL4

As in Specimen DL3, the oil layer in Specimen DL4 also appeared to successfully simulate delaminations, as can be seen in extracted cores shown in Figure 4-35. The deep oil layer induced cracking around the cores; however, the concrete above and below the oil layers did not split apart. Accordingly, the deep oil layer also appeared to simulate a partially bonded delamination. Repeatability in oil delamination simulation between Specimen DL3 and DL4 indicated that the oil layer was likely less sensitive to construction practices than the sand layer. Nonetheless, given the variability in effectiveness of delamination simulation using these techniques, the method for simulating large delaminations would have to be redeveloped for Phase 2 of this project.

X: 40 in., Y: 8 in.	X: 60 in., Y: 16 in.

Figure 4-35: Deep Delamination Simulation using Oil Layer in Specimen DL4

As in Specimens DL1–2, shallow and deep unbonded delamination simulation in Specimens DL5 and DL6 respectively was successful, as observed in Figure 4-36. For both cores shown, the concrete above and below the delamination separated when the cores were extracted. This behavior was observed for all cores retrieved over simulated delaminations in the two specimens.

X: 36 in., Y: 4 in.	X: 8 in., Y: 12 in.

Figure 4-36: Specimen DL5 Shallow Delamination (Left) and Specimen DL6 (Deep Delamination (Right)

Cores extracted from Specimens DL7–8 were useful towards investigating the effectiveness of plastic inserts with checkerboard cuts in simulating partially bonded delaminations. Cores with largely bonded delaminations generally held together after extraction, such as that from Specimen DL7 shown in Figure 4-37. Others cores with a greater fraction of unbonded area might have split apart due to torque caused by the coring rig, such as that from Specimen DL8 also shown in Figure 4-37. Together, the two specimens presented an array of partially bonded delaminations of varying fraction of unbonded area, thickness, and depth simulated using plastic inserts.

X: 68 in., Y: 20 in.

X: 4 in., Y: 20 in.

Figure 4-37: Partially bonded Delaminations in Specimens DL7 (Left) and DL8 (Right)

Deterioration Specimens

Cores were extracted from the deterioration specimens and its control to investigate the use of the various miniature slabs in simulating concrete deterioration. It was of particular interest to determine whether the concrete surrounding the miniature slabs was adequately consolidated such that the only defects existing in the specimens existed in the miniature slabs. Towards this aim, cores extracted from the control specimen can be seen in Figure 4-38. In both cores, a clear, cold joint can be observed between the miniature slab and surrounding concrete. Nonetheless, the quality of concrete appeared to be uniform on either side of the cold joint. Thus, it was hypopthesized that, should a NDT method

suggest there existed a defect over the miniature slab, it would have responded to the cold joint rather than an actual defect in the specimen.

X: 36 in., Y: 8 in.	X: 48 in., Y: 8 in.

Figure 4-38: Cores Exhibiting Cold Joint in Specimen CTRL

Cores were similarly extracted from Specimen DE2, containing a miniature slab in which deterioration was simulated using a high dosage of air-entraining admixture. Two such cores, one including the miniature slab concrete (X: 12, Y: 16) and the other not (X: 64, Y: 4), are shown in Figure 4-39. From those cores, it was observed that the miniature slab concrete generally had a higher air content than that of the surrounding concrete. Additionally, the concrete surrounding the miniature slab had a uniform amount of entrapped air. Thus, it was hypothesized that NDT methods would respond differently when tested over the miniature slab than it would over only sound concrete.

X: 12 in., Y: 16 in.	X: 64 in., Y: 4 in.

Figure 4-39: Specimen DE2 Cores with (Left) and without (Right) Miniature Slab Concrete

Cores were extracted from the remaining deterioration specimens to verify whether deterioration was developed within the miniature slabs as intended. As expected, in cores from Specimen DE3 shown in Figure 4-40, honeycombing was present in the miniature slab concrete. The severity of the honeycombing appeared to vary somewhat among each core which would likely be a good representation of actual honeycombing in a concrete element under construction.

X: 16 in., Y: 16 in.

X: 56 in., Y: 16 in.

Figure 4-40: Honeycombing in Miniature Slab Concrete of Specimen DE3

Cores were also obtained from Specimens DE4 and DE5 to investigate the effects of the high and moderate dosages of anti-cracking fibers respectively added to the miniature slabs of each specimen. From cores of Specimen DE4, the anti-cracking fibers were accompanied by an increased air content relative to the sound concrete in the miniature slab concrete, as can be observed in Figure 4-41.

X: 36 in., Y: 8 in.	X: 48 in., Y: 16 in.

Figure 4-41: Increased Air Content in Miniature Slab Concrete of Specimen DE4

Similarly, cores extracted from Specimen DE5 including the miniature slab concrete demonstrated an increased air content, as observed in Figure 4-42. However, while the air content in the miniature slab concrete might still have been greater than that of the surrounding concrete, the increased air content was distributed more uniformly throughout both concretes than that from Specimen DE4. Cores from both specimens revealed the difficulty in adequately consolidating concrete in/above the miniature slabs, hypothesized to be the result of a low concrete depth in which to place the vibrator.

X: 12 in., Y: 12 in.

X: 64 in., Y: 4 in.

Figure 4-42: Increased Air Content in All Concrete from Specimen DE5

Poor-Construction Specimens

As with the deterioration specimens, cores were extracted from the poor-construction specimens to evaluate the development of simulated defects in the miniature slabs after placing the surrounding concrete. Cores including the miniature slab in Specimen PC1, shown in Figure 4-43, revealed that all concrete in the specimen was generally well-consolidated. Accordingly, it was expected that, should a NDT method respond to an anomaly over the miniature slab, it would be detecting the low-strength concrete from the miniature slab.

X: 32 in., Y: 16 in.

X: 40 in., Y: 8 in.

Figure 4-43: Well-Consolidated Cores from Specimen PC1

For Specimen PC2, it was expected that recovered cores would demonstrate that the concrete from the miniature slab had a high entrapped air content, relative to the surrounding, well-vibrated concrete. Such cores, shown in Figure 4-44, confirmed the higher entrapped air content in the miniature slab; however, there still existed a large amount of entrapped air in the concrete above the miniature slab. This observation further demonstrated the apparent difficulty in consolidating concrete of such a shallow depth above the miniature slabs.

X: 8 in., Y: 8 in.	X: 48 in., Y: 16 in.

Figure 4-44: High Entrapped Air Content in Specimen PC2 Cores

Void Specimens

Cores were extracted from both void specimens to verify that simulated voids remained intact and in their intended locations during concrete placement. As can be observed in cores from Specimens V1 and V2 shown in Figure 4-45, both shallow and deep voids were spatially in their correct locations. However, the water-filled (V1) balloons floated vertically somewhat during concrete placement, as the specific gravity of concrete is much greater than that of water. Accordingly, hereinafter, conclusions concerning the capability of an NDT method to detect a shallow water-filled void assumes the void is present in the top cover layer of the specimen.

X: 36 in., Y: 20 in.

X: 52 in., Y: 4 in.

Figure 4-45: Floated Voids in Specimen V1 (Left) and V2 (Right)

4.5.2 Presentation and Analysis of GPR Contour Plots

GPR data collected from the twenty laboratory test specimens are presented in the form of spatial contour plots. Rather than show all 120 plots corresponding to the plotting of the six subsets of air-dried GPR data and the subsequent 36 plots corresponding to moist GPR data, only the air-dried and moist plots from the Top Bar Passes (All) subsets are presented in this section. Additionally, select plots of depth-corrected data from the foregoing subsets are also presented to demonstrate the most noteworthy observations. The remaining non-depth-corrected plots can be located in Appendix B, and the other depth-corrected plots can be found in Appendix C. Plots shown in this section are superimposed over to-scale plan views of each specimen to facilitate visual analysis of GPR data with respect to the locations of defects. Plots are organized into subsections corresponding to their specimen defects and are accompanied by a discussion of data.

Corrosion Specimens

The non-depth-corrected, air-dried GPR data from the Specimen C1 Top Bar Passes (All) subset are presented in Figure 4-46. From Figure 4-46, it was observed that the reflection amplitudes decreased (became more negative) as data were sampled from Zone 1 to Zone 3. This trend corresponded to an increase in reinforcement corrosion from Zone 1 to Zone 3, indicating that GPR responded to the presence of active corrosion, varying degrees of corrosive environments (e.g. chloride ion concentration), and/or the damage caused by it (e.g. delaminations and vertical cracking). To confidently determine which defect(s) GPR responded to in Specimen C1, it needed first to be determined whether GPR could detect delaminations and/or vertical cracking when not induced by corrosion. Analysis of GPR results from the cracked and delamination specimens allowed for further investigation into this behavior. From Figure 4-46, it was also observed that, by applying the least restrictive BridgeScan (GSSI 2017) threshold to the GPR data—obtained by subtracting 6 dB from the maximum reflection, -17 dB— any reflections less than -23 dB would be considered indicative of a defect. Accordingly, per this approach, one would conclude that there are no defects in the specimen. Thus, for Specimen C1, the BridgeScan (GSSI 2017) threshold was a poor indicator of the specimen condition.

Additionally, the depth-corrected, air-dried GPR data for Specimen C1 were plotted in Figure 4-47 to determine whether depth correction allowed for better correlation of zones of corrosion and GPR data. Comparing that plot to the corresponding non-depth corrected GPR data, one can observe that depth correction did little to change the relative distribution of reflection amplitudes, indicating low cover variation in the specimen.

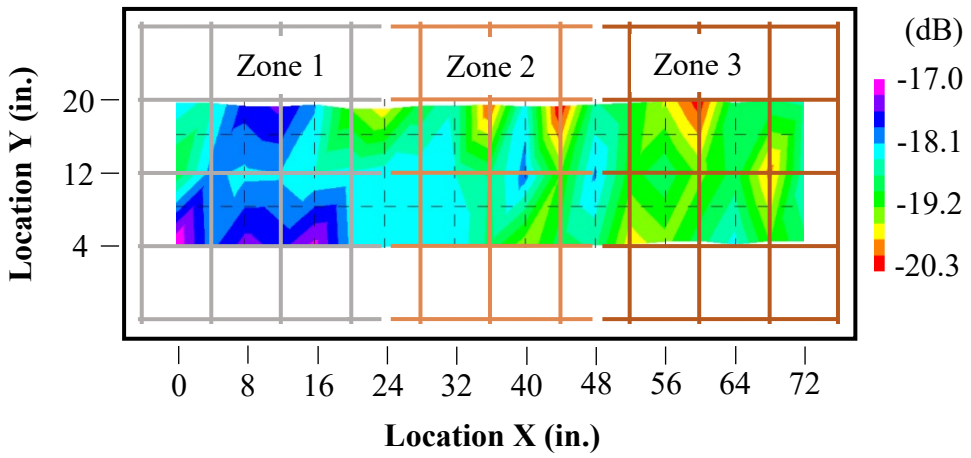

Figure 4-46: Specimen C1 Top Bar Passes (All) Air-Dried Non-Depth-Corrected GPR Data

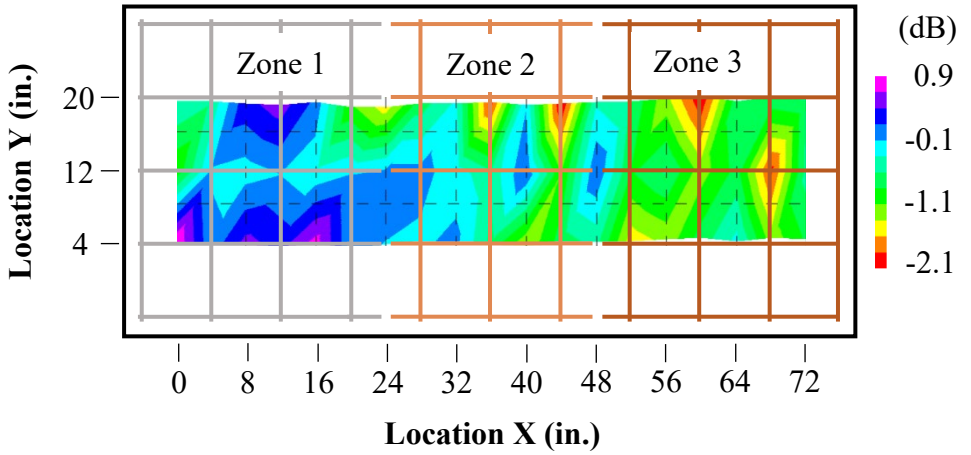

Figure 4-47: Specimen C1 Top Bar Passes (All) Air-Dried Depth-Corrected GPR Data

Similarly, the non-depth-corrected, air-dried GPR data from the Specimen C2 Top Bar Passes (All) dataset can be seen in Figure 4-48. As in Specimen C1, from Figure 4-48, Zones 2 and 3 generally exhibited lower amplitude reflections, further reinforcing the

hypothesis that GPR responds to zones of corroded reinforcement in bridge deck. Additionally, application of the least restrictive BridgeScan (GSSI 2017) threshold (-21.9 dB) also resulted in no defect detection in the specimen. However, it was perplexing that (1) Zone 2 reflections were of a lower amplitude than Zone 3 reflections, and (2) the contrast between Zone 1 and Zone 3 reflections was not as strong in Specimen C2 as it was in Specimen C1. Investigation of the reflection two-way travel times and a B-scan (two-dimensional GPR data) from Specimen C2, shown in Figure 4-49, revealed a non-uniform cover layer which was hypothesized to contribute to peculiarities in non-depth-corrected data.

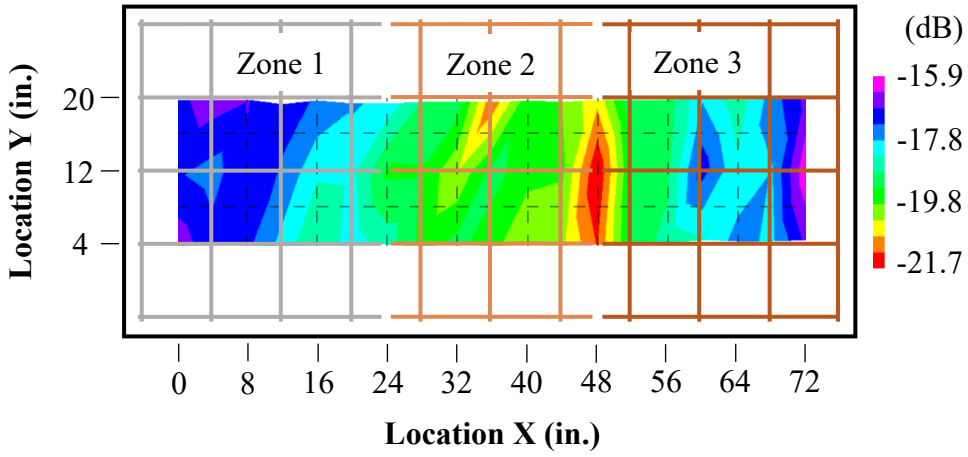

Figure 4-48: Specimen C2 Top Bar Passes (All) Air-Dried Non-Depth-Corrected GPR Data

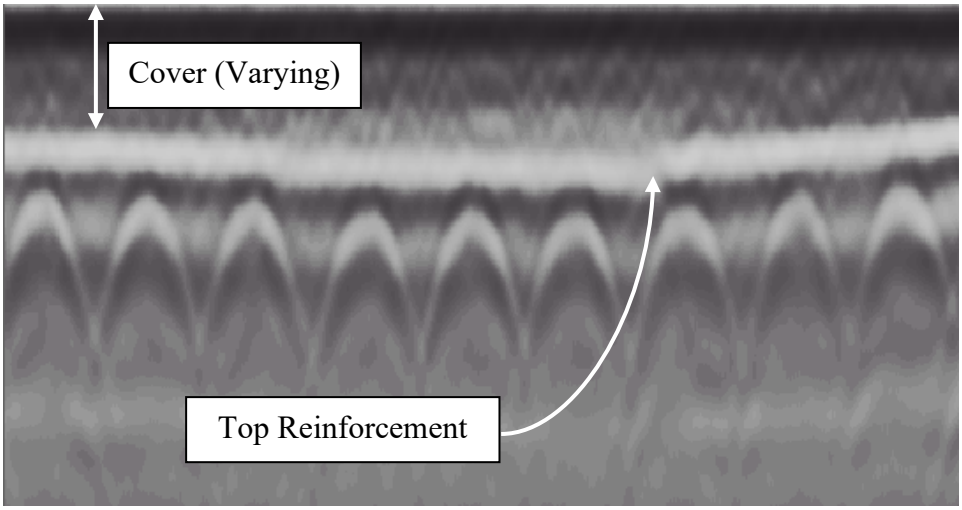

Figure 4-49: Variable Cover in B-Scan of Specimen C2

Accordingly, the GPR data for Specimen C2 were corrected for depth as described in Section 4.4.3 of this thesis. That depth-corrected GPR data are presented in Figure 4-50. Through comparison of the non-depth-corrected and depth-corrected data, it was observed that the depth-correction algorithm resulted in the expected contrast between Zones 1 and 3 and shifted the Zones 2–3 values to be more comparable.

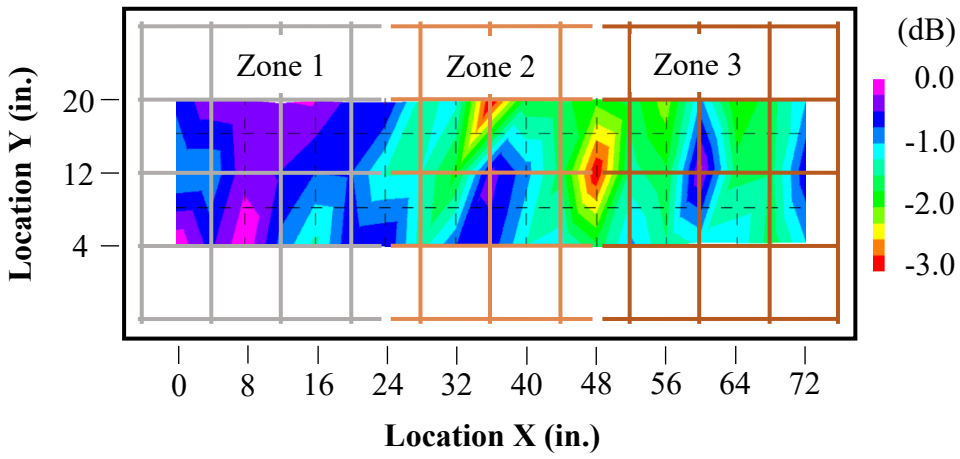

Figure 4-50: Specimen C2 Top Bar Passes (All) Air-Dried Depth-Corrected GPR Data

Cracked Specimen

The non-depth-corrected GPR data for Specimen CR1 are presented in Figure 4-51. From a visual analysis, it was unclear whether GPR was able to accurately discern vertical cracks. It was perplexing that the most attenuated signals (shown in red hues) were recorded over the 10-mil thick crack with a depth of 2 in. and the 30-mil crack with a depth of 3 in., since GPR data over thicker cracks generally had stronger signals. Furthermore, the reflections recorded at the partial-height crack were not consistently attenuated; rather, both strong (shown in green and cyan hues) and attenuated signals were distributed over the crack length. In addition, application of the least-restrictive BridgeScan (2017) threshold resulted in classifying the entire specimen as sound.

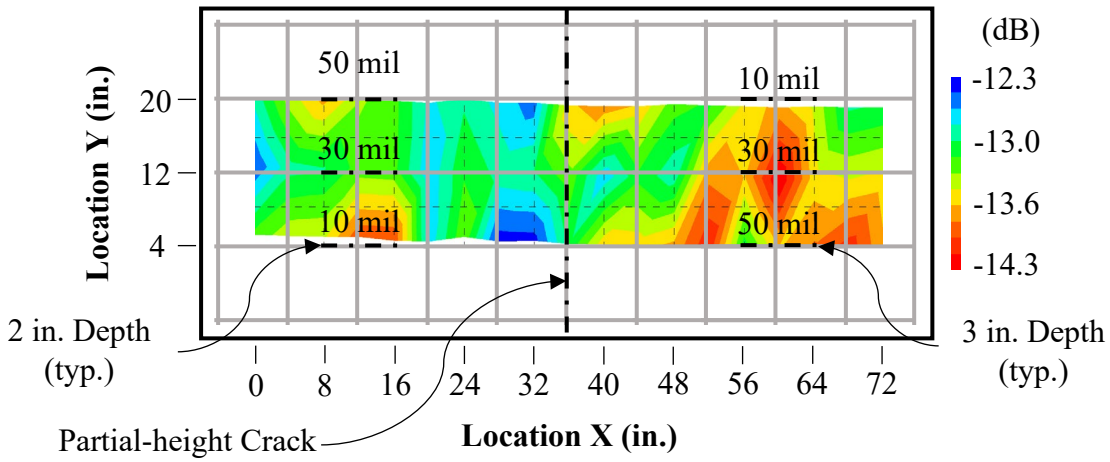

Figure 4-51: Specimen CR1 Top Bar Passes (All) Air-Dried Non-Depth-Corrected GPR Data

To further explore whether GPR could detect the vertical cracks in Specimen CR1, the air-dried, depth-corrected data were plotted and is presented in Figure 4-52. It was observed that highly attenuated signals (shown in red hues) were measured near the 50-mil

thick vertical crack with a depth of 3 in. However, strong reflections (shown in blue hues) were measured at the corresponding 2 in. deep vertical cracking. As the thickness of crack would likely most influence its detectability, it was perplexing that attenuated signals were not collected at both 50-mil thick cracks. Accordingly, it was expected that the highly attenuated signals were the result of signal variability rather than the 50-mil crack. Furthermore, the depth-corrected signals at the partial-height crack were relatively strong, indicating that the crack did not affect GPR waves. From this visual analysis of the depth-corrected data, it was hypothesized that GPR cannot detect vertical cracks with widths of 50 mil or smaller.

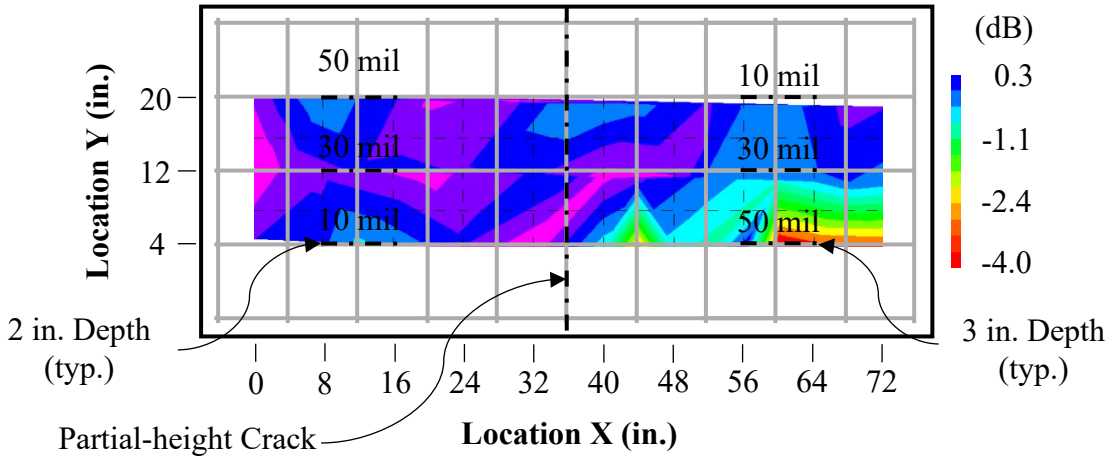

Figure 4-52: Specimen CR1 Top Bar Passes (All) Air-Dried Depth-Corrected GPR Data

Delamination Specimens

The non-depth-corrected GPR data for Specimen DL1 are presented in Figure 4-53. From Figure 4-53, it is observed that, after applying the least restrictive BridgeScan (2017) threshold (-21 dB), the entire specimen was hypothesized to be sound. Thus, this

method of condition assessment was not effective at delineating between sound concrete and areas distressed by delaminations. Additionally, it was noted that there existed no strong correlation between zones of weaker wave reflections and shallow delamination correlation. While GPR appeared to respond to the presence of the 0.79 mm thick, shallow delamination (as evidenced by the weaker, more negative, reflection amplitude there), no such response existed at the other five shallow delaminations. It was perplexing that GPR would not be able to detect a thicker delamination. Accordingly, it was hypothesized that the response at the 0.79 mm thick delamination was simply the result of random variation in GPR data.

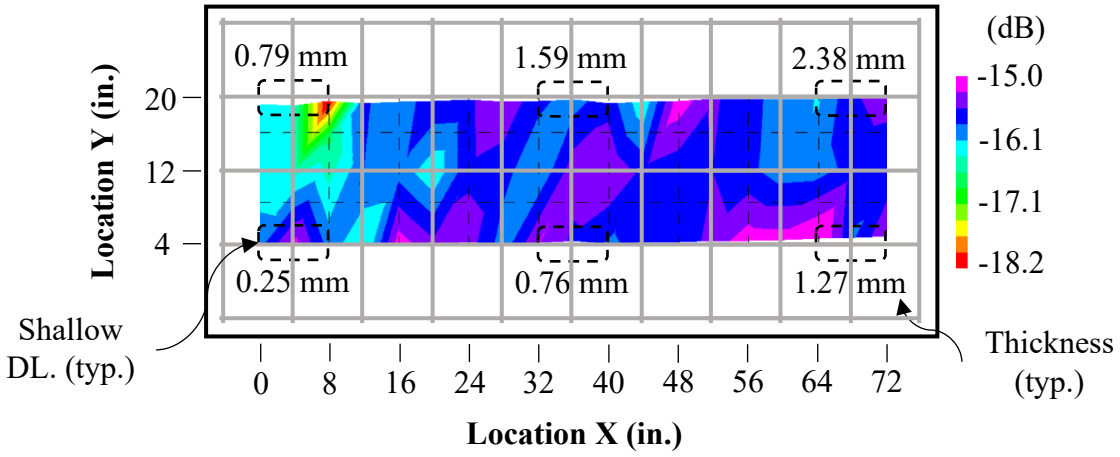

Figure 4-53: Specimen DL1 Top Bar Passes (All) Air-Dried Non-Depth-Corrected GPR Data

Nonetheless, to investigate whether depth correction would better correlate weaker reflection amplitudes with the locations of delaminations, the GPR data were depth-corrected. From Figure 4-54, the distribution of normalized amplitudes was relatively constant along the range of sampled two-way travel times, indicating that the cover length was relatively uniform.

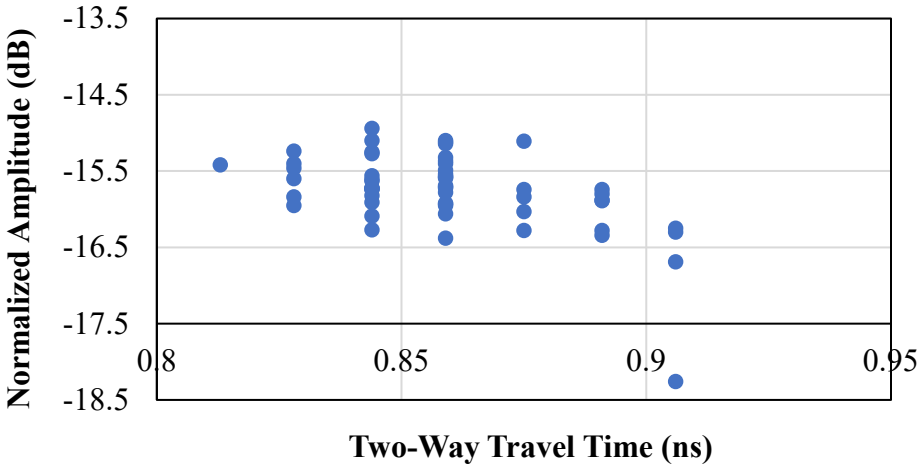

Figure 4-54: Relatively Uniform Distribution of Normalized Amplitudes for Specimen DL1

The air-dried, depth-corrected GPR data for Specimen DL1 are shown in Figure 4-55. Comparison of that frequency contour plot to the non-depth-corrected data shown in Figure 4-53 confirmed that there was little cover variation, as shape and relative reflection amplitude distributions were nearly identical between the two plots. As depth correction did not result in correlation between wave attenuation and delamination location, it was concluded that GPR is not capable of detecting shallow delaminations with thicknesses of 2.38 mm or smaller. For all instances hereinafter in which the depth-correction algorithm did not result in better correlation between the true condition of a specimen and its corresponding GPR data, only the non-depth-corrected data will be presented. Nonetheless, the depth-corrected data omitted from this portion of the text is provided in Appendix B.

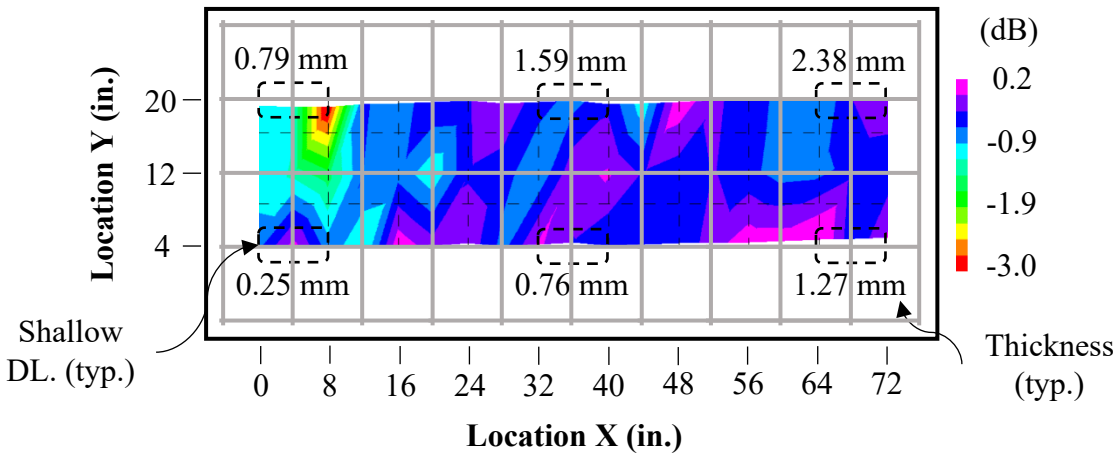

Figure 4-55: Specimen DL1 Top Bar Passes (All) Air-Dried Depth-Corrected GPR Data

The non-depth-corrected GPR data for Specimen DL2 are presented in Figure 4-56. As in Specimen DL1, the GPR data from Specimen DL2 poorly correlated with the location of the delaminations shown in Figure 4-56. Furthermore, the three thickest, deep delaminations were all characterized by the large reflection amplitudes (shown in purple and blue hues) while the most attenuated signals (shown in red and orange hues) did not occur at the locations of deep delaminations. Thus, visual analysis of the air-dried GPR data from Specimen DL2 indicated that GPR is not capable of detecting deep delaminations with thicknesses of 2.38 mm or smaller. The implemented depth-correction algorithm did not result in a compelling distinction between GPR data collected over deep delaminations and over sound concrete, despite a noticeably varying cover layer. Additionally, from Figure 4-56, it was observed that when using the least restrictive deterioration threshold (-22.7 dB) recommended in the BridgeScan (2017) manual, one would conclude that the entire specimen was sound.

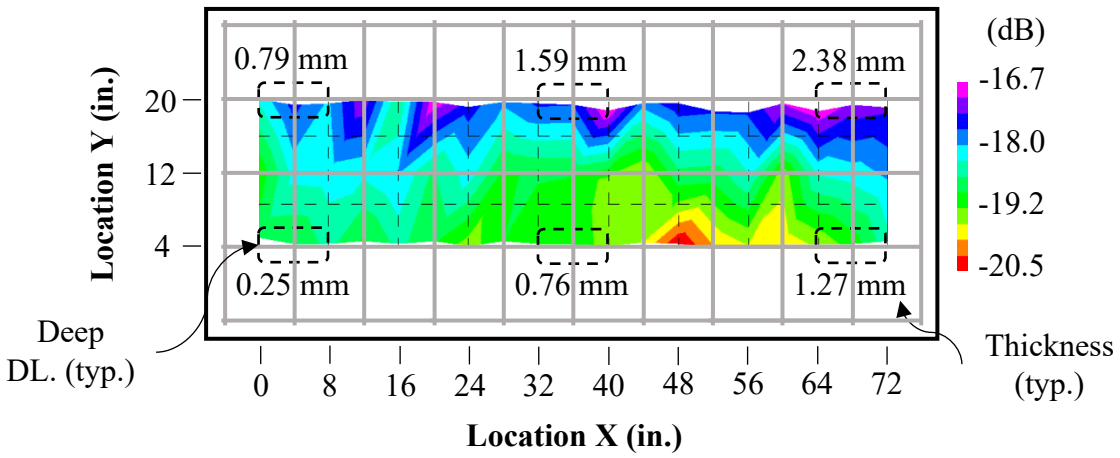

Figure 4-56: Specimen DL2 Top Bar Passes (All) Air-Dried Non-Depth-Corrected GPR Data

Additionally, the non-depth-corrected, air-dried GPR data from the Specimen DL3 Top Bar Passes (All) subset can be seen in Figure 4-57. Visual analysis of the GPR data from Specimen DL3 shown in Figure 4-57 revealed no clear distinction in reflections amplitudes collected over sound concrete and those collected over the shallow sand and oil delaminations. One noticably attenuated signal (shown in green and red hues) could be observed on the border of the oil delamination. However, predominant strong amplitudes (shown in purple and dark blue hues) characterized the GPR data collected over the sand and oil layers, further reinforcing the hypothesis that GPR cannot detect shallow delaminations. Implementation of the depth-correction algorithm to the GPR data did not change this conclusion. In addition, it was observed from Figure 4-57 that using the least restrictive BridgeScan (2017) threshold (-19.5 dB), none of the specimen would be classified as being deteriorated.

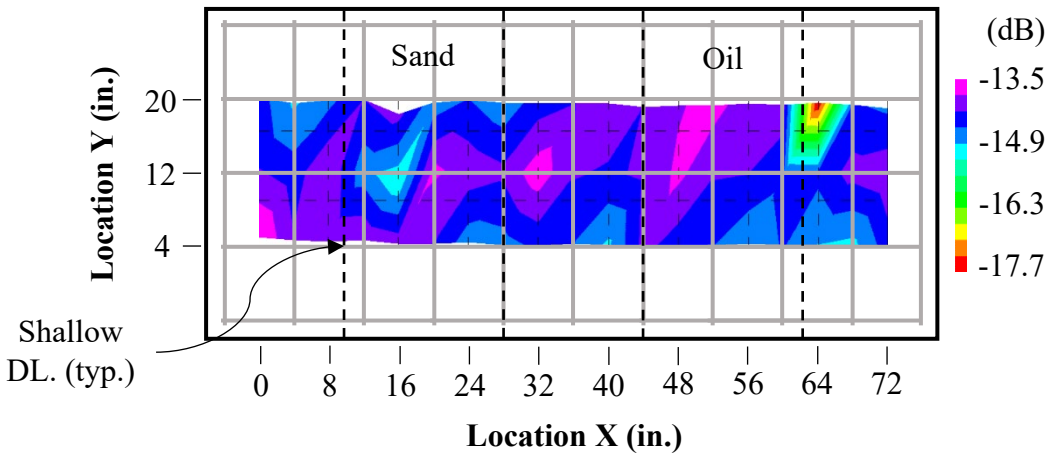

Figure 4-57: Specimen DL3 Top Bar Passes (All) Air-Dried Non-Depth-Corrected GPR Data

The GPR data corresponding to Specimen DL4, distressed from deep sand and oil delaminations, are shown in Figure 4-58. As in Specimen DL3, no clear distinction between GPR signal amplitudes collected over sound and delaminated concrete could be observed through visual analysis. Attenuated signals (shown in green and yellow hues) were distributed throughout both data collected over the simulated delaminations and the sound concrete between them, indicating that GPR is not capable of detecting deep delaminations. As in the foregoing delamination specimens, depth correction implementation did not change the previous conclusion. Furthermore, the use of the least restrictive BridgeScan (2017) threshold (-22.8 dB) resulted in classifying the entire specimen as sound.

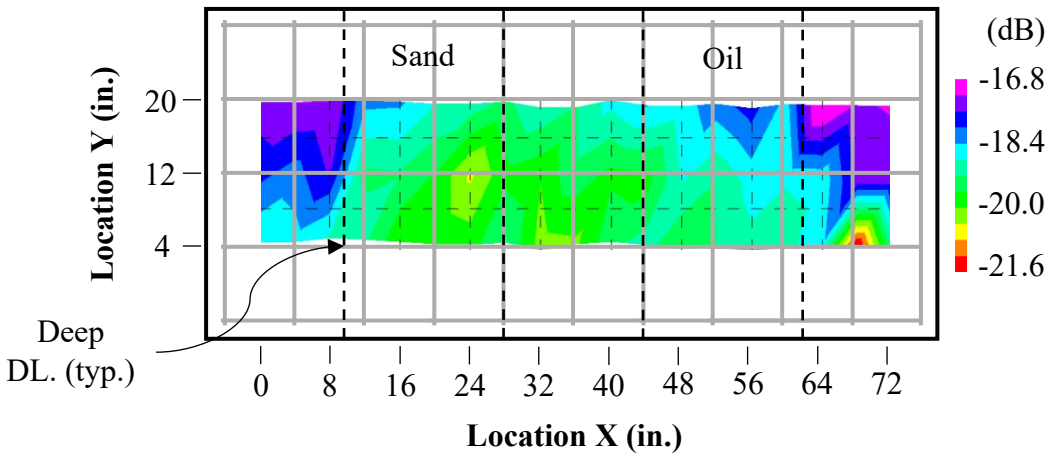

Figure 4-58: Specimen DL4 Top Bar Passes (All) Air-Dried Non-Depth-Corrected GPR Data

Air-dried GPR data of Specimen DL5, distressed from shallow delaminations of varying areas, can be seen in Figure 4-59. From Figure 4-59, it was observed that attenuated signals (shown in red and green hues) were randomly distributed throughout Specimen DL5 such that there was no evident distinction in GPR data between sound concrete and concrete distressed from shallow delaminations. Furthermore, the reflected signal collected over the 8 in^2 delamination was weaker (more negative) than that collected over the larger 32 in^2 delamination, demonstrating the seemingly random distribution of GPR signals throughout the test specimen. Accordingly, from this visual analysis, it was concluded that GPR is not capable of detecting shallow, 30-mil thick delaminations as large as 72 in^2 in area. Visual analysis of the depth-corrected GPR data from this specimen resulted in the same conclusion being reached. Additionally, after applying the least restrictive BridgeScan (2017) threshold (-20.2 dB) to the GPR data, one would conclude that there were no defects in the specimen.

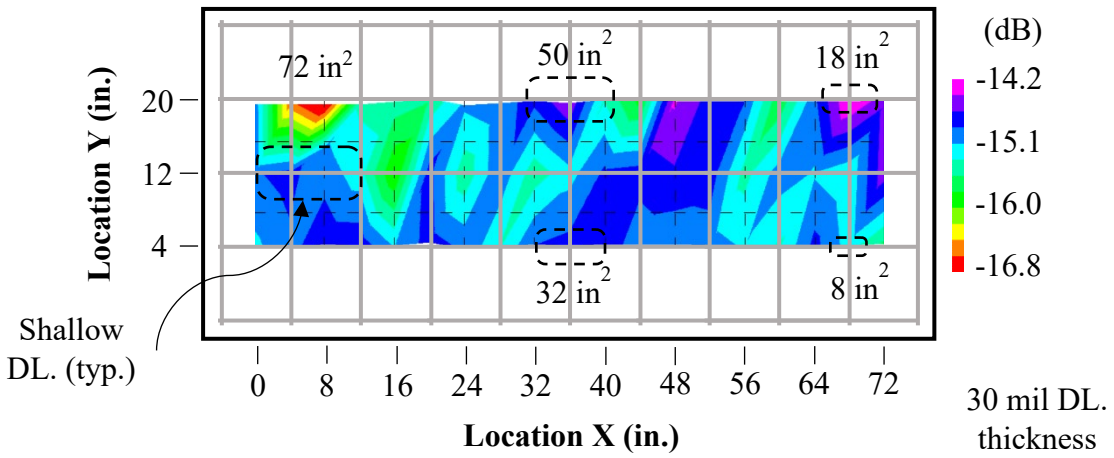

Figure 4-59: Specimen DL5 Top Bar Passes (All) Air-Dried Non-Depth-Corrected GPR Data

Similarly, the air-dried, non-depth-corrected GPR data for Specimen DL6 are presented in Figure 4-60. From a visual analysis, stronger reflections (shown in purple and blue hues) were distributed fairly uniformly across the deck, including over most of the deep delaminations. Furthermore, the weakest reflections (shown in red, yellow, and green hues) did not occur over a delamination. Thus, from this visual analysis, it was concluded that GPR is not capable of detecting deep, 30-mil thick delaminations as large as 72 in^2 in area. As in the previous specimens, should one have applied the least restrictive BridgeScan (2017) threshold (-20.8 dB) to the GPR data, one would falsely conclude that there were no defects in the specimen.

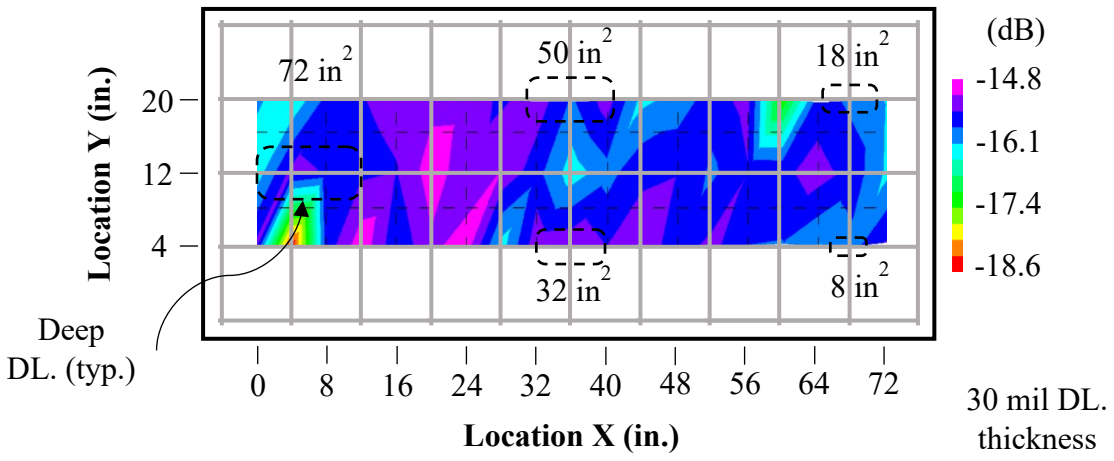

Figure 4-60: Specimen DL6 Top Bar Passes (All) Air-Dried Non-Depth-Corrected GPR Data

The air-dried, non-depth-corrected GPR data for Specimen DL7, distressed by shallow, partially bonded delaminations, are presented in Figure 4-61. From these results, it can be observed that the spatial correlation of attenuated GPR signals with locations of delaminations was poor. Relatively strong GPR signals (shown in purple and dark blue hues) were present over the 30-mil thick delaminations along grid line Y = 20. However, weaker signals (shown in green and light blue hues) were located over the two most-bonded, 10-mil thick delaminations along grid line Y = 4. As thick delaminations would most attenuate GPR signal should they be detectable using the NDT method, these observations indicated that GPR cannot detect partially bonded delaminations with thicknesses of 30 mil or smaller with 75% unbonded area. Visual analysis of depth-corrected GPR data did not change this conclusion. Furthermore, implementation of the least restrictive BridgeScan (2017) deterioration threshold (-20 dB) resulted in the entire specimen being classified as sound.

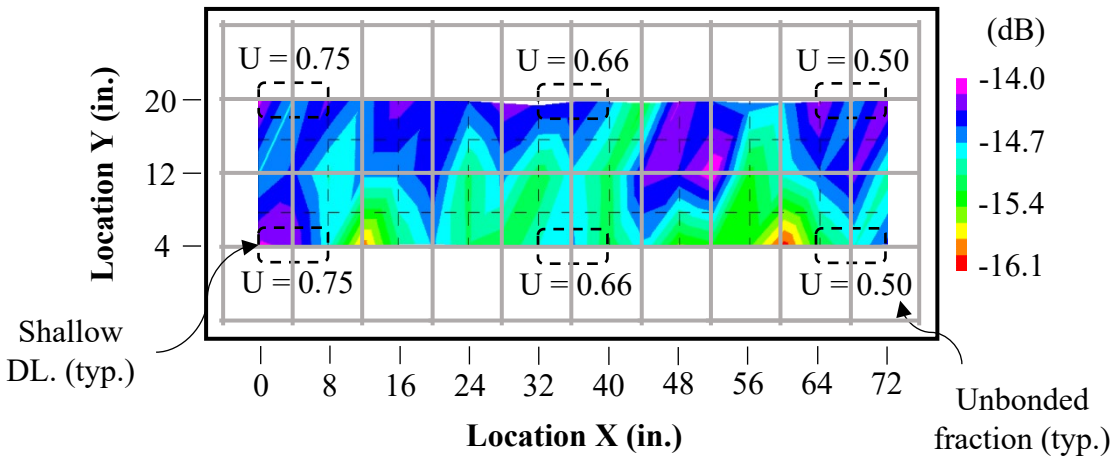

Figure 4-61: Specimen DL7 Top Bar Passes (All) Air-Dried Non-Depth-Corrected GPR Data

In addition, the air-dried, non-depth-corrected GPR data for Specimen DL8, distressed by deep, partially bonded delaminations, are presented in Figure 4-62. While attenuated GPR signals (shown in green, red, and cyan hues) were observed over the 50-mil and 30-mil thick delaminations with 75% unbonded area, similar signals were distributed throughout sound portions of the deck, indicating that GPR could not discern between those delaminations and sound concrete. The same observation was noted through visual analysis of the corresponding depth-corrected GPR data. As with the other delamination specimens, implementation of the least restrictive BridgeScan (2017) deterioration threshold (-20.8 dB) resulted in classifying the entire specimen as being sound.

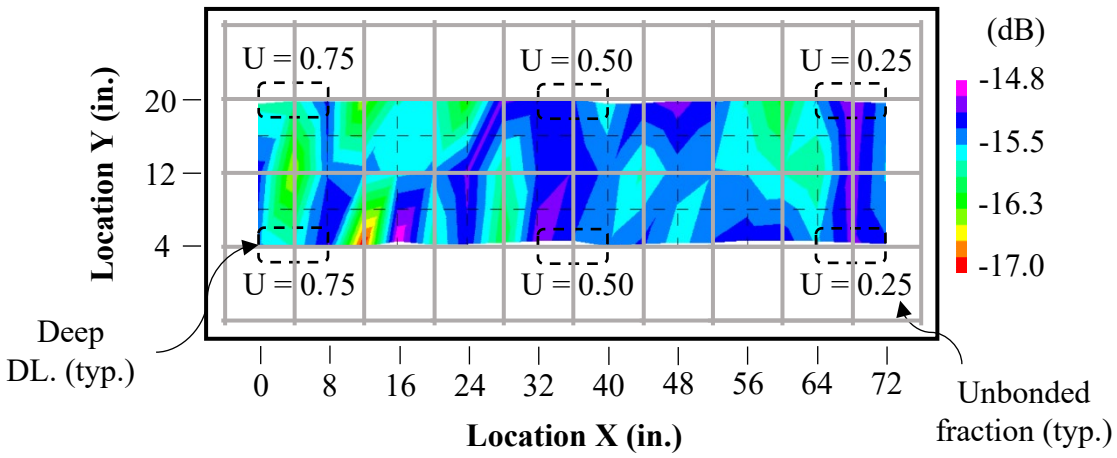

Figure 4-62: Specimen DL8 Top Bar Passes (All) Air-Dried Non-Depth-Corrected GPR Data

Deterioration Specimens

The air-dried, non-depth-corrected GPR data for Specimen CTRL, which contained the embedded miniature slab of sound concrete, are presented in Figure 4-63. Should GPR have responded to the cold joint at the interface of the miniature slab and surrounding concrete, it was hypothesized that reflection amplitudes collected over the miniature slab would be weaker (more negative) than those outside the slab perimeter. However, Figure 4-63 revealed that signals collected over the miniature slab were relatively strong (shown in purple and dark blue hues), disproving the foregoing hypothesis. Furthermore, signals of similar strength were also collected outside the perimeter of the miniature slabs. Visual analysis of the depth-corrected GPR data yielded the same conclusion. Additionally, application of the least restrictive BridgeScan (2017) deterioration threshold (-19.7 dB) resulted in correctly classifying the entire specimen as sound. It was also observed that the range of sound GPR reflection amplitudes was 2.7 dB, not 6 dB, suggesting that the latter range might overestimate the range of sound reflection amplitudes for air-dried GPR data.

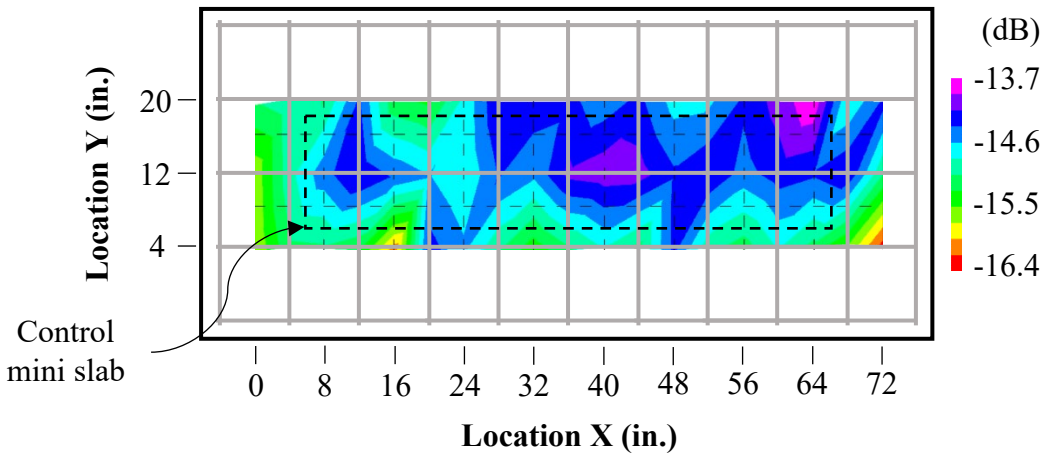

Figure 4-63: Specimen CTRL Top Bar Passes (All) Air-Dried Non-Depth-Corrected GPR Data

Knowing that GPR did not respond to the presence of the cold joint in the control specimen, the air-dried, non-depth-corrected GPR data for Specimen DE2, deteriorated using a high dosage of air entrainment admixture, are presented in Figure 4-64. For this specimen, the other deterioration specimens, and the poor-construction specimens, it was hypothesized that, should GPR respond to the simulated deterioration in the miniature slabs, the reflection amplitudes collected over those slabs would be weaker with respect to the concrete outside the perimeter of those slabs. However, inspecting the GPR data shown in Figure 4-64, it was observed that the weakest signals (shown in red, orange, and yellow hues) were not exclusive to locations over the miniature slab; rather, they were also located in comparable quantities outside the perimeter of the slab. Furthermore, the strong, moderate, and weak signals are all distributed throughout concrete above the miniature slab and outside its perimeter, indicating that GPR is unable to discern sound concrete from deteriorated concrete below the top reinforcement mat. Correcting the GPR data for cover depth variation did not result in a different conclusion being reached. As in the

delamination specimens, application of the least restrictive BridgeScan (2017) deterioration threshold (-21.9 dB) did not result in classifying any of the specimen as deteriorated.

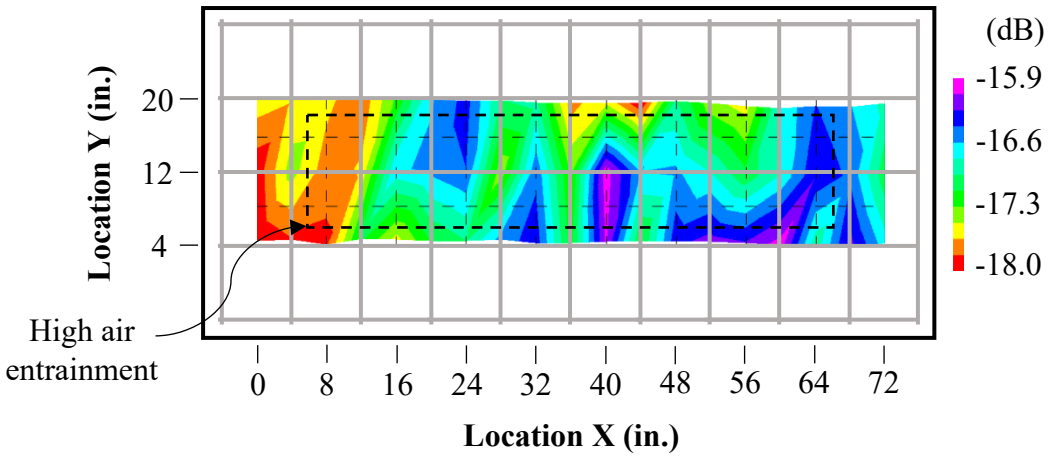

Figure 4-64: Specimen DE2 Top Bar Passes (All) Air-Dried Non-Depth-Corrected GPR Data

Similarly, the air-dried, non-depth-corrected GPR data for Specimen DE3, in which deterioration was simulated using honeycombing, are presented in Figure 4-65. Through visual inspection of that GPR data, it was observed that predominantly strong signals (shown in purple and dark blue hues) were recorded over the miniature slab, indicating that the honeycombed slab did not attenuate GPR waves. On the other hand, weaker signals (shown in green, yellow, orange, and red hues) were distributed outside the perimeter of the slab and somewhat within it. Since the reflection amplitudes collected over the miniature slab were not consistently lower than those outside the slab perimeter, it was concluded that the honeycombing beneath the top reinforcement mat in the miniature slab did not affect GPR data. Similar analysis of the depth-corrected GPR data for Specimen DE3 did not change the aforementioned conclusion. Additionally, it was noted that

implementation of the least restrictive BridgeScan (2017) deterioration threshold (-20.6 dB) resulted in classifying the entire specimen as sound.

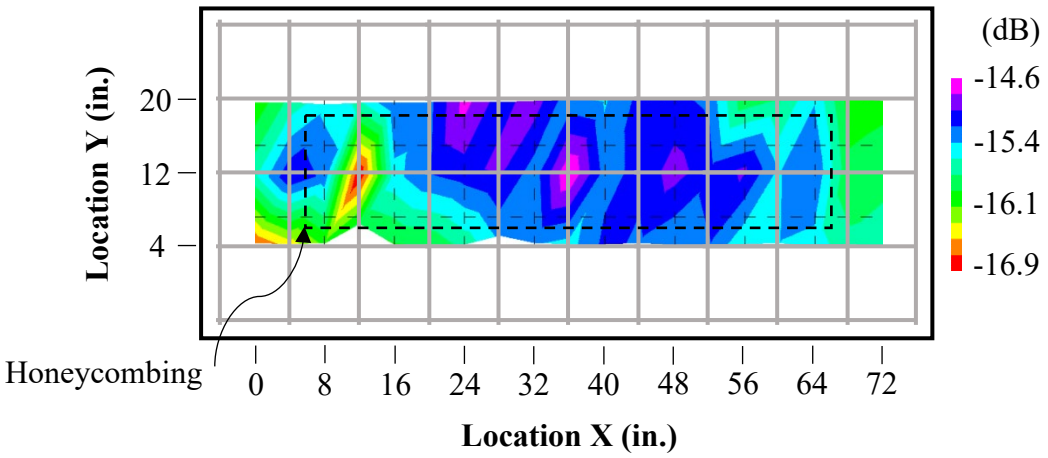

Figure 4-65: Specimen DE3 Top Bar Passes (All) Air-Dried Non-Depth-Corrected GPR Data

The air-dried, non-depth-corrected GPR data for Specimen DE4, in which deterioration was simulated using a high dosage of anti-cracking fibers, are presented in Figure 4-66. As with the other deterioration specimens, visual analysis of the GPR data from Specimen DE4 indicated that GPR is not capable of delineating between sound concrete and concrete deterioration below the level of the top reinforcement mat. Both strong (shown in purple and dark blue hues) and weaker (shown in green) reflection amplitudes were distributed throughout the entire slab. Furthermore, the weakest GPR signals (shown in red hues) were collected outside the perimeter of the miniature slab, indicating that GPR could not detect the simulated deterioration. Visual analysis of the depth-corrected GPR data resulted in the same conclusion being reach. In addition, application of the least restrictive BridgeScan (2017) threshold (-19.8 dB) did not allow for any defect detection in this specimen.

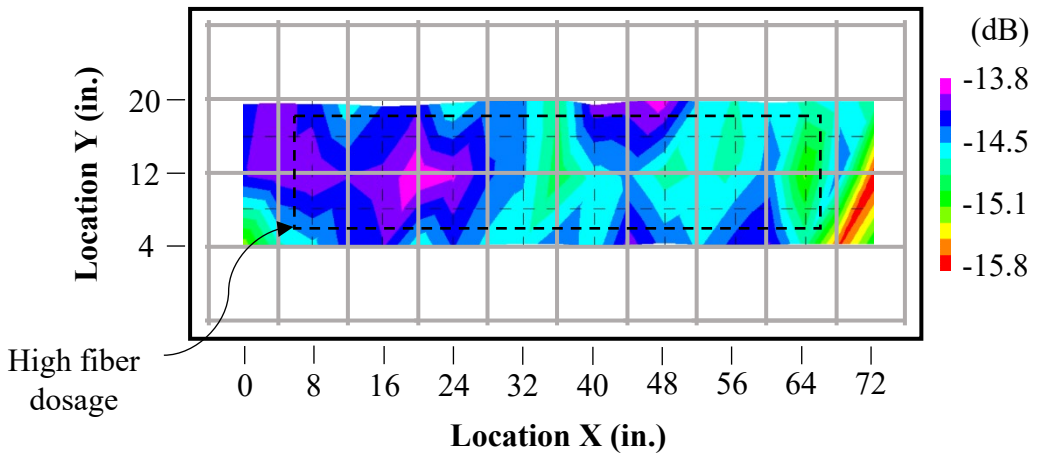

Figure 4-66: Specimen DE4 Top Bar Passes (All) Air-Dried Non-Depth-Corrected GPR Data

Similarly, the air-dried, non-depth-corrected GPR data for Specimen DE5, in which deterioration was simulated using a moderate dosage of anti-cracking fibers, are presented in Figure 4-67. Visual analysis of that data revealed that large quantities of both strong (shown in purple and dark blue hues) and weak (shown in green hues) reflection amplitudes were recorded over the miniature slab. Similar signals were also measured outside the perimeter of the miniature slab. As in the previous deterioration specimens, these results indicated that GPR is not capable of detecting deteriorated concrete below the level of the top reinforcement mat. Inspection of the depth-corrected GPR data resulted in the same conclusion being developed. Additionally, the least restrictive BridgeScan (2017) deterioration threshold (-20.6 dB) resulted in classifying the entire specimen as being defect-free.

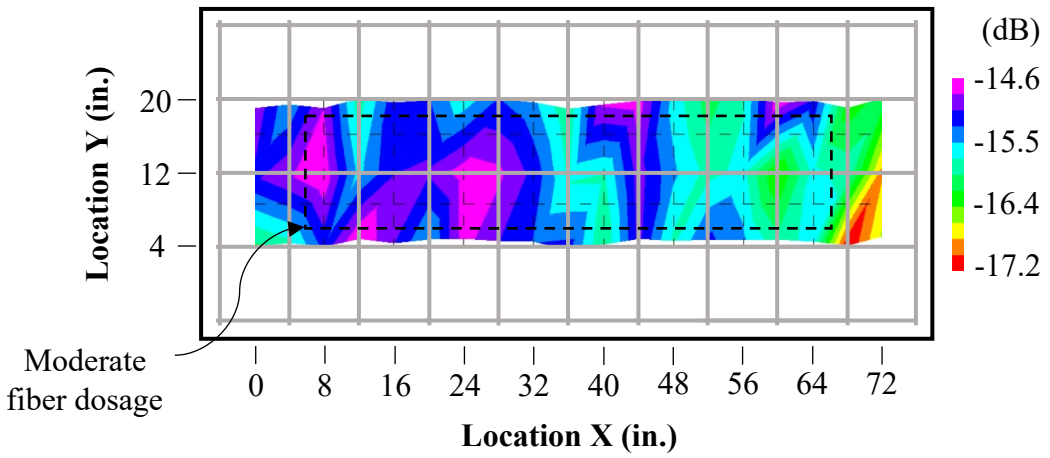

Figure 4-67: Specimen DE5 Top Bar Passes (All) Air-Dried Non-Depth-Corrected GPR Data

Poor-Construction Specimens

The air-dried, non-depth-corrected GPR data for Specimen PC1, in which poor construction was simulated using low-strength concrete, are presented in Figure 4-68. Visual analysis of this GPR data revealed that both strong (shown in purple and dark blue hues) and weaker (shown in green hues) signals were distributed both over the miniature slab and outside its perimeter. Furthermore, there existed no apparent distinction between the signals collected over the sound and defective concrete. Accordingly, this visual analysis suggested that GPR cannot detect poorly constructed concrete in bridge decks without overlays. Depth correction of this GPR data did not result in a different conclusion being developed. In addition, implementation of the least restrictive BridgeScan (2017) deterioration threshold (-19.0 dB) did not allow for detection of any of the poorly constructed concrete.

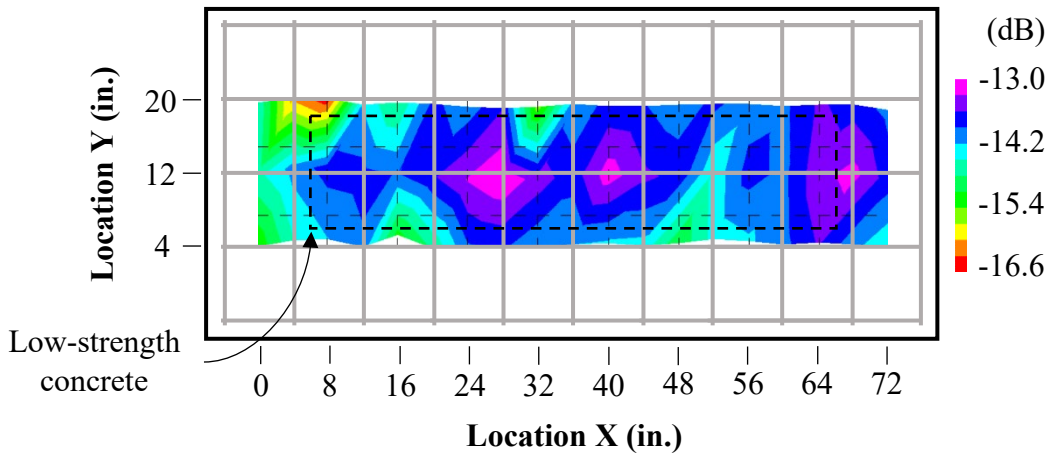

Figure 4-68: Specimen PC1 Top Bar Passes (All) Air-Dried Non-Depth-Corrected GPR Data

The air-dried, non-depth-corrected GPR data for Specimen PC2, in which poorly constructed concrete was simulating by undervibrating the miniature slab, are presented in Figure 4-69. From visual analysis of that data, it was observed that there was no clear distinction in GPR signals collected over the miniature slab and those collected outside its perimeter. Both strong and weaker GPR signals were collected within and outside the perimeter of the miniature slab. Thus, the visual analysis indicated that GPR cannot detect poorly constructed concrete. The same conclusion was reached after visually analyzing the depth-corrected GPR data. Furthermore, application of the least restrictive BridgeScan (2017) deterioration threshold (-20.1 dB) resulted in classifying the entire specimen as sound.

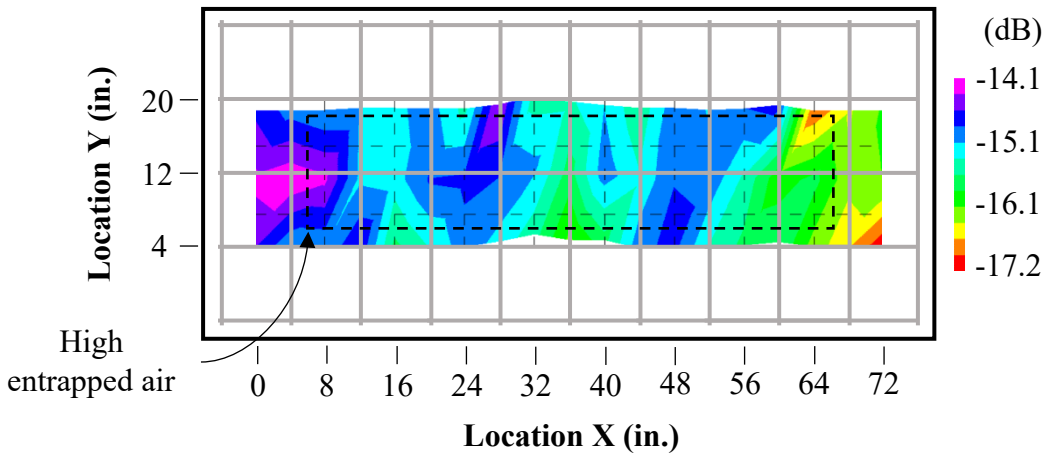

Figure 4-69: Specimen PC2 Top Bar Passes (All) Air-Dried Non-Depth-Corrected GPR Data

Void Specimens

The air-dried, non-depth-corrected GPR data for Specimen V1, that contains defects consisting of water-filled voids of varying diameter, are presented in Figure 4-70. From that data, it was observed that weak reflection amplitudes (shown in red, yellow, and green hues) were collected at the locations of the water-filled voids in the cover layer. The smallest-diameter void detected was ½ in. in diameter, indicating that GPR can respond to water-filled voids as small as ½ in. in diameter within the cover layer. However, strong signals (shown in purple and dark blue hues) were measured at the locations of the deep voids. Accordingly, it was concluded that GPR is not capable of detecting deep, water-filled voids. Visual analysis of the corresponding depth-corrected GPR data supported the two foregoing conclusions. Furthermore, implementation of the least restrictive BridgeScan (2017) deterioration threshold (-19.9 dB) resulted in none of the voids being detected.

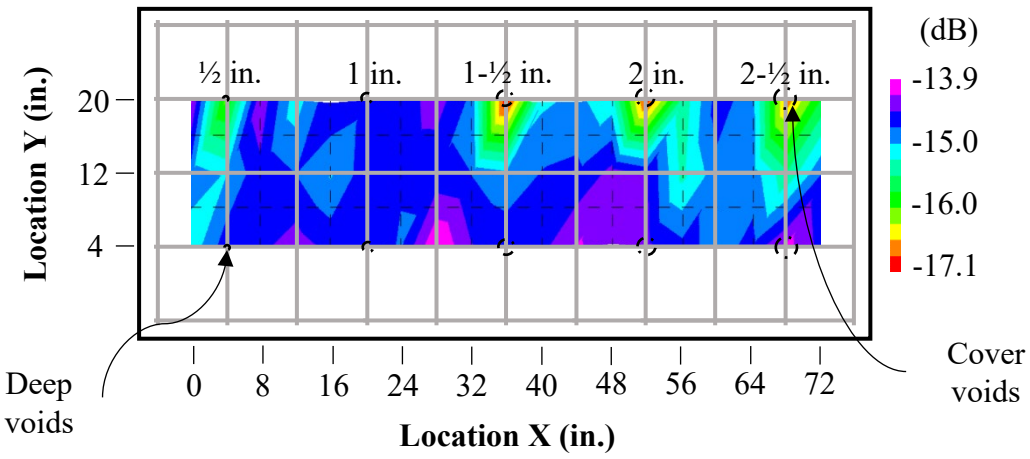

Figure 4-70: Specimen V1 Top Bar Passes (All) Air-Dried Non-Depth-Corrected GPR Data

Additionally, the air-dried, non-depth-corrected GPR data for Specimen V2, with clay-filled voids of varying diameter, are presented in Figure 4-71. Unlike in Specimen V1, weak reflection amplitudes (shown in red, yellow, and green hues) were not present at the locations of each shallow defect. Nonetheless, one such amplitude was recorded at the large, 2-1/2 in. diameter clay void. It was hypothesized that this difference in detectability for voids of the same size between Specimens V1 and V2 was caused by the difference in the dielectric constants of the void-simulating materials. As the dielectric contrast between water and concrete is greater than that between clay and concrete, more pronounced waves would be reflected from the water-filled voids than from the clay voids. Thus, GPR would be able to detect water-filled voids that were smaller than clay-filled voids. However, given that there is an additional signal of weak magnitude, shown at spatial coordinate (12, 4), it is difficult to say with certainty that the weak signal recorded at the largest, shallow, clay-filled void was caused by the void rather than by just random variation in GPR data.

Nonetheless, predominantly strong GPR signals (shown in dark blue and purple hues) were collected at the locations of the deep, clay-filled voids, indicating that GPR cannot detect such deep voids as large as 2-1/2 in. in diameter. Visual analysis of the depth-corrected GPR data for Specimen V2 supported the aforementioned observations. Like with Specimen V1, implementation of the least restrictive BridgeScan (2017) deterioration threshold (-19.9 dB) did not allow for any defect detection in Specimen V2.

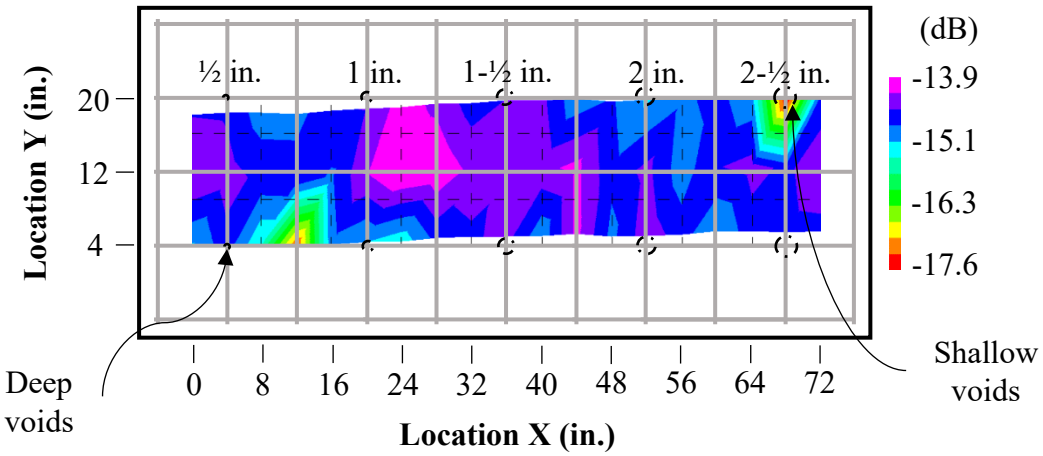

Figure 4-71: Specimen V2 Top Bar Passes (All) Air-Dried Non-Depth-Corrected GPR Data

4.5.3 Hypothesis Testing Results of GPR Data-Collection Orientation

The results of hypothesis testing aimed at determining whether the presence of intersecting reinforcement influenced GPR measurements are presented hereinafter. For both the f-test and t-tests, a 95% confidence level was enforced, resulting in a significance value of 5% (0.05). P-values calculated from the two tests comparing air-dried GPR data collected over and between the intersections of reinforcement when oriented perpendicular to the bottom layer (longitudinal) are presented in Table 4-10. Note that all p-values reported in this thesis are rounded to the nearest thousandths place.

Table 4-10: Results of Hypothesis Testing Comparing Air-Dried Bottom Bar GPR Data Collected Over and Between Reinforcement Intersections

Specimen ID	F-test, p-value	One-tailed t-test, p-value
CTRL	0.368	0.030
CR1	0.397	0.000
C1	0.158	0.000
C2	0.343	0.000
DE2	0.411	0.001
DE3	0.328	0.050
DE4	0.188	0.118
DE5	0.147	0.162
DL1	0.037	0.000
DL2	0.040	0.000
DL3	0.131	0.245
DL4	0.000	0.000
DL5	0.028	0.006
DL6	0.004	0.000
DL7	0.000	0.058
DL8	0.489	0.000
PC1	0.013	0.198
PC2	0.415	0.000
V1	0.000	0.000
V2	0.000	0.001

Of the 20 specimens, only nine of them (V1, V2, DL1, DL2, DL4, DL5, DL6, DL7, and PC1) had a p-value from the f-test that was less than the significance level. Accordingly, there existed no clear pattern as to whether grid location for passes collected perpendicular to the bottom steel in the top mat affected the variance of GPR data for the majority of the specimens. However, of the 20 specimens, 15 of them (V1, V2, DL1, DL2, DL4, DL5, DL6, DL8, CR1, C1, C2, DE2, DE3, PC2, and CTRL) had a p-value from the one-tailed t-test that was less than the significance level. Hence, with 95% confidence, the null hypothesis was rejected, and it was concluded that the mean of GPR data collected over the intersection of reinforcement is less than that of data collected between such

intersections, when collecting data while oriented perpendicular to the bottom layer in the top mat. Consequently, data from GPR inspection passes collected in that manner with sufficient measurements over and between intersections of reinforcement would form two distinct distributions. Therefore, deterioration mapping using thresholds as described in ASTM D6087 (2015) would not be appropriate when data are collected while oriented perpendicular to the bottom layer in the top mat.

Similarly, p-values calculated from the two tests comparing air-dried GPR data collected over and between the intersections of reinforcement when oriented perpendicular to the top layer (transverse direction) are presented in Table 4-11. Of the 20 specimens, only five of them (V1, V2, DL1, DL6, and DL8) had a p-value less than the significance level after the f-test was performed. Thus, for most specimens, with 95% confidence, the null hypothesis was not rejected. Accordingly, it was concluded that there is generally no statistical difference in variance between GPR data collected over and between intersections of reinforcement when oriented perpendicular to the top reinforcement layer. Furthermore, of the 20 specimens, only one of them (C1) had a p-value less than half the significance level from the two-tailed t-test. Hence, with 95% confidence, the null hypothesis was rejected, and it was concluded that there is generally no statistical difference between the means of GPR data collected over and between intersections of reinforcement when oriented perpendicular to the top reinforcement layer. Thus, as the intersections of reinforcement generally do not affect GPR data collected perpendicular to the top layer but do affect those collected perpendicular to the bottom layer, hereinafter, only the former GPR data are used in this thesis as a means of evaluating the capabilities of GPR in assessing the condition of bridge decks.

Table 4-11: Results of Hypothesis Testing Comparing Air-Dried Top Bar GPR Data Collected Over and Between Reinforcement Intersections

Specimen ID	F-test p-value	Two-tailed t-test p-value
CTRL	0.064	0.077
CR1	0.143	0.253
C1	0.137	0.013
C2	0.062	0.488
DE2	0.352	0.284
DE3	0.276	0.435
DE4	0.210	0.216
DE5	0.222	0.380
DL1	0.003	0.407
DL2	0.360	0.492
DL3	0.166	0.312
DL4	0.364	0.155
DL5	0.333	0.454
DL6	0.000	0.106
DL7	0.261	0.492
DL8	0.004	0.058
PC1	0.066	0.158
PC2	0.312	0.424
V1	0.000	0.149
V2	0.000	0.284

4.5.4 Results of ROC Analysis of GPR Data

The results of ROC analysis of the air-dried, non-depth-corrected Top Bar Passes All GPR data are presented in Table 4-12. Along with the ROC accuracy rates, the percentages of defective and sound portions of each specimen correctly identified with the optimal GPR thresholds are also tabulated. Furthermore, two separate ROC analyses were conducted for Specimens V1 and V2 respectively, one in which the data collected over voids in the cover layer were removed and the other in which that collected over deep voids was removed. Accordingly, the capacity of GPR to respond to shallow or deep voids uniquely could be numerically evaluated.

Table 4-12: Accuracy of Receiver Operator Characteristic Analysis of Air-Dried Non-Depth-Corrected Top Bar Passes All GPR Data

Specimen ID	Optimal Threshold (dB)	Maximum Accuracy (%)	Defect Area Detected (%)	Sound Area Detected (%)
CTRL	-16.33	73.7	0.0	100.0
CR1	-13.18	68.4	85.7	58.3
C1	-18.20	84.2	87.2	77.8
C2	-17.60	82.5	89.7	66.7
DE2	-17.97	73.7	0.0	100.0
DE3	-16.71	75.4	6.7	100.0
DE4	-15.80	73.7	0.0	100.0
DE5	-17.23	73.7	0.0	100.0
DL1	-16.69	70.2	5.6	100.0
DL2	-20.48	68.4	0.0	100.0
DL3	-15.16	73.7	0.0	100.0
DL4	-18.17	70.2	96.7	40.7
DL5	-16.94	79.0	0.0	100.0
DL6	-18.58	79.0	0.0	100.0
DL7	-16.08	68.4	0.0	100.0
DL8	-17.00	68.4	0.0	100.0
PC1	-16.52	73.7	0.0	100.0
PC2	-17.15	73.7	0.0	100.0
V1 (Cover)	-16.09	98.1	80.0	100.0
V1 (Deep)	-15.69	90.4	0.0	100.0
V2 (Shallow)	-17.55	92.3	20.0	100.0
V2 (Deep)	-17.27	88.5	0.0	97.9

From Table 4-12, based on a ROC analysis of the air-dried, non-depth-corrected data, GPR was approximately 73.7% accurate in correctly evaluating the condition of Specimen CTRL, assuming that the cold joint from the embedded miniature slab presented a defect. However, the percentage of sound area identified using the accompanying ROC threshold was 100% while the corresponding percent of identified defective area was 0%. In other words, this analysis indicated that for this specimen, when considering the ability of GPR to discern between the miniature slab and surrounding concrete, it is best to assume

the entire specimen as sound. Accordingly, GPR testing in accordance with ASTM D6087 (2015) specifications did not result in identification of the cold joint from the miniature slab.

Similar analysis of the ROC results for Specimen CR1 indicated that GPR is not an effective means of identifying vertical cracks in concrete bridge decks without overlays. The overall accuracy of the optimal threshold was approximately 68.4%. Moreover, this accuracy was accompanied by 58.3% and 85.7% percentages of sound and defective areas respectively correctly identified using the optimal threshold. While the high percentage of correct predictions of defective concrete was compelling, the low overall and sound accuracy rates did not indicate supreme confidence in the ability of GPR to distinguish between vertical cracks and sound portions of the specimen.

Moreover, ROC analysis of Specimens C1 and C2 revealed the ability of GPR to detect different zone of corrosion activity. Treating the passive reinforcement in Zone 1 from both specimens as being sound, the actively corroding reinforcement in Zones 2 and 3 were classified as being defective. Accordingly, a high overall accuracy using ROC analysis (82.5–84.2%) was calculated for each specimen and accompanied by high percentages of defective areas (87.2–89.7%) and sound areas (66.7–77.8%) being correctly identified. These results indicated that GPR can differentiate zones of differing corrosive activities, whether that through interaction with (1) a more conductive pore solution, (2) corrosion products, or (3) damage in zones of active corrosion.

Furthermore, ROC analysis of the four deterioration specimens (DE2–5) suggested that GPR is not capable of detecting deterioration below the top reinforcement mat. While the accuracy rates of the four specimens were promising (all either 73.7% or 75.4%), the

corresponding percentages of correctly identified sound and defective concrete were most revealing. For all deterioration specimens, the percentage of correctly identified deteriorated concrete was either 0.0% or 6.7%. Moreover, the accompanying percentage of correctly identified sound concrete was always 100.0%. Cooperatively, these percentages indicated it was practically most advantageous to assume the entire deck be sound, since the area of sound deck was greater than that of the defective deck. Accordingly, it was determined that GPR has no ability to distinguish between deteriorated concrete below the top reinforcement mat and sound concrete in decks without overlays.

Analysis of the eight delamination specimens resulted in a similar conclusion being made regarding the capability of GPR to detect delaminations in bridge decks without overlays. For all delamination specimens with the exception of Specimen DL4, the percentage of correctly identified defect area was either 5.6% or 0.0%. The accompanying percentage of correctly identified sound area was 100.0% for each of the foregoing specimens. As in the deterioration specimens, the ROC analysis results of these delamination specimens indicated that GPR could provide no better guidance in evaluating a bridge deck than simply assuming the entire deck to be sound. Given that GPR was not able to confidently detect delaminations in Specimens DL2, DL6, and DL8 or the expansive delaminations in DL3, it was hypothesized that the somewhat improved accuracy rates of Specimen DL4 was the result of chance randomness in GPR data. Given these observations, it was concluded that GPR was unable to detect (1) 4 in. by 8 in. shallow and deep delaminations with thicknesses of 3/32 in. or smaller, (2) 30-mil thick delaminations as large as 6 in. by 12 in., (3) shallow 4 in. by 8 in. delaminations with unbonded percentages as large as 75% and thicknesses 30 mil or smaller, and (4) deep 4

in. by 8 in. delaminations with unbonded percentages as large as 75% and thicknesses of 50 mil or smaller.

ROC analysis of the poor-construction specimens revealed that GPR cannot detect poorly constructed concrete below the level of the top reinforcement mat. For both Specimens PC1 and PC2, the accuracy rate was 73.7%. However, the corresponding percentages of correctly identified sound and defective concrete were respectively 100.0% and 0.0%. Similar to other specimens, these results indicated that GPR cannot discern between sound concrete and poorly constructed concrete below the top reinforcement mat.

Lastly, ROC analysis of data from Specimens V1 and V2 revealed the capacity of GPR to detect voids in concrete bridge decks without overlays. For Specimen V1, when only the water-filled voids in the cover layer were considered as defects in the analysis, GPR was 98.1% accurate in predicting the true condition of the deck. With the corresponding optimal threshold, the accompanying percentages of correctly identified sound and defective areas were 100.0% and 80.0% respectively. In conjunction with visual analysis of GPR data from Section 4.5.2, these results indicate that GPR can be an excellent NDT method for detecting, water-filled voids as small as 1/2 in. in diameter in the cover layer of concrete bridge decks without overlays. However, ROC analysis of Specimen V1resulted in 0.0% of the defective area being identified when only the deep-water-filled voids were considered as defects. This result suggested that GPR is not capable of detecting deep, water-filled voids as large as 2-1/2 in. in diameter.

Similar analysis of the data from Specimen V2, considering only the shallow, clay-filled voids as defects, resulted in only 20.0% of the defective area being detected, while 100.0% of the sound area was detected. In conjunction with the visual analysis of the non-

depth-corrected GPR data presented in Section 4.5.2, results from this ROC analysis indicated that GPR may have detected the shallow, 2-1/2 in. clay-filled void. However, this hypothesis cannot be verified with certainty since only one, 2-1/2 in. clay-filled void was placed in Specimen V2. A similar ROC analysis of Specimen V2, considering only the deep, clay-filled voids as defects, resulted in 0.0% of the defective area being detected. Considering the uncertainty of whether GPR truly responded to the presence of the 2-1/2 in. clay-filled void in Specimen V1, it was concluded that GPR cannot detect (1) shallow, clay-filled voids as large as 2 in. in diameter and (2) deep, clay-filled voids as large as 2-1/2 in. in diameter in reinforced concrete bridge decks without overlays.

The results of ROC analysis of the air-dried, depth-corrected GPR data are presented in Table 4-13 to evaluate whether depth correction of GPR data allowed for an improved evaluation of bridge decks over non-depth-corrected data. Such analysis of depth-corrected data might allow for greater confidence in developing claims regarding the capability of GPR to detect different types and sizes of defects. Furthermore, it would allow for a quantitative verification of the hypothesis developed in Section 4.5.2 that depth correction results in better correlation of GPR data with the true condition of a bridge deck.

Through ROC analysis of the non-depth-corrected, air-dried GPR data, it was concluded that the only specimens in which GPR was confidently able to discern defects from sound concrete were Specimens C1, C2, and V1. ROC results of the corresponding depth-corrected data presented in Table 4-13 supported this conclusion, as for all other specimens, GPR predicted that largely the entire deck was either defective or sound.

Table 4-13: Accuracy of Receiver Operator Characteristics Analysis of Air-Dried Depth-Corrected Top Bar Passes All GPR Data

Specimen ID	Optimal Threshold (dB)	Maximum Accuracy (%)	Defect Area Detected (%)	Sound Area Detected (%)
CTRL	-1.95	73.7	0.0	100.0
CR1	-3.96	85.7	0.0	100.0
C1	-0.09	78.9	66.7	84.6
C2	-0.72	82.5	77.8	84.6
DE2	-1.82	73.7	0.0	100.0
DE3	-1.21	75.4	6.7	100.0
DE4	-1.62	73.7	0.0	100.0
DE5	-2.10	73.7	0.0	100.0
DL1	-1.51	70.2	5.6	100.0
DL2	-1.51	70.2	11.1	97.4
DL3	0.26	56.1	100.0	7.4
DL4	0.29	54.4	100.0	3.7
DL5	-2.07	79.0	0.0	100.0
DL6	-3.33	79.0	0.0	100.0
DL7	-0.73	68.4	0.0	100.0
DL8	-1.90	68.4	0.0	100.0
PC1	-2.80	73.7	0.0	100.0
PC2	-1.94	73.7	0.0	100.0
V1 (Cover)	-1.29	98.1	80.0	100.0
V1 (Deep)	-1.29	90.4	0.0	100.0
V2 (Shallow)	-3.07	92.3	20.0	100.0
V2 (Deep)	-3.07	90.4	0.0	100.0

Accordingly, the effectiveness of the depth-correction algorithm in improving correlation between GPR data and the true state of deterioration of a bridge deck could be evaluated by comparing the ROC maximum accuracies of the Specimens C1, C2, and V1 (Cover) datasets. Applying this approach to Tables 4-12 and 4-13, the depth-correction algorithm resulted in (1) a 5.3 percentage point reduction in maximum accuracy from Specimen C1 and (2) no change in maximum accuracy from Specimen C2, or Specimen V1 (Cover). Of these three specimens in which GPR inspection was found to be capable

of defect detection, there existed little to no numerical difference in ROC maximum accuracy between non-depth-corrected and depth-corrected GPR data. This lack of difference was hypothesized to be the result of relatively uniform deck cover observed in the laboratory specimens. Accordingly, evaluation of the effectiveness of the depth-correction algorithm might be more fruitful in a full-scale bridge deck in which construction deviations are higher than those from a laboratory. Accordingly, depth correction of GPR is further explored in collected data from the full-scale bridge deck, discussed in Chapter 5 of this document.

4.5.5 GPR Moisture Content Hypothesis Testing Results

The results of hypothesis testing aimed at determining whether the moisture content of a bridge deck influences GPR measurements are presented hereinafter. As in the foregoing hypothesis test, a 95% confidence level was enforced for both the f-tests and t-tests, resulting in a significance value of 5% (0.05). P-values calculated from the two tests comparing GPR data collected in the specimen air-dried and moist states are presented in Table 4-14.

Table 4-14: Results of Hypothesis Testing Comparing Air-Dried and Moist GPR Data

Specimen ID	F-test p-value	One-tailed t-test p-value
C1	0.014	0.000
C2	0.025	0.000
DE3	0.000	0.000
DL1	0.010	0.000
DL3	0.039	0.000
DL7	0.244	0.000

From Table 4-14, for all specimens except DL7, the f-test p-value was less than the significance value. Accordingly, for tests conducted on those specimens, the null hypothesis was rejected and with 95% confidence, it was observed that the variance of GPR data depended on the moisture content of the evaluated specimen. Furthermore, as can be seen in Table 4-9, the variance of the moist data was greater than that of the dry data for all specimens in which the alternative hypothesis was accepted, except for Specimens DL1 and DL3. Based on these results, the following conclusions were developed:

1. The variance of reinforcement reflection amplitudes for a given slab changes depending on its moisture content; and
2. Slabs with high moisture contents generally exhibit greater variance in reinforcement reflection amplitudes than the same slabs with lower moisture contents.

The two foregoing conclusions carry an important implication in post-processing of GPR data from evaluations of reinforced concrete bridge decks without overlays. Methods in which deterioration thresholds are calculated as a fixed distance from a statistical parameter, as prescribed in the GSSI BridgeScan (2017) manual, are fundamentally flawed as they assume a relatively consistent variance in normally distributed measurements, despite measurable differences in moisture content. Furthermore, universal deterioration thresholds such as that proposed by Martino et al. (2015) may be applicable for a deck with a given moisture content, but not for one in a starkly different moisture state. Accordingly, future research efforts need be tailored towards accounting for the influence of moisture content on deterioration thresholds.

Additionally, from Table 4-14, for all specimens, the paired t-test p-value was less than the significance value. Thus, the null hypothesis was rejected and with 95% confidence, it was observed that the mean of GPR data depended on the moisture content of the evaluate specimen. Moreover, as can be observed in Table 4-9, the mean of moist data was lower (more negative) than that of the corresponding dry data for all specimens except Specimen DL1. This trend was hypothesized to be the result of decreased electrical resistivity of the concrete slabs because of the increased moisture content. Moisture in the pore structure of concrete allows for electrical current to be more easily passed through the concrete. Accordingly, the concrete resistivity is decreased as a specimen becomes more moist; as resistivity is the inverse of electrical conductivity, the concrete conductivity increases. As increases in conductivity correspond with increases in electromagnetic wave attenuation, the increased moisture content in the foregoing specimens facilitated greater GPR wave attenuation, thus resulting in lower (more negative) GPR amplitude measurements. Based on these results, the following conclusions were developed:

1. The mean reinforcement reflection amplitude for a given slab changes depending on its moisture content; and
2. Slabs with high moisture contents generally exhibit lower (more negative) mean reinforcement reflection amplitudes than the same slabs with lower moisture contents.

These conclusions may also translate to more effective GPR evaluations of in-service bridge decks. As the moisture content of a concrete specimen is directly related to its response to GPR, areas of suspected differing moisture content need be investigated separately to properly evaluate their condition. For example, portions of a deck shaded

against rainfall or others subject to splashing from a nearby water source may respond differently than the rest of the deck to GPR waves. Accordingly, conducting GPR evaluations when a bridge deck is believed to be in the most uniform moisture state is recommended to result in the most accurate inspections. However, if this is not possible, locations of distinct moisture contents should be evaluated separately.

4.5.6 Presentation of Impact Echo (IE) Data

Corrosion Specimens

The air-dried IE data for Specimen C1 are presented in Figure 4-72. Dominant frequencies corresponding with the specimen thickness (shown in green hues) primarily characterized Zone 1 and were scattered throughout Zones 2 and 3. These frequency measurements from Zone 1 corresponded with the sound state of the specimen as verified from destructive cores. Moreover, it was expected that such frequencies would be collected in some locations in Zones 2 and 3 because of the shallow cover, which was chosen to facilitate predominantly vertical cracking rather than delaminations. Low frequencies (shown in red and orange hues) were also measured in Zones 2 and 3, associated with the flexural plate bending of concrete above the shallow delaminations (Cheng and Sansalone 1993). These low-frequency measurements corresponded well with the known locations of shallow, corrosion-induced delaminations. Accordingly, it was concluded that impact echo is an effective NDT method for delineating between sound concrete and corrosion-induced, shallow delaminations.

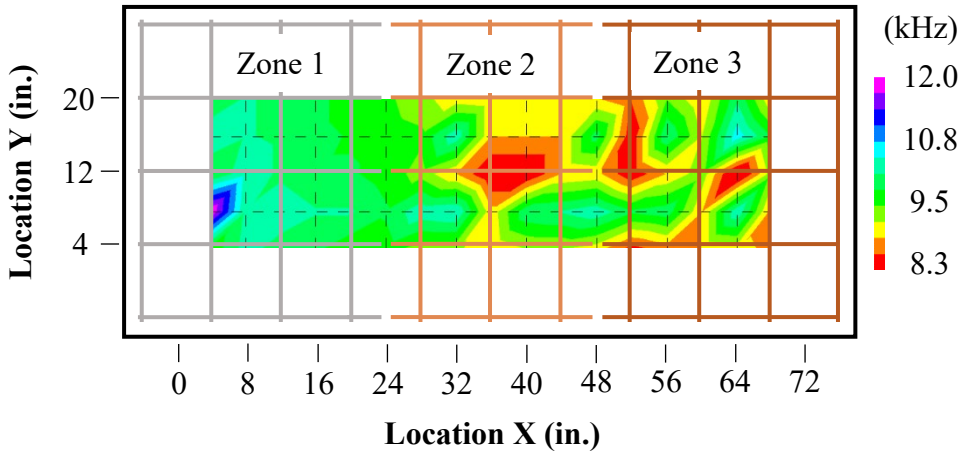

Figure 4-72: Specimen C1 Top Air-Dried IE Data

The moist IE data for Specimen C1 are presented in Figure 4-73 to evaluate whether moisture content in concrete specimens changes the conclusions of IE evaluations. Through visual comparison of the air-dried and moist IE data for Specimen C1, it was observed that the largest frequencies were relatively similar in magnitude between both datasets. However, the lowest frequencies corresponding with delaminations were somewhat larger in the moist data. Despite this, Zones 2 and 3 still exhibited lower frequencies (shown in red, yellow, and light green hues) corresponding with delaminations. Accordingly, per a visual analysis of the two IE datasets, similar conclusions might be reached regarding the state of deterioration of the specimen; nonetheless, ROC analysis executed in Section 4.5.7 more definitively addresses this question.

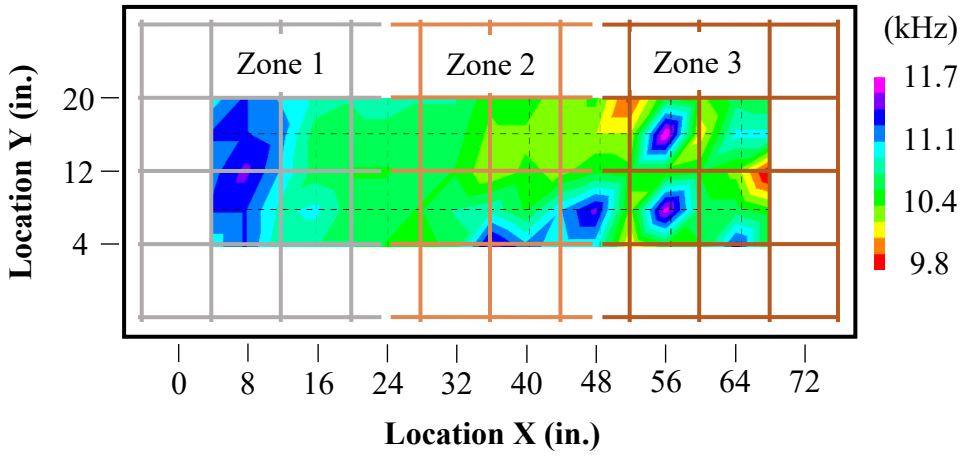

Figure 4-73: Specimen C1 Moist IE Data

Similarly, the air-dried IE data for Specimen C2 are shown in Figure 4-74. In that data, frequencies associated with the slab thickness (shown in blue and purple hues) predominantly characterized Zones 1 and 2. These measurements were consistent with extracted cores which exhibited no deterioration in Zone 1 and corrosion with no severe damage in Zone 2. Furthermore, low frequencies indicative of shallow delaminations were collected in Zone 3, consistent with the presence of corrosion-induced damage observed in extracted cores. These observations further supported the conclusion that impact echo is an excellent NDT method for discerning between shallow, corrosion-induced delaminations and sound concrete.

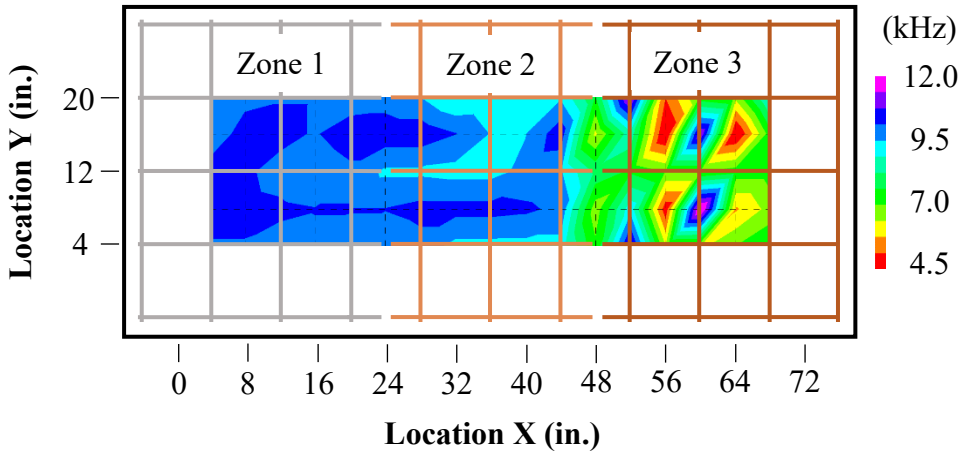

Figure 4-74: Specimen C2 Air-Dried IE Data

As with Specimen C1, the moist data for Specimen C2 are presented in Figure 4-75 to determine whether the moisture content of a concrete element affects conclusions regarding its state of deterioration. Through visual comparison of the air-dried and moist IE data for Specimen C2, it was observed that the relative spatial distribution of frequencies was largely similar between the two datasets. From Figure 4-75, the largest frequencies (shown in purple hues) were approximately of the same magnitude as those from the corresponding air-dried data. Further, the lowest frequencies (shown in red and yellow hues) were somewhat larger in the moist data than the air-dried data. However, from a visual analysis, both the air-dried and moist data sets indicated that Zone 3 was clearly distressed.

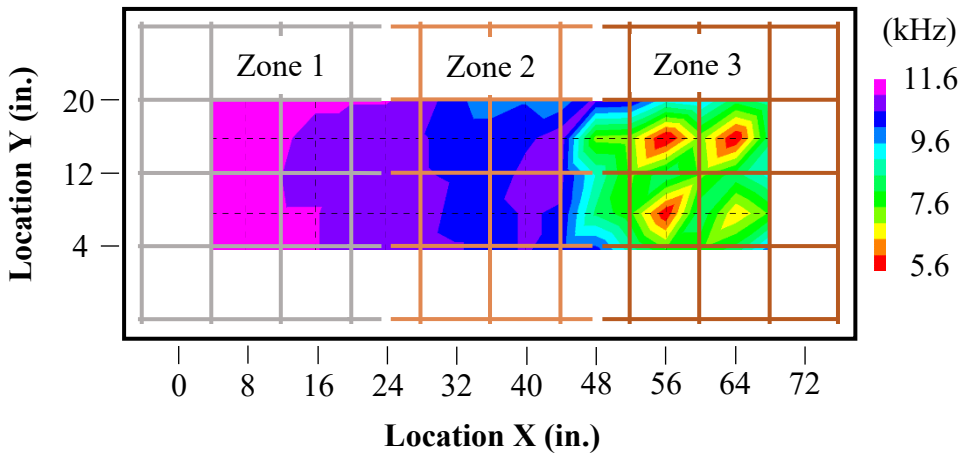

Figure 4-75: Specimen C2 Moist IE Data

Delamination Specimens

The air-dried impact-echo data for Specimen DL1 are presented in Figure 4-76. It was observed that relatively uniform frequencies corresponding to the specimen thickness (shown in purple hues) were collected outside the perimeter of the shallow delaminations. Furthermore, the presence of delaminations was distinctly evident from low frequencies (shown in green, yellow, and red hues) from the sound concrete in the specimen. All six delaminations, the thinnest being 0.25 mm, could be clearly discerned from the sound concrete using impact echo. This result was anticipated from previous work performed by Cheng and Sansalone (1995) in which it was found that the minimum thickness delamination that was detectable was 0.025 mm. Accordingly, it was concluded that impact echo can detect shallow delaminations as thin as 0.25 mm in reinforced concrete bridge decks without overlays.

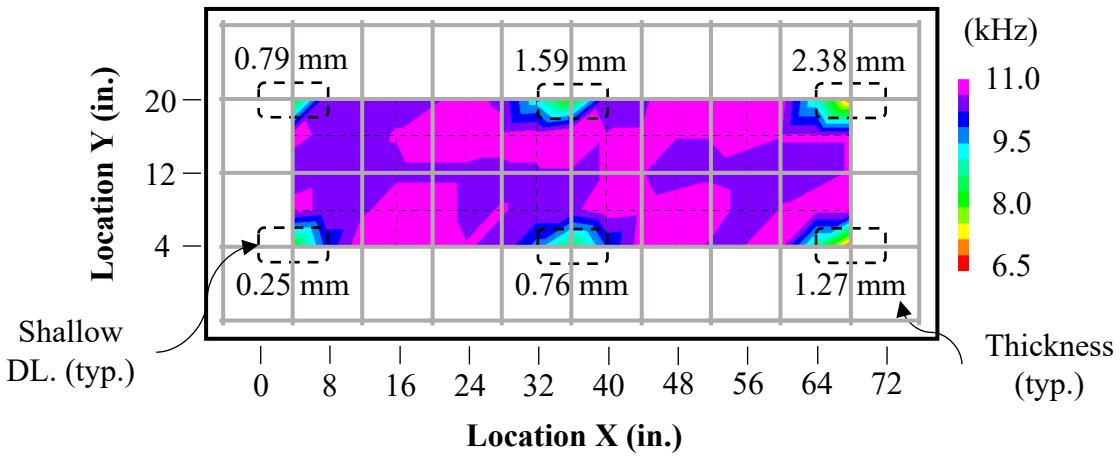

Figure 4-76: Specimen DL1 Air-Dried IE Data

The moist impact-echo data for Specimen DL1 are presented in Figure 4-77. Through visual analysis of both the air-dried and moist IE data of Specimen DL1, it was observed that low-frequency defects (shown in green, yellow, and red hues) correlated well with the known locations of shallow delaminations. Accordingly, both datasets allowed for the same conclusion to be reached regarding the true condition of the specimen. Nonetheless, the lowest frequencies of the moist data were somewhat greater than those from the air-dried data. Moreover, the largest frequencies were relatively comparable between the two datasets.

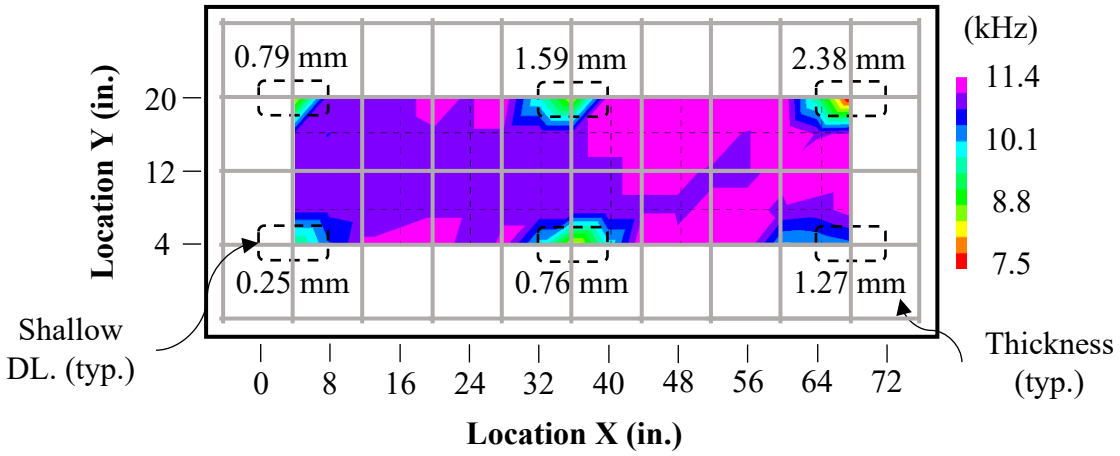

Figure 4-77: Specimen DL1 Moist IE Data

The air-dried, impact-echo data for Specimen DL2 are presented in Figure 4-78. Comparing this data to that from Specimen DL1, it was immediately evident that the correlation of the impact-echo data with the known condition of the deck was not as strong in Specimen DL2 as in DL1. In part, this was the result of the relatively low shifts in frequency caused by defects in Specimen DL2 (approximately 1.5 kHz at the extremes) as compared to the high shifts in Specimen DL1 (4.5 kHz).

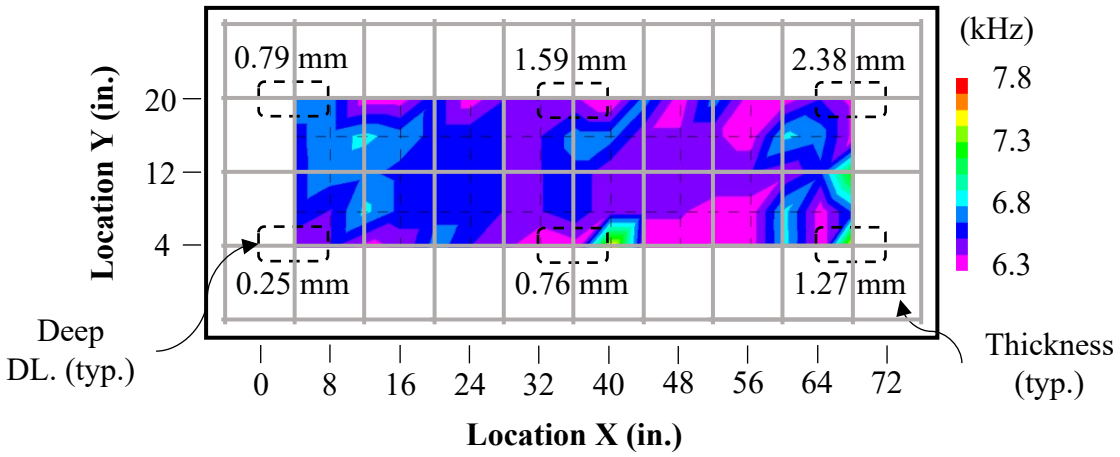

Figure 4-78: Specimen DL2 Air-Dried IE Data

Accordingly, it was observed that a deep delamination has a less pronounced influence on impact-echo frequencies than a shallow delamination of equal dimensions. Furthermore, higher-frequency responses indicative of deep delaminations (shown in cyan and green hues) were located near most of the true defect locations. However, the spatial correlation between predicted defect locations from impact-echo testing and their true locations was not as strong for testing of deep delaminations than testing of the shallow delaminations from Specimen DL1. Additionally, as compared to the 0.25 mm thick shallow delamination from Specimen DL1, the thinnest deep delamination confidently detected by impact echo was 0.76 mm, verified through destructive coring. Thus, a relationship between the detectability of a delamination and its depth-to-thickness ratio is apparent.

The air-dried, impact-echo data for Specimen DL3 are presented in Figure 4-79. From that data, it was observed that the impact-echo response to the sand layer was chiefly different than it was to the oil layer. Typical frequencies collected over the sand layer were within the range of those measured over sound concrete, precluding discernment of the sand layer from the sound concrete. This observation did not reflect a failure of impact echo but rather a failure in defect simulation, as verified with cores through the sand layers shown in Section 4.5.1 and Appendix A. Those cores revealed that no tangible delamination was formed by the sand layer, perhaps due to fabrication practices. Thus, impact echo correctly recognized the sand layer as producing no delamination. Conversely, low-frequency measurements (shown in green, yellow, and red hues) indicative of shallow delaminations were collected over the oil layer. However, the extreme effect of the delamination on frequency measurements (-1.7 kHz) was not nearly

as pronounced as that from Specimen DL1 (-4.5 kHz), which was hypothesized to be the result of different defect simulation techniques. Furthermore, mediocre correlation of impact-echo data with the intended location of the oil layer reflected defect fabrication difficulties, also verified from destructive coring shown in Section 4.5.1 and Appendix A. While not as promising as the results of Specimen DL1, data from Specimen DL3 revealed that impact echo is an effective tool for detecting shallow delaminations.

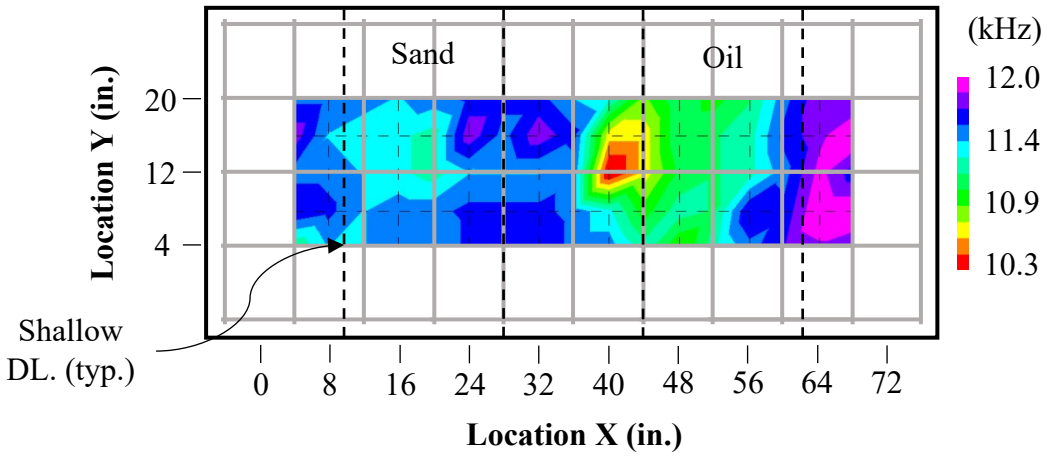

Figure 4-79: Specimen DL3 Air-Dried IE Data

The moist, impact-echo data for Specimen DL3 are presented in Figure 4-80. From Figure 4-80, it was observed that the shallow oil delamination was generally pronounced with respect to the sound concrete, as in the air-dried data. Several lower frequencies (shown in green hues) were observed over the sand delamination; however, the sand layer was not generally as distinct from the sound concrete as the oil layer, further indicating a sand layer fabrication error. Generally, the relative distribution of frequencies across the specimen was fairly comparable between the air-dried and moist data. Furthermore, the extreme frequencies were nearly the same between the two datasets. Accordingly, similar

conditions regarding the condition of the specimen would be made from a visual analysis, regardless of the moisture content.

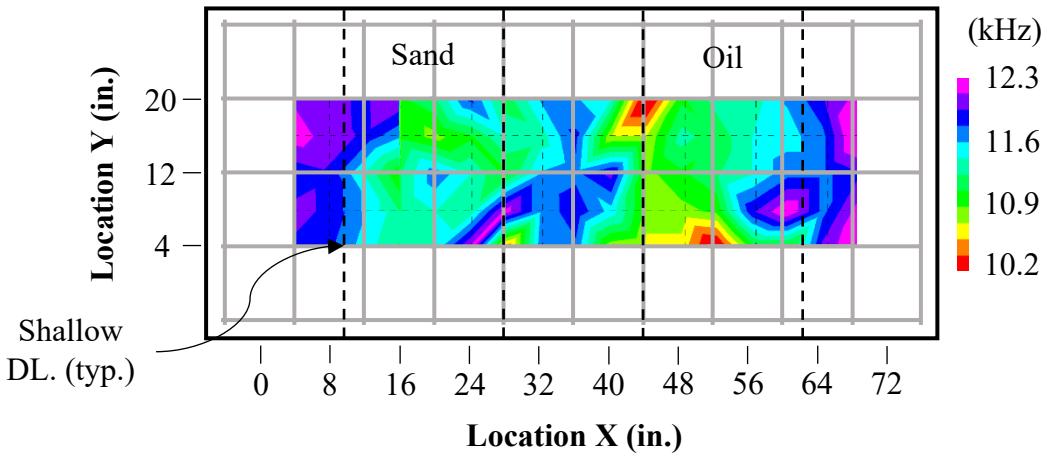

Figure 4-80: Specimen DL3 Moist IE Data

The air-dried, impact-echo data for Specimen DL4 are presented in Figure 4-81. From a visual analysis, it was noted that the spatial correlation of impact-echo data with the intended locations of delaminations was stronger in Specimen DL4 than DL3. High-frequency measurements (shown in cyan, green, yellow, and red hues) were chiefly collected over the deep sand and oil delaminations. Extracted cores through the sand layer (shown in Section 4.5.1 and Appendix A) revealed that defect simulation in Specimen DL4 largely resulted in delaminations, unlike in Specimen DL3. The differing effects of the sand layer simulation reaffirmed fabrication difficulties using this technique, presenting the need for a revised method for the full-scale bridge deck. Moreover, extracted cores from the locations of high-frequency measurements revealed the presence of deep delaminations. Nonetheless, the presence of low-frequency measurements (shown in purple hues) indicative of the specimen thickness within the profile of the oil layer further

reinforced variability in the effectiveness of delamination simulation. In addition, the extreme effect of the deep delaminations on frequency measurements in Specimen DL4 (+6 kHz) was much more pronounced than that in Specimen DL2 (+1.5 kHz). These varying shifts in dominant frequency caused by deep delamination were thought to be the result of differences in delamination characteristics (e.g. thickness, extent, unbonded fraction, etc.). In conjunction with impact-echo data from Specimen DL2, these results from Specimen DL4 reinforced that impact echo is an effective NDT method for discerning between deep delaminations and sound concrete.

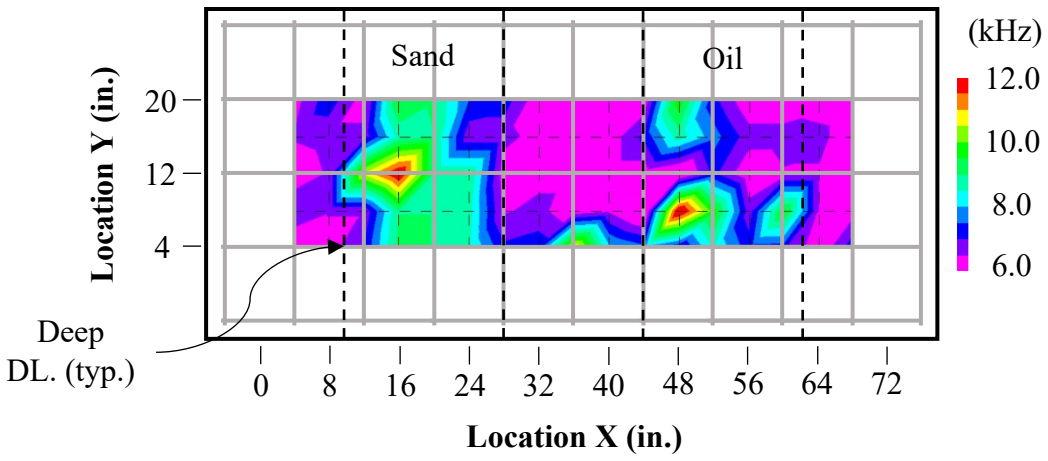

Figure 4-81: Specimen DL4 Air-Dried IE Data

The air-dried, impact-echo data for Specimen DL5 are presented in Figure 4-82. It was observed that low frequencies (shown in red, yellow, and green hues) indicative of shallow delaminations were measured over all delaminations except that with an area of 8 in^2. Of the detected delaminations, their spatial agreement with the low frequencies was excellent. Moreover, this data revealed that impact echo can detect shallow, 30 mil delaminations as small as 3 in. by 6 in. The inability to locate the 2 in. by 4 in. delamination

with testing on the 4 in. by 4 in. grid was consistent with previous work conduct by Kee et al. (2012) demonstrating that impact echo struggles to detect shallow delaminations with in-plane dimensions smaller than half the testing grid spacing. As in Specimen DL1, it was observed that delamination characteristics affected the shift in dominant frequency caused by the delamination. This observation revealed that an initially undetectable delamination may become detectable as either its thickness or areal extent increase.

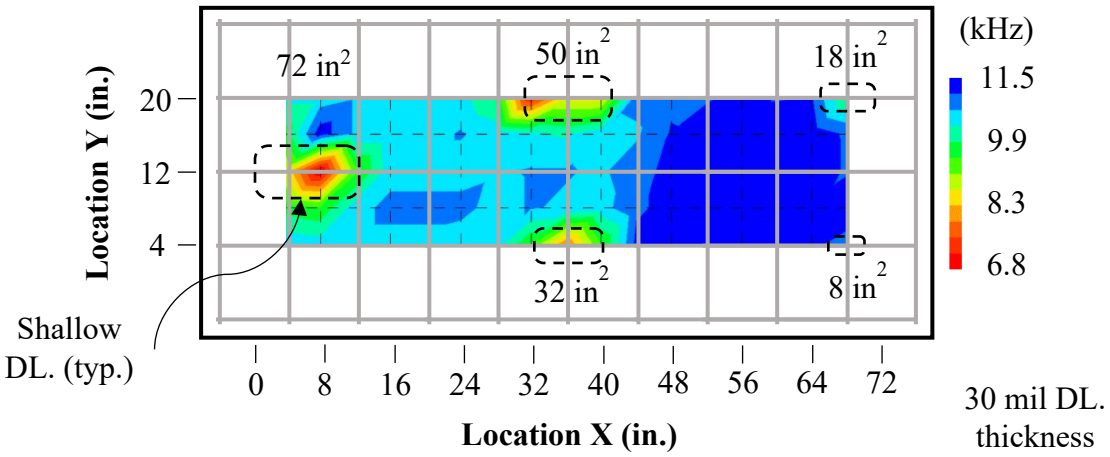

Figure 4-82: Specimen DL5 Air-Dried IE Data

The air-dried, impact-echo data for Specimen DL6 are presented in Figure 4-83. High frequencies (shown in yellow, orange, and red hues) corresponding to deep delaminations were located close to the true locations of the 72, 50, and 32 in^2 delaminations. As in Specimen DL2, this observation revealed that impact echo responds to the presence of deep delaminations but struggles to precisely locate them. Furthermore, visual analysis of the impact-echo data did not allow for confident discernment of the 3 in. by 6 in. delamination from sound concrete. However, the corresponding shallow delamination was detected in Specimen DL5, demonstrating that the detectability of a

delamination is related to its ratio of depth to smallest in-plane dimension. For Specimen DL6, impact echo struggled to locate defects with in-plane dimensions equal to or smaller than 75% of the testing grid spacing.

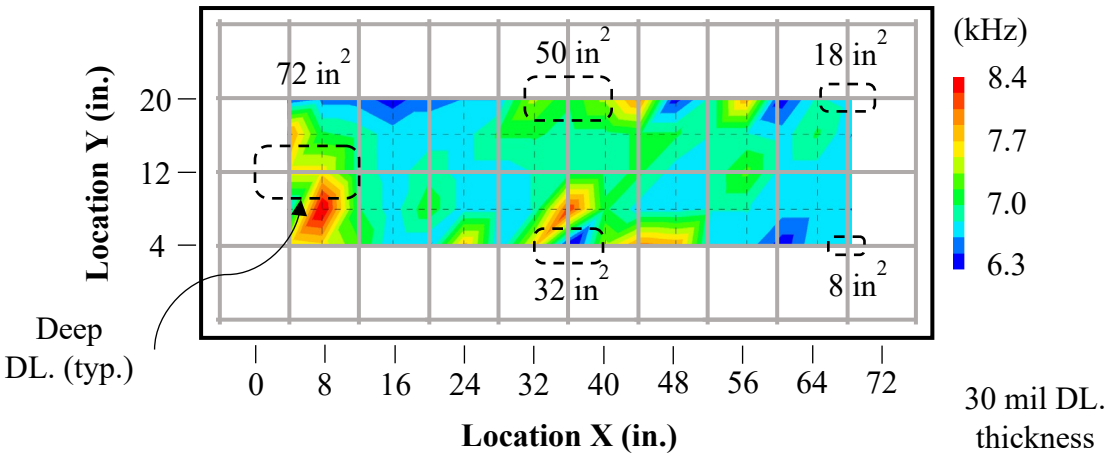

Figure 4-83: Specimen DL6 Air-Dried IE Data

The air-dried, impact-echo data for Specimen DL7 are presented in Figure 4-84. Through visual analysis of that data, it was observed that relatively high frequencies (shown in purple hues) corresponding to the bottom of the specimen were fairly uniformly distributed throughout the portions of the specimen known to be sound. Moreover, lower frequency measurements (shown in cyan, green, and yellow hues) were collected over all delaminations except the 10 mil thick, 66% unbonded delamination. From this analysis, it was concluded that impact-echo testing can be used to detect shallow delaminations with a thickness of 10 mil and 50% unbonded area. Furthermore, all else being equal, the higher the unbonded fraction of a delamination, the greater its detectability. Thus, a delamination that is originally not detectable as it is significantly bonded may become detectable as time progresses and the delamination propagates.

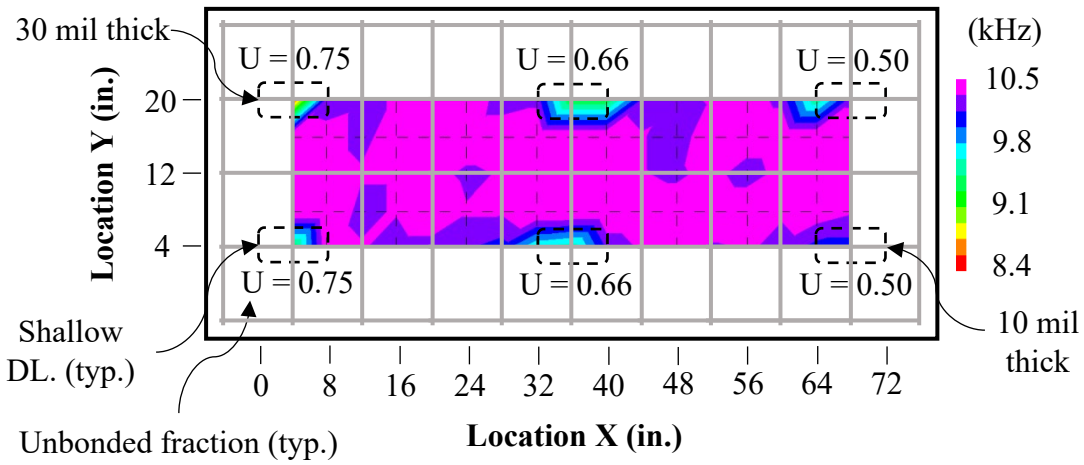

Figure 4-84: Specimen DL7 Air-Dried IE Data

Additionally, the moist IE data for Specimen DL7 are presented in Figure 4-85. Through visual analysis of the spatial contour plot of moist data, it was observed that the six partially bonded delaminations were characterized by low frequency responses (shown in red, yellow, and yellow-green hues). Visually, the contrast between the areas of delamination and those of sound concrete was not as strong from the moist data as that from the air-dried data. Nonetheless, the added moisture did not visually preclude a response from the delaminations. Both the extreme frequencies measured appeared to increase in the moist data relative to the air-dried data.

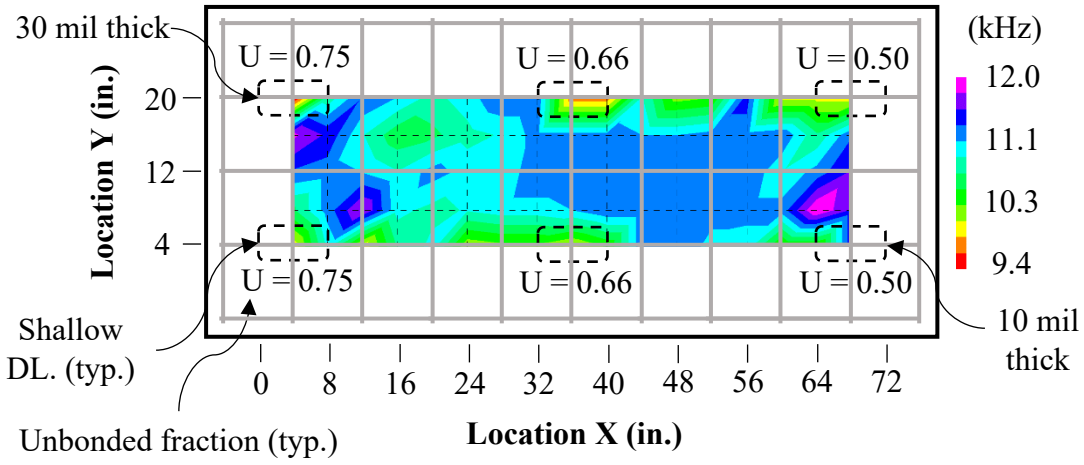

Figure 4-85: Specimen DL7 Moist IE Data

The air-dried, impact-echo data for Specimen DL8 are presented in Figure 4-86. High frequencies (shown in red, green, and cyan hues) were measured near each deep, partially bonded delamination except the 30 mil thick delamination with 25% unbonded area. As in Specimens DL2 and DL6, the spatial correlation of high-frequency measurements with the true location of the deep delaminations was not as strong as the correlation of low frequencies exhibited with the shallow delaminations. Furthermore, the 30-mil thick delamination with 50% unbonded area was the thinnest and most bonded delamination that impact echo was able to detect. In conjunction with the results from Specimens DL2, DL4, and DL6, impact-echo data from Specimen DL8 demonstrated that impact echo can respond to the presence of deep delaminations but may not accurately locate them.

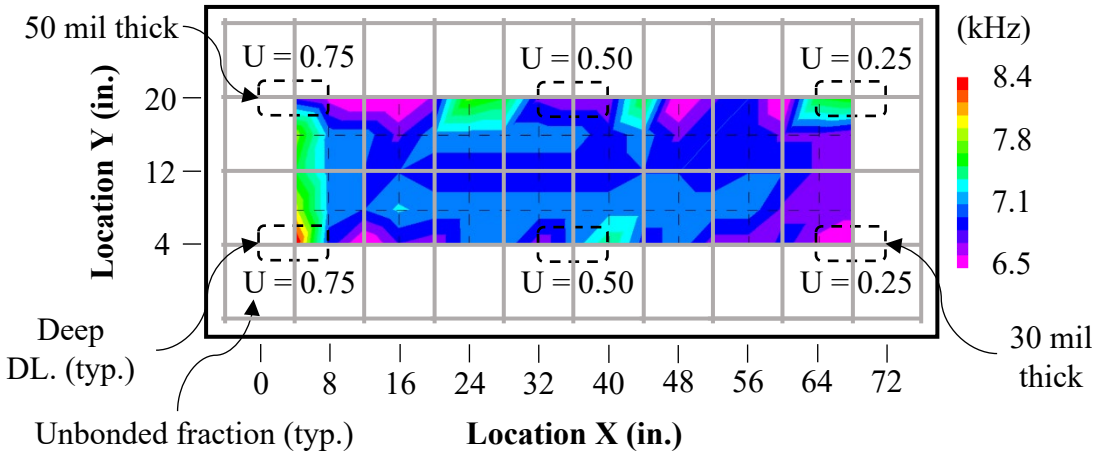

Figure 4-86: Specimen DL8 Air-Dried IE Data

Deterioration Specimens

The air-dried, impact-echo data for Specimen CTRL are presented in Figure 4-87. From a visual analysis, chiefly high frequencies (shown in red, orange, and yellow hues) were collected within the profile of the control miniature slab. Conversely, lower-frequency measurements (shown in green hues) corresponding to the slab thickness were largely collected outside the perimeter of the miniature slab. This observation suggested that impact echo responded to the presence of the cold joint formed between the miniature slab and the surrounding concrete. However, extracted cores from Specimen CTRL (Shown in Section 4.5.1 and Appendix A) confirmed that the concrete in the miniature slab and that surrounding it were (1) well-bonded with one another, and (2) generally well-consolidated. Accordingly, it was interesting that impact echo had discerned the miniature slab from the surrounding concrete, since the entire slab was made with the same mixture proportions.

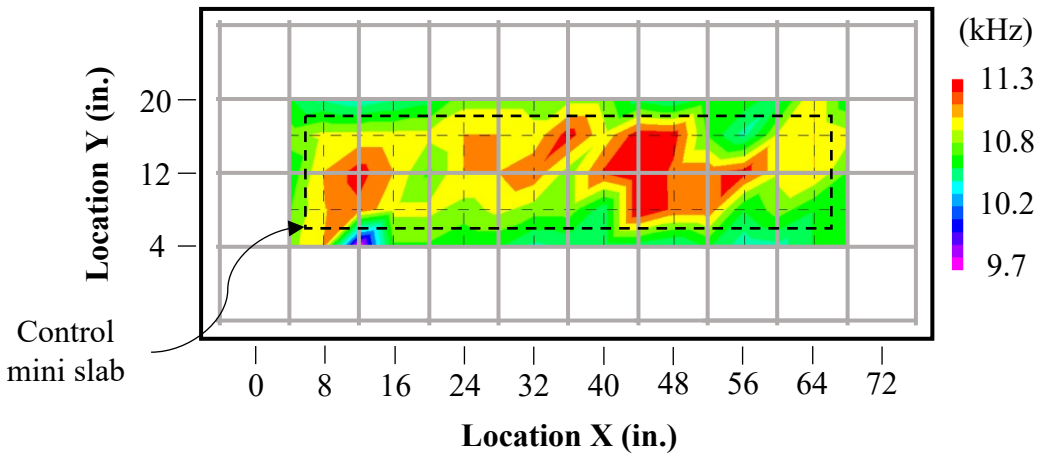

Figure 4-87: Specimen CTRL Air-Dried IE Data

As there were no flaws (e.g. delaminations, honeycombing, etc.) within the specimen, it was hypothesized that the higher frequencies collected over the miniature slab were caused by differing compression wave velocities in the miniature slab and the surrounding concrete. ACI Committee 228 (2013) notes that the compression wave velocity in an isotropic, elastic solid is related to its modulus of elasticity, density, and Poisson ratio in accordance with the following equation:

$$C_p = \sqrt{\frac{E(1-\upsilon)}{\rho(1+\upsilon)(1-2\upsilon)}} \tag{4.9}$$

where

C_p = the compressive wave speed;

E = the Young's modulus of elasticity of the material;

ρ = the material density; and

υ = the Poisson's ratio of the material.

It was hypothesized that the difference in compression wave speed between the two concretes was predominantly the result of differences in elastic modulus (i.e the Poisson ratio and density vales were assumed to be practically equivalent between the two concretes). The hypothesized difference in the elastic modulus of the miniature slab concrete and surrounding concrete was investigated by conducting compressive strength testing of each concrete in accordance with ASTM C39 (2020) testing specifications and correlating the results to concrete elastic modulus. Each of the five cores extracted from Specimen CTRL were sawed in half to produce two cylinders with equivalent length to diameter ratios, each greater than 1.0. Of the two cylinders in a core, one was composed of the miniature slab concrete and the other was composed of the surrounding concrete.

The concrete compressive strength measured for each cylinder break and the location from which the cores were extracted are reported in Table 4-15.

Table 4-15: Compressive Strength of Concretes in Specimen CTRL from ASTM C39 Testing Procedures

Core Location (in., in.)	Mini Slab Strength (psi)	Other Concrete Strength (psi)
(12, 12)	13,460	7,340
(24, 12)	9,070	8,130
(36, 8)	9,440	7,600
(48, 8)	9,100	7,550
(48, 16)	7,760	8,060

From the cylinder breaks reported in Table 4-15, it was hypothesized that the compressive strength of the miniature slab concrete was higher than that of the other, surrounding concrete. Accordingly, a one-tail, two-sample t-test was conducted to compare the compressive strengths of the two concretes. Descriptive statistics in support of that t-test

are provided below in Table 4-16. Note that the 13,460 psi compressive strength of the miniature slab concrete from the core extracted at grid point (12, 12) was not included in this analysis as irregular apparent strength growth was observed during testing post-cracking as neoprene pads on either end of the cylinder substantially confined crack propagation. This phenomenon was not observed during the other cylinder tests.

Table 4-16: Descriptive Statistics for Hypothesis Testing of Specimen CTRL Concretes

Mini-Slab Concrete			Other Concrete		
n	**μ (psi)**	**s (psi)**	**n**	**μ (psi)**	**s (psi)**
4	8843	741	5	7736	343

The hypotheses corresponding to this t-test are listed as follows.

$$H_o: \mu_{MS} \leq \mu_{OC}$$

$$H_1: \mu_{MS} > \mu_{OC}$$

where

μ_{MS} = the mean of the miniature slab compressive strength sample, psi; and

μ_{OC} = the mean of the other surrounding concrete compressive strength sample, psi.

A 95% confidence interval was enforced in the hypothesis testing, corresponding to a significance level of 0.05 (5%). The resulting p-value for the one-tailed t-test was 0.010. Since the p-value was less than the significance level, the null hypothesis was rejected, and it could be said with 95% confidence that the compressive strength of the miniature-slab concrete was statistically greater than that of the other surrounding concrete.

Knowing that the compressive strength of the miniature-slab concrete was greater than that of the surrounding concrete by a factor of 1.143 (considering the mean strengths

of both concrete), the relationship in elastic modulus between the two concretes could be estimated using the following equation provided by ACI Committee 318 (2019).

$$E_c = 33{w_c}^{1.5}\sqrt{f'_c} \tag{4.10}$$

where

E_c = the modulus of elasticity of concrete, psi;

w_c = the unit weight of concrete, pcf; and

f'_c = the specified compressive strength of concrete, psi.

Assuming that the unit weights of the two concretes were approximately equivalent, the elastic modulus of the miniature slab concrete would be greater than that of the surrounding concrete by the square root of the ratio of compressive strengths. Thus, the elastic modulus of the miniature slab concrete was approximately 1.069 times greater than that of the surrounding concrete.

Using a similar approach, the effect of the differing elastic moduli on the compression wave speed can be estimated using Equation 4.9 (accounting for the shape factor—0.96—correcting for the testing of plate-like elements). Assuming that the Poisson's ratio and density of the two concretes were approximately equivalent, the relationship in wave speed between the two concretes would be dictated by the square root of the ratio of elastic moduli. Thus, the compression wave speed of the miniature slab concrete was approximately 1.034 times greater than that of the surrounding concrete.

Using Equation 2.2, the known specimen depth, and the recorded dominant frequency data, the compression wave speed outside the perimeter of the miniature slab was calculated to be 13,390 ft/s. Multiplying this value by 1.034 resulted in the

approximate wave speed within the profile of the miniature slab, 13,845 ft/s. The difference in frequency between samples collected within the profile of the miniature slab and outside it was computed to be approximately 361 Hz. This theoretical difference in dominant frequencies was then compared to the measured difference in frequency between the two concretes of 349 Hz. As the theoretical and measured differences in mean frequency between the two concretes were nearly identical by correcting for the difference in elastic modulus, it was concluded that the higher frequencies measured within the profile of the miniature slab were not the result of the cold joint. Rather, they were the result of the use of two concretes of different stiffness in the specimen. Hereinafter, Specimen CTRL is regarded as being defective by poor-construction practices in which concretes of different strength/stiffness would be used. Thus, based on the delineation of the miniature slab concrete from the concrete outside its profile (evidenced in Figure 4-87), it was concluded that impact echo is an effective NDT method for detecting differences in concrete stiffness.

Similarly, the air-dried IE data for Specimen DE2 are presented in Figure 4-89. As in Specimen CTRL, high frequencies (shown in red, orange, yellow, and green hues) were measured within the profile on the miniature slab. However, the data over the miniature slab in Specimen DE2 were not as uniformly characterized by high frequencies as the data in Specimen CTRL. Moreover, lower frequencies (shown in blue and purple hues) indicative of sound concrete largely constituted data collected outside the perimeter of the miniature slab. Thus, it was concluded that impact echo can distinguish between sound and deteriorated concrete in bridge decks; however, its ability to detect the deterioration may depend on the severity of the defect.

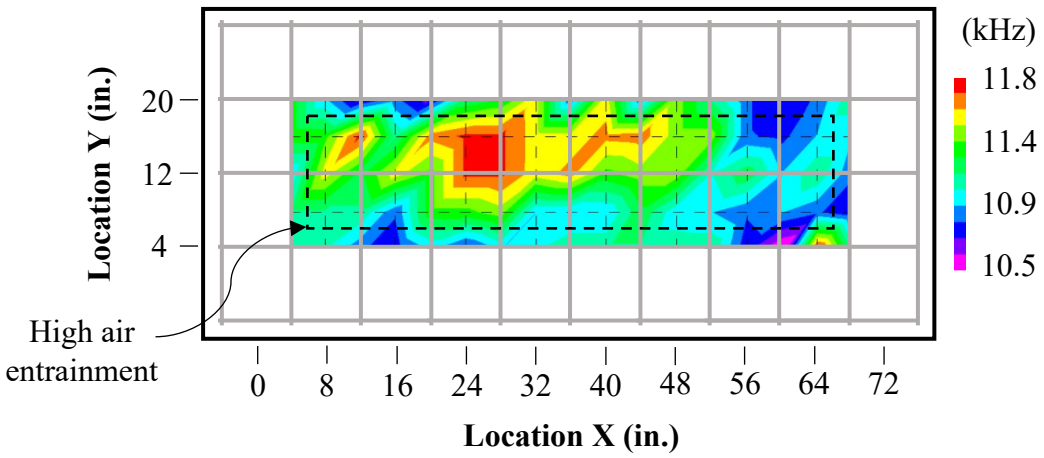

Figure 4-89: Specimen DE2 Air-Dried IE Data

The air-dried, impact-echo data for Specimen DE3 are presented in Figure 4-90. Visual analysis of that data revealed that high frequencies (shown in red, orange, and yellow hues) indicative of honeycombing were collected within nearly the entire profile of the miniature slab. Furthermore, lower frequencies (shown in blue hues) were chiefly collected outside the miniature slab perimeter. This analysis revealed that impact echo can detect honeycombing caused by poor-construction practices. Moreover, as the state of deterioration was more severe in Specimen DE3 than in DE2 and impact-echo data better correlated with the true state of deterioration in the former specimen, impact echo may be able to identify deterioration not initially detected as that deterioration becomes more severe.

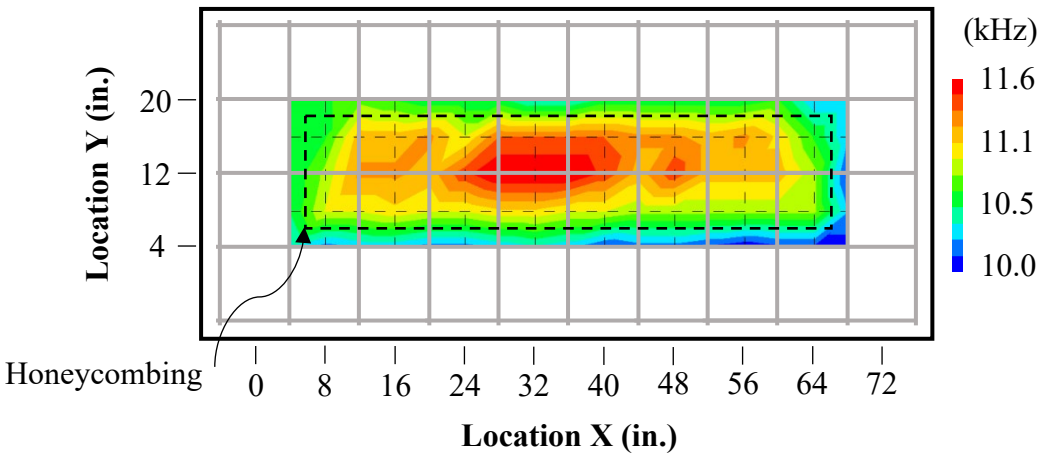

Figure 4-90: Specimen DE3 Air-Dried IE Data

In addition, the moist IE data for Specimen DE3 are presented in Figure 4-91. Through visual comparison of the moist and air-dried IE data, it was observed that, for both datasets, honeycombing can be largely identified apart from sound concrete. High frequencies (shown in red, orange, and yellow hues) were generally measured within the perimeter of the miniature slab in the moist IE dataset. Further, lower frequencies (shown in green, blue, and purple hues) were generally observed outside the perimeter of that slab. Additionally, the maximum recorded frequency for the moist data was larger than that or the air-dried data, and the smallest frequency from the former dataset was practically the same as that from the latter. Considering the effect of moisture content on the extreme recorded frequencies for the six specimens tested in both the air-dried and moist states, the differences in extreme frequencies appeared random. Accordingly, it was hypothesized that the moisture content of a concrete element did not elicit a strong change in the distribution of recorded IE frequencies as it had in GPR reflection amplitudes. Moreover, for Specimen DE3 and the other five moist specimens, a visual analysis comparing the

moist and air-dried IE data did not result in significantly different conclusions being reached regarding the condition of the specimens.

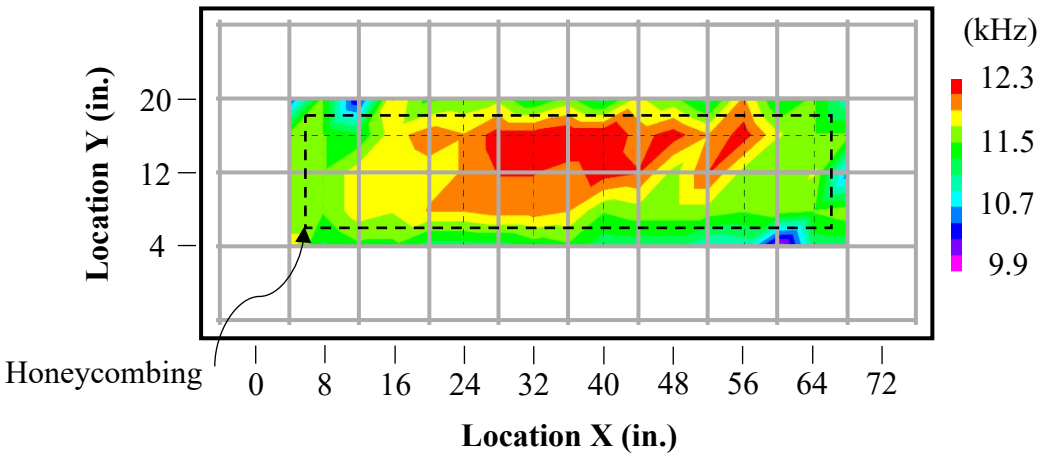

Figure 4-91: Specimen DE3 Moist IE Data

The air-dried, impact-echo data for Specimen DE4 are presented in Figure 4-92. Low frequencies (shown in purple and dark blue hues) indicative of sound concrete were primarily measured outside the perimeter of the miniature slab, but also within it. Furthermore, higher frequencies (shown in cyan, green, yellow, and red hues) corresponding to deterioration were generally measured within the profile of the miniature slab. However, similar frequencies were collected in locations outside that slab profile, making it more difficult to discern between the sound concrete and the miniature slab with the high fiber dosage. The high variability of frequencies within the profile of the miniature slab might have been the result of a varying distribution of entrapped air accompanying the fibers in the slab, as observed in extracted cores shown in Section 4.5.1 and Appendix A. Accordingly, it was unclear whether impact echo responded to the microfibers present in the concrete, the above-average entrapped air content in the miniature slab, or both.

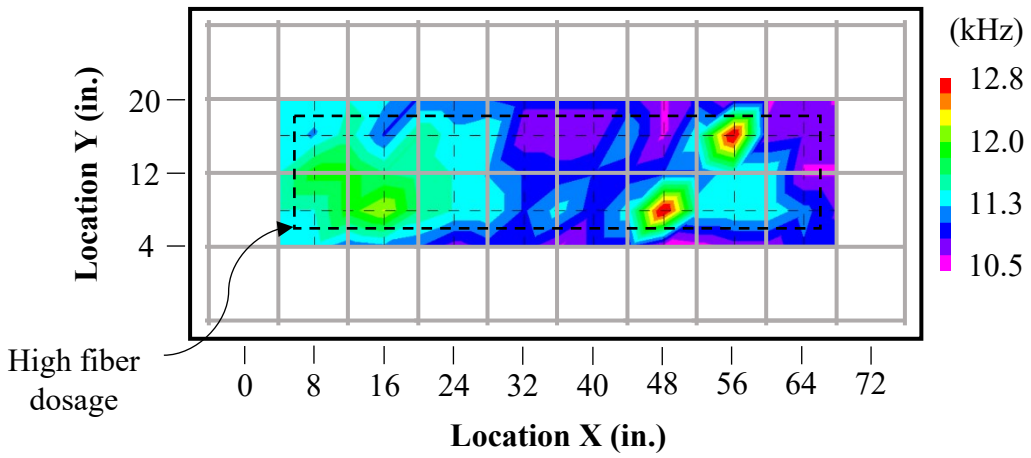

Figure 4-92: Specimen DE4 Air-Dried IE Data

Similarly, the air-dried, impact-echo data for Specimen DE5, in which deterioration was simulated using a moderate dosage of anti-cracking fibers, are presented in Figure 4-93. From Figure 4-93, it was observed that low frequencies (shown in purple and dark blue hues) indicative of the specimen thickness predominantly characterized the data collected outside the profile of the miniature slab. Furthermore, many of the data sampled within the profile of the miniature slab were high frequencies (shown in green, yellow, and red hues) indicative of concrete deterioration. Comparing the impact-echo data from Specimen DE4 to that of DE5, it was puzzling that there was seemingly better correlation of impact-echo data with the true state of deterioration in Specimen DE5 than with that of Specimen DE4. It was believed that the lower dosage of anti-cracking fibers in Specimen DE5 would elicit a less pronounced response from impact-echo testing than the higher dosage from Specimen DE4. Based on visual examination of the extracted cores from Specimen DE5 shown in Section 4.5.1 and Appendix A, it was hypothesized that this peculiar phenomenon was the result of the greater entrapped air content in Specimen DE5 than in DE4. Accordingly, while it was still unclear whether impact echo was significantly impacted by

the anti-cracking fibers, it was concluded that differences in air content throughout the two specimens most influenced the varying impact-echo response throughout the miniature slabs.

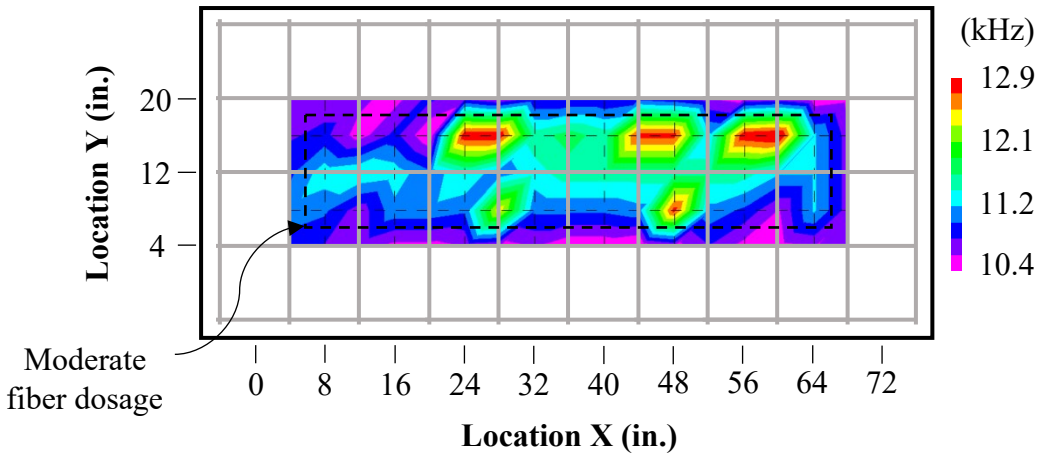

Figure 4-93: Specimen DE5 Air-Dried IE Data

Poor-Construction Specimens

The air-dried, impact-echo data for Specimen PC1 are presented in Figure 4-94. It was observed that high frequencies (shown in red, yellow, and green hues) indicative of poorly constructed concrete primarily characterized the impact-echo data collected within the profile of the miniature slab. Nonetheless, some higher frequencies were also collected outside the perimeter of the slab. Moreover, low frequencies (shown in purple and blue hues) corresponding to the specimen thickness were also collected around the miniature slab. Thus, the impact-echo data appeared to correlate well with the true state of deterioration of the specimen. However, ROC analysis was implemented to verify this hypothesis.

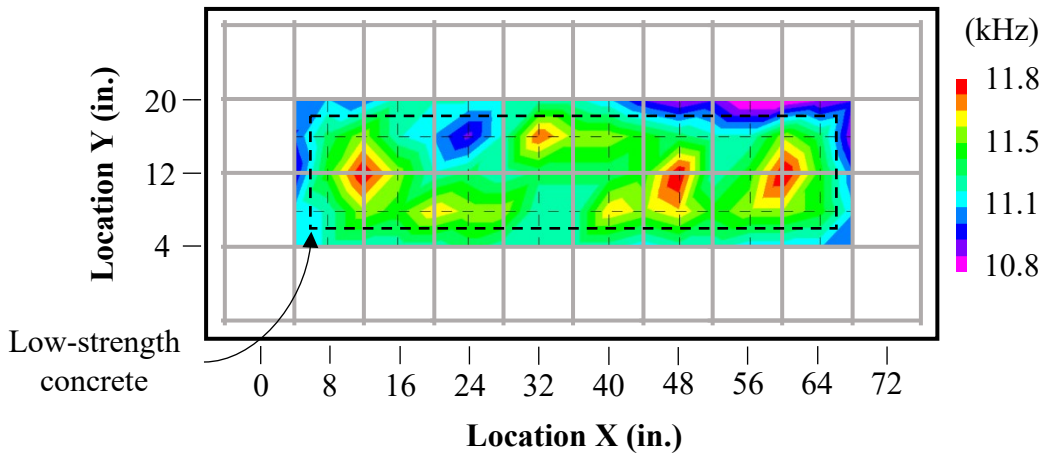

Figure 4-94: Specimen PC1 Air-Dried IE Data

The air-dried, impact-echo data for Specimen PC2 are presented in Figure 4-95. From a visual analysis, it was observed that the impact-echo data collected within the profile of the miniature slab were primarily high frequencies (shown in red, green, and cyan hues) corresponding to poorly constructed concrete. Furthermore, low frequencies (shown in purple and dark blue hues) indicative of the slab thickness were largely collected around the perimeter of the slab. Given the distinct difference in impact-echo response over the sound and defective portions of Specimen PC2, per the visual analysis, it was observed that impact echo is a good NDT method for detecting poorly constructed concrete in bridge decks without overlays.

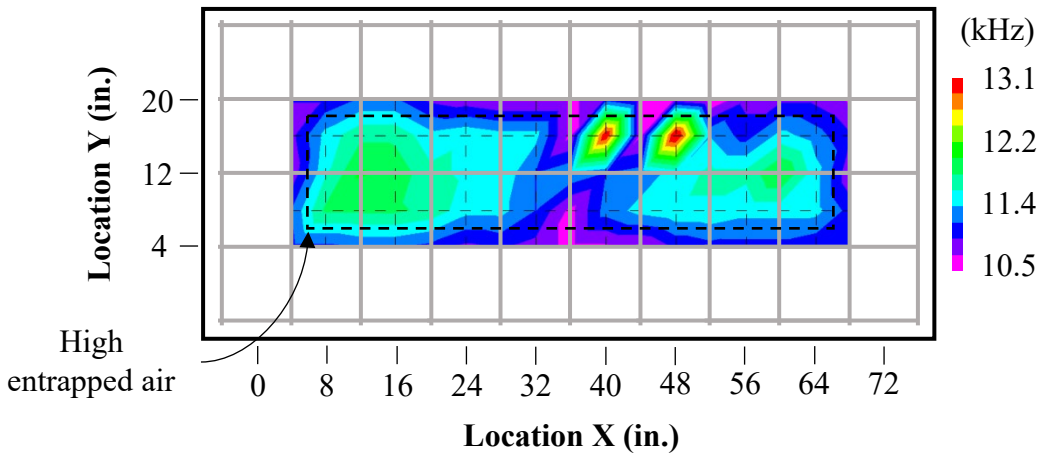

Figure 4-95: Specimen PC2 Air-Dried IE Data

Void Specimens

The air-dried, impact-echo data for Specimen V1 are presented in Figure 4-96. From Figure 4-96, high frequencies (shown in red, yellow, and green hues) were observed near water-filled voids as small as ½ in. in diameter. Moreover, low frequencies (shown in purple and dark blue hues) corresponding to the specimen thickness were measured at most locations in which the specimen was known to be sound. As with the deep delaminations, the correlation of the impact-echo data with the true location of the cover layer voids and deep voids was not strong. Rather, for many of the voids, impact echo predicted that the voids were located at least 4 in. away from their true location. Thus, impact echo was able to detect both cover layer voids and deep voids as small as ½ in. in diameter; however, it was not able to consistently locate them accurately.

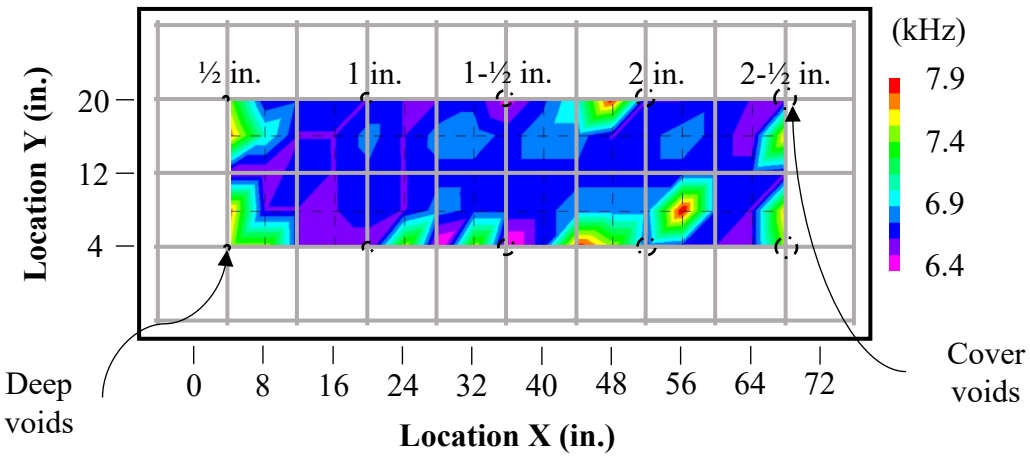

Figure 4-96: Specimen V1 Air-Dried IE Data

The air-dried, impact-echo data for Specimen V2 are presented in Figure 4-97. Visual analysis of the impact-echo data from Specimen V2 affirmed the conclusions developed from the data from Specimen V1. High frequencies (shown in red, yellow, and green hues) indicative of defects were measured near shallow and deep clay-filled voids as small as ½ in. in diameter. Furthermore, most locations of the specimen known to be sound were characterized by low frequencies corresponding to the specimen thickness. Accordingly, it was concluded that impact echo can detect both shallow and deep clay-filled voids as small as ½ in. in diameter in concrete bridge decks without overlays. Nonetheless, it may not always accurately locate them. However, the difference in the predicted and true locations of the defects in the void specimens was often only a few inches which would likely be acceptable when making repairs on an in-service bridge deck.

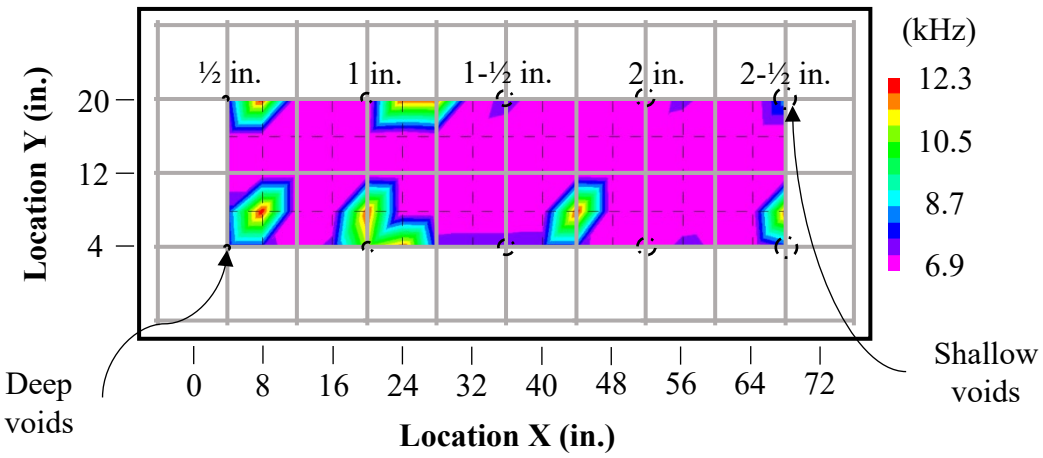

Figure 4-97: Specimen V2 Air-Dried IE Data

4.5.7 Results of ROC Analysis of IE Data

The results of ROC analysis of the air-dried IE data are presented in Table 4-17. Note that, Zone 2 of Specimen C2 was regarded as sound from an impact-echo perspective, as destructive coring of Zone 2 revealed corrosion but no pronounced significant delaminations. It was observed that ROC analysis of the impact-echo data from the two corrosion specimens resulted in fairly high accuracies and percentages of sound/defective concrete detected. Accordingly, it was concluded that impact echo is an excellent NDT method for detecting shallow, corrosion-induced delaminations. It is worth noting that ROC analysis could be used to develop universal thresholds for defect determination; however, those thresholds may not be sensitive to the properties and conditions of individual bridge decks, making them potentially unideal to use universally. While beyond the scope of this thesis, discussion of the development of a post-processing algorithm for impact-echo data to interpret measured frequencies is provided in Appendix D.

Table 4-17: Accuracy of Receiver Operator Characteristics Analysis of Air-Dried IE Data

Specimen ID	Maximum Accuracy (%)	Defect Area Detected (%)	Sound Area Detected (%)
CTRL	83.5	75.6	92.5
C1	83.5	83.3	83.9
C2	97.7	93.3	100.0
DE2	70.6	60.0	82.5
DE3	95.3	91.5	100.0
DE4	69.4	62.2	77.5
DE5	89.4	82.6	97.4
DL1	98.8	92.9	100.0
DL2	88.2	28.6	100.0
DL3	85.9	72.0	91.7
DL4	78.8	82.0	74.3
DL5	97.6	81.8	100.0
DL6	89.4	18.2	100.0
DL7	92.9	64.3	98.6
DL8	84.7	7.1	100.0
PC1	84.7	73.3	97.5
PC2	91.8	84.4	100.0
V1	89.4	20.0	98.7
V2	88.2	0.0	100.0

Furthermore, good accuracies and percentage of sound/defective concrete detected were noted for the four deterioration specimens. The highest overall accuracy (95.3%) from Specimen DE3 indicated that impact echo is a particularly accurate NDT method for identifying honeycombing below the level of the top reinforcing mat. Overall accuracy rates for the other three deterioration specimens exhibited fair-to-good accuracy rates (roughly 70–90%) in discerning between sound and defective concrete. It was initially perplexing that the accuracy rate of impact echo for Specimen DE5 was 20 percentage points larger than that from Specimen DE4, even though the latter specimen contained a higher dosage of anti-cracking fibers simulating deterioration. It was hypothesized that

this phenomenon was the result of the higher entrapped air content observed in Specimen DE5 relative to that of Specimen DE4. Localized differences in air content would affect the localized density and concrete elastic modulus which accordingly would affect the compression wave velocity, per Equation 4.6. Higher entrapped air contents, such as that in Specimen DE5, would likely have a more pronounced effect on the compression wave velocity and thus create more pronounced frequency shifts to delineate between sound and deteriorated concrete, facilitating the foregoing phenomenon. Nonetheless, in total, impact echo was an effective NDT method for discerning between sound and deteriorated concrete.

In evaluating the performance of ROC analysis to indicate the effectiveness of impact echo in detecting delaminations in bridge decks without overlays, it was necessary to consider the specimens with shallow delaminations (DL1, DL3, DL5, and DL7) separately from those with deep delaminations (DL2, DL4, DL6, and DL8). Note that, from an impact-echo perspective, the sand layer in Specimen DL3 was analyzed as sound since no tangible delaminations were produced by it in extracted cores. Considering the four specimens with shallow delaminations, all resulted in quite high overall accuracies and compelling percentages of sound/defective concrete detected. The lowest overall accuracy calculated was 85.9% (for Specimen DL3), and the highest was 98.8% (for Specimen DL1), indicating excellent overall capability in detecting shallow delaminations. Nonetheless, for all those specimens, the percentage of defective concrete detected was approximately 7 to 25 percent lower than that of sound concrete detected. Comparing this finding with the spatial contour plots of the foregoing specimens, it was concluded that impact echo is an effective NDT method for locating shallow delaminations but may not

be able to accurately map the areal extent of a delamination, unless progressively closer-spaced tests are conducted over an identified delamination.

The results of ROC analysis of the specimens with deep delaminations were not as compelling as those from the shallow delaminations. The overall accuracy rates of Specimens DL2, DL4, DL6, and DL8 were relatively high (approximately 79–88%); however, the corresponding percentages of sound/defective concrete, at first glance, pointed to an inability of impact echo to detect deep delaminations. The percentage of defective concrete detected using ROC analysis for Specimens DL2, DL6, and DL8 approximately ranged between 7 to 29 percent. It was hypothesized that these low percentages were the result of the frequency shifts indicative of deep delaminations not spatially correlating well with the truth locations of the defects, evidenced in the corresponding spatial contour plots presented in Section 4.5.6. As ROC analysis relies on assigning each test point as defective or sound based on ground truthing, a frequency shift from a deep delamination measured over sound concrete but near the defective location would cause ROC analysis to falsely predict the state of the specimen at both locations. Accordingly, for specimens in which a frequency shift from a defect does not correlate well with the true location of that defect, ROC analysis will likely not produce results representative of the capability of the implemented NDT method. Nonetheless, for Specimen DE4, relatively comparable percentages of sound/defective concrete detected (74.3% and 82.0% respectively) resulted from ROC analysis. It was hypothesized that ROC analysis performed well for this specimen with deep delaminations because the defects were large (1 ft - 6 in. by 3 ft) with respect to that of the other three such specimens.

Thus, the spatial correlation of frequency shifts with respect to the true location of deep delaminations may increase as the areal extent of those delaminations increases.

ROC analysis of the poor-construction and control specimen (also a poorly constructed specimen per Section 4.5.6) also indicated that impact echo is a good NDT method for identifying poorly constructed concrete in bridge decks without overlays. The overall accuracies and percentages of sound/defective concrete detected of the three specimens were all fairly high, indicating that impact echo responded to the entrapped air and differing water-cement ratios in the miniature slabs. Accordingly, impact echo is an effective NDT method for locating such poorly constructed concrete in bridge decks without overlays.

Furthermore, the results of ROC analysis of the two void specimens were similar to those of the specimens with deep delaminations in which the percentage of defective area detected was low. For Specimens V1 and V2, that percentage was 20% and 0% respectively. While this result suggested that IE was incapable of discerning voids from sound concrete, visual analysis of the spatial contour plots of Specimen V1 and V2 offered a better assessment of the capability of the impact-echo method. As with the specimens with deep delaminations, the spatial correlation of the known locations of the defects with the high-frequency responses indicative of the defects was poor. Accordingly, ROC analysis, which assumed that frequencies corresponding to defects would be measured at the locations of the defects, falsely indicated that impact echo is not an effective NDT method for detecting voids in bridge decks.

Additionally, the results of ROC analysis of the moist IE data are presented in Table 4-18. Comparing the ROC results presented in Table 4-18 to those from Table 4-17, the influence of moisture content on the results on impact-echo evaluations could be investigated. For Specimens C1, C2, DL1, and DL7, the maximum accuracies from ROC analysis of the moist IE data were between approximately 2 and 6 percentage points lower than those of the dry IE data. As these differences were small, it was hypothesized that other variables such as differences in the precise location of the impact/receiving points between tests might have partially accounted for the calculated differences. Thus, differences in moisture content did not result in significant changes in condition assessments using impact echo.

Table 4-18: Accuracy of Receiver Operator Characteristics Analysis of Moist IE Data

Specimen ID	Maximum Accuracy (%)	Defect Area Detected (%)	Sound Area Detected (%)
C1	77.7	85.2	64.5
C2	95.3	86.7	100
DE3	81.2	93.6	65.8
DL1	96.5	85.7	98.6
DL3	77.6	44.0	91.7
DL7	89.4	50.0	97.2

Nonetheless, at face value, the difference in percentage points between the moist data and air-dried data for Specimens DE3 and DL4 were somewhat significant (14.1 and 8.3 percentage points respectively). Concerning Specimen DE3, it was unclear as to why such a large decrease in accuracy was observed when the element was tested in the moist state. One might hypothesize that voids in the honeycombing concrete were filled with moisture, thus increasing the miniature slab concrete density when compared to the same

air-dried concrete. Accordingly, if one was to idealize the concrete as an elastic, isotropic solid, per Equation 4.6, one would suspect that this increase in density would correspond with a lower compression wave velocity and thus smaller shifts in the dominant frequency from the honeycombed concrete. However, this hypothesis would indicate that the locations of most honeycombing would experience the greatest decrease in dominant frequency shift since their density would be most changed through the addition of moisture. However, through visual analysis of the air-dried and moist IE data for Specimen DE3, the locations with the most pronounced shift in dominant frequency are of roughly the same magnitude and location in both contour plots (Figures 4-90 and 4-91). In fact, the locations that became less pronounced with respect to the sound concrete in the moist data were the locations of least distinction in the air-dried data (towards the perimeter of the miniature slab). Thus, it was hypothesized that the change in moisture content did not significantly affect the impact-echo response as in the previous suggestion. As only one deterioration specimen was tested in the moist condition, and the four previously mentioned specimens exhibited little change in ROC accuracy between tests of different moisture contents, it was not confidently concluded that the difference in moisture content facilitated the 14.1 percentage point difference in overall accuracy of Specimen DE3.

Moreover, the ROC analysis results of Specimen DL3 were not hypothesized to definitively indicate that moisture content elicited a significant difference in air-dried and moist impact-echo data. First, extracted cores from Specimen DL3 revealed fabrication errors in the sand layer and perhaps the oil layer that could preclude an accurate ROC analysis. Furthermore, Specimen C2, one which also had true delaminations which could be filled with water, exhibited only a 2.4 percentage points difference in overall ROC

accuracy between the air-dried and moist data. Thus, it was hypothesized that comparison of ROC results of the air-dried and moist data for Specimen DL3 could not confidently attribute the difference in accuracies to difference in moisture content.

Overall, considering specimens tested in both the air-dried and moist states, impact echo was able to accurately discern between sound and defective concrete. Any potential effect of moisture content on predicted locations of defects derived from impact-echo data was likely quite small. Accordingly, it was concluded that impact-echo evaluations conducted on the same bridge deck in different moisture conditions do not produce significantly different conclusions regarding the condition of the deck.

4.5.8 Presentation and Analysis of HCP Data

As ASTM C876 (2015) covers the use of either spatial contour plots or cumulative frequency plots to present half-cell potential measurements, select spatial contour plots are first presented in this section. Such plots for Specimens C1 and C2 for data collected on 09/19/19 and 10/07/19 respectively are shown in Figure 4-98. Note that the two selected dates correspond with the last date that each specimen was respectively subjected to accelerated corrosion.

For both specimens, stark delineations were observed between locations of no corrosion (Zone 1) and areas of active corrosion (Zones 2 and 3). For Specimen C1, the difference in half-cell measurements between Zone 2 and 3 was somewhat pronounced; however, that difference for Specimen C2 was not as significant. Surprisingly, the half-cell measurements in Zone 2 of Specimen C1 were lower (more negative) than those of Zone 3. As Zone 3 in each specimen was corroded for twice the length of Zone 2, it was

expected that the half-cell measurements would be more negative in Zone 3 than Zone 2. Nonetheless, this expected trend was observed in the half-cell data for Specimen C2, shown in Figure 4-98(b). Accordingly, it was concluded that the half-cell corrosion potential method (1) can be an excellent method for discerning zones of active corrosion from sound portions of a deck, and (2) can detect different severities of corrosion.

Furthermore, application of the proposed half-cell threshold values from ASTM C876 (2015), shown in Table 2-2, resulted in variable success in correctly predicting the conditions of Specimens C1 and C2. Since the half-cell measurements in Zone 1 of Specimen C1 were between -200 and -350 mV, corrosion activity in that area was predicted to be uncertain through use of the foregoing thresholds. Moreover, since the half-cell measurements in Zones 2 and 3 of Specimen C1 were lower (more negative) than -350 mV, they were predicted with 90% confidence to be indicative of active corrosion. While the predicted conditions of Zones 2 and 3 were correct, that of Zone 1 failed to indicate with significant certainty that the embedded reinforcement was uncorroded. While an uncertain prediction of the condition of Zone 1 was technically not incorrect, such a prediction was generally not useful as one would be none the wiser using the half-cell corrosion method to assess Zone 1 than simply guessing its condition.

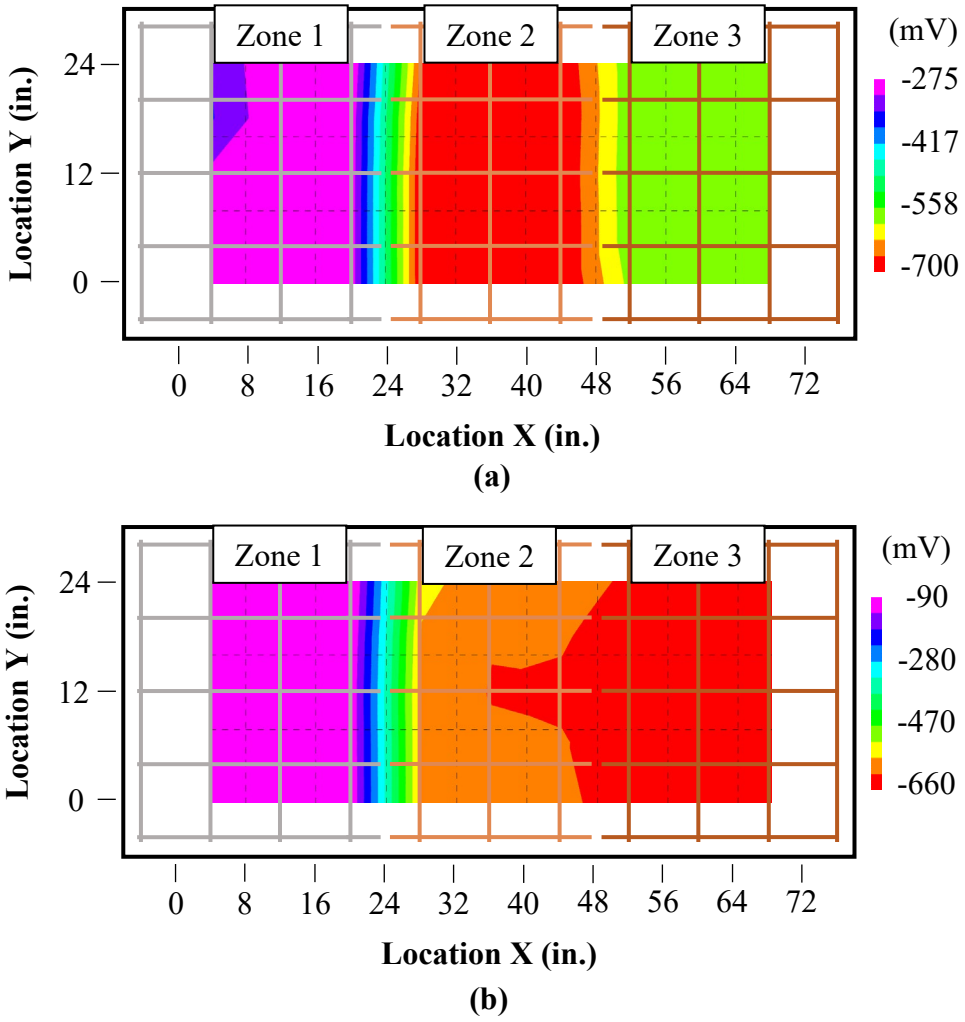

Figure 4-98: HCP Contour Plots for (a) Specimen C1 (09/19/19) and (b) Specimen C2 (10/07/19)

Similar application of the ASTM C876 (2015) thresholds to the half-cell measurements from Specimen C2, shown in Figure 4-98(b), resulted in a more useful and accurate prediction than that of Specimen C1. Since the half-cell readings in Zone 1 were greater (less negative) than -200 mV, those readings were correctly predicted to be indicative of no corrosion activity. Furthermore, since the readings from Zones 2 and 3 were less (more negative) than -350 mV, those zones were correctly predicted to contain

actively corroding embedded steel reinforcement. Thus, for Specimen C2 tested on 10/07/19 (27 days of accelerated corrosion), the ASTM C876 (2015) thresholds perfectly predicted the state of corrosion in the specimen.

To investigate how half-cell measurements for both slabs changed as the length of accelerated corrosion increased, measurements for all testing dates (listed in Table 4-6) were plotted as transformed cumulative probability distributions, as described in Section 4.4.7. The transformed cumulative probability distributions of all half-cell measurements collected during accelerated corrosion of Specimen C1 are presented in Figure 4-99. From those distributions, it was observed that three distinct groupings of corrosion activity could be identified. All three appeared fairly linear, indicating that they were all likely normally distributed. Furthermore, as the duration of accelerated corrosion increased, the three groups (corresponding to Zones 1–3) generally shifted in the negative direction. Thus, in regions of active corrosion, half-cell measurements can become increasingly negative as the concrete chloride content increases and moisture penetrates further into the cover layer.

Despite no active corrosion existing in Zone 1 (as verified by coring), the half-cell measurements still became somewhat more negative. While the magnitude of this effect might not have been as significant in Zone 1 as in the two corroded zones, it was hypothesized that the increased chloride ion and moisture contents in the cover layer of Zone 1 also caused this negative shift in potential measurements. As both the foregoing would lower the resistivity of the concrete cover layer, current could more easily be transferred between the passive reinforcement mat and reference electrode. Since it was observed that half-cell measurements can fluctuate depending on at least the moisture content and chloride ion concentration, it was expected that the use of universal thresholds

to predict corrosion may not consistently result in accurate condition assessments. Rather, the end points of linear behavior in each grouping might be more reliable thresholds delineating corrosive activity. Accordingly, the potential measurement "gaps" between groupings could be analogous to the uncertainty classification used in ASTM C876 (2015).

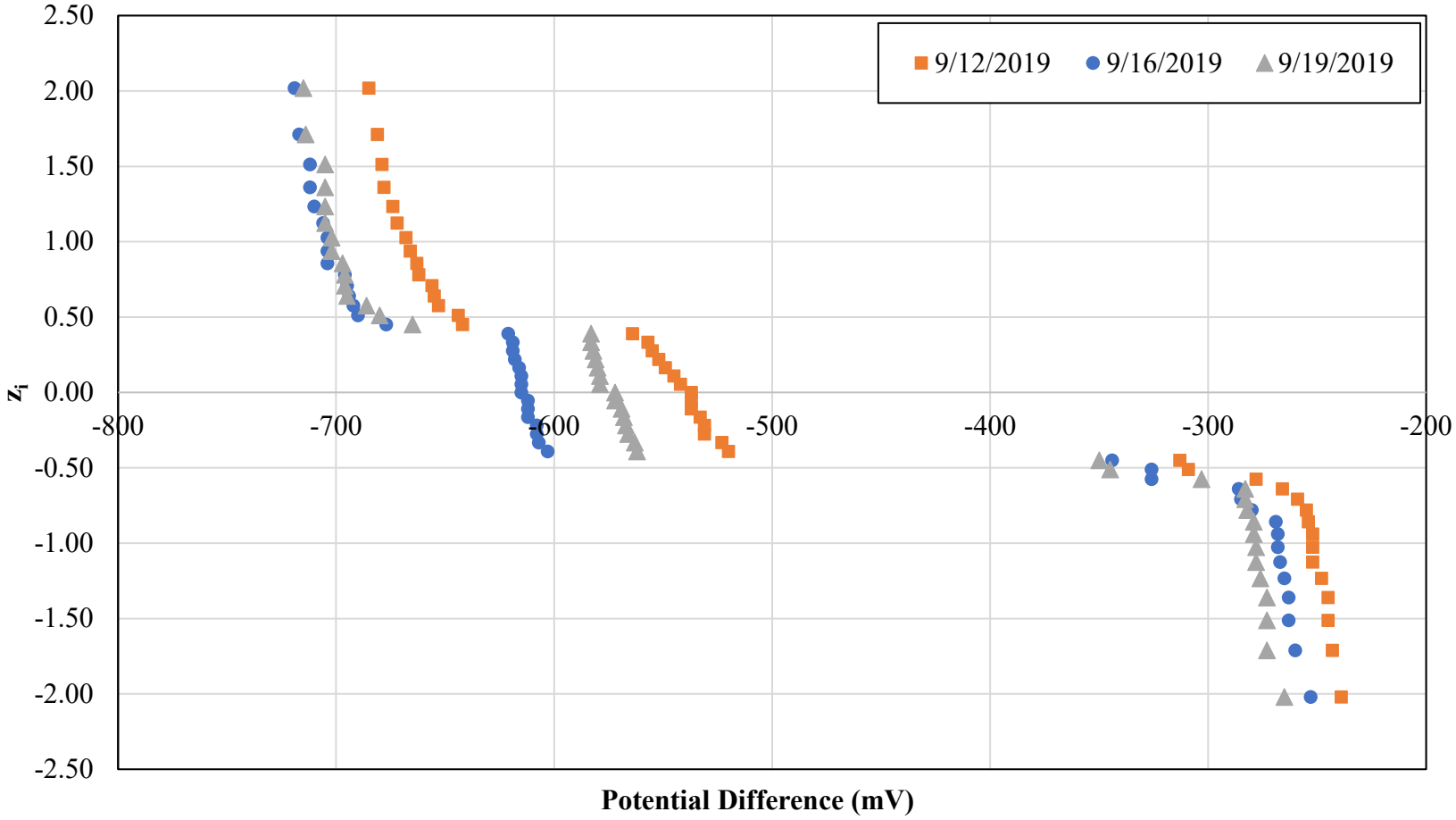

Figure 4-99: Transformed Cumulative Probability Distributions of Specimen C1 Potential Measurements during Accelerated Corrosion

Similarly, the transformed cumulative probability distributions for Specimen C2 during accelerated corrosion are presented in Figure 4-100. In Figure 4-100, two distinct groupings of corrosion activity could be observed, the more negative corresponding to active corrosion and the more positive corresponding to passive reinforcement. As in the spatial contour plot of half-cell measurements of Specimen C2 (shown in Figure 4-98), the distinction between Zones 2 and 3 measurements was not strong. Furthermore, as in Specimen C1, it was observed that the half-cell measurements shifted as the duration of accelerated corrosion increased. For the measurements indicative of active corrosion, increases in the duration of accelerated corrosion generally corresponded with more negative potential measurements. Curiously, the measurements corresponding to passive reinforcement became more positive as the duration increased, in opposition to the trend observed in cumulative probability distributions from Specimen C1. Given that only two corroded specimens were tested, it was difficult to confidently establish how exactly the duration of accelerated corrosion affected potential measurements. Nonetheless, it was clear that the length of corrosion did tangibly affect potentials corresponding to both passive and corroded portions of the deck.

Under the varying conditions, ASTM C876 (2015) correctly identified each measurement associated with active corrosion; however, for the datasets collected on 09/12/19 and 09/16/19, there existed some potentials indicative of sound reinforcement which were classified as “uncertain”. As early as 09/26/19, those same points became correctly reclassified as sound (with 90% confidence). Thus, given the variability of condition predictions that can be obtained using ASTM C876 (2015) on the same specimen

in different states, it was postulated that those universal thresholds should not be relied upon to assess the likelihood of active corrosion in reinforced concrete elements.

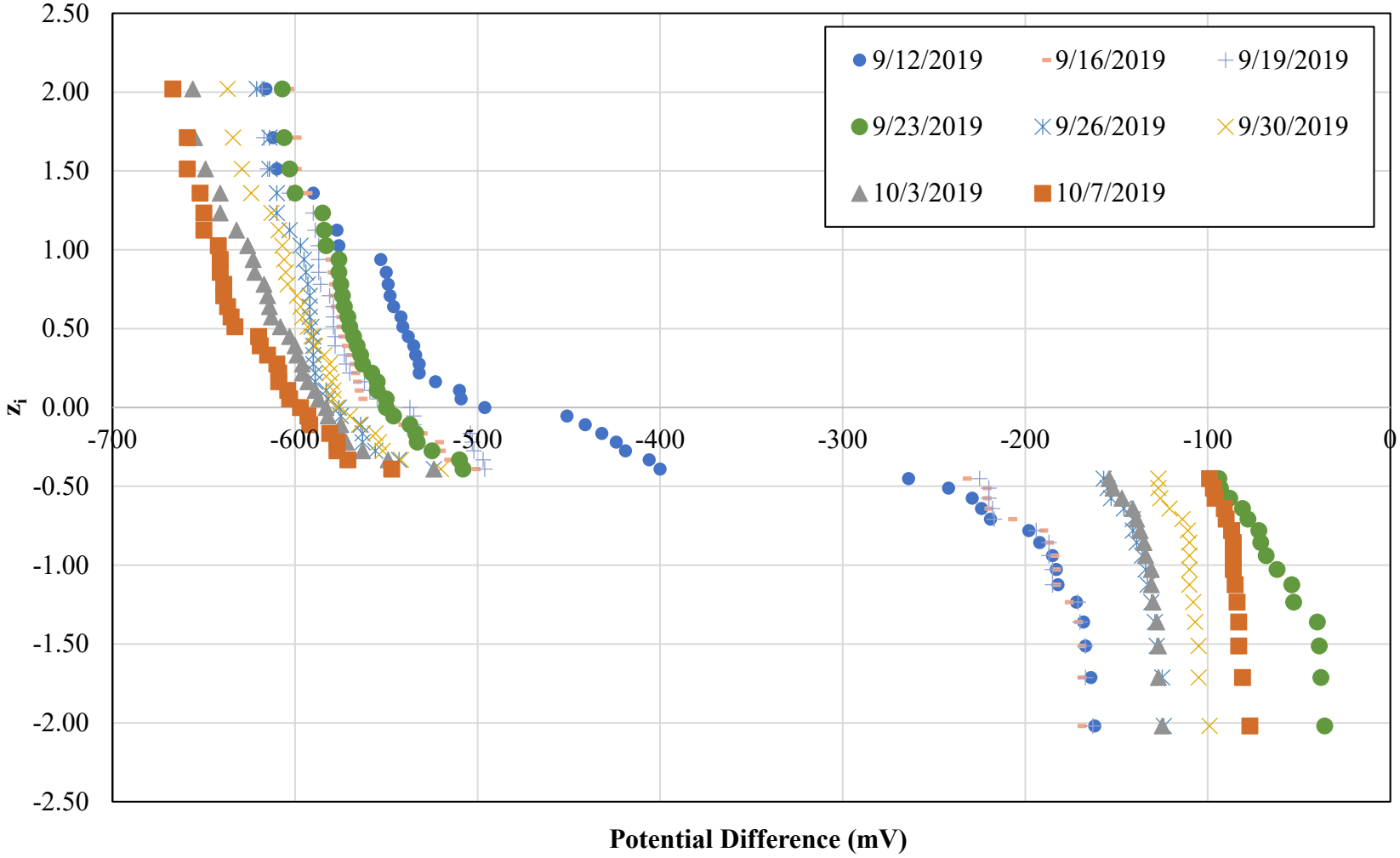

Figure 4-100: Transformed Cumulative Probability Distributions of Specimen C2 Potential Measurements during Accelerated Corrosion

Half-cell potential contour plots of Specimens C1 and C2 when tested in the moist state are presented in Figure 4-101. Comparing the moist HCP measurements from Figure 4-101(a) to the corresponding data under accelerated corrosion from Figure 4-98(a) for Specimen C1, it was observed that the range and relative distribution of potentials were fairly comparable between the two contour plots. In the moist dataset, the potentials measured in Zone 2 were still curiously more negative than those of Zone 3. Furthermore, application of the ASTM C876 (2015) thresholds resulted in Zones 2 and 3 being correctly classified as actively corroded (with 90% confidence) while a confident prediction of Zone 1 still could not be established.

However, similar comparison of the half-cell potentials for Specimen C2 from Figures 4-98(b) and 4-101(b) did not result in the same observations as those made for Specimen C1. On both the maximum and minimum extremes, half-cell potentials from the moist dataset were somewhat lower (more negative) than those from the accelerated corrosion dataset. Furthermore, the distinction between potentials from Zones 2 and 3 was significantly more pronounced for the moist dataset (approximately -220 mV) than for the accelerated corrosion dataset (approximately -50 mV). Accordingly, it was observed that moisture content can have a strong effect on the degree in which different regions of corrosion activity are distinct from one another. While application of the ASTM C876 (2015) thresholds also resulted in perfect condition assessment for Specimen C2 in the moist state, it was hypothesized that the foregoing observed influence of moisture content on half-cell potentials would affect successful threshold assessment in a variety of different specimen moisture contents.

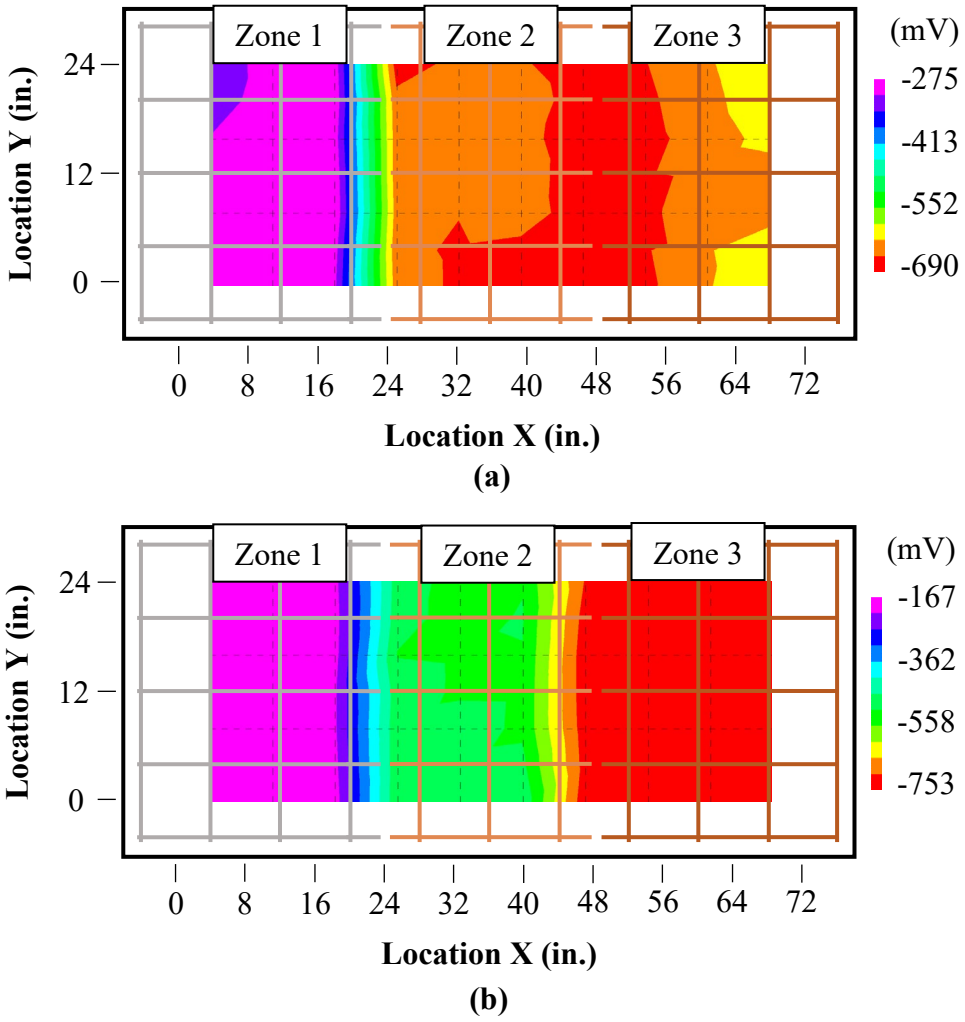

Figure 4-101: HCP Contour Plots for (a) Specimen C1 and (b) Specimen C2 in Moist States

To assist in directly testing this hypothesis, HCP contour plots of Specimens C1 and C2 in the air-dried state (with about 30 minutes of pre-moistening) are provided in Figure 4-102. Comparing the air-dried potentials of Specimen C1 from Figure 4-102(a) to the corresponding moist potentials from Figure 4-101(a), stark differences between the two datasets were observed. Chiefly, the spatial agreement of potentials within the three zones of corrosion activity was much worse in the air-dried data than in the moist data. While

the distinction between Zone 1 and 2 was clear for the moist data, it was highly obfuscated in the air-dried data as some of the most positive potentials (shown in blue and purple hues) were distributed across all three zones.

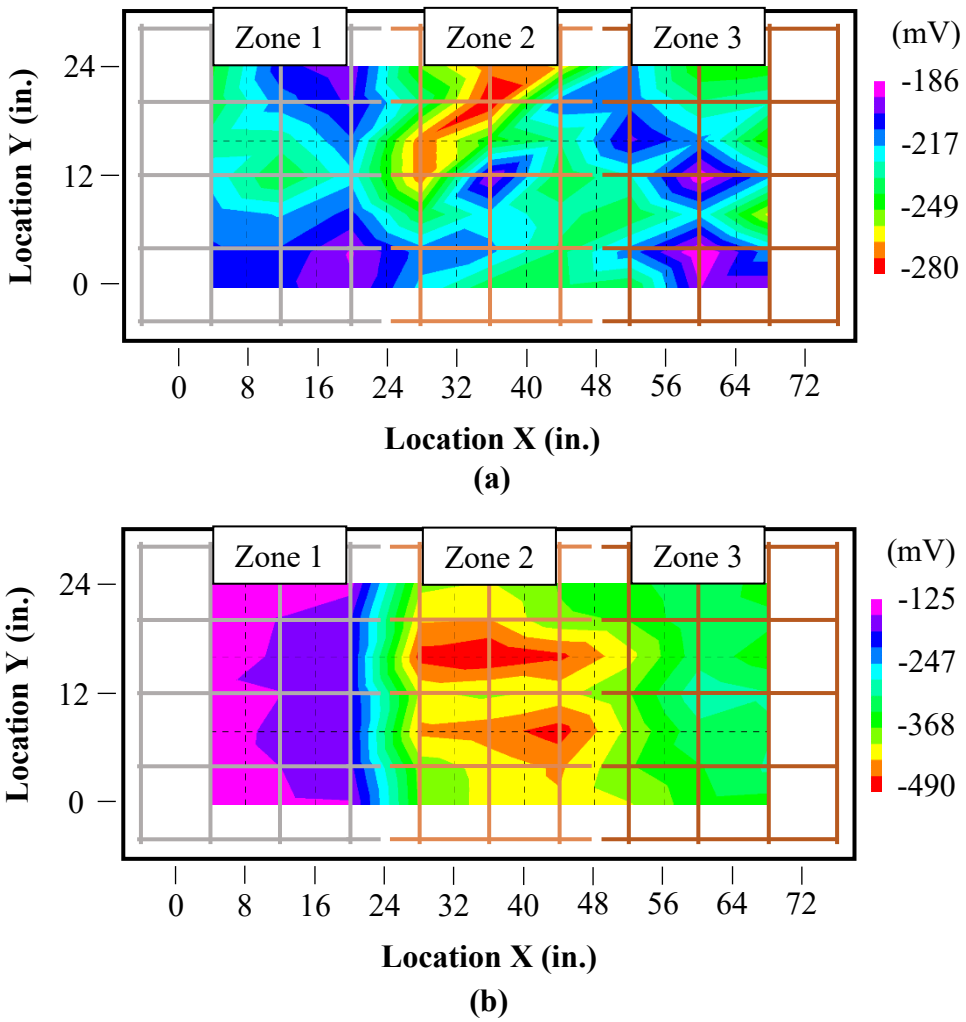

Figure 4-102: HCP Contour Plots for (a) Specimen C1 and (b) Specimen C2 in Air-dried States (30 Minutes Pre-moistening)

Additionally, the range of potentials of the air-dried data (-186 to -280 mV) was much smaller than that of the moist potentials (-275 to -690 mV). Moreover, the decrease in moisture content between the moist and air-dried potentials shifted the extreme

potentials in the positive direction. Thus, for Specimen C1, decreasing the moisture content resulted in (1) a worsening in the spatial correlation between the true specimen condition and potential measurements, (2) a much narrower range of potentials, and 3) an overall positive shift in potential measurements. Furthermore, implementation of the ASTM C876 (2015) thresholds resulted in falsely classifying the entirety of Specimen C1 as either uncorroded (90% confidence) or uncertain.

Comparing the air-dried and moist potentials for Specimen C2, shown in Figures 4-101(b) and 4-102(b) respectively, further serves to demonstrate the influence of moisture content on HCP evaluations. While the spatial agreement of air-dried/moist potentials and the true corrosion state was much stronger for Specimen C2 than C1, the range of potential measurements also became narrower when Specimen C2 was tested in the air-dried state (-125 to -490 mV) rather than the moist state (-167 to -753 mV). Moreover, the decrease in moisture content of Specimen C2 also resulted in a positive shift in potential measurements. Thus, many of the same effects of moisture content on half-cell potentials observed in Specimen C1 were also noted in Specimen C2. Implementation of the ASTM C876 (2015) thresholds resulted in several locations in Specimen C2 previously correctly identified as corroded in a moister state being classified as uncertain in the air-dried state.

Additionally, it was observed that the potentials in Zone 2 of Specimen C2 were more negative than those in Zone 3 when the specimen was tested in the air-dried state, opposite of the trend noticed in the moist data. It was hypothesized that this peculiar phenomenon was the result of (1) the differential moisture content between the two datasets and (2) the prominent presence of delaminations in Zone 3, as illustrated in Figure 4-103. Considering the case of a half-cell measurement over an air-filled delamination, the

delamination acts as a localized, highly resistive anomaly that inhibits a strong flow of current between the anode and reference electrode. Should that same delamination become water-filled, the corresponding half-cell measurement would become more negative, as current could be more easily conducted across the delamination. Accordingly, the measured potential over a water-filled delamination (e.g. -350 mV) would be more negative than that over the same delamination filled with air (e.g. -200 mV). As Zone 2 of Specimen C2 was found to be less delaminated than Zone 3 (through inspection of cores), it was hypothesized that this foregoing behavior resulted in the redistribution of most negative potentials in Specimen C2 when tested in either the moist or air-dried states. Thus, it was concluded that the presence of delaminations between the corrosion anode and reference electrode can have a varying effect on half-cell potentials, depending on the moisture state of the delamination.

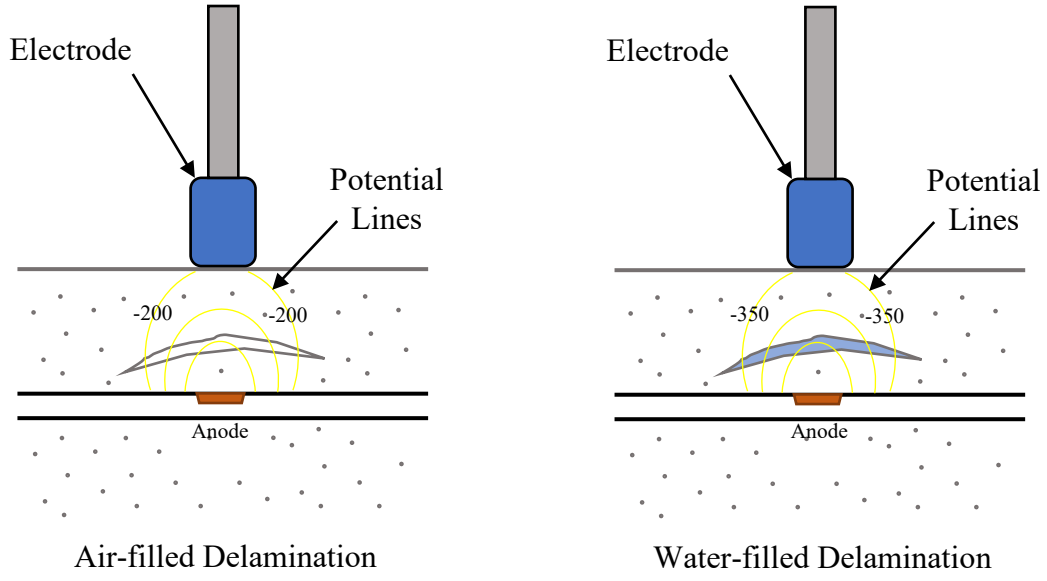

Figure 4-103: Effect of Delaminations on Half-cell Potentials in Concrete Elements of Varying Moisture Content

Falf-cell potentials collected from Specimens C1 and C2 in the air-dried state after differing lengths of pre-moistening are presented in Figures 4-104 and 4-105 respectively to investigate the influence of pre-moistening duration on half-cell potentials. From Figure 4-104, it was observed that the general shape of the potential measurements was stabilized after 12 minutes of pre-moistening. However, the additional 19 minutes of pre-moistening resulted in a fairly uniform shift in potential measurements of about -20 mV, reinforcing the influence of moisture content on potential measurements.

Similar to Specimen C1, the general shape of potential measurements of Specimen C2 stabilized after 14 minutes of pre-moistening, as evidenced in Figure 4-105. However, the effect of further pre-moistening on potential measurements was not as uniform in Specimen C2 as in C1. In Specimen C2, the additional 16 minutes of pre-moistening generally resulted in a -10 to -20 mV shift in measurements. Nonetheless, in both specimens, it was further concluded that (1) moisture content can have a significant effect on potential measurements and (2) after approximately 15 minutes of pre-moistening, the general shape of potentials should be fairly stabilized. This latter conclusion is consistent with guidance published by Proceq (2017) recommending that concrete surfaces be pre-moistened between 10 and 20 minutes before taking measurements.

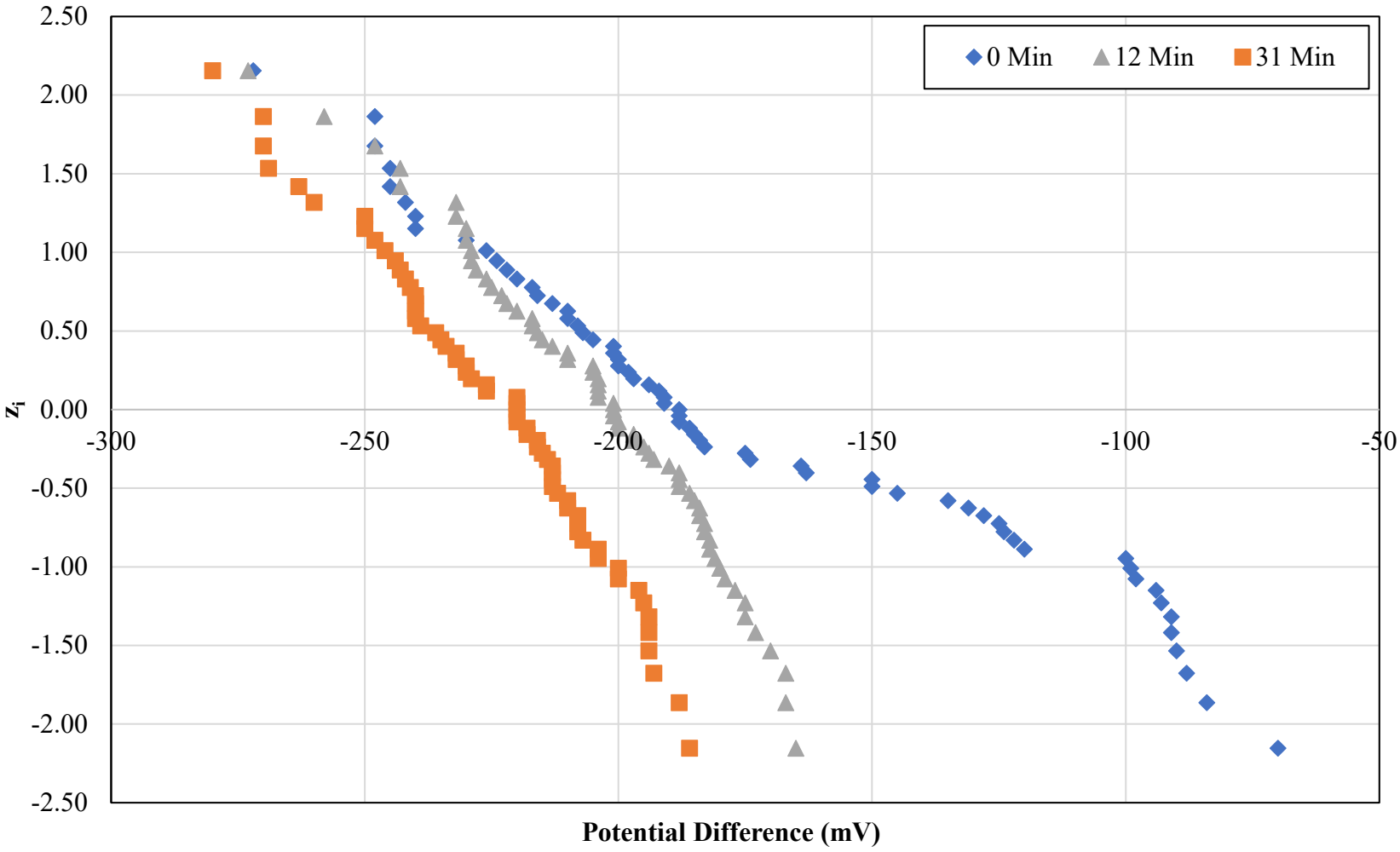

Figure 4-104: Air-dried HCP Measurements for Specimen C1 after Various Pre-moistening Durations

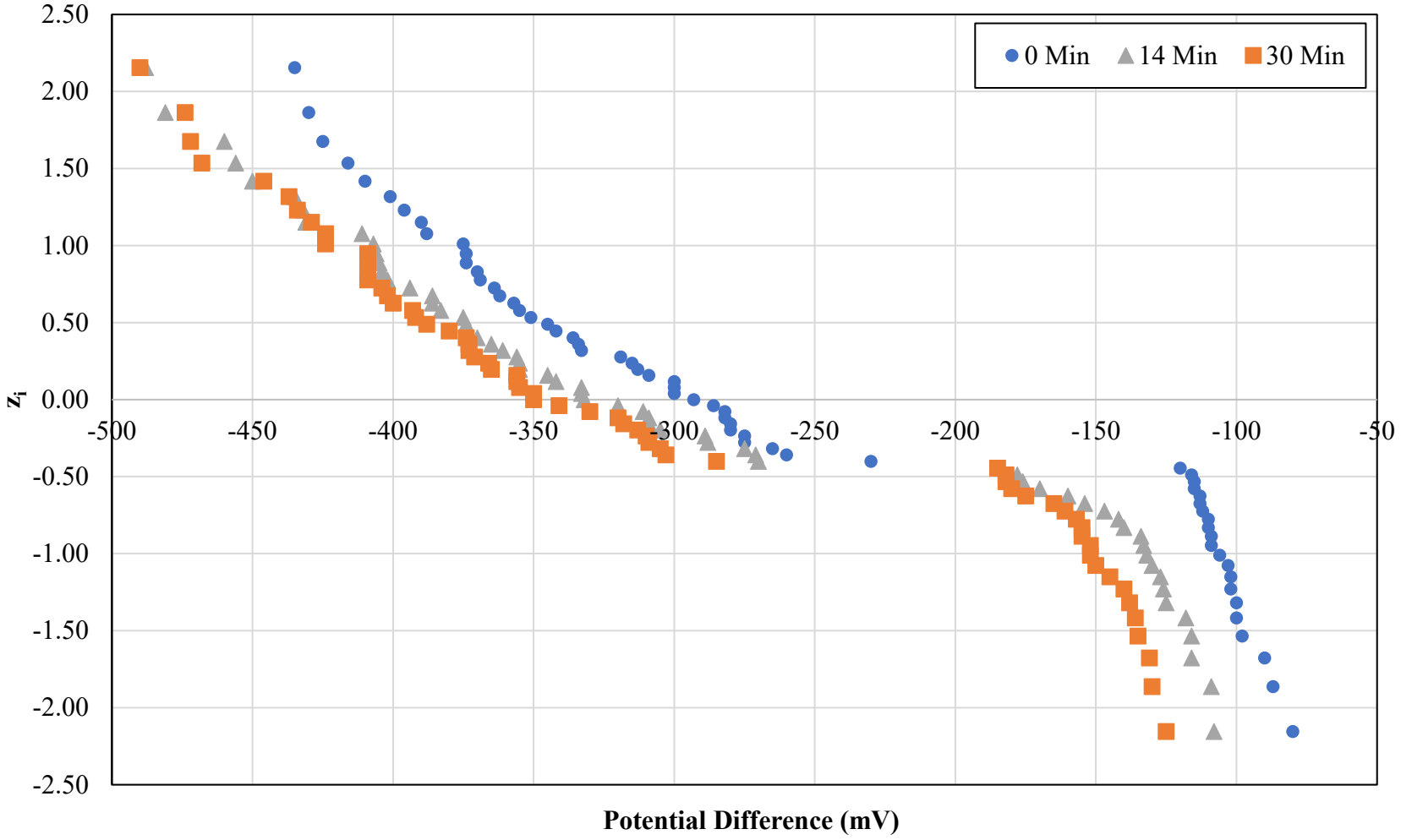

Figure 4-105: Air-dried HCP Measurements for Specimen C2 after Various Pre-moistening Durations

Considering the foregoing presented data, it was consistently observed that moisture content can have a significant effect on half-cell potential measurements such that application of the ASTM C876 (2015) thresholds may (1) not consistently produce accurate condition assessments of reinforced concrete bridge decks and (2) result in varying predictions as environmental conditions such as moisture content fluctuate. To overcome these weaknesses of relying on universal thresholds for condition assessment, a statistical method aimed at selecting corrosion thresholds unique to a given HCP dataset is described and tested in the next section of this document.

4.5.9 Segmented Linear Regression to Process HCP Data

Inspired by the flaws inherent in using universal thresholds to predict the state of corrosion of a bridge deck, segmented linear regression analysis was investigated as an alternative method of post-processing HCP data. Segmented linear regression analysis is implemented when it is suspected that the dependent variable, y, is characterized by two or more linear response functions of the independent variable, x, over different intervals rather than one unique linear function. As can be observed in Figure 4-106, the "segments" over which distinct linear functions best fit the recorded data meet at "breakpoints" where the governing response function, $y(x)$, abruptly changes.

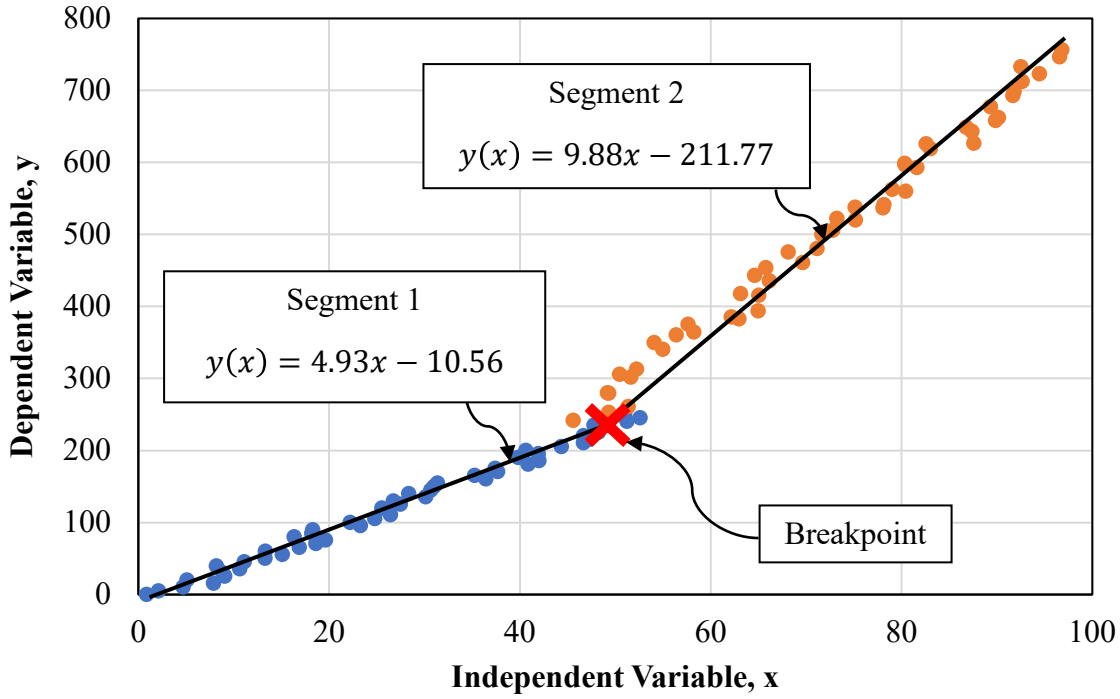

Figure 4-106: Segmented Linear Regression for Two Linear Response Functions

The breakpoint is of principal importance in segmented linear regression as it can be quite useful in decision making. Concerning HCP data presented in a transformed cumulative probability distribution, a breakpoint can be analogous to a threshold potential separating potential measurements respectively indicative of two different corrosion activities (e.g. corroded and passive reinforcement). Many different approaches have been developed to accurately estimate the breakpoint, a few of which were compiled in the following list by Muggeo (2003):

1. Methods that separately approximate breakpoints. For a fixed breakpoint, the breakpoint has been determined through inspection of scatter smooth plots (Kunst et al. 1993, Vermont et al. 1991) or through an exact or grid-search type algorithm (Ertel and Fowlkes 1976; Stasinopoulos and Rigby 1992; Ulm 1991,);

2. Methods that use a continuous, differentiable function over the range of the independent variable to approximate the various segmented relationships between the dependent and independent variables (Bacon and Watts 1976; Tishler and Zang 1981,);
3. Bayesian Markov Chain Monte Carlo methods that may be computationally expensive (Gössl and Küchenhoff. 2001).

In lieu of the foregoing methods which Muggeo (2003) believed most to be inappropriate, he proposed an algorithm for detecting breakpoints involving using an initial guess for a breakpoint location. That guess is iteratively updated using maximum likelihood estimation until the algorithm converges upon a solution for the breakpoint. That algorithm is available for free use as a downloadable package *segmented* to the statistical analysis environment, R, and was updated in 2017 to include a smoothed score-based approach for computing a confidence interval for a given breakpoint (Muggeo 2017).

Considering its use in analysis of HCP data, the foregoing segmented linear regression approach was expected to be most useful when groups of corrosion activity were not easily discernable when data was presented on cumulative frequency distributions (such as in Figure 4-104). Moreover, there would be no need to conduct this analysis if groups of corrosion activity could easily be distinguished from one another (such as in Figure 4-99). One possible scenario in which this method could be advantageously implemented could be when the HCP method is applied in regions of low ambient relative humidity.

To evaluate the effectiveness of the Muggeo (2017) algorithm in discerning between passive and corroding portions of a bridge deck, both ROC analysis and the *segmented* R package were used to analyze Specimen C1 air-dried datasets collected after 12 and 31 minutes of pre-moistening respectively (from Figure 4-104). ROC analysis was used to determine the "best case" accuracy of interpreting half-cell potentials to classify the specimen condition, providing a benchmark from which to compare the effectiveness of the segmented linear regression approach. For the ROC analysis, Zones 2 and 3 were classified as defective, and Zone 1 was classified as sound. To evaluate the sensitivity of the *segmented* package to the required breakpoint guess, the initial guess was iteratively changed to define the bounds of initial guesses that would converge to the optimal breakpoint location. A high range of such guesses would be more forgiving to a "bad guess" that might preclude effective implementation of this method in the field. Within this range, the breakpoint which the algorithm converged upon was used as a predictor of the specimen condition, and the corresponding accuracy was calculated (as one would in ROC analysis).

The results of ROC and segmented linear regression analyses of the two foregoing datasets are presented in Table 4-19. For each breakpoint identified through regression analysis, the corresponding accuracy and standard error are provided. The extreme bounds of guesses that converged to that breakpoint were not presented because, for both datasets, every guess admitted by the algorithm resulted in the breakpoint presented in Table 4-19 being reached. This result was an excellent indication of the low sensitivity to initial guesses this algorithm exhibits when attempting to locate the true breakpoint for this application.

Table 4-19: Results of ROC and Segmented Linear Regression Analyses in Correctly Classifying Air-Dried Specimen C1 Condition

Dataset ID	ROC Analysis		Segmented Linear Regression Analysis		
	Threshold (mV)	Accuracy (%)	Threshold (mV)	Accuracy (%)	Standard Error (mV)
C1 12 Mins	-183	84.1	-188	82.5	1.21
C1 31 Mins	-211	73.0	-219	65.1	2.04

Furthermore, the extremely low standard error (1.21 and 2.04 mV) of the respective breakpoints of the two datasets elicited a high sense of confidence in the breakpoint output by the algorithm. From Table 4-19, it was observed that, even when testing Specimen C1 in an air-dried state, the HCP method could still be used to discern between passive and actively corroding reinforcement with 73.0–84.1% accuracy, per ROC analysis. While these accuracy rates were not as compelling as those from the moist specimens, they did indicate that the HCP method may still be a viable method for testing elements in a somewhat dry state. Moreover, the difference between the breakpoint threshold identified using the *segmented* package and ROC analysis was only 5–8 mV. This result indicated excellent applicability of the segmented linear regression approach when the bounds of two groups of corrosive activity were not easily distinguishable from one another. To this point, the differences in prediction accuracy of the thresholds from ROC analysis and segmented linear regression were between 1.6–7.9 percentage points.

4.5.10 Presentation and Analysis of ER Data

As with the half-cell potential data, electrical resistivity measurements are presented either as spatial contour plots or cumulative frequency distributions. Such contour plots for

Specimens C1 and C2 collected on 09/19/19 and 10/07/19 respectively are shown in Figure 4-107.

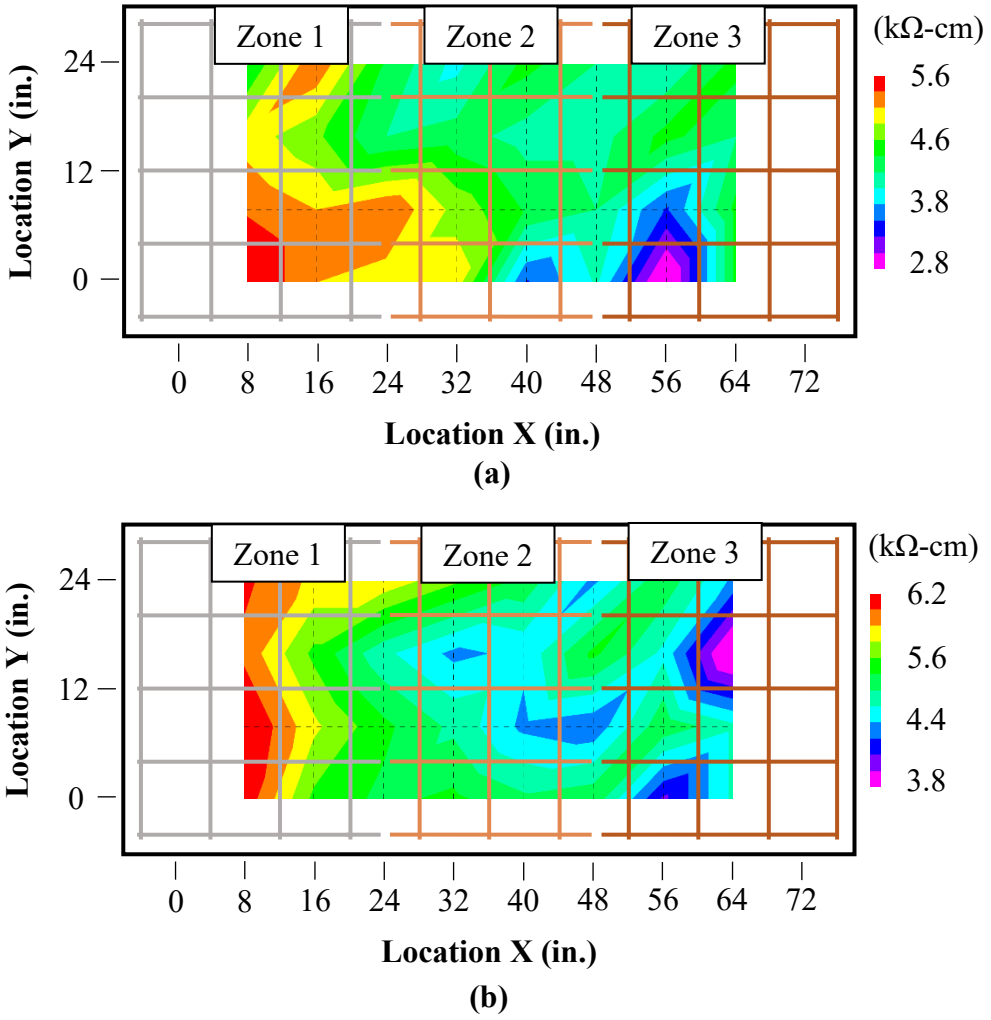

Figure 4-107: ER Contour Plots for (a) Specimen C1 (09/19/19) and (b) Specimen C2 (10/07/19)

Comparing the ER data from Figure 4-107 to the corresponding HCP measurements collected on the same dates (Figure 4-98), it was observed that the distinction between differing zones of corrosive activity was not nearly as strong in the ER plots as in the HCP plots. This observation served to reinforce the notion from literature

that electrical resistivity measurements do not predict active corrosion; rather, they can indicate the risk or rate of corrosion. While, for both datasets, there seemingly exists a trend of decreasing resistivity measurements from Zone 1 to Zone 3, the general difference in measurements between zones (1 to 2 kΩ-cm) did not seem substantially consequential relative to the various resistivity criteria presented in Chapter 3 of this document.

Nonetheless, this trend was hypothesized to be the result of differential chloride ion concentration in the pore networks of Zones 1–3. In each specimen, no current was applied to Zone 1, current was applied to Zone 2, and current was applied to Zone 3 for twice the duration of that from Zone 2. Accordingly, the varying lengths of applied current among the three zones resulted in different quantities of ponded chloride ions being pulled into the respective zones, thus causing the chloride ion concentration to be smallest in Zone 1 and largest in Zone 3. By considering ER data from a day in which equal quantities of current had been applied to both Zones 2 and 3, e.g. Specimen C2 09/12/19, this hypothesis could be verified. That corresponding contour plot, shown in Figure 4-108, revealed that the relative magnitudes of resistivity measurements from Zones 2 and 3 were generally distinct from Zone 1, but practically the same with respect to one another. Since, at this testing date, Zones 2 and 3 had experienced the same length of impressed current, their resistivity profiles were quite similar; thus validating the hypothesis that, the higher the chloride ion concentration of the pore solution, the lower the measured resistivity.

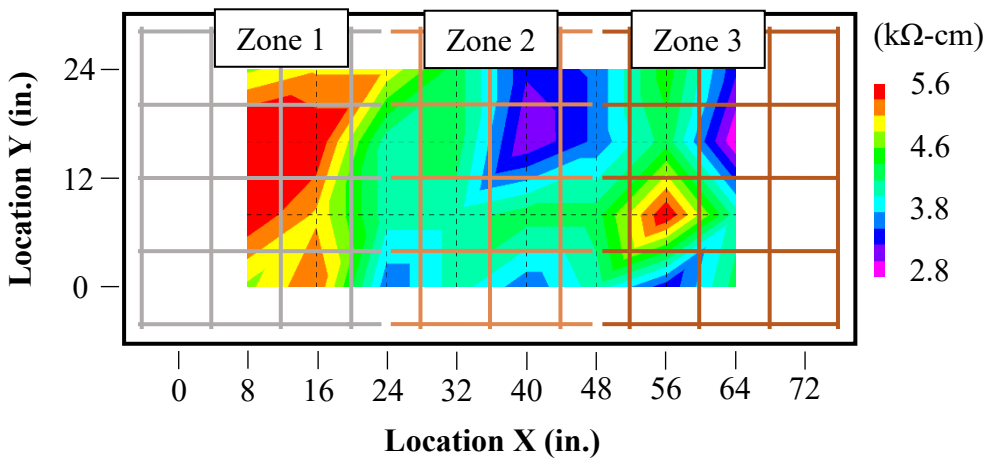

Figure 4-108: ER Contour Plot for Specimen C2 (09/12/19)

To investigate how electrical resistivity measurements changed when the length of accelerated corrosion measures increased, cumulative frequency distributions of all resistivity datasets collected during accelerated corrosion of Specimen C1 are presented in Figure 4-109. As can be observed from Figure 4-109, the relative shape of the four ER datasets are fairly consistent, indicating good repeatability of the NDT method. No significant differences were noticed among the four datasets. Nonetheless, as the length of accelerated corrosion increased, the resistivity measurements appeared to increase slightly (roughly about 0.5 kΩ-cm increase). It is hypothesized that this slight increase was caused by microstructure densification beyond initial curing, facilitated by the constantly supplied moisture to the specimen surface.

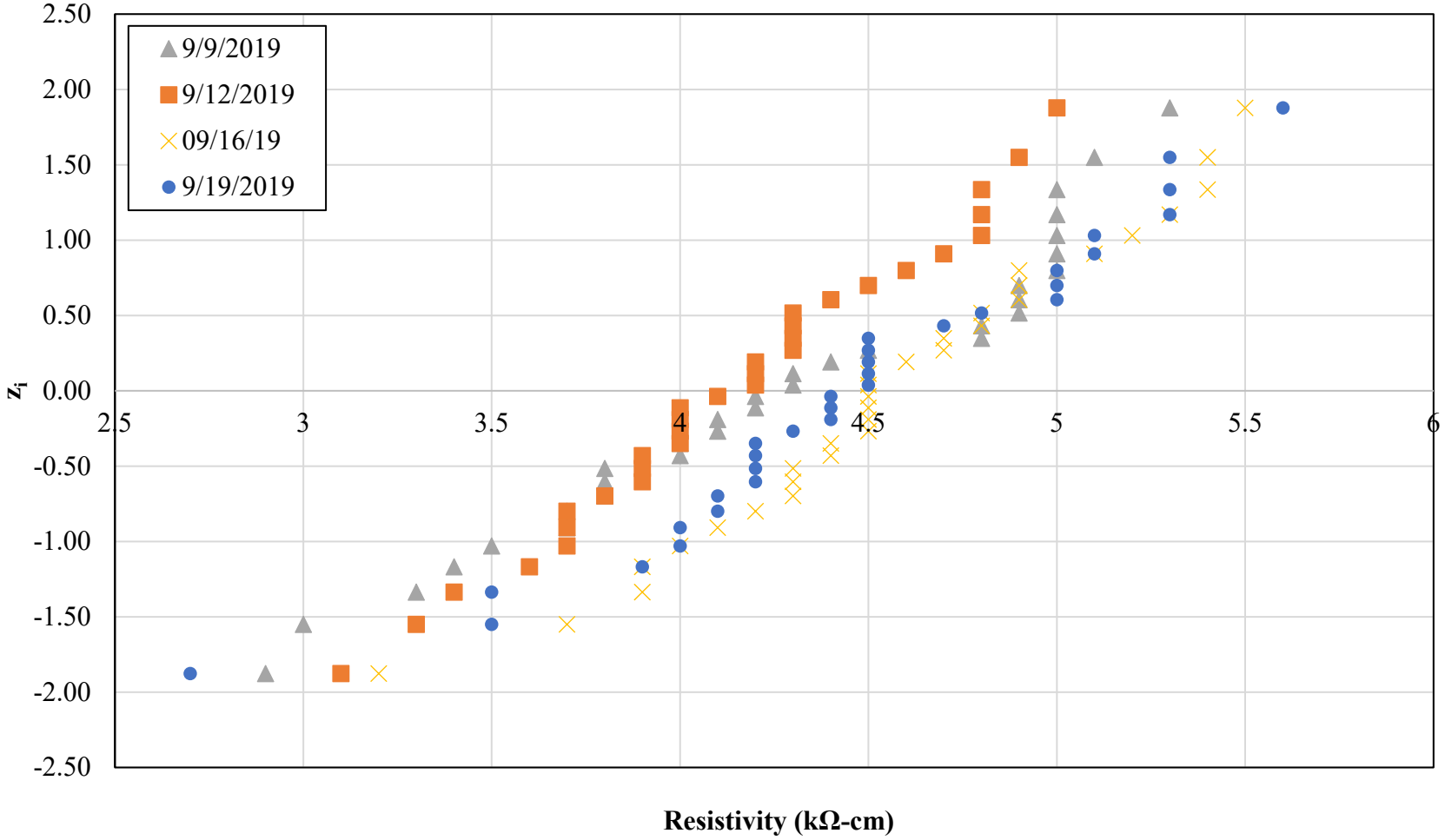

Figure 4-109: Transformed Cumulative Probability Distributions of Specimen C2 Resistivity Measurements during Accelerated Corrosion

Considering the appropriateness of the corrosion rate criteria proposed by Broomfield and Millard (2002) most resistivity measurements from Zones 2 and 3 were classified as having a very high rate of corrosion (<5 kΩ-cm) while most measurements from Zone 1 were classified as having a high rate of corrosion (5–10 kΩ-cm). Knowing that Zones 2 and 3 were actively corroding while Zone 1 was not, the foregoing criteria were likely an excellent indicator of the corrosion rate of embedded reinforcement in Zones 2 and 3. While the resistivity measurements from Zone 1 might suggest a high rate of corrosion, it is important to remember that the criteria proposed by Broomfield and Millard (2002) are only applicable after depassivation of the embedded steel reinforcement. As the reinforcement in Zone 1 was not depassivated, implementation of the Broomfield and Millard (2002) criteria without first verifying that the reinforcement was actively corroding (e.g. via the HCP method) would have falsely led to the conclusion that the Zone 1 reinforcement was corroding at a high rate. Accordingly, rather than being an indication of the rate of corrosion, the resistivity measurements from Zone 1 were representative of the risk of corrosion in that area. Filled with external chloride ions and moisture, the pore solution of Zone 1 presented an environment conducive to corrosive activity. In this regard, resistivity measurements conducted in areas of passive reinforcement may be good indicators of the risk of chloride-induced corrosive activity in the future.

Similarly, the cumulative frequency distributions of ER measurements collected from Specimen C2 during accelerated corrosion are shown in Figure 4-110. As in Specimen C1, it was observed that the relative shapes of the resistivity profiles were largely the same, despite being shifted, except for the 09/09/2019 dataset. It was hypothesized that this dataset exhibited a somewhat different distribution of low resistivities because the data were

collected early in the accelerated corrosion process and the chloride ion profile of Zones 2 and 3 were rapidly changing (thus resulting in the observed greater variance in low resistivities). Furthermore, the Specimen C2 resistivity values also shifted positively somewhat during accelerated corrosion; this was also hypothesized to be the result of microstructure densification. Nonetheless, this shift was generally small (about 0.5 kΩ-cmincrease) and not terribly consequential when interpreting the resistivity measurements using the Broomfield and Millard (2002) criteria. Moreover, in agreeance with the conclusions developed from Specimen C1 resistivity measurements, it was observed that the Broomfield and Millard (2002) criteria appeared to accurately predict the corrosion rate of Zones 2 and 3. However, for the reasons mentioned previously, their implementation for Zone 1 was not appropriate, as the embedded reinforcement in that area was still passive. Yet, the low resistivities in Zone 1 from Specimen C2 were indicative of the high risk of chloride-induced corrosion.

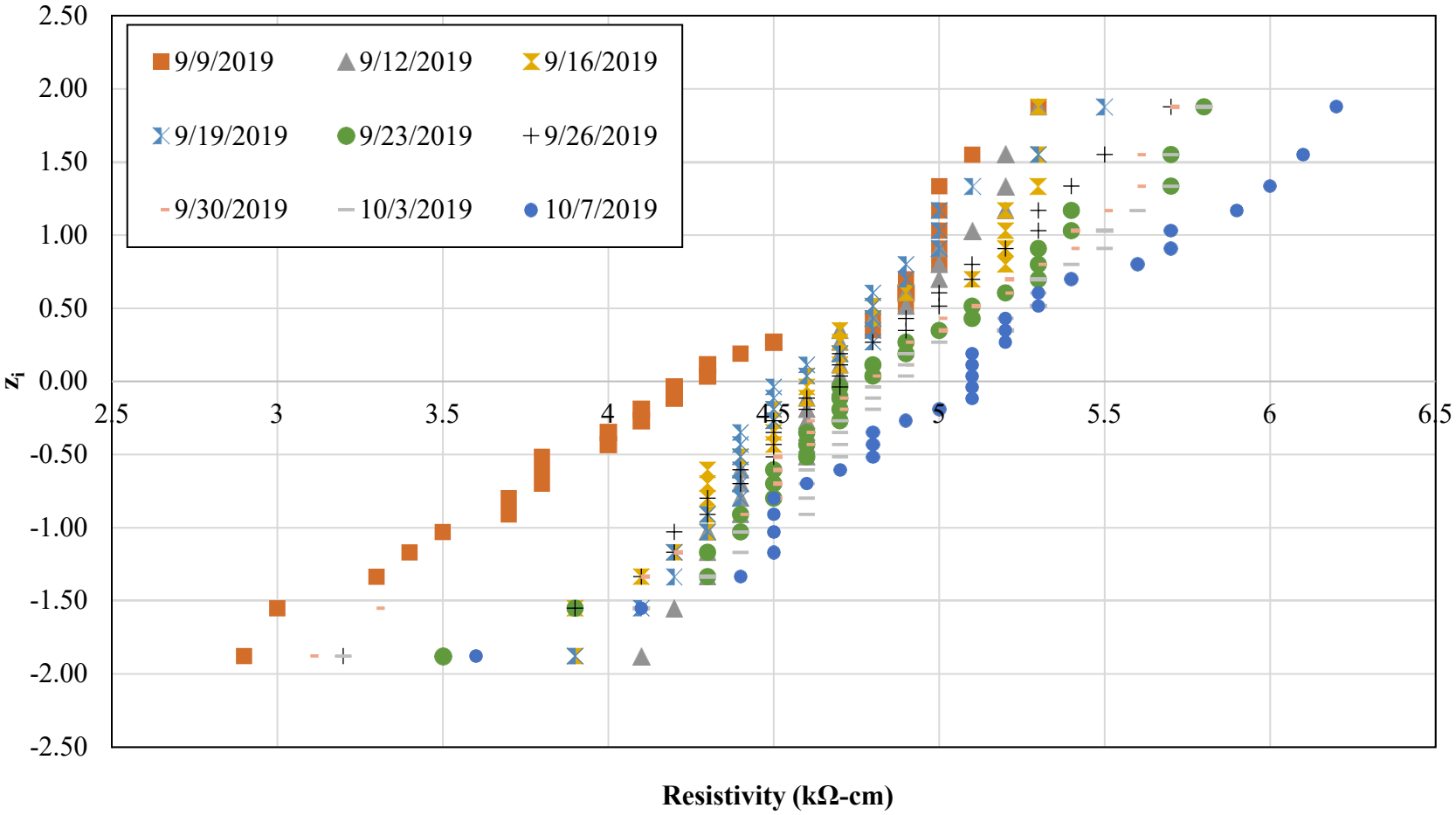

Figure 4-110: Transformed Cumulative Probability Distributions of Specimen C2 Resistivity Measurements during Accelerated Corrosion

To investigate the influence of moisture content and time on resistivity measurements, the cumulative frequency distributions of the moist data, air-dried data, and last accelerated corrosion (A.C.) data for each specimen are presented in Figure 4-111. Comparing the three resistivity profiles from Specimen C1 to those from Specimen C2, it was observed that corresponding pairs (e.g. C1 Dry 09/28/20 and C2 Dry 09/28/20) had very similar distributions in both magnitude and variance. This was likely an indicator that the effort to create similar corrosive environments in Specimens C1 and C2 through different lengths of impressed current was successful. Furthermore, it was observed that, for each specimen, the resistivities measured during accelerated corrosion measures were the lowest, those measured from the air-dried specimens were the largest, and those measured from the moist specimens were in between the two aforementioned groups. It was initially perplexing that the resistivities measured during accelerated corrosion were lower than those of the moist specimens, since the two datasets were expected to have been collected in similar specimen moisture contents. Since approximately nine months passed between collecting the resistivity measurements during accelerated corrosion and collecting them in the specimen moist states, it was hypothesized that the resistivities from the moist dataset were larger because of significant chloride-ion diffusion that occurred during those nine months. While the cover layer chloride concentration was likely very high during accelerated corrosion since it was being constantly supplied with water-soluble chloride ions, once ponding was ceased, the chloride ions in the pore solution likely began diffusing to other portions of the two specimens. Accordingly, when resistivity measurements were performed on 05/20/20, the lower ionic concentration in the pore solution reduced the concrete conductivity, thus increasing its resistivity.

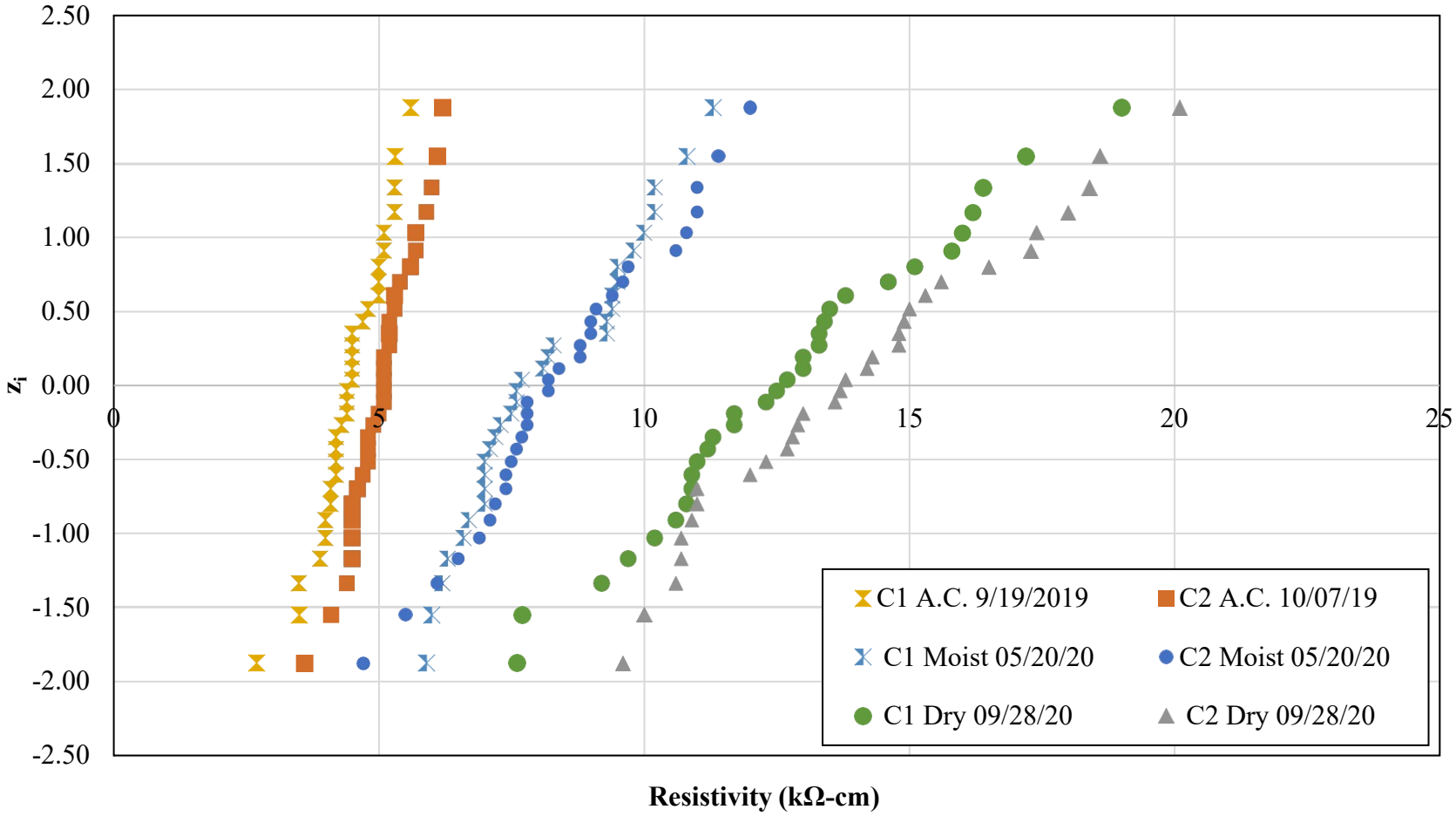

Figure 4-111: Transformed Cumulative Probability Distributions of Specimens C1 and C2 Resistivity Measurements for Different Moisture Contents and Times

Moreover, the resistivity distribution observed during testing of the air-dried specimens was greater than either of the other two distributions, largely because of the decreased moisture content in the pore network. Applying the Broomfield and Millard (2002) criteria to the air-dried distribution would result in most of the Zone 2 and 3 locations being classified as experiencing a low-to-moderate rate of corrosion, rather than the high to very high corrosion rate indicated from the moist and accelerated corrosion distributions. These results were consistent with the hypothesis that a concrete with a low moisture content does not conduct current to the same magnitude as a concrete with a higher moisture content. Nonetheless, the observed influence of moisture content on resistivity measurements introduced a flaw in using interpretation criteria such as that proposed by Broomfield and Miller (2002) in assessing the rate of corrosion on a bridge deck. A location on a bridge deck classified as having a high rate of corrosion could be classified on a different day as having a low-to moderate rate of corrosion if the deck dries out substantially. Thus, it may be best to perform resistivity measurements on a day in which an average, representative moisture content for the bridge deck exists to develop a sense of the distribution of average corrosion rates throughout the year.

Additionally, it was observed that the variance of resistivity measurements was smallest for the accelerated corrosion dataset, largest for the air-dried dataset, and the variance of the moist dataset was in between the other two. As the principal difference in specimen condition between the accelerated corrosion dataset and the moist dataset was believed to be chloride ion concentration in the pore solution, it was hypothesized that resistivity measurements are more sensitive and variable to lower chloride ion concentrations in the pore solution. Furthermore, as the chief difference between the moist

and air-dried datasets was the specimen moisture content, it was also hypothesized that resistivity measurements are more sensitive and variable to lower moisture contents in the pore network.

4.1.1 Presentation and Analysis of IRT Data

Despite using two different infrared cameras and scanning multiple specimens, simulated defects could not be discerned from sound concrete using infrared thermography. Nonetheless, thermal images from each camera are provided for several specimens to demonstrate the testing results.

A progression of thermal images of Specimen DL5 (shallow delaminations of varying areal extent) captured after different lengths of exposure to sunlight is shown in Figure 4-112. The images are focused over the west end of the specimen in which the large 6 in. by 12 in. shallow delamination was simulated. From Figure 4-112, it was observed that no evident surface heating anomaly was located over the aforementioned delamination.

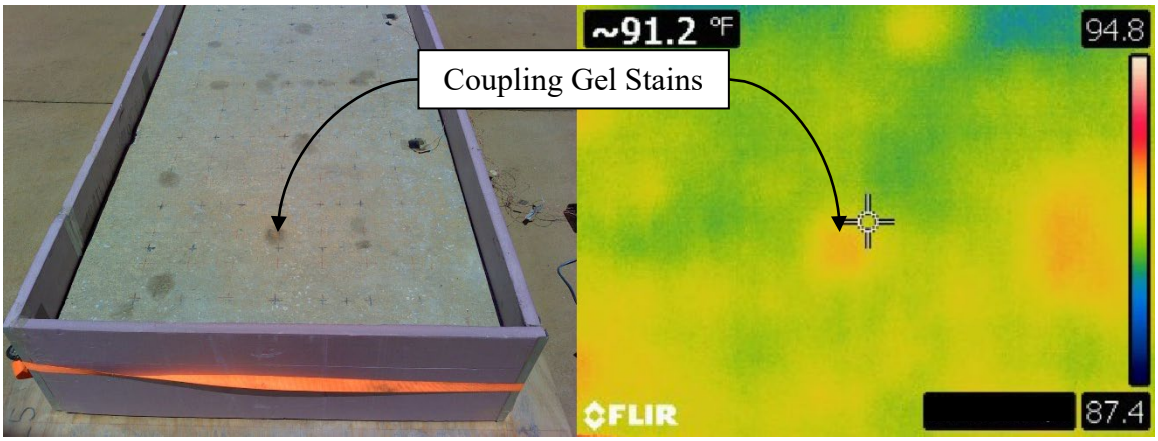

(a) 15 Min. Exposure

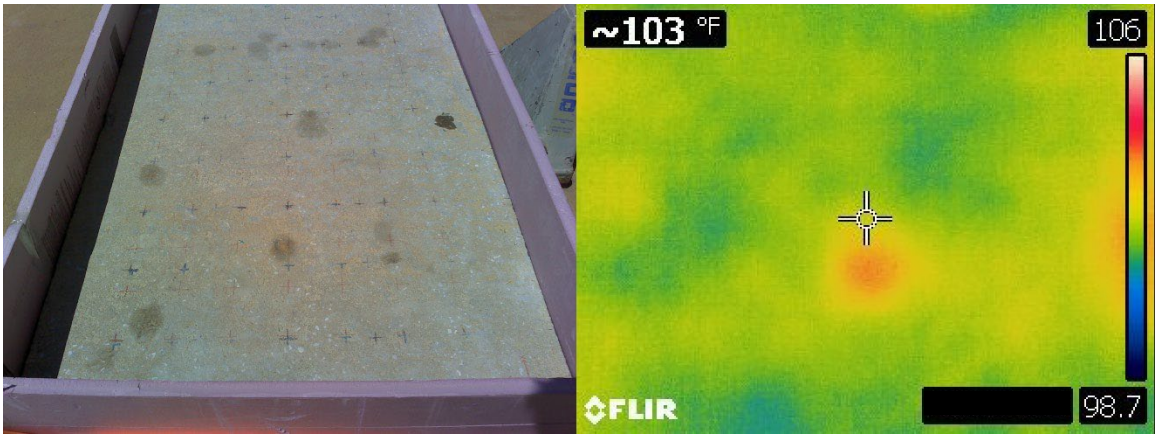

(b) 90 Min. Exposure

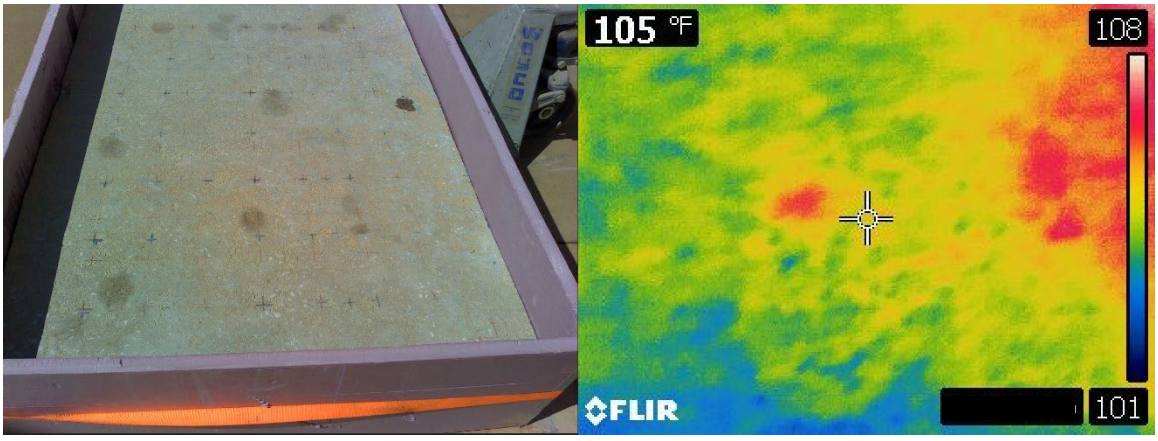

(c) 170 Min. Exposure

Figure 4-112: FLIR Images of Specimen DL5 After (a) 15 Min., (b) 90 Min., and (c) 170 Min. of Sun Exposure

As early as in the first image recorded 15 minutes after the specimen was exposed to direct sunlight, “hot spots” could be observed over darkened stains on Specimen DL5 where coupling gel had been used to ensure good contact between heat flux sensors and the concrete surface. These hot spots remained in the FLIR images throughout the entire test period. Moreover, from Figure 4-112, it was observed that the south edge of the specimen became relatively hot with respect to the rest of the concrete surface. Accordingly, one possible explanation for the inability to detect the shallow delaminations using IRT was that the test specimens were too small to preclude edge effects from obfuscating surface temperature anomalies caused by the delaminations. One other hypothesis was that the delaminations, which were placed 2-5/8 in. below the surface, were too deep to be detected using IRT. Nonetheless, from these FLIR images, it was concluded that surface discolorations can change the local changes in the concrete emissivity which can lead to differentials in surface temperature.

A thermal scan of Specimen DL5 acquired using the MOBA thermal camera is shown in Figure 4-113 to further investigate whether infrared thermography could be used to detect the simulated shallow delaminations. Note that the surface temperature had decreased substantially as time had progressed to later in the afternoon of the same day FLIR images were obtained. Nonetheless, there still existed significant surface temperature differentials that theoretically corresponded to either differential surface emissivity or internal defects. While some of the observed hot spots at least partially coincided with the locations of the shallow delaminations, much of the area of hot spots was located over portions of the specimen known to be sound. Even though some portions of those hot spots might have been attributed to the surface staining caused by the coupling

gel, the area of those stains was not large enough to explain the majority of thermal differential anomalies. Accordingly, between the two cameras, there did not exist sufficient evidence to demonstrate that IRT could detect the embedded shallow delaminations.

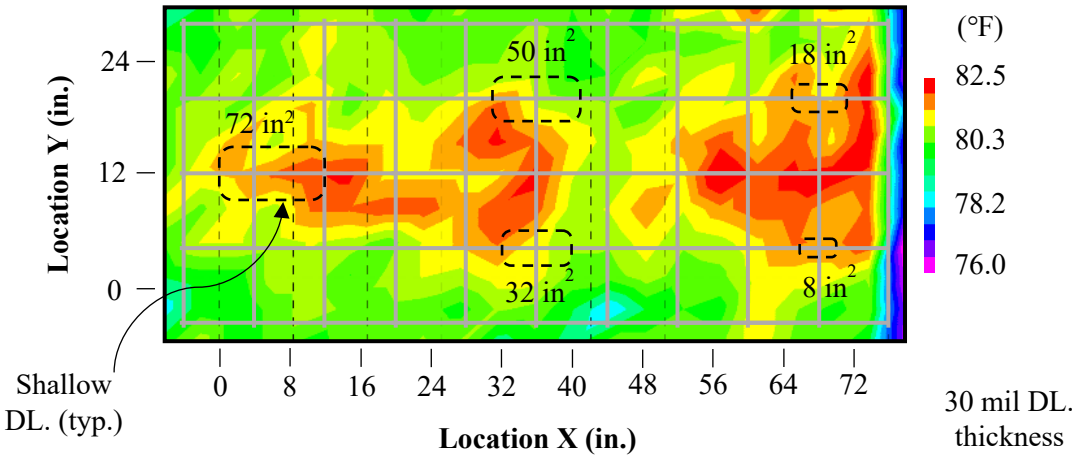

Figure 4-113: MOBA IRT Scan of Specimen DL5 After 290 Min. of Sun Exposure

Surface temperatures were measured after varying lengths of sun exposure to Specimen C2 with the FLIR camera to further assess the capabilities of infrared thermography in nondestructive evaluations. Through destructive core testing, it was observed that substantial delaminations existed in Zone 3 (the east end) of Specimen C2. Accordingly, thermal images of the east end are provided in Figure 4-114 to assess whether the shallow delaminations could be imaged using IRT.

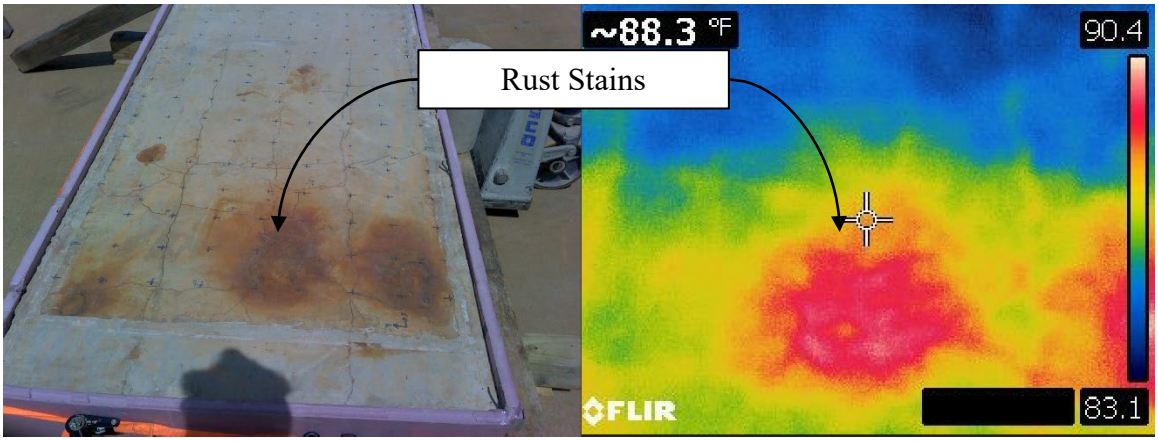

(a) 20 Min. Exposure

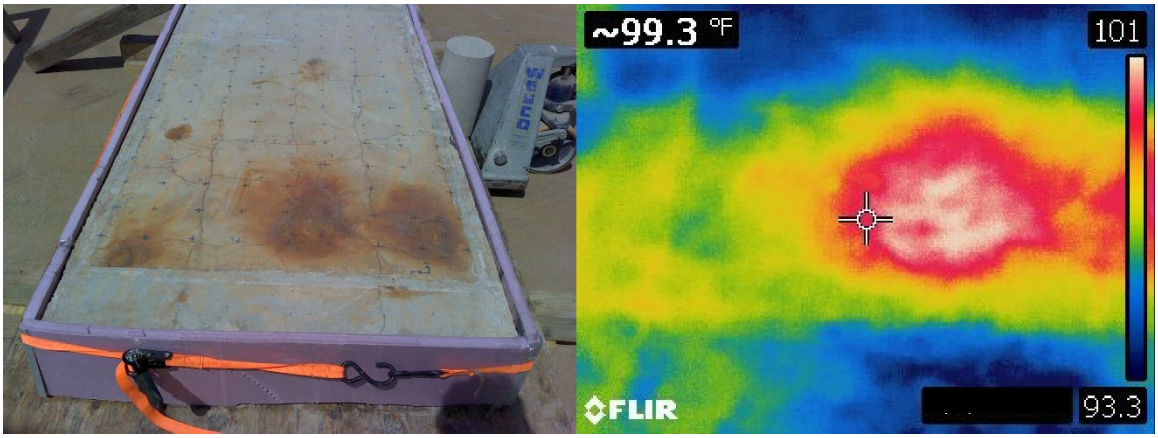

(b) 100 Min.

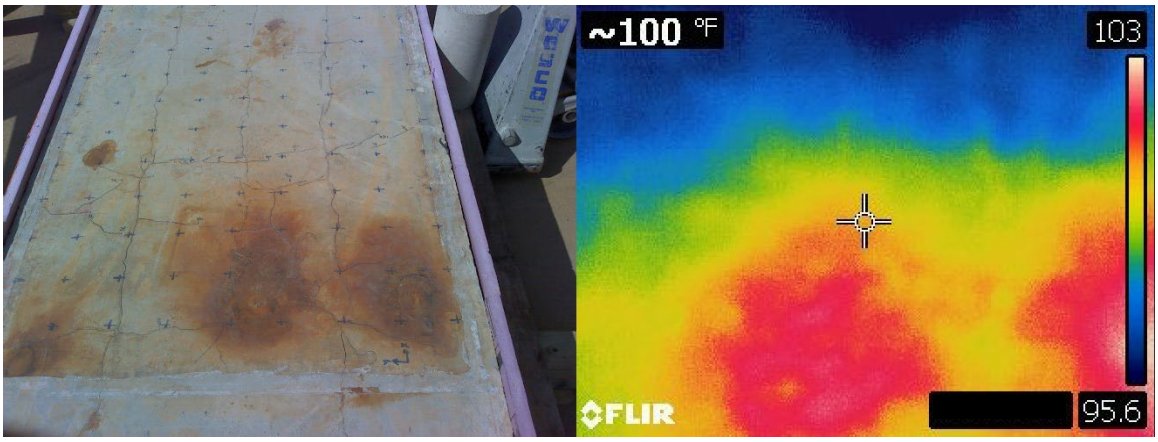

(c) 170 Min. Exposure

Figure 4-114: FLIR Images of Specimen DL5 After (a) 20 Min., (b) 100 Min., and (c) 170 Min. of Sun Exposure

From as early as 20 minutes of sun exposure, temperature differentials were established (shown in red and white hues) at the locations of the rust staining. It was unclear whether these differentials were the result of rust staining or the corrosion-induced delaminations in Zone 3. Other surfaces in Zone 3 that were not stained exhibited similar temperatures, creating further doubt whether the IRT approach could detect corrosion-induced delaminations 2 in. below the surface. Nonetheless, the strong influence of local differences in emissivity on thermal imaging was emphasized in this exercise. It was hypothesized that, to best assess the effectiveness of IRT in detecting subsurface defects, testing would have to be conducted on a larger element free of surface staining.

4.6 Conclusions

Conclusions developed from Phase 1 of this project aimed at assessing the usefulness of NDT technologies available to ALDOT are presented hereinafter. For convenience, conclusions pertaining to each NDT method are separated into their own subsections.

4.6.1 Phase 1 GPR Conclusions

Concerning the use of the "Top Reinforcing Reflection Attenuation Technique" data processing method, as termed by ASTM D6087 (2015), the following conclusions were made regarding the defect-detection capabilities of GPR in evaluations of bridge decks without overlays:

- GPR is incapable of detecting either shallow or deep delaminations with thicknesses of 3/32 in. or smaller, regardless of whether they are unbonded or partially bonded;
- GPR is incapable of detecting either concrete deterioration or poorly constructed concrete below the level of the top reinforcement mat;

- GPR is incapable of locating vertical cracks with widths of 50 mil or smaller and at depths of 3 in.;
- GPR is capable of detecting water-filled voids as small as 1/2 in. in diameter in the cover layer;
- GPR is incapable of detecting deep, water-filled voids as large as 2-1/2 in. in diameter;
- GPR is incapable of detecting either shallow or deep clay balls as large as 2 in. in diameter; and
- GPR is capable of detecting environments of active chloride-induced reinforcement corrosion within bridge decks.

Furthermore, when conducting GPR evaluations in this manner, the following conclusions were developed regarding the hypothesized factors that could affect GPR reflection amplitudes:

- While oriented perpendicular to the top layer of reinforcing steel, the position of the antenna either directly over or between parallel reinforcement does not influence measured reflection amplitudes;
- While oriented perpendicular to the bottom layer of reinforcing steel, the position of the antenna either directly over or between parallel reinforcement does influence measured reflection amplitudes. Measurements collected directly over parallel reinforcement centralize about a different mean than measurements collected between parallel reinforcement; there is no significant difference in variance;

- GPR data collected from a bridge deck in a moist state will exhibit greater variance and will be more attenuated than data collected from the same deck in a drier state.

4.6.2 Phase 1 IE Conclusions

Regarding the defect-detection capabilities of ground-coupled impact echo in nondestructive evaluations of bridge decks without overlays, it was determined that:

- IE can detect shallow, unbonded delaminations with thicknesses of 10 mil or larger;
- IE cannot reliably detect shallow delaminations with in-plane dimensions smaller than half the testing grid spacing nor deep delaminations with in-plane dimensions smaller than 75% of the grid spacing;
- The spatial correlation of the true delamination location and predicted location from IE is much stronger for shallow than deep delaminations;
- IE can detect shallow, 10-mil thick (or larger), partially bonded delaminations with 50% unbonded area and deep, 50-mil thick (or larger), partially bonded delaminations with 75% unbonded area;
- IE can identify concrete deterioration or poorly constructed concrete below the level of the top reinforcement mat;
- IE can detect both shallow and deep voids or voids in the cover layer as small as 1/2 in. in diameter but may not accurately locate them;

Furthermore, it was determined that the moisture content of a bridge deck does not significantly influence the conclusions from IE condition assessments.

4.6.3 Phase 1 HCP Conclusions

In assessing the defect-detection capabilities of the HCP method, the following conclusions were developed:

- HCP is capable of detecting actively corroding steel reinforcement with a high degree of confidence;
- Numeric magnitude criteria proposed by ASTM C876 (2015) concerning interpretation of half-cell potentials are not reliable predictors of the condition of embedded reinforcement in bridge decks;
- Half-cell potential measurements are strongly affected by changes in moisture. An increase in moisture content causes half-cell potentials to decrease (become more negative). For an equal increase in moisture content, the magnitude of this decrease in half-cell potentials is not equal between locations of passive and actively corroding reinforcement;
- The higher the moisture content of a bridge deck, the more pronounced the difference between passive and actively corroding reinforcement becomes;
- The most negative potential measured over passive reinforcement in laboratory testing was -350 mV and corresponded to moist, chloride-contaminated concrete. Accordingly, there exists a high degree of probability that potentials more negative than -350 mV are not associated with passive reinforcement in evaluations of bridge decks without overlays;
- Delaminations can disrupt the flow of current between the two half-cells when using the HCP method. When a delamination is air-filled, it presents an abnormally

high localized resistivity. When a delamination is water-filled, it presents a resistivity more similar to moist concrete;

- When testing bridge decks in a dried state, differentiating between passive and actively corroding portions of the deck can be difficult without statistical analysis. Use of the segmented linear regression algorithm proposed by Muggeo (2017) facilitates this decision making, resulting in prediction accuracies as low as 1.6 percentage points lower than the maximum accuracy obtained using receiver operator characteristic (ROC) analysis.

4.6.4 Phase 1 ER Conclusions

Through laboratory testing of specimens subjected to accelerated chloride-induced corrosion, the following conclusions concerning the use of the ER method in nondestructive evaluations of bridge decks were developed:

- The ER method is not appropriate for detecting active corrosion of embedded reinforcement. Before reinforcement depassivation, it may be used to assess the risk of corrosion. After reinforcement depassivation, it may be used to estimate the rate of corrosion.
- The moisture content of a bridge deck has a strong influence on concrete resistivity measurements. All else being equal, the lower the moisture content, the higher the resistivity.
- Low moisture contents and chloride ion concentrations result in more variable resistivity measurements than high moisture contents and chloride ion concentrations;

- After reinforcement depassivation has occurred, Broomfield and Millard (2002) interpretation criteria seem appropriate for corrosion rate prediction.

4.6.5 Phase 1 IRT Conclusions

Limited conclusions regarding the effectiveness of IRT in nondestructive evaluations of concrete bridge decks could be made from the experimental results of Phase 1 of this project. It could not be definitively established whether IRT could not detect any simulated defects or whether the size of the laboratory specimens precluded an accurate evaluation of the method. Accordingly, further work would need to be performed on the full-scale bridge deck developed in Phase 2 of this project to fairly assess the capabilities of IRT. Nonetheless, from Phase 1 of this project, it was observed that discolorations on surfaces tested by IRT can cause significant thermal differentials to develop because of the local change in emissivity. Thus, IRT evaluations of bridge decks may be complicated by local emissivity differences caused by staining, certain repair materials, and other similar local surface stains not attributed to any concrete distress.

Chapter 5: Phase 2 - Development and Testing of Full-Scale Bridge Deck

5.1 Chapter Objectives and Outline

Phase 2 of this project aimed to develop a full-scale bridge deck with simulated defects to create a nondestructive testing facility for ALDOT and further validate the conclusions developed from Phase 1 outside of a laboratory environment. In this chapter, methods of simulating different defects in the full-scale bridge based on the successes and challenges from the laboratory specimens are described. The results of preliminary testing of the bridge deck using the five aforementioned NDT methods are presented. Further conclusions concerning the utility of each NDT method in condition assessments of bridge deck are offered.

5.2 Bridge Design for Condition Assessment

The test bridge to be used for nondestructive evaluation was designed using Load and Resistance Factor Design (LRFD) considering anticipated dead loads and live loads during testing. Methods of simulating concrete deterioration, poorly constructed concrete, delaminations, voids, and corrosion were selected to best emulate defects one may encounter within in-service bridge decks.

5.2.1 Test Bridge Design

Half-section drawings of the transverse and longitudinal sides of the test bridge are shown in Figures 5-1 and 5-2 respectively. Normalweight concrete with a specified compressive strength of 4,000 psi was used in design of all reinforced concrete elements in the test bridge. Grade 60, uncoated reinforcing steel was used to design the reinforced concrete

bridge deck, girders, and grade beams. Grade beams were used in lieu of piers to support the girders since the bridge deck was not suspended high above the ground surface.

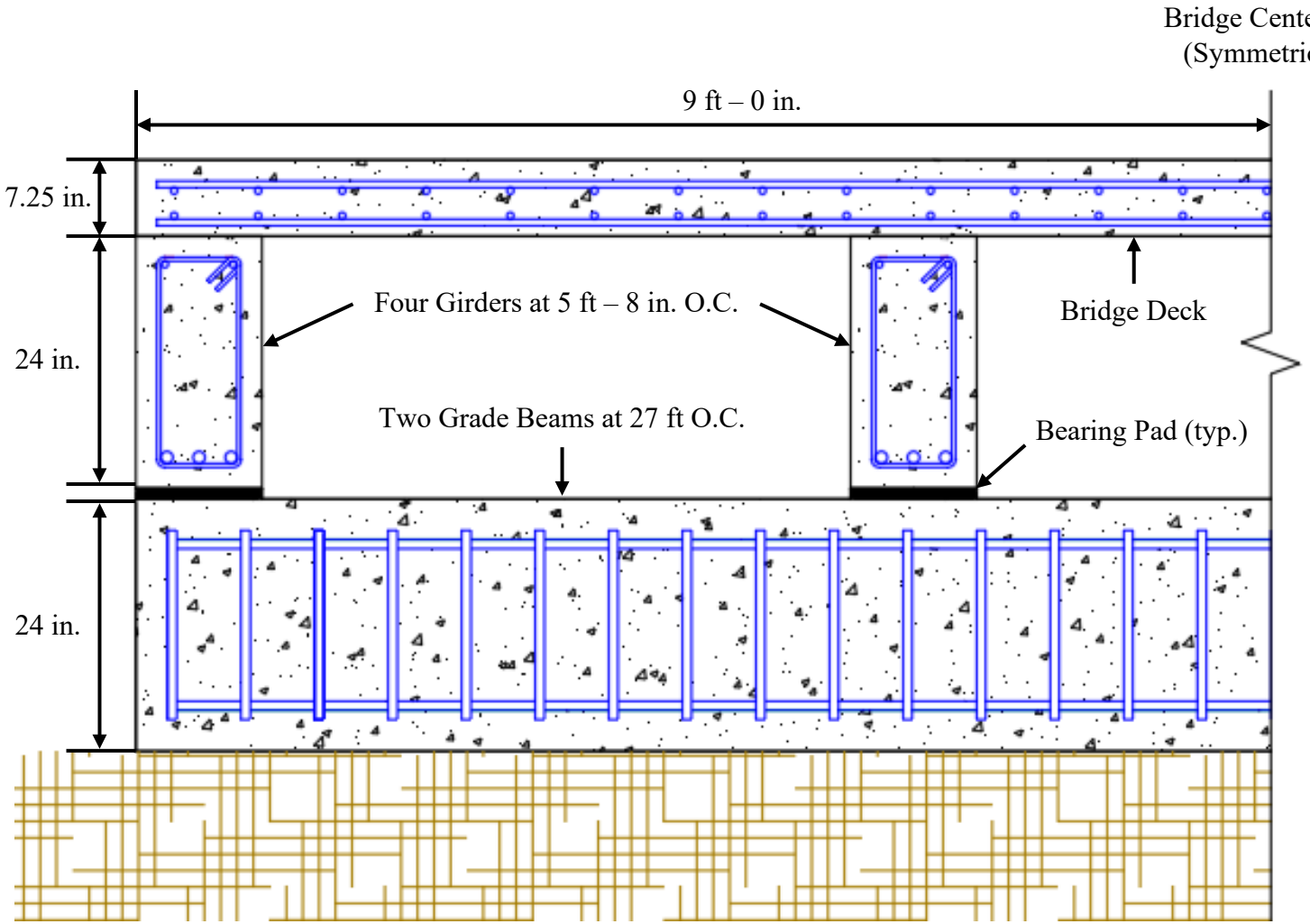

Note: Test bridge is symmetric about shown centerline

Figure 5-1: Half-Section Drawing of Transverse Side of Test Bridge

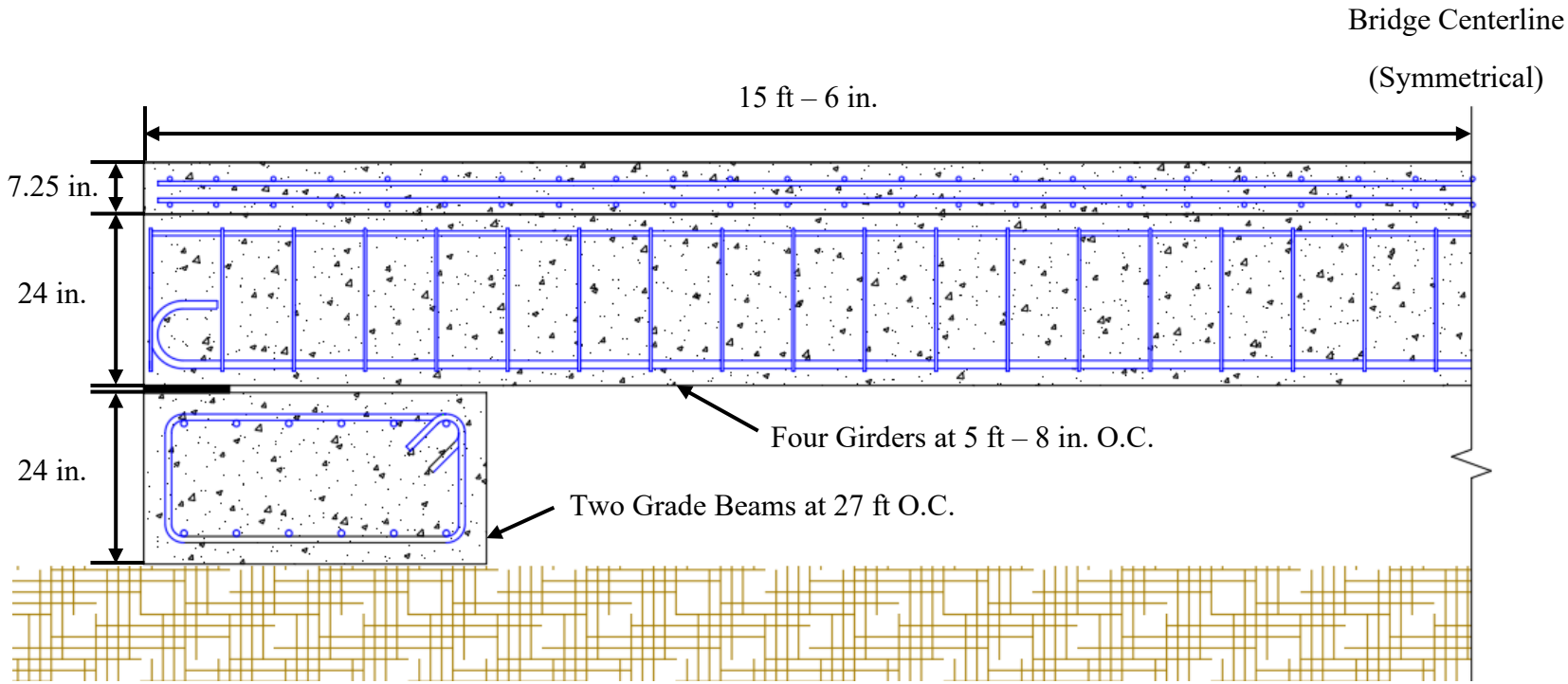

Note: Test bridge is symmetric about shown centerline

Figure 5-2: Half-Section Drawing of Longitudinal Side of Test Bridge

5.2.2 Defect Simulation

A conceptual layout of the bridge deck including the defects simulated within it is shown in Figure 5-3. The defect abbreviations are similar to those used in Chapter 4 of this document. A discussion of each of those defects is included hereinafter.

Corrosion

As efforts to rapidly corroded embedded reinforcement in Phase 1 Specimens C1 and C2 were successful, similar accelerated corrosion methods were implemented in the bridge deck. Since the test bridge deck was built with 2 inches of clear cover to the negative flexural reinforcement, the corrosion schedule for Specimen C2 was initially implemented on the bridge deck. However, for the same corrosion schedule given in Table 4-6, the test bridge was not sufficiently corroded, as determined through HCP testing. Further, at the time of writing of this thesis, reinforcement in the bridge deck was still not sufficiently corroded. Thus, testing results of active corrosion zones are not presented in this document.

Concrete Deterioration

Given the lack of predictability in the simulation of deterioration when anti-cracking fibers were used in the laboratory, deterioration simulation using (1) a high dosage of air-entraining admixture and (2) honeycombing in miniature slabs was implemented. As termed in Figure 5-3, Defect DE1 was a 1 ft by 5 ft miniature slab with a high dosage of air-entraining admixture and the same specified compressive strength as the rest of the bridge deck. Furthermore, Defect DE2 was a 1 ft by 5 ft miniature slab composed of concrete with severe honeycombing and the same specified compressive strength as the rest of the deck. Defects DE1 and DE2 can be observed in Figure 5-4.

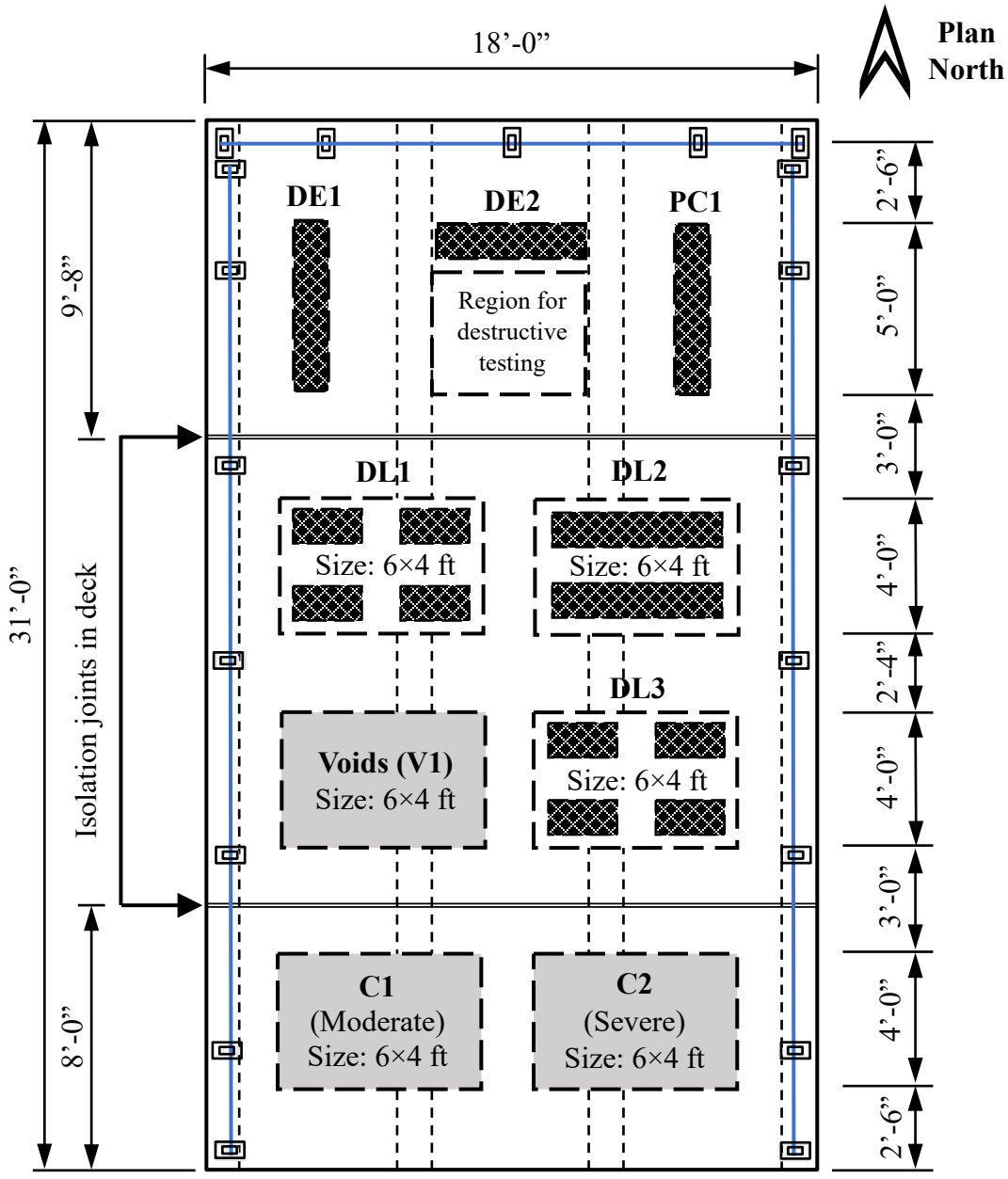

Plan View of Defect Layout

(Not to scale)

Notes:

1) Deck is supported by four reinforced concrete girders (shown in dashed lines)

2) Intended slab thickness is 7.25 in.

Figure 5-3: Conceptual Layout of Full-Scale Test Bridge Deck

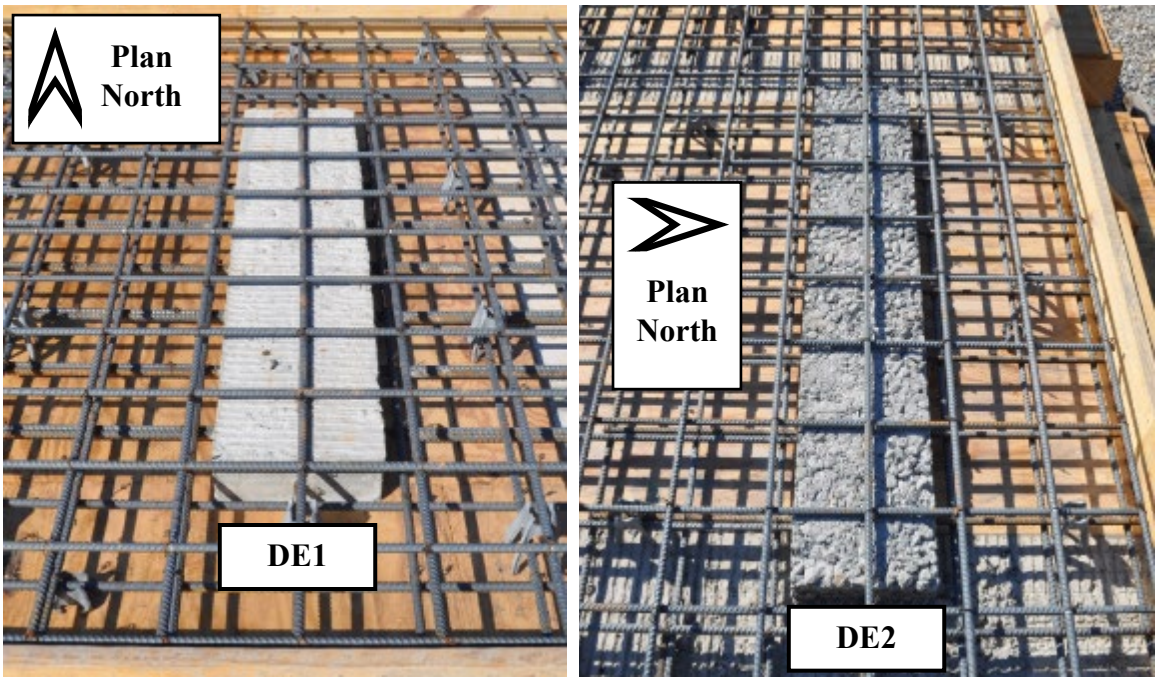

Figure 5-4: Defect DE1 (Left) and DE2 (Right)

Delaminations

Success in shallow and deep delamination simulation using plastic sheeting during Phase 1 of this project inspired similar simulation efforts in Defects DL1 and DL3. Within Defects DL1 and DL3 respectively, 1 ft by 2 ft by 10 mil plastic and 1 ft by 2 ft by 30 mil plastic were used to replicate both shallow and deep delaminations. As can be observed in Figure 5-5, such plastic sheets were secured between perpendicular reinforcement to emulate delaminations occurring at the level of the reinforcement mats within in-service bridge decks. During installation of the plastic sheets, a lift of concrete was placed and vibrated below the level of the sheet. Subsequently, the sheeting was placed, and a second lift of concrete was placed above the simulated delamination.

Figure 5-5: Plastic Sheeting Delamination Simulation in Test Bridge

As the reliability of delamination simulation using sand and oil layers in Phase 1 of this project was not consistent, simulation of delaminations with a large areal extent needed to be redeveloped. Visual analysis of the extracted cores from Laboratory Specimens DL3 and DL4 revealed that (1) when the sand layer was sufficiently thick, it caused a fully unbonded delamination to develop and (2) the oil layer was generally reliable in delaminating the surrounding concrete; however, the degree to which the delamination was unbonded was variable. Accordingly, it was expected that either (1) a sufficiently thick sand layer mixed with form oil or (2) a thick sand layer would cause an unbonded delamination of large areal extent in the test bridge deck. To create such layers, 1 ft by 5 ft miniature slabs (similar to those used for Phase 1 DE and PC specimens) with a ¼ in. trough on their tops and made from concrete of the same specified compressive strength as the bridge deck were fabricated. For one miniature slab, the ¼ in. trough was filled with

sand and sprayed with form oil; for the other, the trough was filled completely with sand. These redeveloped sand/oil delaminations were positioned at Defect DL2, as shown in Figure 5-3, and can be seen in Figure 5-6.

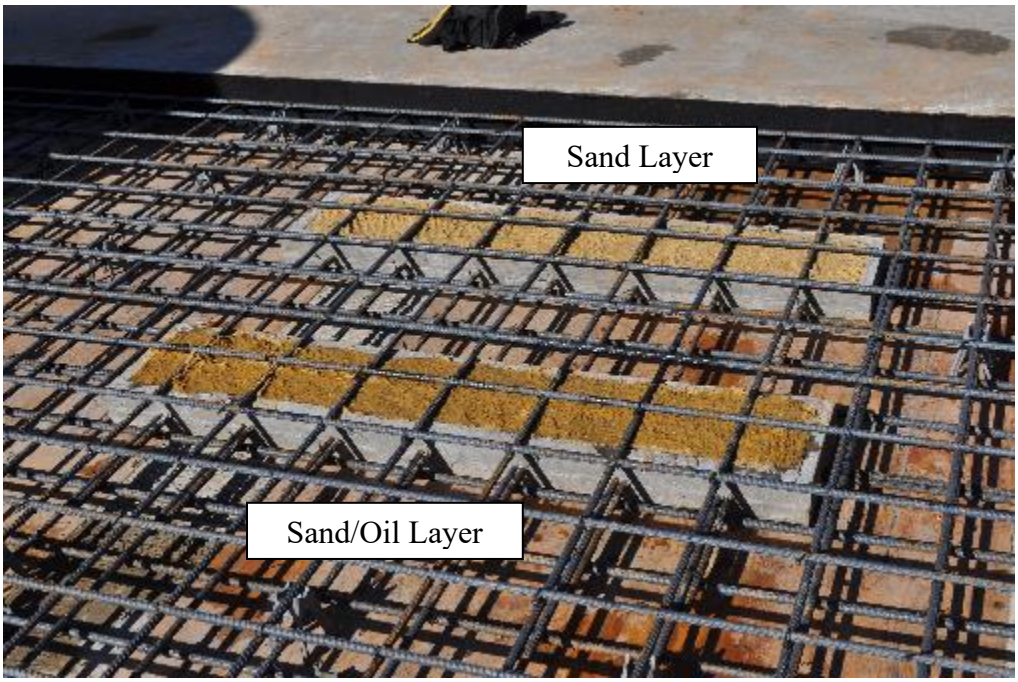

Figure 5-6: Redeveloped Sand/Oil Delamination Simulation in Defect DL2

Poor Construction

During Phase 1 of this project, it was observed that only impact-echo testing could identify poorly constructed concrete in laboratory specimens. Moreover, results of ROC analysis of air-dried IE data from Specimens CTRL and PC1 (shown in Table 4-17) revealed that impact-echo testing exhibited good accuracy in detecting differences in concrete strength resulting from poor construction. Accordingly, Defect PC1 was selected to be made using a 1 ft by 5 ft miniature slab with a specified compressive strength of 2,500 psi (1,500 psi less than that of the surrounding bridge deck concrete). Defect PC1 can be seen in Figure 5-7, before the entire deck was constructed.

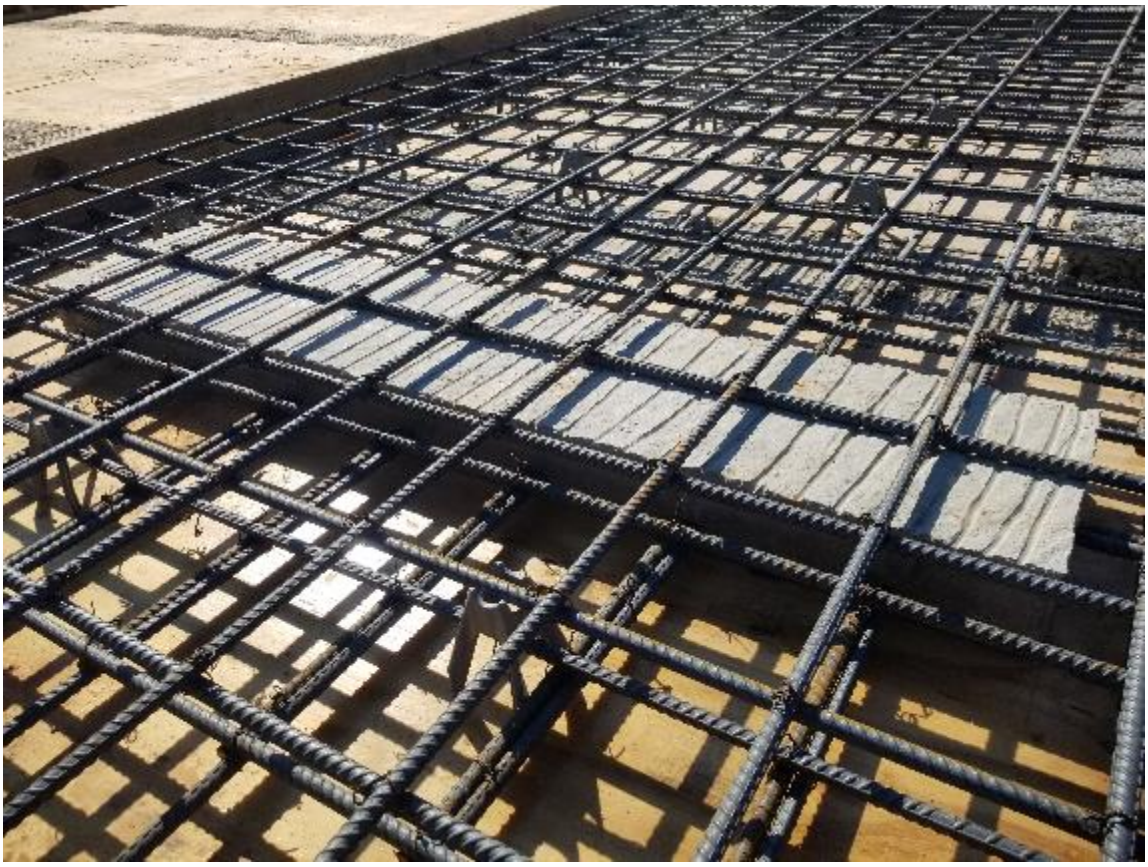

Figure 5-7: Defect PC1

Voids

Void simulation using clay-filled and water-filled balloons was successful in Phase 1 of this project, as verified through visual analysis of extracted cores. Thus, 1 in., 2 in., and 3 in. diameter shallow and deep voids were constructed in Defect V1 of the test bridge using the same simulation techniques. As can be observed in Figure 5-8, balloons were installed in their proper locations by tying them to either the upper or lower reinforcement mat. Balloons were more deliberately affixed to the reinforcement mats to mitigate the risk of them floating into the cover layer during placement. Concrete around the voids was

carefully consolidated using a vibrator to prevent the balloons from bursting open during concrete placement.

Figure 5-8: Shallow Void Simulation in Defect V1

5.3 Bridge Deck Testing and Analysis

The test bridge deck was discretely tested on two 8 in. by 8 in. grids with the GPR, IE, and IRT methods. Neither HCP nor ER testing were conducted because accelerated corrosion was not complete before the writing of this thesis. Two grid origin points were established in two of the three deck sections (the portions of the test deck within the deck perimeter and neighboring isolation joint) as shown in Figure 5-9. The two corresponding testing grids were aligned with the location of the reinforcement mat. Using the following naming scheme, the bottommost, middle, and topmost portions of deck (as illustrated in Figure 5-9) were termed “Section 1”, “Section 2”, and “Section 3” respectively. Furthermore, the as-built locations of the deck defects, shown in Figures 5-9 and 5-10, were used as ground truth data to quantify the accuracy of NDT methods using ROC analysis.

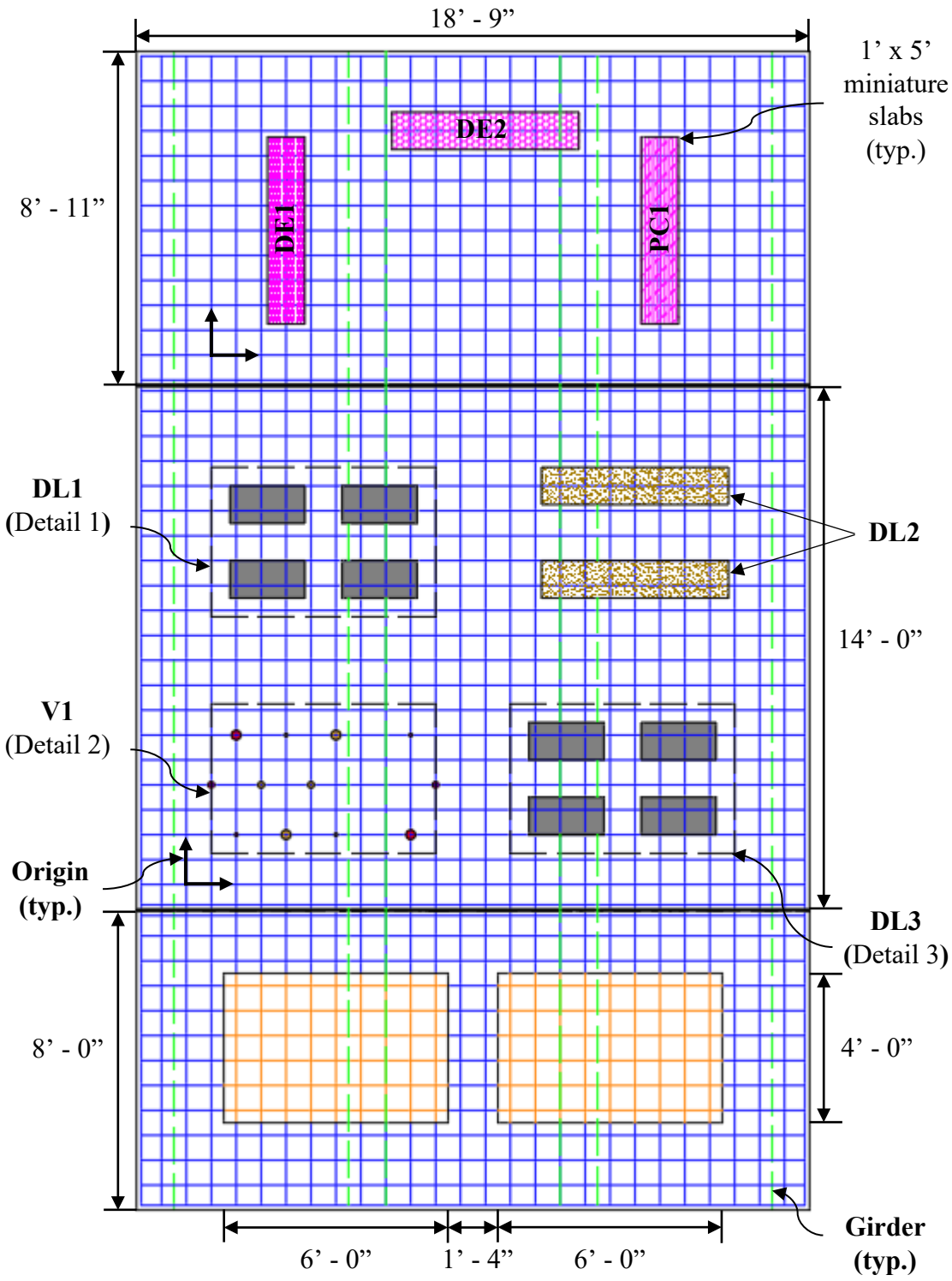

Notes: (1) Reinforcement spacing is 8 in. on center (shown as blue lines)

(2) Sections 1, 2, and 3 are shown from bottom to top of drawing

Figure 5-9: As-Built Layout of Test Bridge Deck (To Scale)

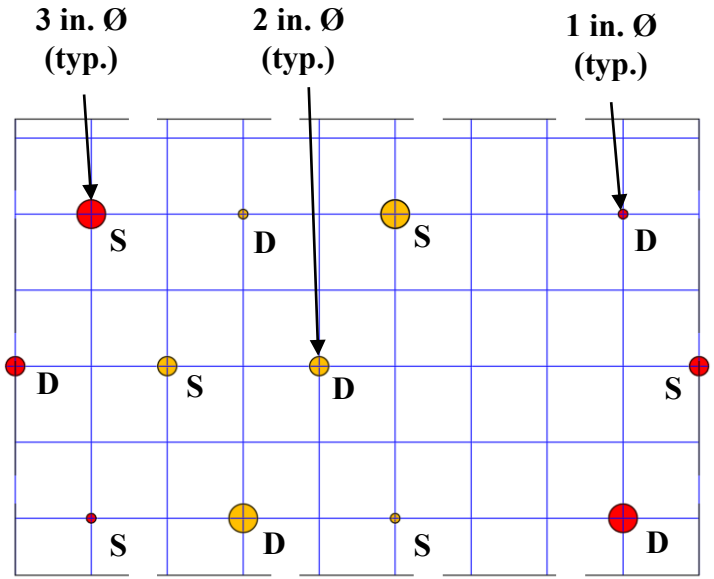

Notes:
(1) Yellow circles represent clay-filled balloons
(2) Red circles represent water-filled balloons
(3) **S**: Shallow; **D**: Deep

Detail 2

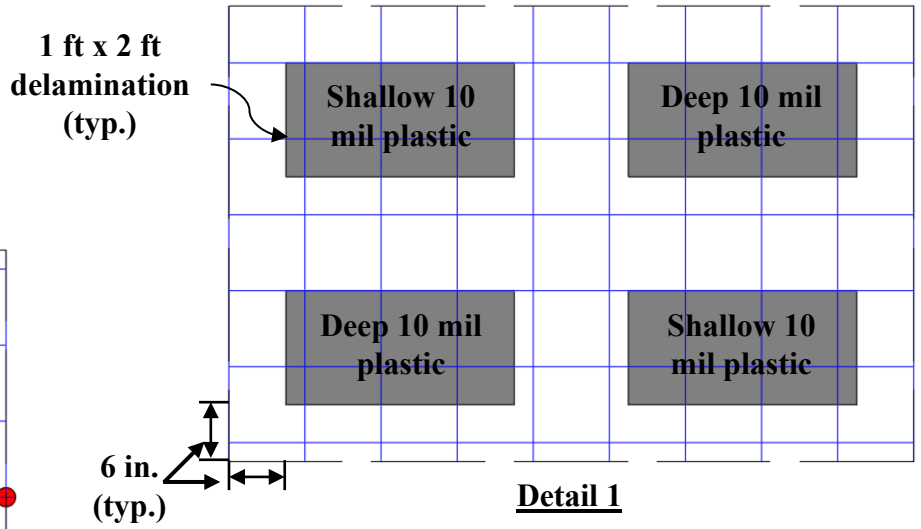

Detail 1

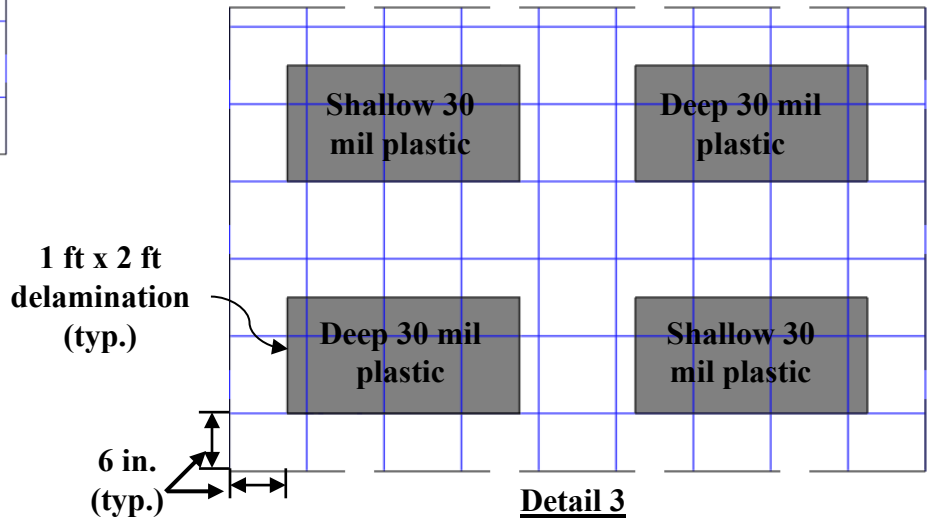

Detail 3

Figure 5-10: Details for As-Built Test Bridge Deck

5.3.1 Ground-Penetrating Radar Data Collection and Processing

As in Phase 1 of this work, GPR data were collected from the test bridge deck using a 2600 MHz antenna with the same data acquisition settings given in Table 4-2. Data collection was oriented perpendicular to the top bar in the top reinforcement mat (longitudinal direction of bridge) using the "Top Reinforcing Reflection Attenuation Technique" (ASTM D6087 2015). Reflection amplitudes from the top bar were corrected for cover depth variations in accordance with the method described by Barnes et al. (2008). The dielectric constants and corresponding wave velocities used in Sections 2 and 3 are provided in Table 5-1 as follows.

Table 5-1: Dielectric Constants and Wave Velocities of Test Bridge Sections

Section ID	Dielectric Constant	Wave Velocity (in/ns)
2	9.25	3.88
3	9.25	3.88

5.3.2 Impact-Echo Data Collection and Processing

IE data were collected as described in Section 4.3.2 of this thesis on the 8 in. by 8 in. testing grid. The calibrated compression wave velocities from each section of the bridge deck are presented in Table 5-2.

Table 5-2: Compression Wave Velocity of Test Bridge Sections

Section ID	Compression Wave Velocity (ft/s)
2	12,980
3	13,334

It was observed that the quality of impact-echo waveforms collected directly over the bridge deck girders was poor. As can be observed in one such waveform, shown in Figure 5-11, seemingly many different vibration modes were excited by the impact force.

Accordingly, such waveforms were not deemed reliable indicators of the bridge deck condition as no singular dominant frequency could be confidently selected. Thus, waveforms collected from impacts over the bridge deck girders were not analyzed for inclusion in frequency contour plots or ROC analysis.

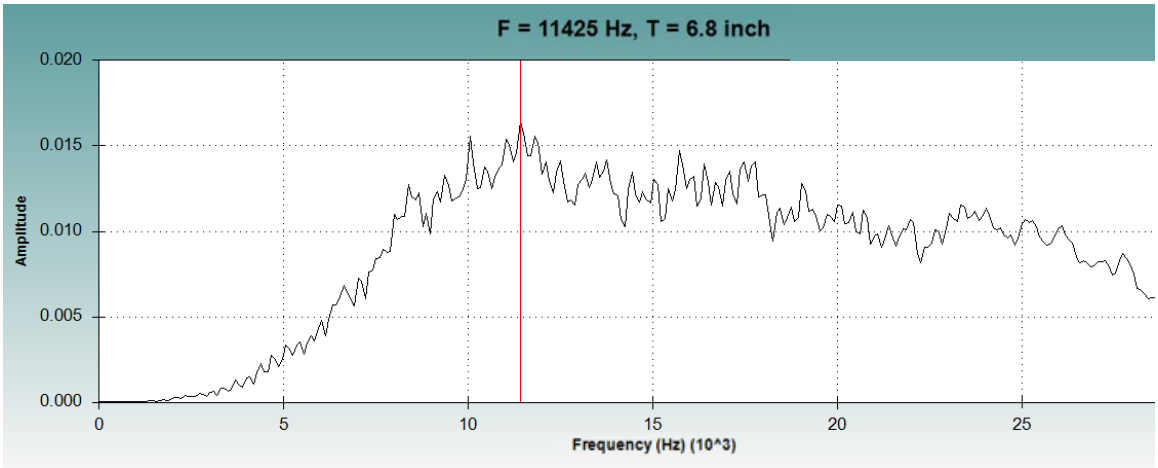

Figure 5-11: Impact-Echo Waveform Over Bridge Deck Girder

5.3.3 Infrared Thermography Data Collection

As in Phase 1 of this project, IRT data were collected from the bridge deck using the MOBA MTPS-100 and FLIR E60 thermal cameras around midday. As can be observed in Figure 5-12, surface temperature estimations were obtained with the MOBA MTPS-100 by pushing a cart along the bridge deck. The cart was pushed in the longitudinal direction of the bridge in five passes, each three feet in width. The edges of adjacent passes were spaced at 1 in. such that the entire width of the testing grid (184 in.) was scanned with the MOBA MTPS-100. Within each pass, IRT data were collected every 6 in. and 3.6 in. in the longitudinal and transverse directions of the bridge respectively. Thermal images were captured with the FLIR 360 camera behind the cart in the same pass.

Figure 5-12: IRT Evaluation of Bridge Deck using the MOBA MTPS-100 Cart System

During data collection, it was observed that the estimated surface temperatures of the expansion joints were significantly higher than those of the bridge deck, as can be observed in the thermal image of the joint shown in Figure 5-13. While the thermal reading of the expansion joint could not be filtered out of images captured with the FLIR E60, measurements collected over the joints could be removed in postprocessing of the data collected with the MOBA MTPS-100. This was performed such that differences in estimated surface temperature could be most easily discerned when visually analyzing the data on a spatial contour plot.

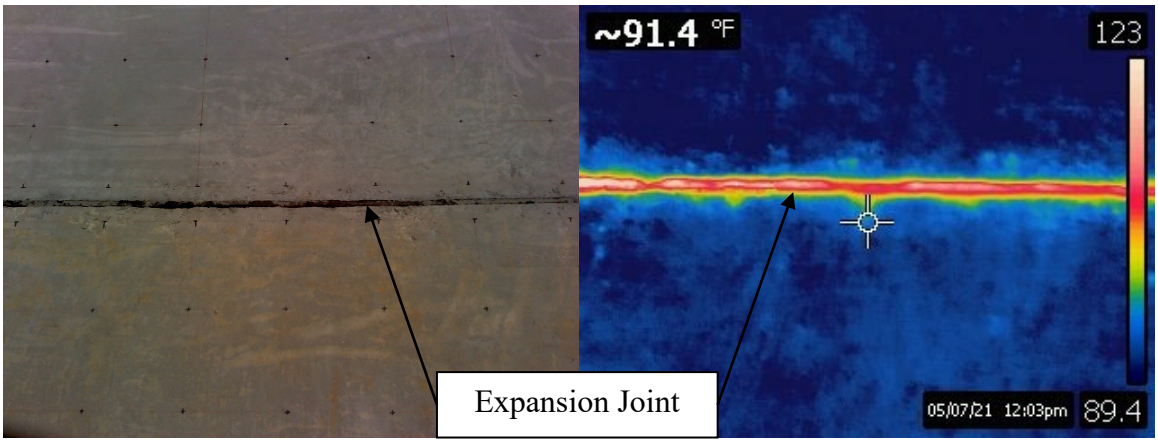

Figure 5-13: Increased Estimated Surface Temperature at Expansion Joints

5.4 Presentation of NDT Data and Corresponding Results

As NDT data were not always collected over Sections 2 and 3 in one day, the results of nondestructive testing for each section are largely presented separately. For each nondestructive test method, data collected from applicable bridge sections are presented in the following subsections.

5.4.1 Presentation and Visual Analysis of GPR Bridge Deck Data

Depth-corrected GPR data collected from Section 2 of the bridge deck are shown in Figure 5-14. Visually analyzing that spatial contour plot, it was observed that the weakest reflection amplitudes (shown in red, orange, and yellow hues) were predominantly located at sound portions of the bridge deck. Furthermore, the strongest reflection amplitudes (shown in purple and dark blue hues) were well-distributed throughout both sound and defective portions of the bridge deck. Given this seemingly random distribution of reflection amplitudes and the lack of distinction between sound and delaminated portions of the deck, it was concluded from the visual analysis that GPR cannot detect either shallow or deep delaminations.

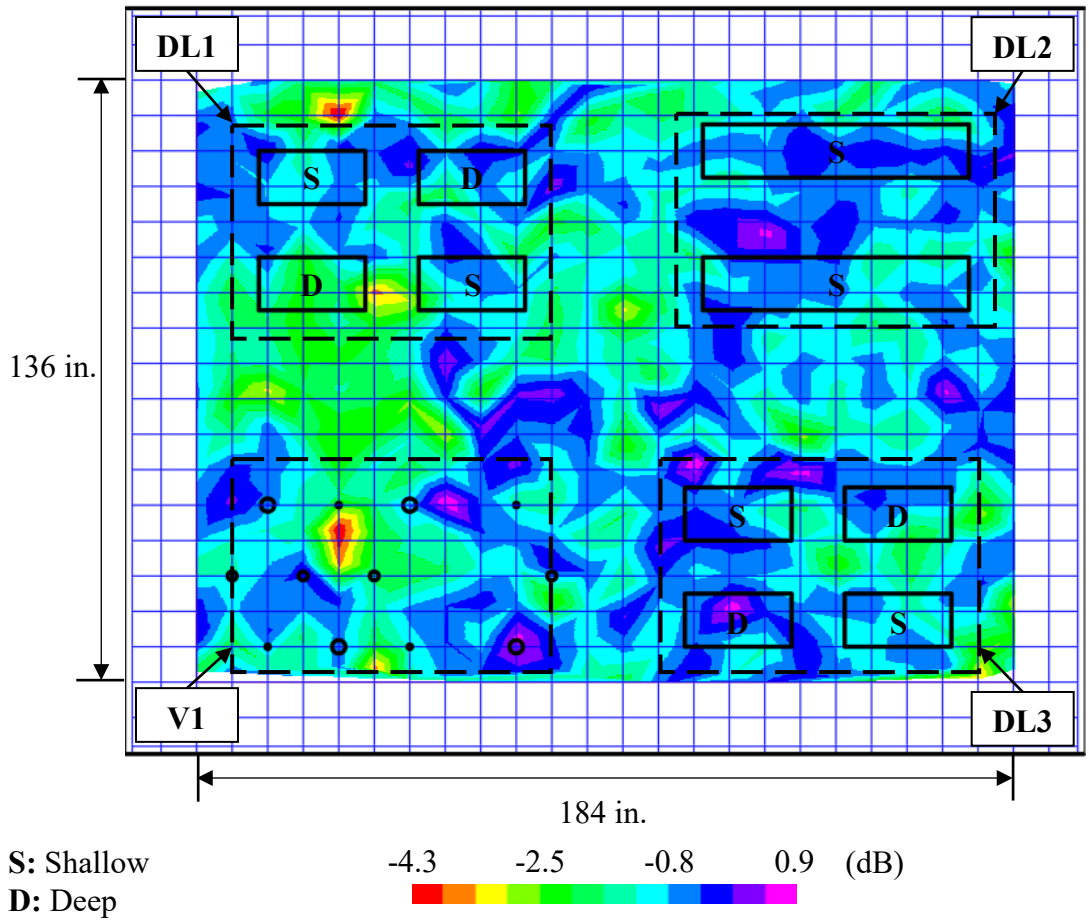

Figure 5-14: Section 2 Spatial Contour Plot of GPR Data

Similarly comparing the reflection amplitudes measured over the voids to those over sound portions of the deck, no apparent distinction between the two groups was observed. The most negative reflection amplitude measured over the voids was still more positive (stronger) than that measured over sound portions of the deck. Thus, the GPR response over the voids was not reliably different than that over the rest of Section 2 such that an operator would not be able to confidently locate a shallow or deep void filled with either clay or water. While GPR was able to detect water-filled voids in the cover layer of specimens built in Phase 1 of this document, it could not detect similar voids anchored to remain at the levels of the top and bottom reinforcement mats.

The depth-corrected GPR data for Section 3 of the bridge deck are presented in Figure 5-15. The weakest reflections (shown in red, orange, and yellow hues) were measured over sound portions of the bridge deck. Moreover, the strongest reflections (shown in purple and dark blue hues) were seemingly well-distributed throughout both sound and defective portions of the deck. As most reflections measured over the deterioration and poor-construction miniature slabs were of the same general strength as those from sound portions of the deck, no clear change in the deck response to GPR was observed over the simulated defects. Thus, from a visual analysis, it was concluded that GPR is not capable of detecting concrete deterioration or poorly constructed concrete below the level of the top reinforcement mat.

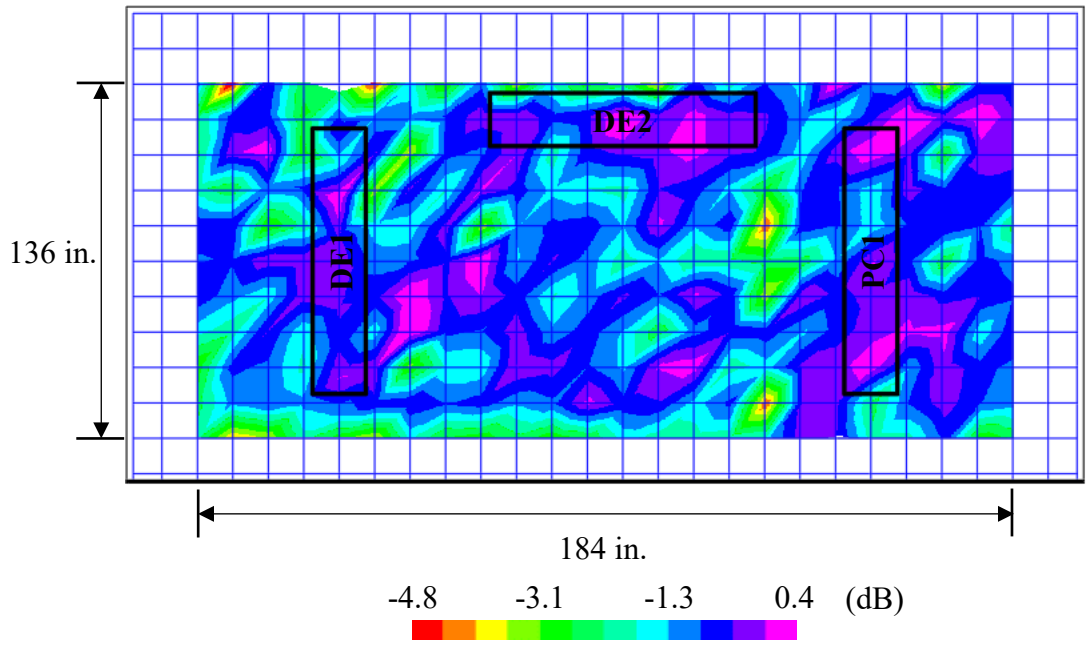

Figure 5-15: Section 3 Spatial Contour Plot of GPR Data

5.4.2 ROC Analysis of GPR Data Results

The results of ROC analysis of the depth-corrected GPR data collected from Sections 2 and 3 of the bridge deck are presented in Table 5-3. As in ROC analysis conducted in

Phase 1 of this study, the percentages of defective and sound portions of the bridge deck correctly identified using the optimal GPR threshold were also tabulated to further assess the defect-detection capabilities of GPR. ROC analysis of data from Section 2 resulted in 83.9% of the deck state being correctly predicted. While this may seem like a promising indicator of the capabilities of GPR in condition assessment of bridge decks, this overall accuracy was accompanied by 0.0% of the defective area and 100.0% of the sound area being correctly identified. As discussed in Section 4.5.4, this result indicates that when assessing bridge decks with defects like those from Section 2 of the test bridge, an operator would incorrectly determine that the entire deck is sound. In other words, GPR cannot discern either shallow or deep delaminations or voids from sound concrete.

Table 5-3: Accuracy of Receiver Operator Characteristic Analysis of Depth-Corrected Bridge GPR Data

Section ID	Optimal Threshold (dB)	Maximum Accuracy (%)	Defect Area Detected (%)	Sound Area Detected (%)
2	-4.28	83.9	0.0	100.0
3	-4.90	92.0	0.0	100.0

Considering the ROC analysis results from Section 3 of the deck, a similar conclusion was reached concerning the capability of GPR to detect either concrete deterioration or poorly constructed concrete. While the maximum overall accuracy achieved from ROC analysis was 92%, the corresponding percentages of defective and sound area identified were respectively 0.0% and 100.0%. As before, these results indicate that GPR could not discern between sound and defective portions of the deck. Accordingly, GPR is not an effective NDT method for detecting concrete deterioration or poorly constructed concrete below the top reinforcement mat in bridge decks.

5.4.3 Presentation and Visual Analysis of IE Bridge Deck Data

The impact-echo data collected from Section 2 of the test bridge deck are shown in Figure 5-16. Through visual analysis of that spatial contour plot, it was observed that the dominant frequency excited during testing was fairly uniform (shown in light green and yellow hues) throughout the sound portions of the deck. Nonetheless, other distinct frequencies were excited at the four zones of defective concrete. At DL1, low frequencies (shown in red and orange hues) were measured over the two shallow, 10-mil thick delaminations, corresponding to an excited flexural mode. Moreover, high frequencies (shown in dark green and blue hues) were collected at the locations of both deep delaminations. Both of these shifts were sufficiently distinct from a visual perspective to allow for detection of the shallow and deep delaminations. Nonetheless, ROC analysis (to be presented in the next subsection) served to numerically assess whether there existed a compelling distinction between the impact-echo response over the DL1 delaminations and sound portions of the bridge deck.

Similar visual analysis of the redeveloped sand/oil delaminations in DL2 indicated that impact-echo testing could identify the shallow delaminations. Low frequencies were measured over the thick sand layer suggesting that delamination simulation efforts were successful in producing a detectable delamination. While not as predominant as in the thick sand layer, some low frequencies were also measured over the sand/oil delamination. However, very high frequencies (shown in purple and dark blue hues) were also measured over that delamination, suggesting that compression waves were exciting a different mode other than that of the deck thickness or flexural plate bending above the shallow delamination.

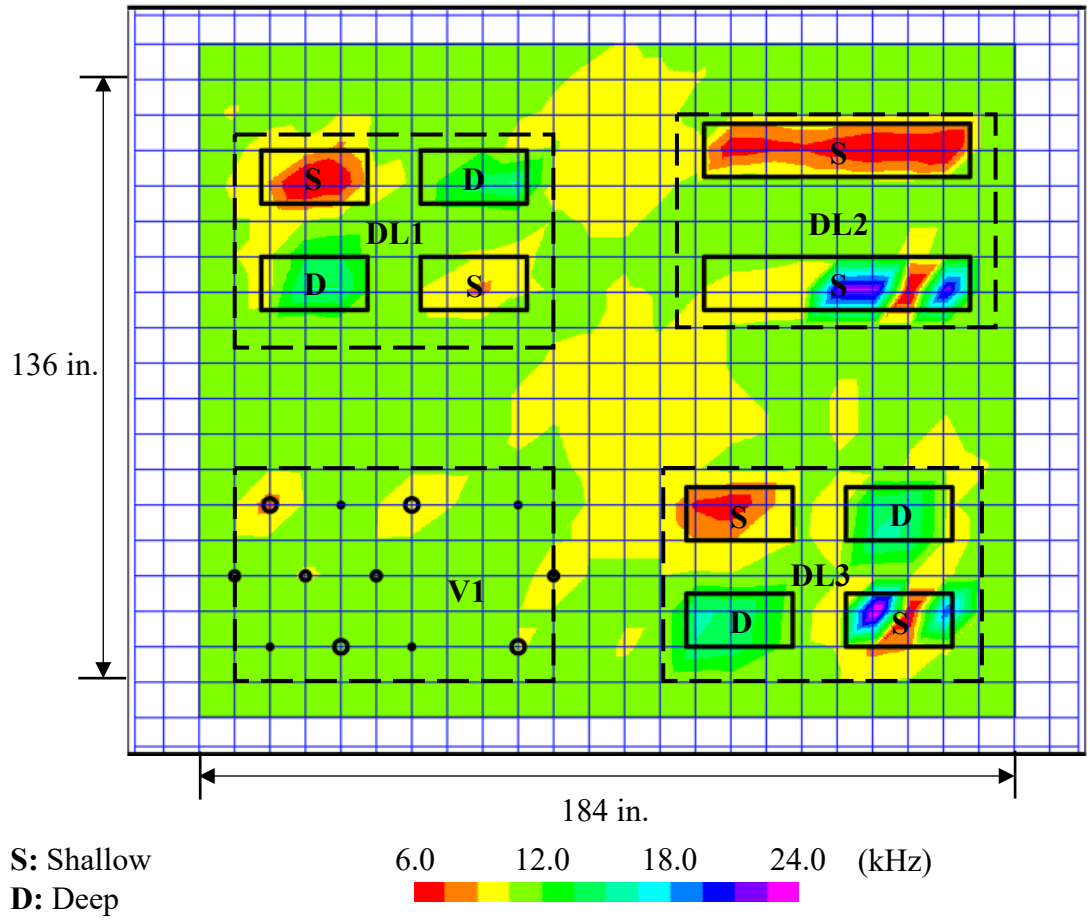

Figure 5-16: Section 2 Spatial Contour Plot of IE Data

To investigate this phenomena, one characteristic impact-echo spectral response measured over the sand/oil delamination is shown in Figure 5-17. As can be seen in Figure 5-17, the dominant frequency excited was 6,152 Hz, which was significantly lower than the frequency associated with the deck thickness mode, estimated to be approximately 11,000 Hz from Figure 5-16. This decrease in magnitude of the dominant frequency was consistent with previous observations noted in Phase 1 of this project regarding the impact-echo response of shallow delaminations. What is most perplexing about the spectral response is the very high-amplitude secondary frequency excited at roughly 22,300 Hz. Using Equation 2.2 and the calibrated compression wave velocity (βC_p) for Section 2 from

Table 5-2, the depth to the reflecting interface corresponding with the high frequency was approximately 3.49 in., close to the sand/oil layer depth of 3.25 in. below the deck surface. Accordingly, distinct from the flexural plate-bending frequency excited during shallow delamination testing, the secondary frequency excited appears to be indicative of compression of concrete above the delamination. As noted by Sansalone and Carino (1989), this secondary frequency may be termed the thickness frequency. By observation of Figure 5-16, either of the two frequencies could be more dominant than the other, thus leading to both high and low dominant frequencies being recorded over the shallow delaminations of DL2 and DL3. Theoretically, either frequency could become dominant if the impact stress contained frequency components of sufficient energy up to the flexural plate-bending and thickness frequencies.

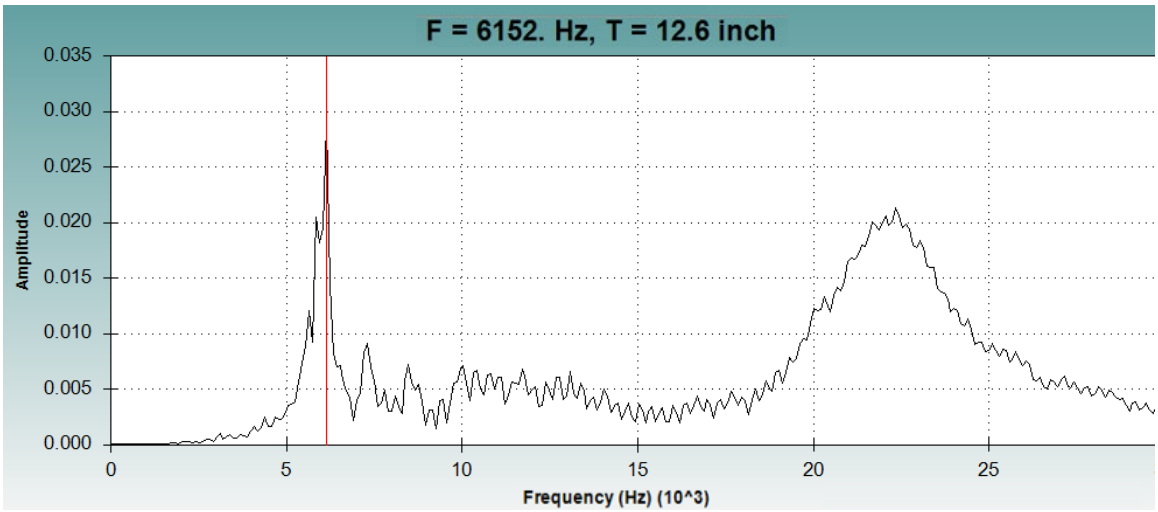

Figure 5-17: Spectral Response Over Shallow Delamination Showing Two Pronounced Excited Frequencies

Further visual analysis of the impact-echo data shown in Figure 5-16 revealed that impact-echo testing could be used to detect the 30-mil thick delaminations from DL3. Both

low (shown in red hues) and very high frequencies (shown in dark blue and purple hues) were measured over the shallow delaminations, distinct from the deck thickness response (shown in a light green hue). Further, high frequencies (shown in dark green and blue hues) were recorded over both deep delaminations, indicating that impact-echo testing can be used to distinguish deep delaminations from sound portions of deck.

Visual analysis of the impact-echo data collected over V1 shown in Figure 5-16 demonstrated difficulty in detecting the simulated voids with impact-echo testing. By and large, the impact-echo response of V1 was consistent, resulting in frequencies indicative of the deck thickness (shown in a light green hue). However, some lower frequencies (shown in yellow and orange hues) were measured over several of the voids. Checking the location of those responses against Detail 2 shown in Figure 5-10, it was observed that the lower frequencies were measured over 2–3 in. shallow voids, except for the deep, water-filled void 3 in. in diameter. Several hypotheses can be formulated from this observation. First, as none of the 1 in. diameter voids were seemingly detected in testing of Section 2 yet were detected in Phase 1 of this study, it may be hypothesized that the larger the grid spacing, the less likely it becomes that impact echo will detect a small void. Further, as it was observed in laboratory testing that the response indicative of a void may be offset from its true location, some of the undetected voids may have been identified should a smaller grid such as the 4 in. by 4 in. grid used from Phase 1 have been used. Moreover, as all but one of the voids identified from visual analysis were shallow, it is possible that given the same size testing grid, shallow voids are more readily identifiable than deep voids.

The spatial contour plot of impact-echo data collected from Section 3 of the test bridge deck are shown in Figure 5-18. Unlike in Section 2 in which the measured

frequency associated with the deck thickness was generally fairly consistent across all sound portions, that frequency seemed to vary somewhat more in Section 3. Visually inspecting the impact-echo response over sound deck in Figure 5-18, it was observed that the measured frequencies (ranging from green to purple hues) appeared to increase from west to east. From Equation 2.2, an increase in the dominant frequency of the thickness mode may be caused by a decrease in the deck thickness or an increase in the compression wave velocity. As it is not likely that the material or mechanical properties of the deck changed from east to west since the deck was produced from the same concrete, it is more likely that the increase in frequency was caused by a decrease in deck thickness from construction.

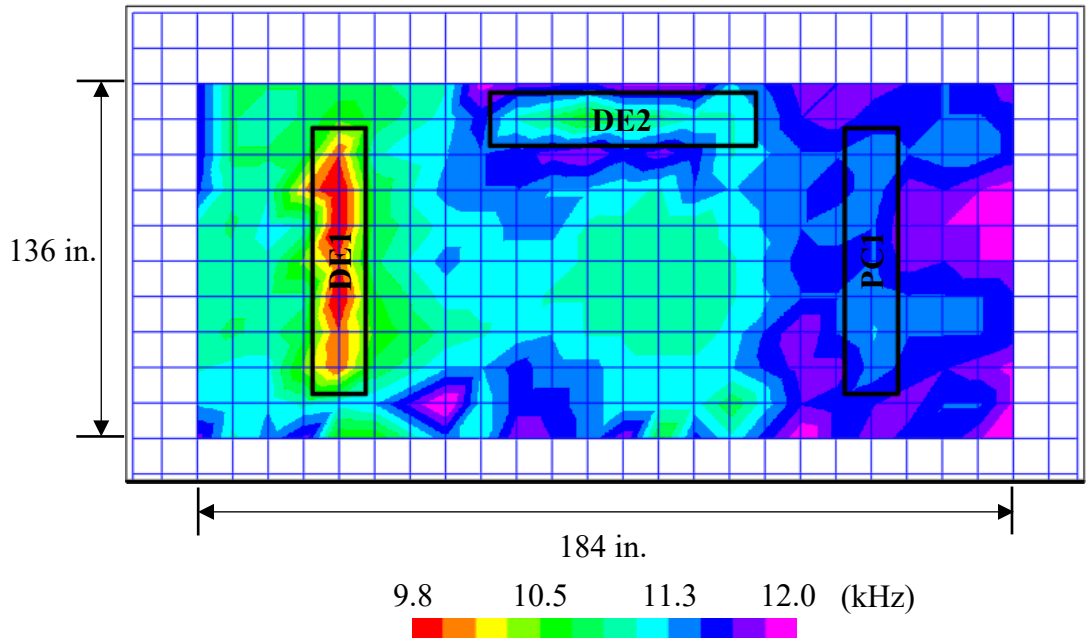

Figure 5-18: Section 3 Spatial Contour Plot of IE Data

Further visual analysis of the impact-echo response over the miniature slabs relative to that of sound portions of the deck revealed that impact echo was not as effective at locating concrete deterioration and poorly constructed concrete as in Phase 1 of this study.

During Phase 1 laboratory testing, frequencies measured over either defect were generally higher than that measured over sound concrete and resulted in a high degree of detectability. However, the results of impact-echo testing from Section 3 were contrary to these two observations. First, the frequencies measured over DE1 (shown in red, orange, and yellow hues) were low with respect to the frequencies typical of sound deck rather than high. Nonetheless, the impact-echo response over DE1 was still distinct from that of the surrounding sound deck facilitating visual identification. Second, DE2 and PC1 were not readily detectable from a visual analysis as frequencies measured over those defects were of similar magnitude to those of surrounding portions of sound deck. It is perplexing that no strong visual distinction existed between either of these defects and the sound deck as such distinctions had existed for the same defects in Phase 1 laboratory testing. Nonetheless, ROC analysis of impact-echo data numerically assessed whether DE2 and PC1 could be detected.

5.4.4 ROC Analysis of IE Data Results

The results of ROC analysis of IE data from Sections 2 and 3 of the test bridge deck are presented in Table 5-4. ROC analysis of the IE data from Section 2 resulted in 95.2% of the condition of the deck being correctly predicted. Further, 72.2% and 98.4% of the defective and sound portions of the deck were respectively identified. These high percentages of defective and sound deck correctly predicted reveal that impact echo is an effective NDT method for accurately assessing the condition of Section 2. Moreover, ROC analysis of the IE data from Section 3 allowed for 94.2% of locations being correctly classified as either sound or defective. Corresponding to this accuracy, 33.3% and 100.0% of the defective and sound portions of the deck were respectively identified. Despite

resulting in a high maximum accuracy rate and percentage of sound area detected, ROC analysis indicated that impact echo was not an effective method for locating the miniature slabs in Section 3.

Table 5-4: Accuracy of Receiver Operator Characteristic Analysis of IE Data

Section ID	Maximum Accuracy (%)	Defect Area Detected (%)	Sound Area Detected (%)
2	95.2	72.2	98.4
3	94.2	33.3	100.0

To further investigate which types of defects IE was effective in detecting, the breakdown of locations from each defect zone (e.g. DL1) correctly identified using the optimal ROC thresholds is presented in Table 5-5. Considering DL1, five of the ten locations of shallow delaminations were detected as opposed to nine of the ten locations of deep delaminations being detected. This result is somewhat surprising as laboratory testing from Phase 1 of this study demonstrated that impact-echo testing is generally more effective at mapping the areal extent of shallow delaminations rather than deep delaminations. Nonetheless, nine of the ten locations of shallow delaminations were detected from DL3 while only eight of the ten locations of deep delaminations were detected, further indicating the effectiveness of impact-echo testing in mapping the areal extent of shallow delaminations, given a small enough testing grid. It is possible that, the larger the area of a deep delamination, the better its correlation with IE data. Moreover, all 12 locations of shallow delaminations from DL2 were detected using optimal thresholds from ROC analysis.

Table 5-5: Breakdown of Defect Area Located from Optimal ROC Analysis of Test Bridge Deck

		DL1	DL2	DL3	V1	DE1	DE2	PC1
Shallow	Total Locations	10	12	10	6	7	7	7
	Detected Locations	5	12	9	3	7	0	0
	Accuracy (%)	50	100	90	50	100	0	0
Deep	Total Locations	10	n/a	10	6	n/a	n/a	n/a
	Detected Locations	9	n/a	8	0	n/a	n/a	n/a
	Accuracy (%)	90	n/a	80	0	n/a	n/a	n/a

n/a: Not Applicable

From Table 5-5, three of the six shallow voids were detected, consistent with the conclusion from visual analysis of impact-echo data that a significant percentage of shallow voids were undetected by testing. Furthermore, zero of the six deep voids were detected from ROC analysis of impact-echo data. This result that more shallow voids were detected than deep voids supports the hypothesis developed from visual analysis of impact-echo data that, given the same size testing grid, shallow voids are more readily detectable than deep voids of the same size.

Further, results from Table 5-5 regarding the detected area of miniature slabs DE1, DE2, and PC1 affirm conclusions developed from visual analysis of Section 3 impact-echo data. Note that the breakdown of defective locations for each of the three defects is presented in the "Shallow" row as the top of each miniature slab was in contact with the top reinforcement mat. While each of the three slabs had seven total defective locations within the testing grid, none of them were detected from impact-echo testing of DE2 and

PC1, yet all seven of them were detected from DE1. This result is consistent with the hypothesis from visual analysis that there existed no meaningful distinction in impact-echo response between data collected either over DE2 or PC1 and sound portions of Section 3. Nonetheless, the compelling visual distinction between IE data collected over DE1 and sound deck was also numerically affirmed from ROC analysis, indicating that IE was an effective NDT method for detecting the very highly air-entrained concrete of DE1.

5.4.5 Presentation and Visual Analysis of IRT Bridge Deck Data

IRT data collected from Sections 2 and 3 of the test bridge deck using the MOBA MTPS-100 are presented in Figure 5-19. Surface temperatures estimated with the camera were largely between 84 °F and 90 °F (shown in cyan and dark green hues). Nonetheless, several cool and hot zones existed relative to the foregoing temperature range. Pronounced higher surface temperatures were recorded over the sand/oil delamination in DL2. Thermal images captured from that location using the FLIR E60, provided in Figure 5-20, allow for an explanation for the higher estimated surface temperatures. From Figure 5-20, significant surface staining is observed directly over the sand/oil delamination. It is hypothesized that this staining was caused by the vertical movement of form oil used for delamination simulation during bridge deck curing. As the shape of the hot spot from the FLIR E60 image mimics that of the surface staining, and the staining may have caused significant localized differences in emissivity, it is plausible to believe that the hot spot was caused by the oil stains rather than a subsurface delamination. Moreover, since both the thick sand and sand/oil delaminations were clearly detectable from impact-echo testing, it is most likely that if the sand/oil delamination caused the hot spot to develop, a similar hot spot would have occurred over the thick sand delamination in DL2.

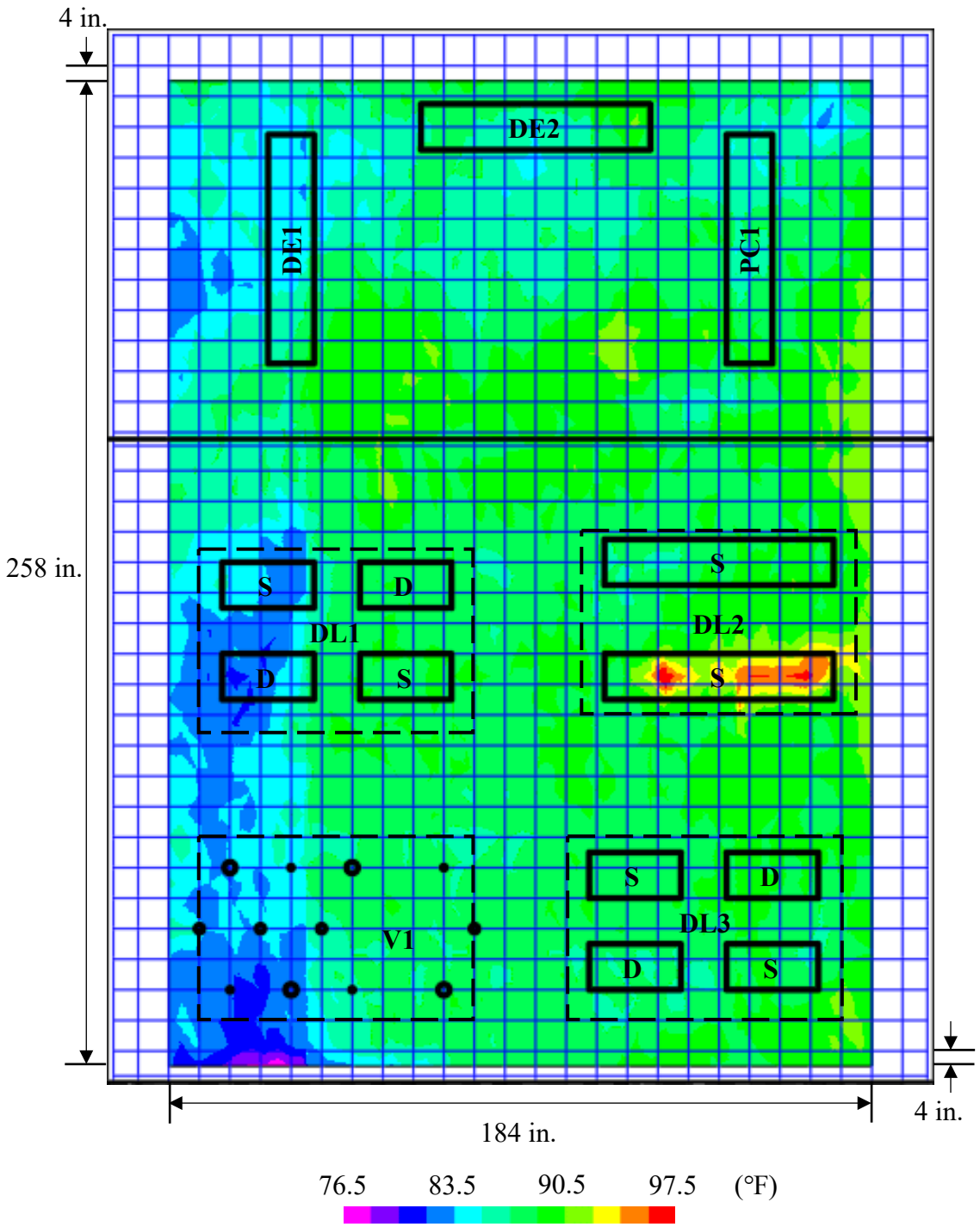

S: Shallow
D: Deep

Figure 5-19: Spatial Contour Plot of MOBA IRT Data

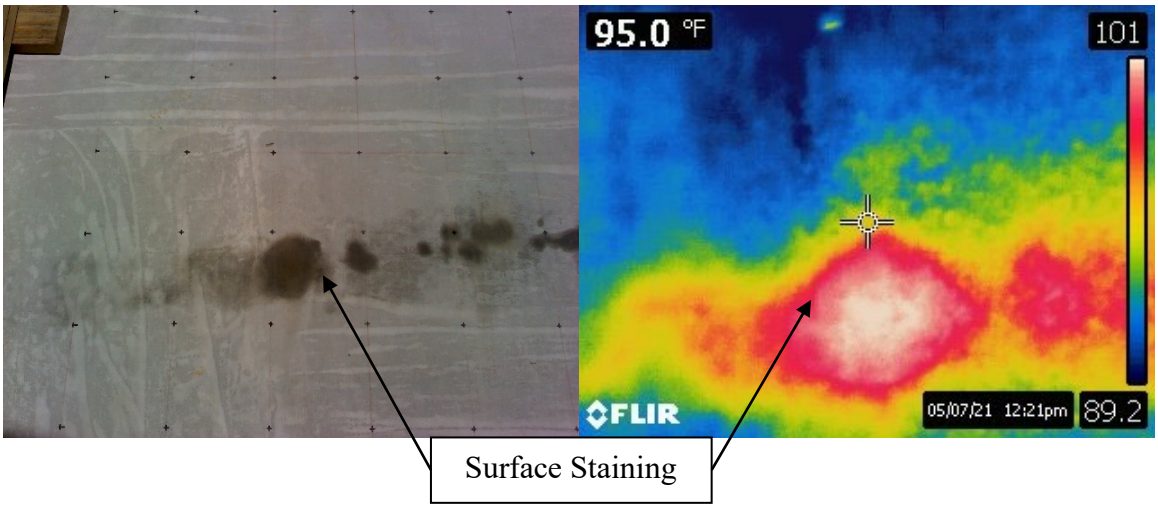

Figure 5-20: Increased Estimated Surface Temperature from Staining at DL2

Further visually analyzing the IRT data presented in Figure 5-19, a cold spot (shown in dark blue and purple hues) was observed on the west side of the deck, most concentrated in Section 2. Images captured of that location with the FLIR E60, presented in Figure 5-21, assist in explaining the presence of the cold spot. Immediately prior to IRT testing, the 3% sodium chloride solution could be seen leaking from the western pond wall from Section 1 into Section 2. The water in the solution had a cooling effect on the concrete surface, as evidenced by the thermal image shown in Figure 5-21. The shape of the surface solution mimicked that of the cold spot indicated by both thermal cameras. Moreover, upon drying, the salt present from the leaked solution had further stained the deck which may have affected the localized emissivity thus exacerbating any temperature differences. While this result does not necessarily explain the similar cold spot on the western edge of Section 3, it reinforces the sensitivity of IRT evaluations to surface conditions and staining. To further investigate the capabilities of the IRT method in assessing bridge decks, the test

deck would have to be cleaned and prepared to avoid staining and differential surface moisture contents.

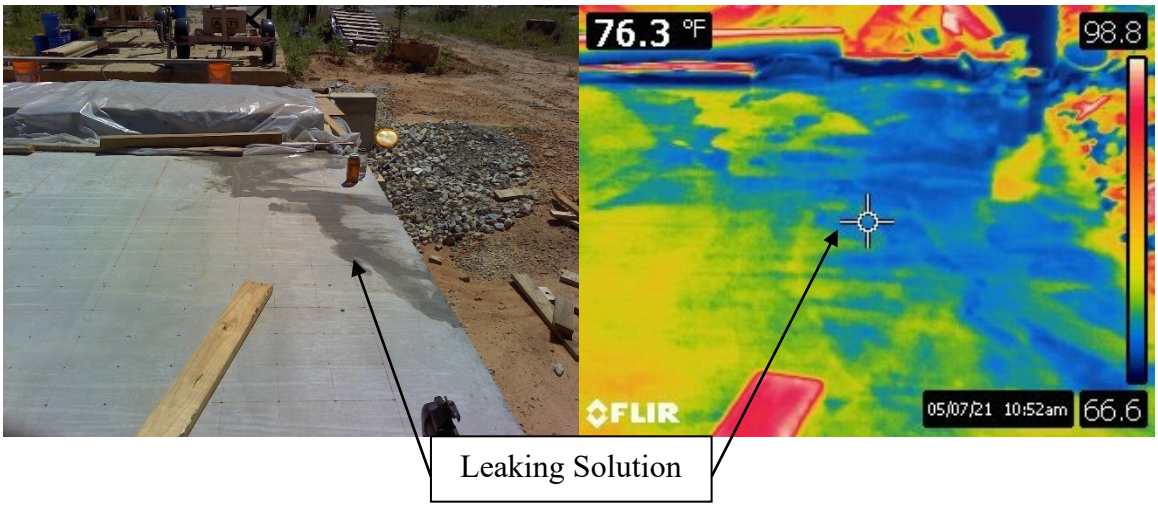

Figure 5-21: Surface Cooling Caused by Leaking Sodium Chloride Solution

5.5 Conclusions

Conclusions developed from GPR, IE, and IRT testing of the bridge deck constructed in Phase 2 of this study are provided in the following subsections.

5.5.1 Phase 2 GPR Conclusions

Regarding the defect-detection capabilities of GPR in bridge decks without overlays, when using the ASTM D6087 (2015) "Top Reinforcing Reflection Attenuation Technique" method, the following conclusions were made:

- GPR is incapable of detecting either shallow or deep unbonded delaminations as thick as 30 mil;
- GPR is incapable of detecting either deteriorated or poorly constructed concrete below the level of the top reinforcement mat; and

- GPR is incapable of detecting either shallow or deep voids as large as 3 in. in diameter, regardless of whether they are filled with water or clay.

5.5.2 Phase 2 IE Conclusions

In impact-echo evaluations of bridge decks without overlays, it was determined that:

- IE can detect both deep and shallow unbonded delaminations as thin as 10 mil;
- IE testing of shallow delaminations may excite two distinct frequencies, leading to either a positive or negative shift in dominant frequency relative to the deck thickness frequency;
- IE can detect shallow voids as small as 2 in. in diameter;
- Coarser grid spacing may result in deep voids becoming less detectable than shallow delaminations;
- Depending on deck thickness frequency variability and the severity of defect, concrete deterioration or poorly constructed concrete may not be detectable;
- Concrete deterioration can cause negative shifts in the dominant frequency excited during impact-echo testing.

5.5.3 Phase 2 IRT Conclusions

As in Phase 1 of this study, limited conclusions regarding IRT condition assessments of bridge decks could be developed based on work discussed in this chapter. Neither shallow or deep voids and delaminations nor deteriorated or poorly constructed concrete could be identified from midday IRT testing of the bridge deck. Nonetheless, surface cooling in select locations by water and local emissivity differences caused by oil stains and saltwater solution may have precluded an optimal evaluation of the capabilities of IRT. Regardless,

these factors were identified as having tangible effects on estimated surface temperatures that could obfuscate correct interpretation of IRT data.

Chapter 6: Summary, Conclusions, and Recommendations

6.1 Summary of Work

Due to loading, concrete deterioration mechanisms, poor-construction practices, and thermal effects, reinforced concrete bridge decks may deteriorate, threatening both the service life and structural integrity of the deck. Nondestructive test (NDT) methods are relied upon to assess the condition of bridge decks and locate defects in a noninvasive manner, thus mitigating the two foregoing threats. Nonetheless, uncertainty regarding the capabilities of a given NDT method to detect bridge deck defects, how best to post-process/interpret NDT data, and the influence of testing conditions on collected data have resulted in ineffective implementation and frustration with NDT methods. Motivated by these existing uncertainties, the Alabama Department of Transportation (ALDOT) funded an investigation to determine how best to implement ground-penetrating radar (GPR), impact echo (IE), infrared thermography (IRT), half-cell corrosion potential (HCP), and electrical resistivity (ER) to nondestructively evaluate the in-place condition of reinforced concrete bridge decks.

To accomplish this goal, small-scale laboratory specimens and a full-scale field bridge deck, all with simulated defects, were evaluated with the five NDT methods available to ALDOT. Receiver operator characteristic (ROC) and visual analyses were used to determine the types and characteristics of defects that could be detected by each NDT method. Available post-processing techniques and data-interpretation guidance were applied to data collected from tested elements, using ground truth information to determine

their appropriateness. Hypothesis testing, parametric studies, and other experiments were performed to investigate how testing conditions affected NDT data.

6.2 Conclusions and Recommendations

Conclusions and recommendations concerning the types of defects a given NDT method can detect, the influence of testing conditions on nondestructive evaluations, and how best to post-process and interpret NDT data are presented in the following subsections.

6.2.1 Defect-Detection Capabilities of NDT Methods

For this thesis recall that, as termed in Section 4.2.4, a "shallow" defect refers to one at the level of the top reinforcement mat while a "deep" defect refers to one at the level of the bottom reinforcement mat.

Ground-Penetrating Radar

In an effort to detect vertical cracking, delaminations, concrete deterioration, voids, corrosion of embedded steel reinforcement, and poorly constructed concrete using the ASTM D6087 (2015) "Top Reinforcing Reflection Attenuation Technique" method on depth-corrected data, GPR was found to have limited utility to reliably detect defects. The following additional conclusions are offered based on the work previously covered:

- GPR is not capable of detecting vertical cracks with widths of 50 mil or smaller and 3 in. deep;
- GPR cannot detect either unbonded or partially bonded delaminations with thicknesses of 3/32 in. or smaller, regardless of whether they are shallow or deep;
- GPR cannot detect either concrete deterioration or poorly constructed concrete below the top reinforcement mat;

- GPR cannot detect shallow or deep voids as large as 3 in. in diameter, regardless of whether they are filled with clay or water;
- GPR can detect water-filled voids within the cover layer as small as 1/2 in. in diameter; and
- GPR is capable of detecting environments of active chloride-induced corrosion in bridge decks.

Impact Echo

Considering the NDT methods employed in this study to locate delaminations, concrete deterioration, voids, and poorly constructed concrete, ground-coupled impact echo was found to be the most effective NDT method for defect detection. Further, it is concluded that:

- IE can detect unbonded, shallow or deep delaminations with thicknesses of 10 mil or larger;
- IE can detect 10-mil thick (or larger), shallow delaminations with 50% unbonded area;
- IE can detect 50-mil thick (or larger), deep delaminations with 75% unbonded area;
- The spatial correlation between the true delamination location and predicted location from IE is much stronger for shallow than deep delaminations;
- IE can detect concrete deterioration and poorly constructed concrete below the level of the top reinforcement mat provided that the defects are sufficiently severe; and
- With a sufficiently fine grid, IE can detect shallow and deep voids or voids in the cover layer as small as 1/2 in. in diameter but may not precisely locate them.

Half-Cell Corrosion Potential

Within this study, the half-cell corrosion potential method was found to be the most accurate NDT method for detecting actively corroding reinforcing steel. When deployed in ideal conditions and data are interpreted with care, the half-cell corrosion potential method can be used to locate active corrosion with a high degree of confidence.

Electrical Resistivity

From testing of laboratory specimens subjected to accelerated chloride-induced corrosion (discussed in Chapter 4), it was determined that the electrical resistivity method is not appropriate for detecting regions of active corrosion.

6.2.2 Influence of Testing Conditions on NDT Data

Ground-Penetrating Radar

Based on hypothesis testing presented in Chapter 4 of this document, the following conclusions are offered regarding the influence of testing conditions on GPR data:

- The position of the antenna either directly over or between parallel reinforcement does not influence the measured reflection amplitudes when data collection is oriented perpendicular to the top bar in the top reinforcement mat;
- The position of the antenna either directly over or between parallel reinforcement does influence the measured reflection amplitudes when data collected is oriented perpendicular to the bottom bar in the top mat. The mean of reflection amplitudes collected directly over parallel reinforcement is statistically different than that of reflection amplitudes collected between parallel reinforcement; there is no significant difference in variance between the two groups;

- For the same bridge deck, GPR data collected when the deck is moist will exhibit greater variance and a lower (more negative) mean than data collected when the bridge is drier.

Half-Cell Corrosion Potential

Based on testing conducted in Chapter 4 of this document, the following conclusions were developed regarding the influence of testing conditions on HCP data:

- Deck moisture content has a pronounced influence on HCP data. All else being equal, an increase in moisture content causes half-cell potentials to decrease (become more negative). For an equal increase in moisture content, the magnitude of this decrease is not equivalent between regions of passive and actively corroding reinforcement;
- The higher the moisture content of a bridge deck, the more distinct HCP values from passive and active reinforcement become from one another;
- Depending on the moisture content of the concrete, delaminations can disrupt the flow of current between the two half-cells when using the HCP method. Delaminations that are air-filled result in abnormally high localized electrical resistivity. When a delamination is water filled, it creates a localized resistivity signal more similar to that of moist concrete.

Electrical Resistivity

From testing of chloride-contaminated specimens with both active and passive reinforcement in Chapter 4, it is concluded that:

- The moisture content of a bridge deck has a strong influence on the electrical resistivity of concrete. All else being equal, the lower the moisture content, the higher the electrical resistivity;
- Low moisture contents and chloride ion concentrations result in greater variability in electrical resistivity than higher moisture contents and chloride ion concentrations.

Infrared Thermography

From testing of laboratory specimens and a full-scale bridge deck with simulated defects (discussed in Chapters 4 and 5 respectively), the following conclusions can be made regarding the influence of testing conditions on IRT data:

- Surface staining or other features that significantly affect the deck emissivity can cause significant surface temperature differentials which may lead to false predictions of deck condition; and
- Water has a cooling effect on the deck surface temperature such that false predictions of deck condition could be developed should select portions of the deck be exposed to water.

6.2.3 Processing and Interpretation of NDT Data

Ground-Penetrating Radar

Considering the influence of testing conditions on GPR data and the evaluation of available interpretation criteria of GPR data from Chapter 4, the following conclusions can be drawn:

- Given the influence of moisture content on GPR data, the use of universal, constant threshold values to discern between sound and deteriorated portions of bridge decks is not applicable to the non-saturated concretes tested in this study; and
- Thresholds developed from BridgeScan (2017) recommendations to detect deck deterioration did not result in any known defects being identified. Accordingly, it is recommended that ALDOT does not use those thresholds to identify potential defective concrete in bridge decks based on GPR test results.

Half-Cell Corrosion Potential

Based on evaluation of the effectiveness of available HCP data, the following conclusions can be made:

- The numeric threshold values provided in ASTM C876 (2015) to classify active and passive reinforcement corrosion regions within the concrete are not reliable predictors of the condition of embedded, uncoated steel reinforcement in bridge decks;
- The most negative potential corresponding to passive reinforcement (i.e. no corrosion observed) measured in laboratory testing of moist, chloride-contaminated concrete was -350 mV. Accordingly, in bridge deck condition assessments, there exists a high degree of probability that potentials more negative than -350 mV are not associated with passive reinforcement.
- When a bridge deck is tested in the air-dried state, it may be difficult to differentiate between regions with passive and active reinforcement corrosion within the bridge deck without statistical analysis. This decision making can be facilitated through use of the segmented linear regression algorithm proposed by Muggeo (2017).

Through the use of this algorithm, prediction accuracies as low as 1.6 percentage points lower than the maximum possible accuracy determined by ROC analysis were attained from datasets of air-dried specimens.

Electrical Resistivity

Based on ER testing of laboratory specimens discussed in Chapter 4, the following conclusions are offered:

- All else being equal, the electrical resistivity from passive and active reinforcement corrosion portions of bridge decks can be so similar that they are practically indiscernible from one another;
- If a half-cell corrosion potential measurement at a location indicates a passive-state of reinforcement corrosion, then electrical resistivity can be used to assess the risk of corrosion. Else, it may be used to estimate the rate of corrosion; and
- After reinforcement depassivation has occurred, the Broomfield and Millard (2002) interpretation criteria seem appropriate to predict the chloride-induced corrosion rate.

6.2.4 Recommendations for NDT Method Implementation

Among the NDT methods investigated in this study, impact-echo and half-cell corrosion potential methods offer the most value in determining the in-place condition of a bridge deck that could be defective with delaminations, corrosion of embedded reinforcing steel, voids, concrete deterioration, and/or poorly constructed concrete. Nonetheless, comments and recommendations concerning the implementation of each NDT method for bridge deck condition assessment are offered below.

Ground-Penetrating Radar

Considering the bridge deck defects simulated in this study, GPR may be deployed to locate active chloride-induced reinforcement corrosion or voids in the top cover region of the deck. GPR is benefited by its relatively rapid testing ability, especially when using air-launched equipment, with respect to the HCP method. Nonetheless, it would be good practice to cross-examine GPR predictions of defects with those determined with HCP and IE, which are more reliable indicators of active reinforcement corrosion and voids, respectively.

GPR evaluations should not be conducted when it is believed the moisture content of a bridge deck varies significantly from one location to another. Should this situation be unavoidable, distinct portions of the deck of suspected differing moisture contents should be analyzed separate from one another. Furthermore, it is recommended that, when using the ASTM D6087 (2015) "Top Reinforcing Reflection Attenuation Technique" method, data be collected perpendicular to the top bar in the top reinforcement mat to preclude the influence of reinforcement intersections on GPR data. If data cannot be collected in this manner (e.g. in an evaluation of a steel truss bridge with air-launched GPR equipment), it is recommended that data be separated into two subsets, each respectively containing data collected either directly over or between parallel reinforcement.

Moreover, it is not recommended that universal or BridgeScan (2017) thresholds be used to interpret GPR data. Rather, GPR data should be statistically analyzed to use them as indicators of the condition of a bridge deck.

Impact Echo

Ground-coupled impact echo should be deployed to locate delaminations, voids, concrete deterioration, or poorly constructed concrete in bridge decks. Among the NDT methods evaluated in this study, there are no other methods capable of detecting the wide range of deck defects of varying characteristics as is detectable by the impact echo method. If accuracy in detecting these defects is of primary concern, then impact echo should be the primary NDT method utilized. Nonetheless, depending upon the equipment used and the degree to which the deck surface needs to be prepared (e.g. grinding of rough surface texture) to ensure sufficient instrument contact, impact-echo testing can be very slow. Thus, the benefit of high accuracy needs to be considered in tandem with the relative slowness of the impact echo method when weighing options for bridge deck condition assessment.

Care should be taken when interpreting impact-echo data to be cognizant of the effects of testing location relative to other bridge deck features. The dominant frequency excited during testing near the boundaries of a deck (e.g. its edges and at expansion joints) may be somewhat different than that excited away from the edges. Furthermore, the presence of girders or other structural elements (e.g. the web of a box girder) below the testing location may disturb the amplitude-frequency spectra such that clear selection of a dominant frequency may not be possible.

Half-Cell Corrosion Potential

In moist conditions and with proper data interpretation, the HCP method can provide the most accurate prediction of actively corroding reinforcement, among the NDT methods used in this study. Nonetheless, lane-closures are required to deploy the HCP method

which should be considered when weighing the costs/benefits of the HCP method against other methods such as GPR which may not require those closures.

HCP data should not be collected if a deck is dry, because in the dry state it is difficult to use measured potentials as indicators of the corrosion state. Rather it will be best to deploy the HCP method when the bridge deck is fairly moist as in this state greater accuracy in deck condition predictions from the HCP data will be obtained which will reduce the difficulty in data interpretation. HCP data should be assessed by using both spatial contour plots and cumulative probability distributions presented on normal probability graphs. Use of the segmented linear regression algorithm proposed by Muggeo (2017) is recommended to assist in selecting appropriate thresholds for data interpretation. The numeric threshold values provided in ASTM C876 (2015) to classify active and passive reinforcement corrosion regions within the concrete should not be relied upon to assess the state of corrosion of bridge deck reinforcement.

As with GPR, given the strong influence of moisture content on HCP data, should it be known that locations on a bridge deck are of significantly dissimilar moisture content, they should be analyzed separately from one another.

Electrical Resistivity

Depending on whether the state of embedded reinforcement corrosion is passive or active, electrical resistivity should be measured to evaluate the risk of corrosion or predict the corrosion rate. As knowledge of the corrosion state at a location is required to properly interpret a resistivity measurement, it is intuitive to deploy the HCP method at the same time as the ER method. Furthermore, as with the HCP method, ER data obtained from

locations of significantly different moisture content on the deck should be analyzed separately.

Infrared Thermography

When conducting IRT evaluations of bridge deck, an operator must be aware of any phenomena which could significantly affect estimated surface temperatures to use the method for defect detection. Surface staining can have a pronounced influence on estimated surface temperatures, as they cause a localized anomaly in deck emissivity. Stains should be removed before initiating IR testing, if possible. Alternatively, photographs consistent with the locations of IRT data need be collected such that stained regions can be identified in post-processing and disregarded. Furthermore, operators should be aware of the presence of locations on a deck which may have recently been cooled by water or other liquids.

6.3 Future Research

From the work presented in this thesis, the following recommendations for future research to be conducted are offered:

- Among the NDT methods discussed herein, there exist much guidance and many empirical thresholds aiming to assist in interpretation of NDT data. Most of this guidance has been developed within the last few decades and needs to be further assessed and improved. Furthermore, bridge deck moisture content was identified as a common factor capable of affecting NDT data and accordingly potentially impacting the prediction accuracy when using existing threshold cutoff values. Thus, it is recommended that further statistical approaches be developed to handle

NDT data processing in a manner tailored to the properties and conditions surrounding a given bridge deck.

- NDT methods such as impact echo and half-cell corrosion potential reflect a high degree of accuracy in detecting bridge deck defects; however, they may be limited to varying extents by their relatively slow rate of data collection compared to GPR. Thus, further technological innovations in the application of the two aforementioned technologies to make them faster while not sacrificing accuracy could allow for more cost-efficient bridge deck condition assessments.
- Surface staining and other phenomena affecting the bridge deck temperature distribution measured using IRT during this study highlighted the difficulties present when using this method. Nonetheless, the capability of the IRT method to detect the simulated defects in this study could not be evaluated distinctly from the foregoing factors affecting the temperature distribution within the time constraints of this project. Accordingly, future work should aim to definitively determine which types of defects are detectable using IRT so NDT operators can make informed decisions regarding its utility.

References

ACI. 2018. *ACI Concrete Terminology*. ACI CT-18. American Concrete Institute, Farmington Hills, Michigan.

ACI Committee 222. 2001. *Protection of Metals in Concrete Against Corrosion*. Report ACI 222R-01. American Concrete Institute, Farmington Hills, Michigan.

ACI Committee 228. 2013. *Report on Nondestructive Test Methods for Evaluation of Concrete in Structures*. Report ACI 228.2R-13. American Concrete Institute, Farmington Hills, Michigan.

ACI Committee 318. 2019. *Building Code Requirements for Structural Concrete*. Standard and Report ACI 318-19. American Concrete Institute, Farmington Hills, Michigan.

Alumusallam, A., A. Al-Gahtani, A. Aziz, F. Dakhil, and Rasheeduzzafar. 1996. "Effect of Reinforcement Corrosion on Flexural Behavior of Concrete Slabs*." Journal of Materials in Civil Engineering* 8(3): 123–127.

ASTM International. 2013. *Standard Test Method for Detecting Delaminations in Bridge Decks Using Infrared Thermography*. D4788-03. West Conshohocken, PA.

ASTM International. 2015. *Standard Test Method for Corrosion Potentials of Uncoated Reinforcing Steel in Concrete*. C876-15. West Conshohocken, PA.

ASTM International. 2015. *Standard Test Method for Evaluating Asphalt-Covered Concrete Bridge Decks Using Ground Penetrating Radar*. D6087-08. West Conshohocken, PA.

ASTM International. 2020. *Standard Test Method for Compressive Strength of Cylindrical Concrete Specimens*. C39/C39M-20. West Conshohocken, PA.

Bacon D.W., and D.G. Watts. 1971. "Estimating the Transition Between Two Intersecting Straight Lines." *Biometrika* 58: 525–534.

Barnes, C.L., and J. Trottier. 2004. "Effectiveness of Ground Penetrating Radar in Predicting Deck Repair Quantities." *Journal of Infrastructure Systems* 10(2): 67–76.

Barnes, C.L., J. Trottier, and D. Forgeron. 2008. "Improved Concrete Bridge Deck Evaluation Using GPR by Accounting for Signal-Depth Amplitude Effects." *NDT&E International* 41: 427–433.

Broomfield, J., and S. Millard. 2002. "Measuring Concrete Resistivity to Assess Corrosion Rates." *The Concrete Society/Institute of Corrosion, Current Practice Sheet No. 128*.

Cheng, C., and M. Sansalone. 1993. "The Impact-Echo Response of Concrete Plates Containing Delaminations: Numerical, Experimental and Field Studies." *Materials and Structures* 26: 274–285.

Cheng, C., and M. Sansalone. 1995. "Determining the Minimum Crack Width that can be Detected using the Impact-echo Method. Part 1: Experimental Study." *Materials and Structures* 28(2): 74–82.

Cheng, C., and M. Sansalone. 1995. "Determining the Minimum Crack Width that can be Detected using the Impact-echo Method. Part 2: Numerical Fracture Analyses." *Materials and Structures* 28(3): 125–32.

Cheng, C., T. Cheng, and C. Chiang. 2008. “Defect Detection of Concrete Structures Using Both Infrared Thermography and Elastic Waves.” *Automation in Construction* 18: 87–92.

Clemeña, G.G. 1992. *Benefits of Measuring Half-Cell Potentials and Rebar Corrosion Rates in Condition Surveys of Concrete Bridge Decks.* FHWA/VA-92R16. Virginia Department of Transportation, Charlottesville, Virginia.

COST 509. 1997. *Corrosion and Protection of Metals in Contact with Concrete*. Final Report. European Commission, Directorate-General XII Science, Research and Development.

Davis, J., Y. Huang, S.G. Millard, and J.H. Bungey. 2003. “Determination of Dielectric Properties of in situ Concrete at Radar Frequencies.” *In Proc. International Symposium Non-Destructive Testing in Civil Engineering (NDT-CE)*. Berlin, Germany.

Dinh, K., N. Gucunski, J. Kim, and T.H. Duong. 2016. “Understanding Depth-amplitude Effects in Assessment of GPR Data from Concrete Bridge Decks.” *NDT&E International* 83: 48–58.

Elsener, B., S. Müller, M. Suter, and H. Böhni. 1990. “Corrosion Monitoring of Steel in Concrete – Theory and Practice.” *In Proc. the Third International Symposium on ‘Corrosion of Reinforcement in Concrete Construction’*. Warwickshire, United Kingdom.

Emmons, P.H. 1993. *Concrete Repair and Maintenance Illustrated*. RSMeans, Kingston, Massachusetts.

Ertel J.E., E.B. Fowlkes. 1976. “Some Algorithms for Linear Spline and Piecewise Multiple Linear Regression.” *Journal of the American Statistical Association* 71: 640–648.

Feliú, S., J.A. Gonzálex, and C. Andrade. 1996. "Electrochemical Methods for On-Site Determinations of Corrosion Rates of Rebars." *Techniques to Assess the Corrosion Activity of Steel Reinforced Concrete Structures,* ASTM STP 1276. N. Berke, E. Escalante, C. Nmai, and D. Whiting. Eds., American Society for Testing and Materials.

FLIR. 2014. *Technical Data FLIR E60 (incl. Wi-Fi)*. Wilsonville, Oregon.

Gössl C., H. Küchenhoff. 2001. "Bayesian Analysis of Logistic Regression with an Unknown Change Point and Covariate Measurement Error." *Statistics in Medicine* 20: 3109–3121.

Gowers, K.R., and S.G. Millard. 1999. "Measurement of Concrete Resistivity for Assessment of Corrosion Severity of Steel Using Wenner Technique." *ACI Materials Journal* 96 (5): 536–541.

GSSI. 2017. *BridgeScan Handbook GPR Inspection of Bridge Decks*. Nashua, New Hampshire.

Gucunski, N., A. Imani, F. Romero, S. Nazarian, D. Yuan, H. Wiggenhauser, P. Shokouhi, A. Taffe, and D. Kutrubes. 2013. *Nondestructive Testing to Identify Concrete Bridge Deck Deterioration*. SHRP 2 Report S2-R06A-RR-1. Transportation Research Board, Washington, D.C.

Gumbel, E.J. 1954. "Statistical Theory of Extreme Values and Some Practical Applications." *Applied Mathematics Series* 33, National Bureau of Standards, Washington, D.C.

Guo, A., H. Li, X. Guan, and H. Li. 2015. "Experimental Investigation of the Cyclic Performance of Reinforced Concrete Piers with Chloride-induced Corrosion in Marine Environment." Engineering Structures 105: 1–11.

Guthrie, W.S., J.L. Larsen, J.S. Baxter, and B.A. Mazzeo. 2019. “Automated Air-Coupled Impact Echo Testing of a Concrete Bridge Deck from a Continuously Moving Platform.” *Journal of Nondestructive Evaluation* 38(32).

Ham, S., H. Song, M.L. Oelze, and J.S. Popovics. 2016. “A Contactless Ultrasonic Surface Wave Approach to Characterize Distributed Cracking Damage in Concrete.” *Ultrasonics* 75: 46–57.

Hong, S., H. Wiggenhauser, R. Helmerich, B. Dong, P. Dong, and F. Xing. 2017. “Long-term Monitoring of Reinforcement Corrosion in Concrete Using Ground Penetrating Radar.” *Corrosion Science* 114: 123–132.

Janku, M., P. Cikrle, J. Grošek, O. Anton; and J. Stryk. 2019. “Comparison of Infrared Thermography, Ground-Penetrating Radar and Ultrasonic Pulse Echo for Detecting Delaminations in Concrete Bridges.” *Construction and Building Materials* 225: 1098–1111.

Jayaprakash, J., E. Pournasiri, and F. De’nan. 2012. “Effect of Bond Strength on Fiber Reinforced Polymer Enveloped Concrete Cylinders with Rebars Exposed to Corrosion Activity.” *Journal of Reinforced Plastics and Composites* 31(12): 845–854.

Jol, H.M. 2008. *Ground Penetrating Radar Theory and Applications*. Elsevier Science, Amsterdam, the Netherlands.

Kee, S., T. Oh, J.S. Popovics, R.W. Arndt, and J. Zhu. 2012. “Nondestructive Bridge Deck Testing with Air-Coupled Impact-Echo and Infrared Thermography.” *Journal of Bridge Engineering* 17(6): 928–939.

Koch, G.H., Brongers, M.P.H., Thompson, N.G., Virmani, Y.P., and Payer, J.H. 2002. “Corrosion Costs and Preventive Strategies in the United States.” *Rep. No. FHWA-RD-01-156*.

Kosmatka, S.H., and M.L. Wilson. 2011. *Design and Control of Concrete Mixtures.* The Portland Cement Association, Stokie, Illonois.

Kunst A.E., C.W.N. Looman, and J.P. Mackenbach. 1993. “Outdoor Air Temperature and Mortality in the Netherlands: a Time Series Analysis.” *American Journal of Epidemiology* 137: 331– 341.

Langford, P., and J. Broomfield. 1987. “Monitoring the Corrosion of Reinforcing Steel.” *Construction Repair* 1(2): 32–36.

Lemieux, M., R. Gagné, B. Bissonnette, and M. Lachemi. 2005. “Behavior of Overlaid Reinforced Concrete Slab Panels Under Cyclic Loading—Effect of Interface Location and Overlay Thickness.” *ACI Structural Journal* 102(3): 454–461.

Lin, S., and M. Sansalone. 1996. “Impact-Echo Studies of Interfacial Bond Quality in Concrete: Part 1—Effects of Unbonded Fraction Area.” *ACI Materials Journal* 93(3): 223–231.

Lin, S., D. Meng, H. Choi, S. Shams, and H. Azari. 2018. “Laboratory assessment of nine methods for nondestructive evaluation of concrete bridge decks without overlays.” *Construction and Building Materials* 188: 966–982.

Martino, N., K. Maser, R. Birken, and M. Wang. 2015. “Determining Ground Penetrating Radar Amplitude Thresholds for the Corrosion State of Reinforced Concrete Bridge Decks.” *Journal of Environmental and Engineering Geophysics* 19(3): 175–181.

Meng, D., S. Lin, and H. Azari. 2020. “Nondestructive Corrosion Evaluation of Reinforced Concrete Bridge Decks with Overlays: An Experimental Study.” *Journal of Testing and Evaluation* 48(1): 516–537.

Mehta, P.K., and J.M. Monteiro. 2013. *Concrete Microstructure, Properties, and Materials*. McGraw, New York, New York.

MOBA. 2014. *Specification IR Thermal Profile Sensor MTPS-100*. Limburg, Germany.

MOBA. 2014. *User Manual PAVE-IR Scan*. Limburg, Germany.

Muggeo, V.M.R. 2003. “Estimating Regression Models with Unknown Break-points.” *Statistics in Medicine* 22: 3055–3071.

Muggeo, V.M.R. 2017. “Interval Estimation for the Breakpoint in Segmented Regression: a Smoothed Score-based Approach.” *Australian & New Zealand Journal of Statistics* 59(3): 311–322.

Nadelman, E.I., and K.E. Kurtis. 2014 “A Resistivity-Based Approach to Optimizing Concrete Performance.” *Concrete International* 36(5). Farmington Hills, MI: American Concrete Institute.

Nowak, A.S., and K.R. Collins. 2013. *Reliability of Structures*. CRC Press, Boca Raton, Florida.

Olson Instruments, Inc. 2015. *Freedom Data PC Platform System Reference Manual*. Wheat Ridge, Colorado.

Pashoutani, S., and J. Zhu. 2020. “Ground Penetrating Radar Processing for Concrete Bridge Deck Evaluation.” *Journal of Bridge Engineering* 25(7): 04020030.Polder, R.B. 2001. “Test

Methods for on Site Measurement of Resistivity of Concrete — a RILEM TC-154 Technical Recommendation." *Construction and Building Materials* 15: 125–131.

Popovics, J.S., and J.L. Rose. 1994. "A Survey of Developments in Ultrasonic NDE of Concrete." *IEEE Transactions of Ultrasonics, Ferroelectrics, and Frequency Control* 41(3): 1–4.

Proceq SA. 2017. *Operating Instructions Concrete Durability Testing*. Schwerzenbach, Switzerland.

Proceq SA. 2017. *Profometer Operating Instructions*. Schwerzenbach, Switzerland.

Raja, B.N.K., S. Miramini, C. Duffield, M. Sofi, P. Mendis, and L. Zhang. 2020. "The Influence of Ambeint Conditions in Detecting Bridge Concrete Deck Delamination Using Infrared Thermography (IRT)." *Structural Control Health Monit*., e2506.

RILEM TC 154-EMC. 2003. "'Electrochemical Techniques for Measuring Metallic Corrosion' Reommendations." *Materials and Science* 36: 461–471.

Sansalone, M., and N.J. Carino. 1989. "Detecting Delaminations in Concrete Slabs with and without Overlays Using the Impact-Echo Method." *ACI Materials Journal* 86(2).

Sansalone, M. 1997. "Impact Echo: The Complete Story." *ACI Structural Journal* 94(6): 777–785.

Scott, M., A. Rezaizadeh, and M. Moore. 2001. *Phenomenology Study of HERMES Ground-Penetrating Radar Technology for Detection and Identification of Common Bridge Deck Features*. Federal Highway Administration, Rep. No. FHWA-RD-01-090.

Spellman, D.L., and R.F. Stratfull. 1973. "Concrete Variables and Corrosion Testing." *Highway Research Record* 423: 27–45.

Stasinopoulos D.M., and R.A. Rigby. 1992. “Detecting Break Points in Generalized Linear Models.” *Computational Statistics and Data Analysis* 13: 461–471.

Stefan, M., V. Salvador, and S. David. 2018. “Validation of Artificial Defects for Non-destructive Testing Measurements on a Reference Structure.” *In Proc., 5th Int. Conference on Concrete Repair, Rehabilitation and Retrofitting*. Cape Town, South Africa.

Stratfull, R.F. 1973. “Half-Cell Potentials and the Corrosion of Reinforcing Steel in Concrete.” *Highway Research* 433: 12–20.

Sultan, A.A., and G.A. Washer. 2018. “Reliability Analysis of Ground-Penetrating Radar for the Detection of Subsurface Delamination.” *Journal of Bridge Engineering* 23(2): 1–11.

Tishler A., and I. Zang. 1981. “A New Maximum Likelihood Algorithm for Piecewise Regression.” *Applied Statistics* 76: 980–987.

Ulm K. 1991. “A Statistical Method for Assessing a Threshold in Epidemiological Studies.” *Statistics in Medicine* 10: 341– 349.

Vaghefi, K., T.M. Ahlborn, D.K. Harris, and C.N. Brooks. 2013. “Combined Imaging Technologies for Concrete Bridge Deck Condition Assessment.” *Journal of Performance of Construction Facilities* 29(4).

Vassie, R.P.W. 1978. *Evaluation of Techniques for Investigating the Corrosion of Steel in Concrete*. TRRL Supplementary Report 39, Transport and Road Research Laboratory, London, England.

Vermont J., J.L. Bosson, P. Francois, R.C. Rue, and J.A. Demongeot. 1991. Strategies for Graphical Threshold Determination." *Computer Methods and Programs in Biomedicine* 35:141–150.

Washer, G., R. Fenwick, and N. Bolleni. 2010. "Effects of Solar Loading on Infrared Imaging of Subsurface Features in Concrete." *Journal of Bridge Engineering* 15(4): 384–390.

Wong T.W.P, and C.S. Poon. 2018. "Laboratory Validation of Corrosion-induced Delamination in Concrete by Ground Penetrating Radar." *In Proc., the 17th International Conference on Ground Penetrating Radar*. Rapperswil: Institute of Electrical and Electronics Engineers.

Yodsudjai, W., and T. Pattarakittam. 2017. "Factors Influencing Half-Cell Potential Measurement and its Relationship with Corrosion Level." *Measurement* 104: 159–168.

Yoon, I., and C. Change. 2020. "Effect of Chloride on Electrical Resistivity in Carbonated and Non-Carbonated Concrete." *Applied Sciences* 10, 6272.

Appendix A: Extracted Cores from Laboratory Specimens not Shown in Main Text

The extracted cores collected from each laboratory test specimen not shown in Section 4.5.1 are presented hereinafter in this appendix. Cores are shown in the same order as that in which the specimens were presented in Chapter 5. 'X' and 'Y' shown under each image designate the spatial coordinates from which each core was extracted, in accordance with the grid and origin system defined in Section 4.3.

On each of the following core images shown, alphabetical symbols may be used as applicable to indicate a note regarding the status of the core. For example, the symbol 'S' indicates that the core was completely separated on either side of the horizontal cracking plane shown. This symbology legend used for indicating core condition is shown below. Special conditions unique to a given core are addressed within figures. Note that more than one condition may be applicable for a given core.

S: a core that is completely separated on either side of the horizontal cracking plane;

D: a core that was damaged during extraction; and

P: a core that reflects a partial-depth removal of the deck. The remainder of the core could not be removed from the coring hole.

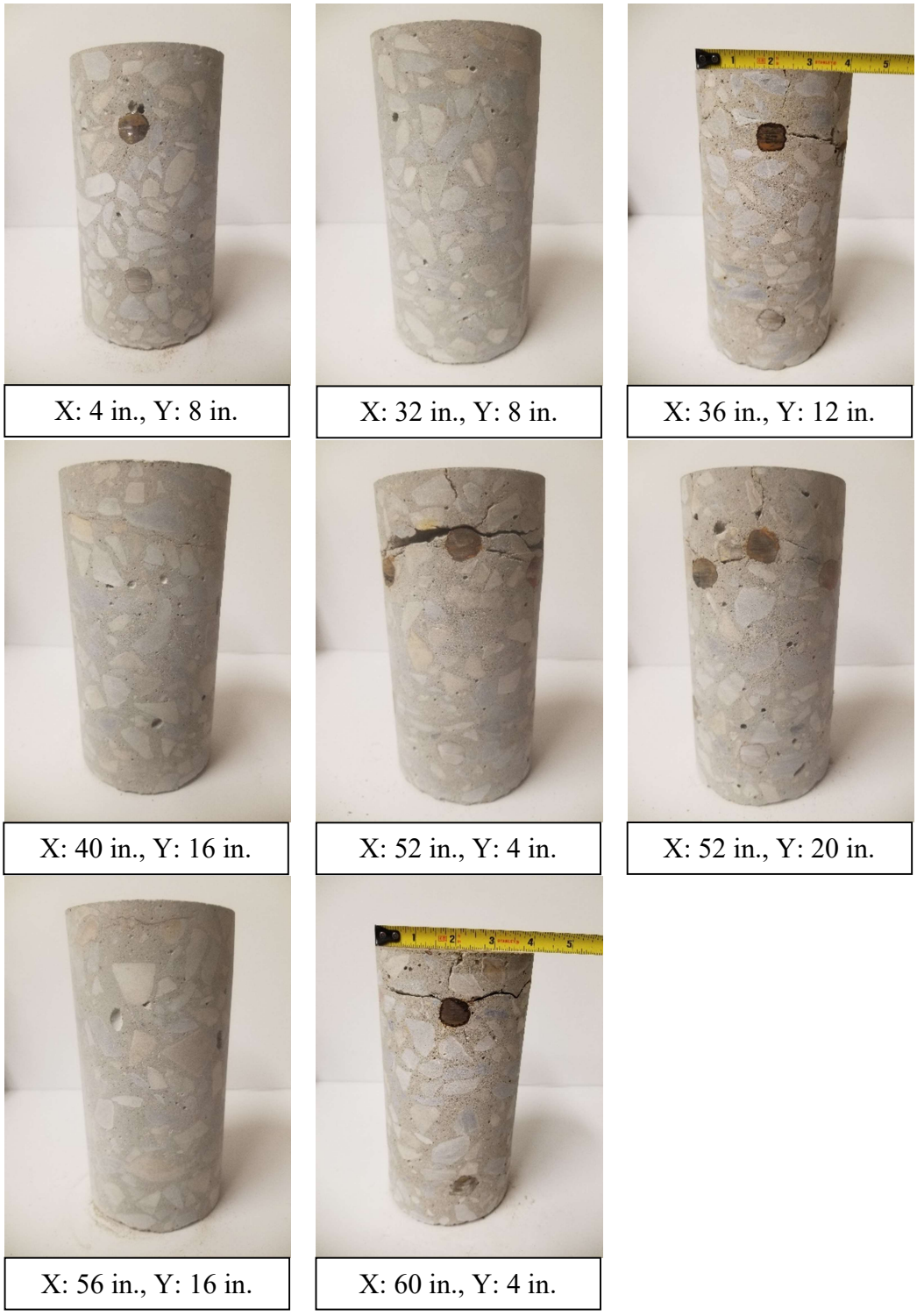

Figure A1: Specimen C1 Extracted Cores

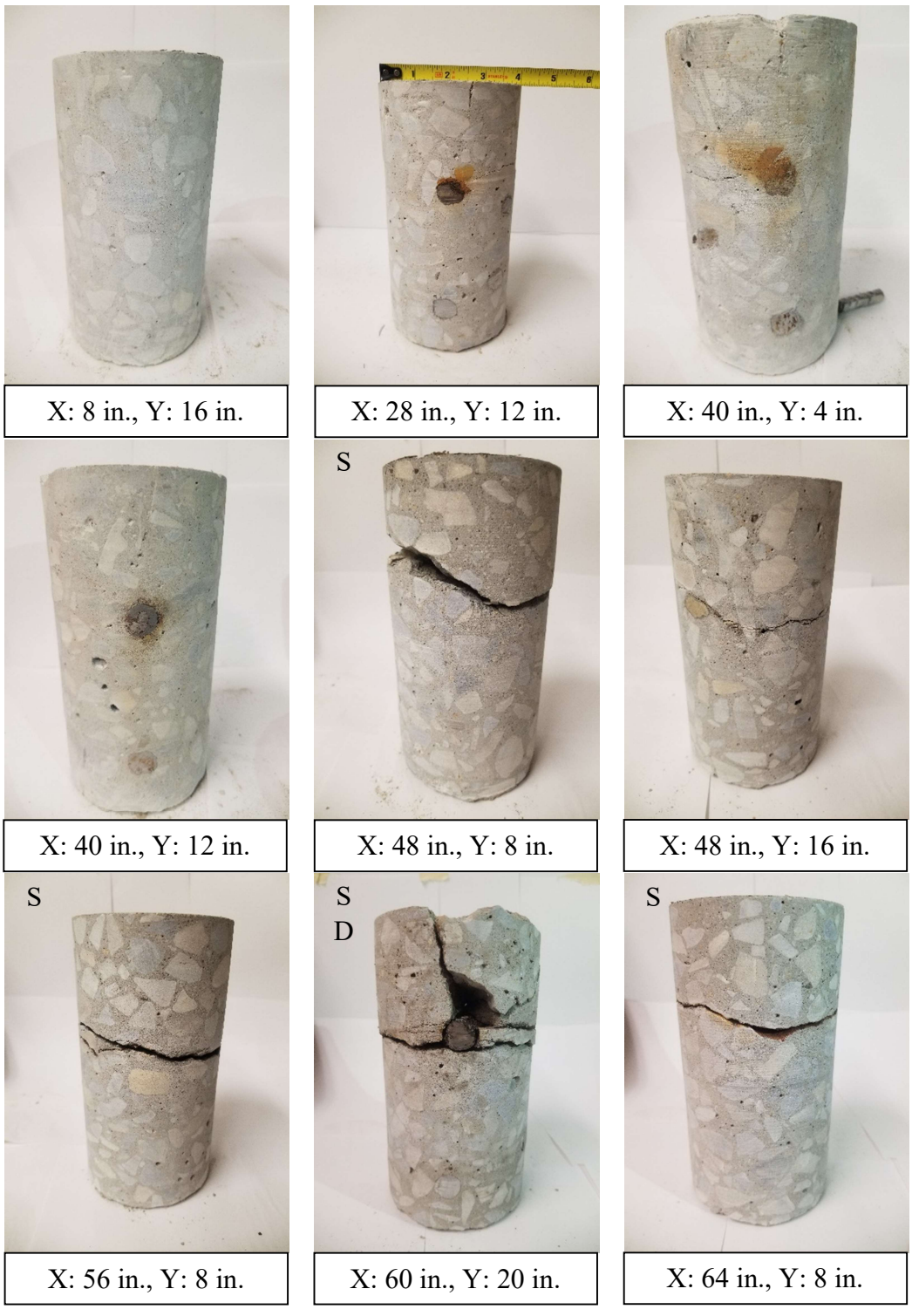

Figure A2: Specimen C2 Extracted Cores

Note:

Two delamination planes were encountered during coring, as seen on the right.

X: 64 in., Y: 16 in.

Figure A3: Specimen C2 Extracted Cores (cont.)

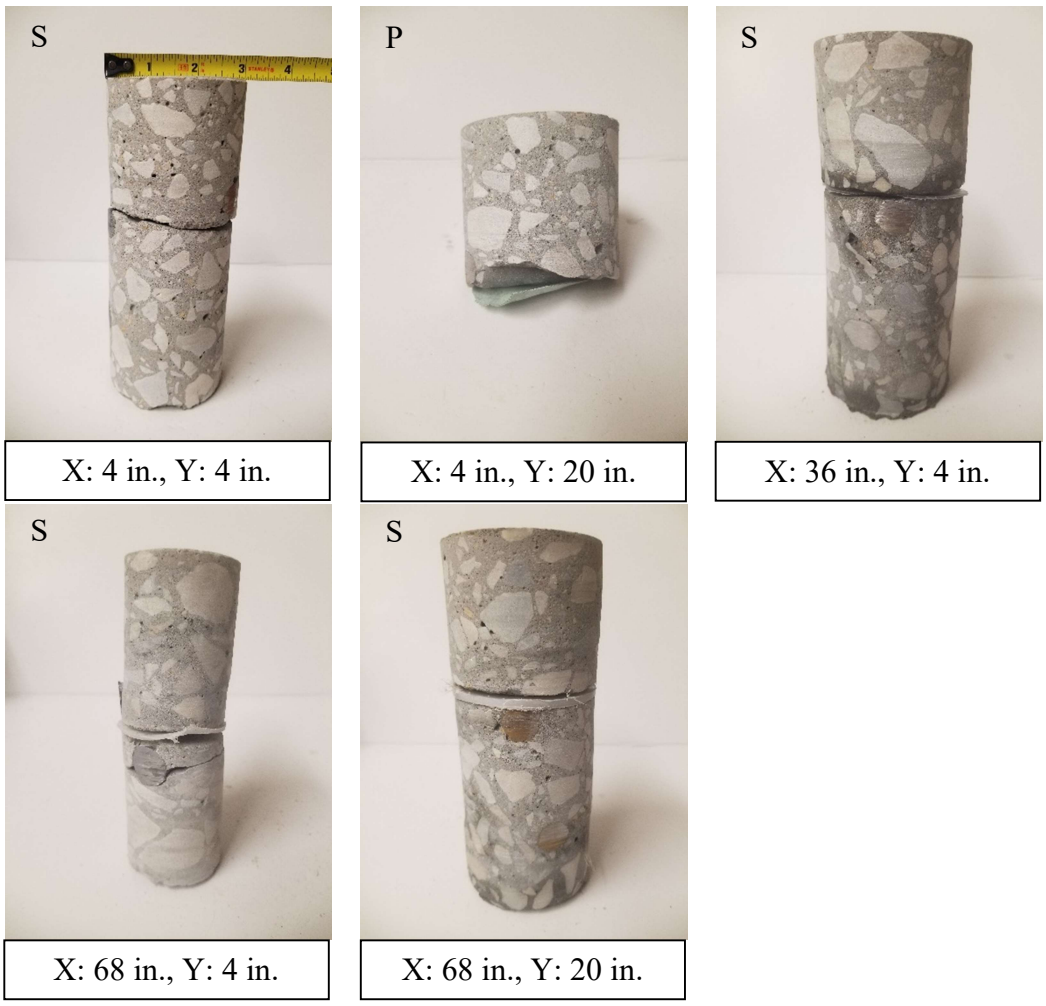

Figure A4: Specimen DL1 Extracted Cores

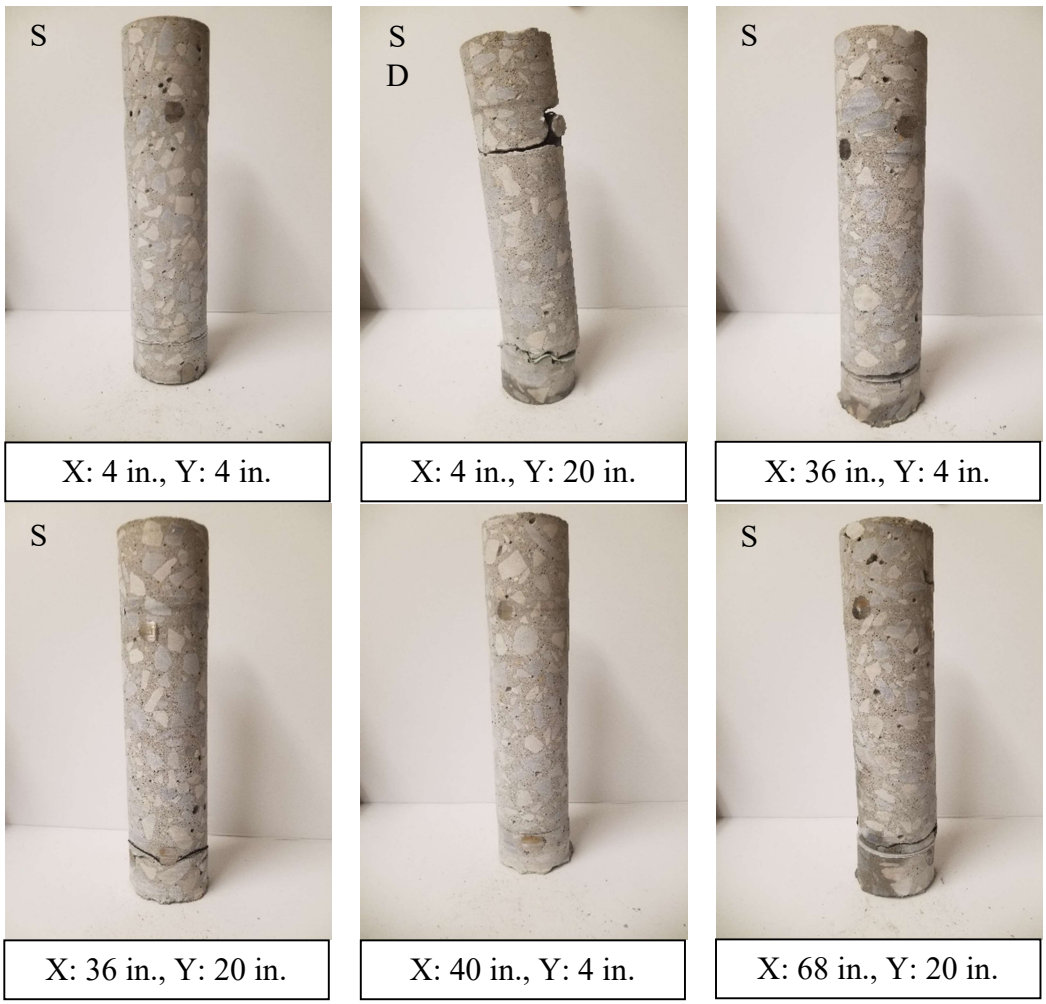

Figure A5: Specimen DL2 Extracted Cores

X: 20 in., Y: 16 in.	X: 36 in., Y: 8 in.	X: 68 in., Y: 4 in.

Figure A6: Specimen DL3 Extracted Cores

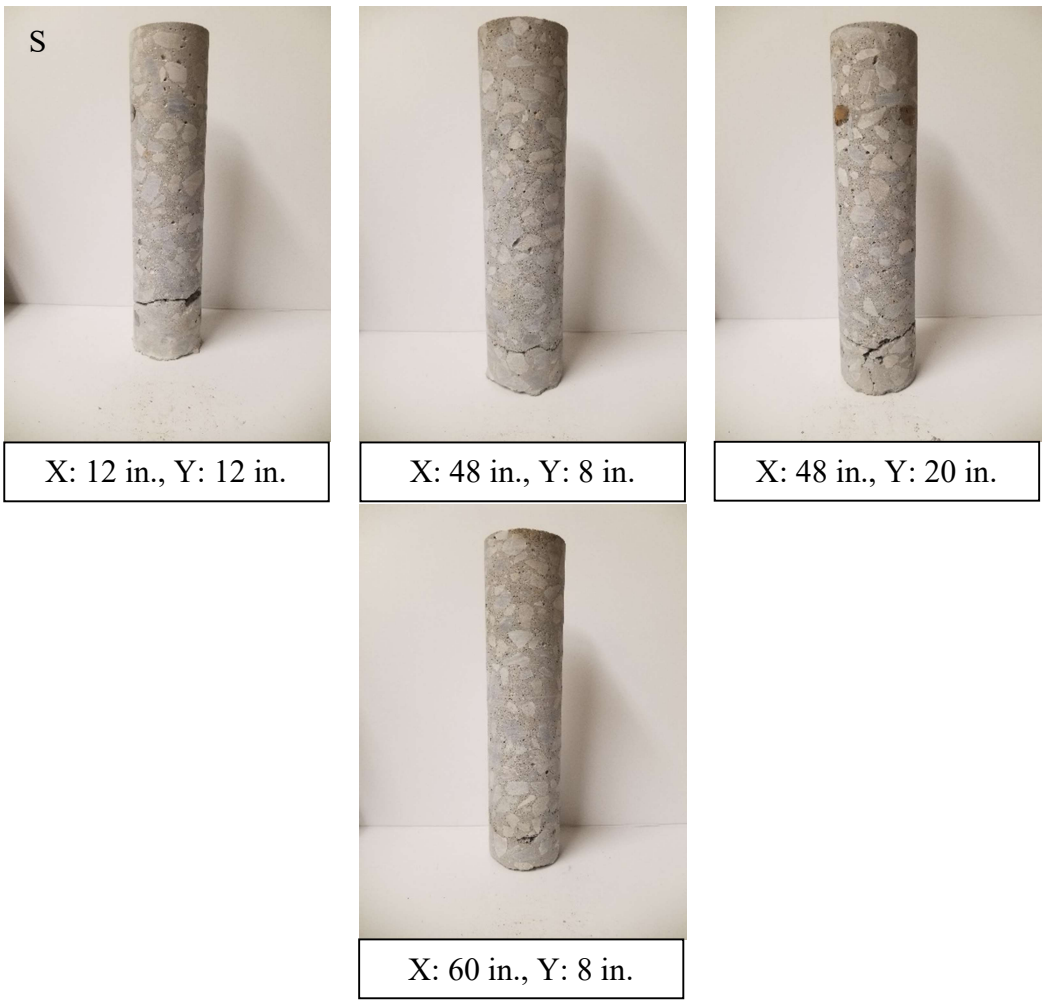

Figure A7: Specimen DL4 Extracted Cores

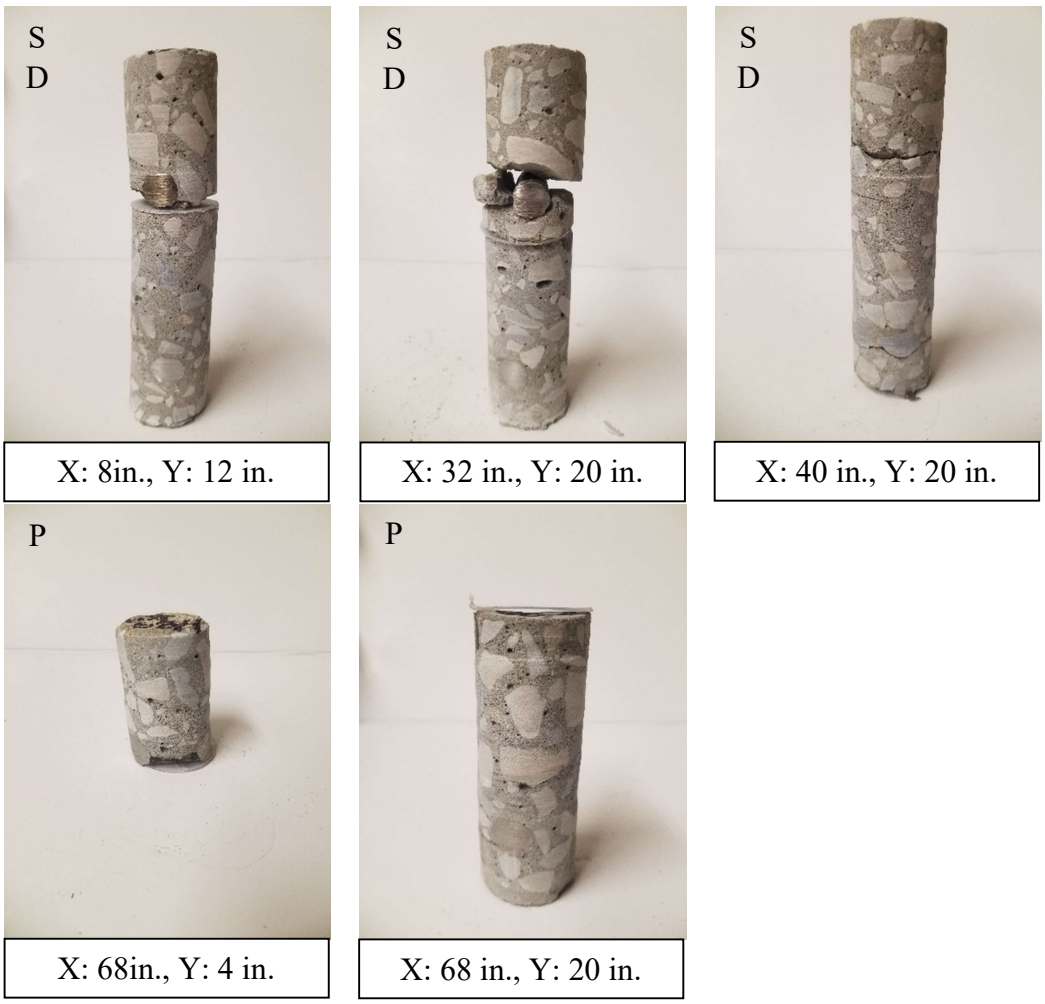

Figure A8: Specimen DL5 Extracted Cores

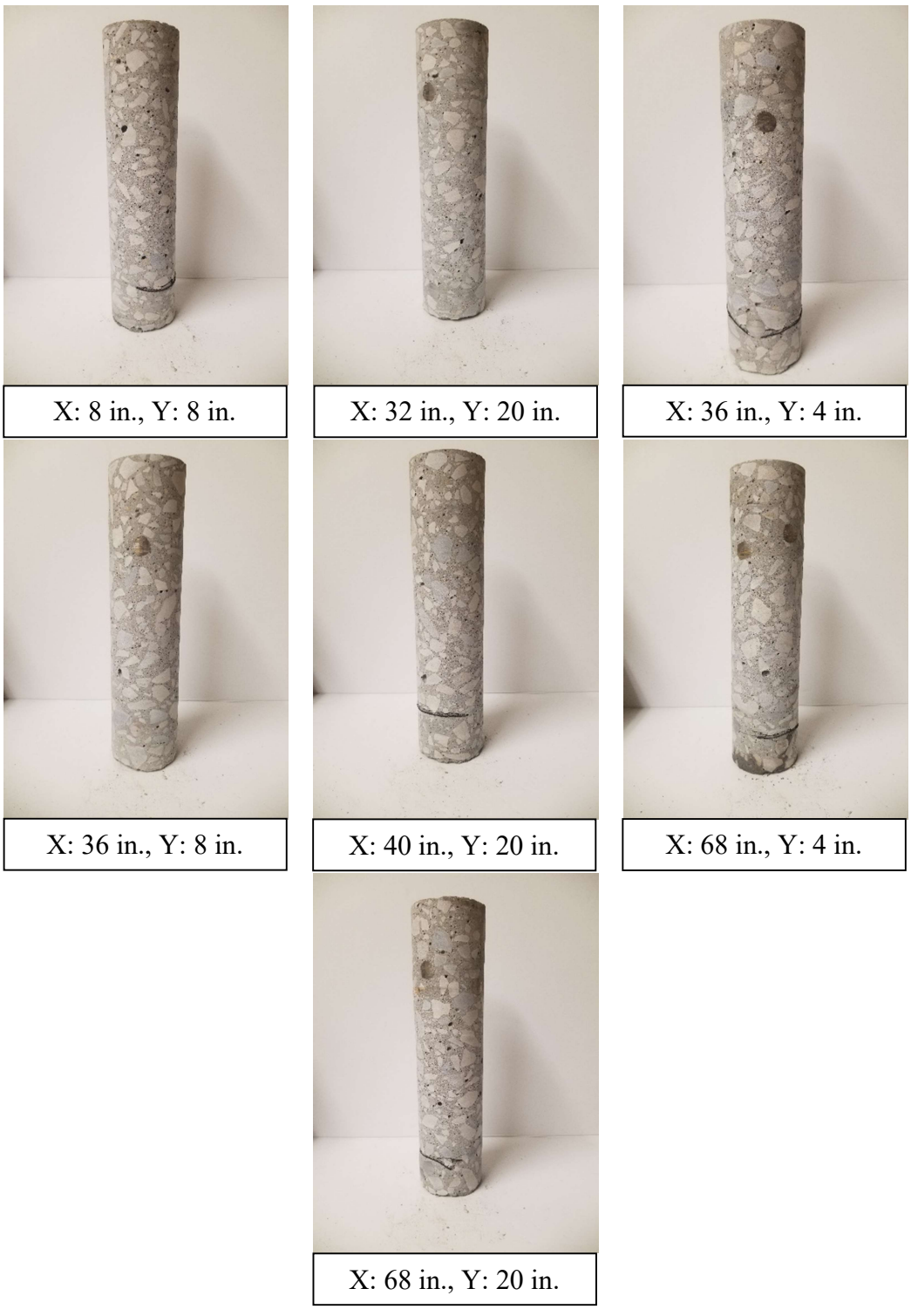

Figure A9: Specimen DL6 Extracted Cores

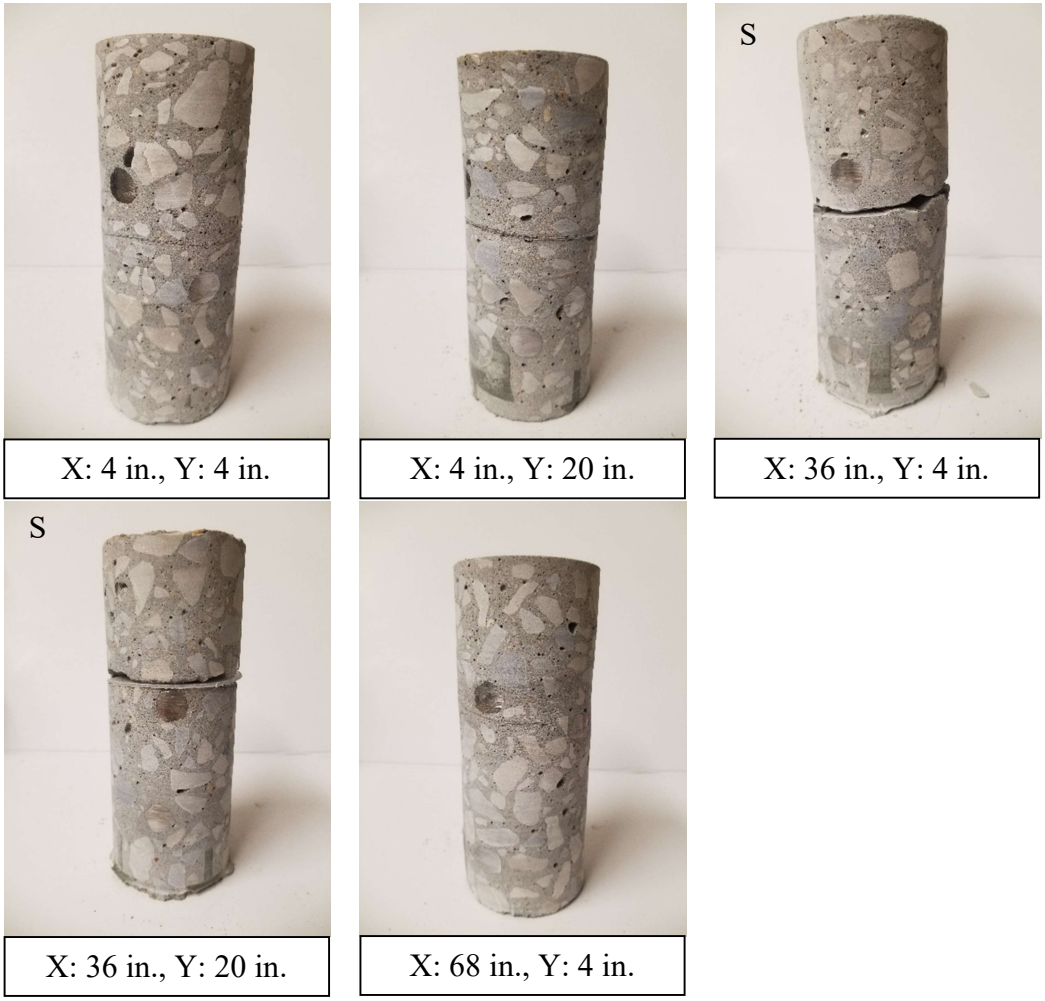

Figure A10: Specimen DL7 Extracted Cores

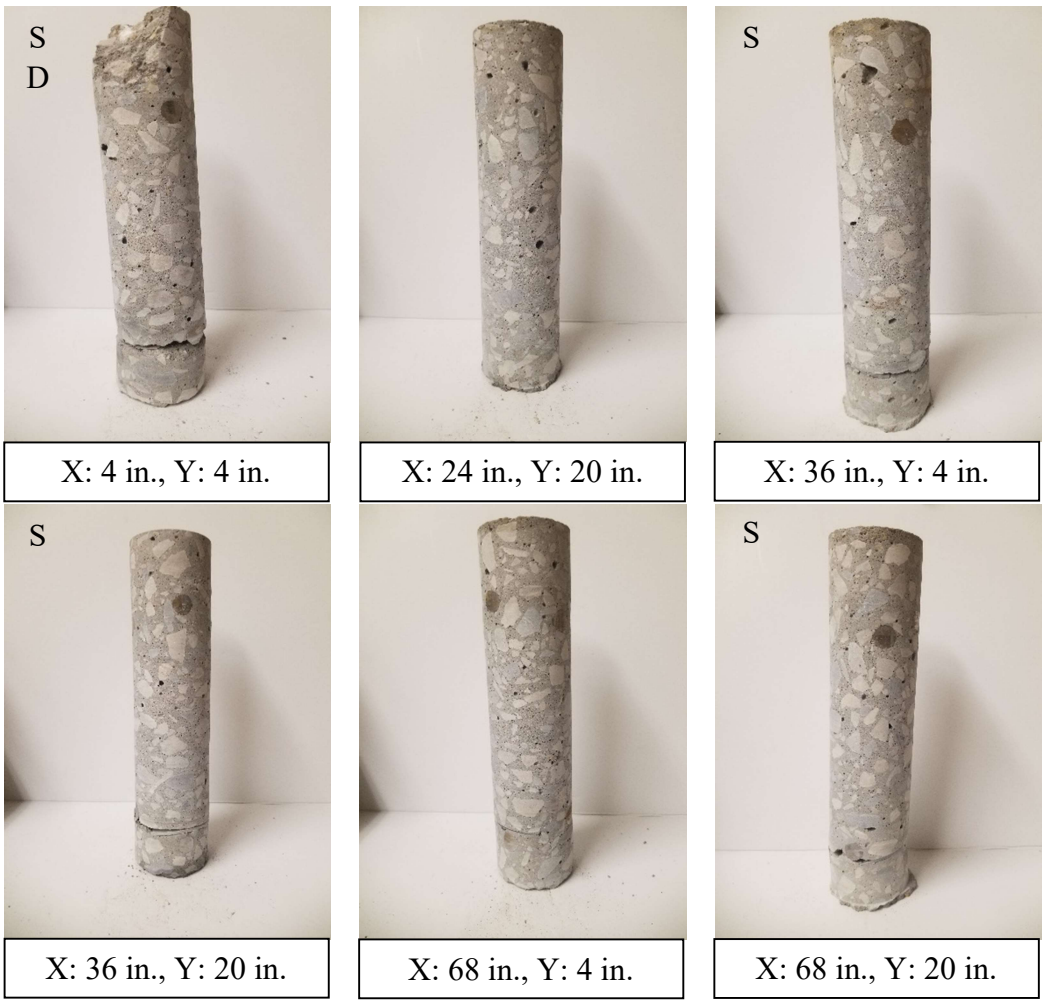

Figure A11: Specimen DL8 Extracted Cores

X: 12 in., Y: 12 in.

X: 24 in., Y: 12 in.

X: 36 in., Y: 16 in.

X: 48 in., Y: 16 in.

Figure A12: Specimen CTRL Extracted Cores

X: 28 in., Y: 16 in.

X: 36 in., Y: 16 in.

X: 44 in., Y: 16 in.

X: 56 in., Y: 12 in.

Figure A13: Specimen DE2 Extracted Cores

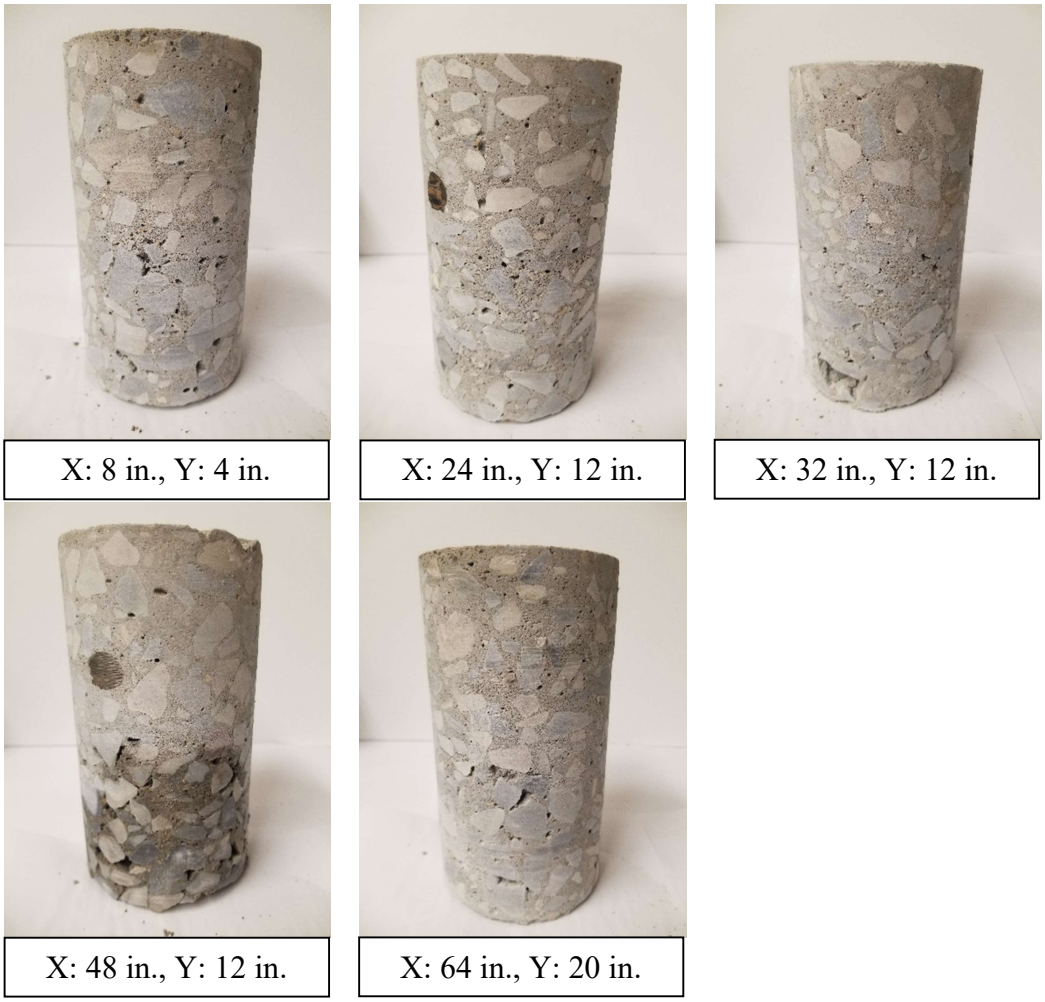

Figure A14: Specimen DE3 Extracted Cores

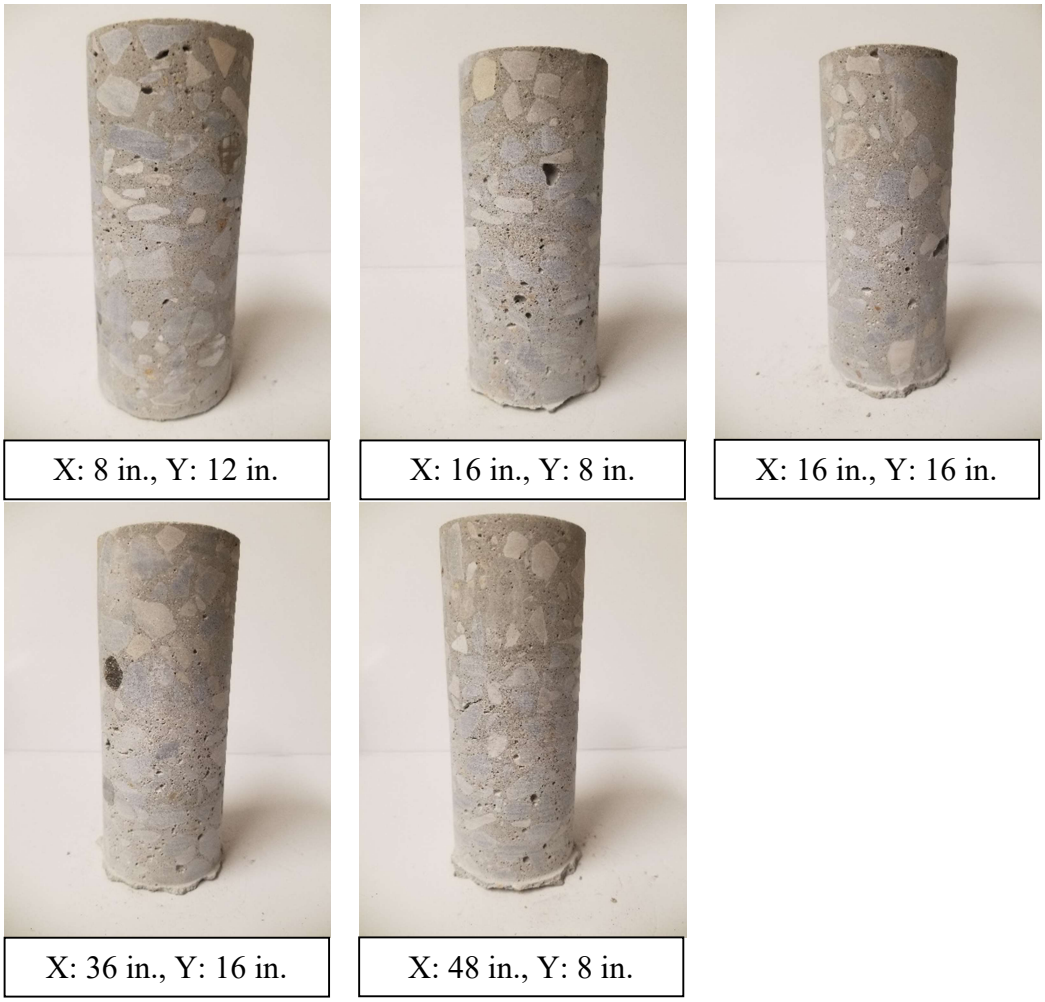

Figure A15: Specimen DE4 Extracted Cores

X: 24 in., Y: 16 in.	X: 36 in., Y: 8 in.	X: 44 in., Y: 16 in.

Figure A16: Specimen DE5 Extracted Cores

X: 12 in., Y: 12 in.

X: 20 in., Y: 8 in.

X: 32 in., Y: 8 in.

X: 48 in, Y: 12 in

Figure A17: Specimen PC1 Extracted Cores

X: 8 in., Y: 16 in.	X: 16 in., Y: 20 in.	X: 36 in., Y: 8 in.

Figure A18: Specimen PC2 Extracted Cores

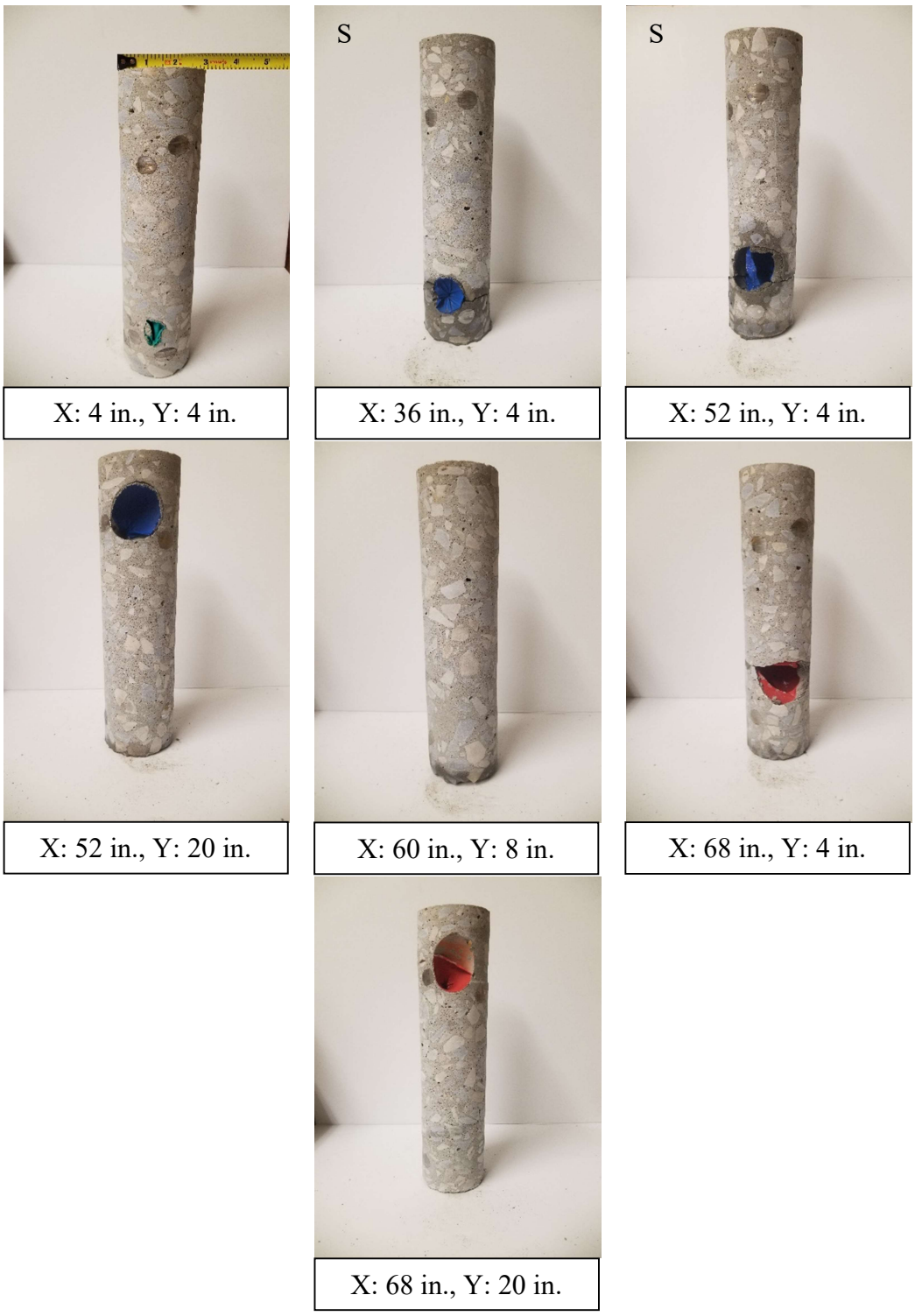

Figure A19: Specimen V1 Extracted Cores

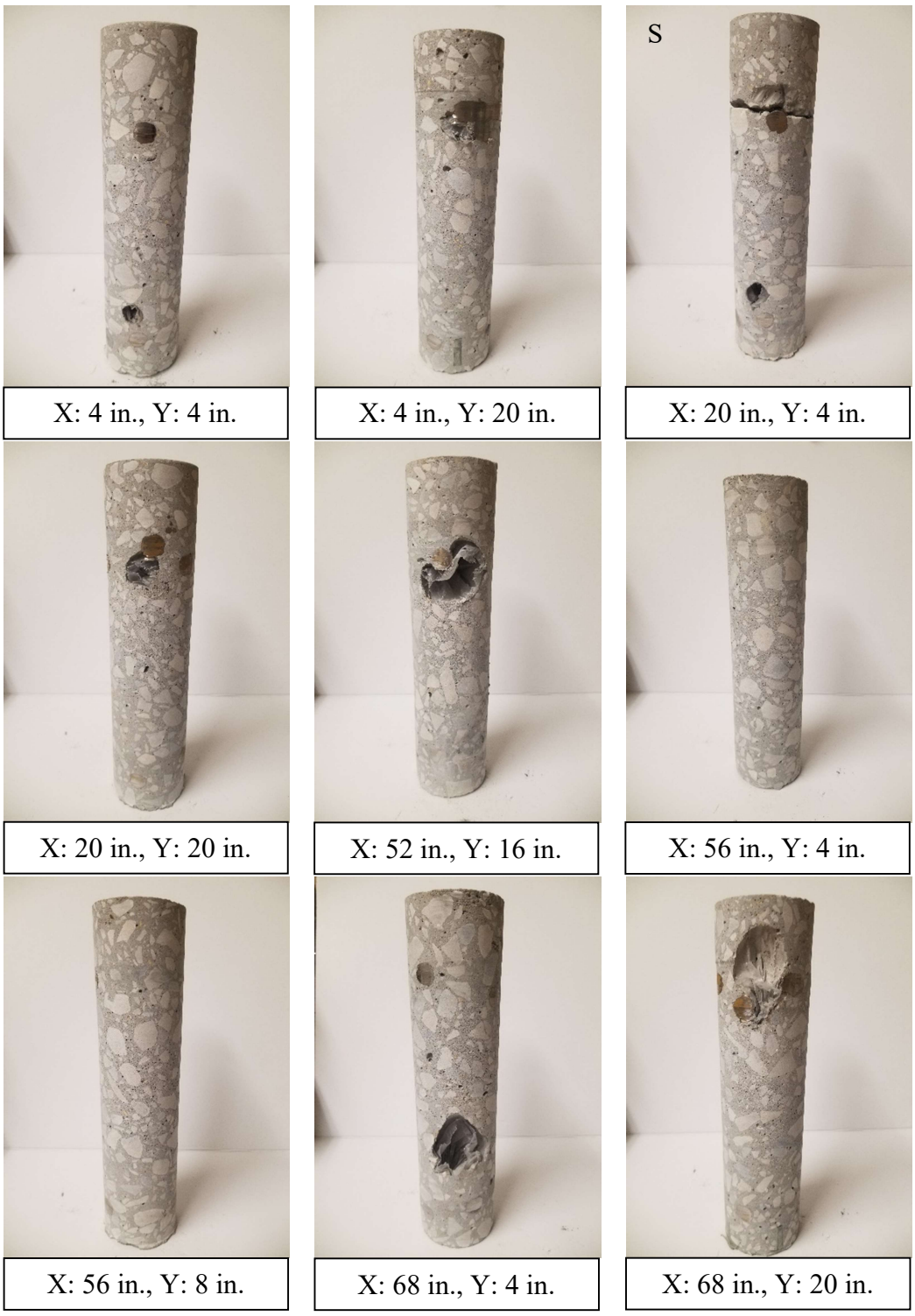

Figure A20: Specimen V2 Extracted Cores

Appendix B: Additional Non-Depth-Corrected GPR Data Contour Plots for Laboratory Specimens

Appendix B presents those contour plots of non-depth-corrected GPR data of the twenty laboratory specimens not shown in Chapter 4. Accordingly air-dried and moist GPR data from inspection passes perpendicular to the top steel in the top reinforcement mat—Top Bar Passes (All)—are shown hereinafter as applicable. Additionally, air-dried and moist GPR data from inspection passes perpendicular to the bottom steel in the top reinforcement mat—Bottom Bar Passes (All)—are shown.

B.1 Non-Depth-Corrected GPR Contour Plots for Test Specimen C1

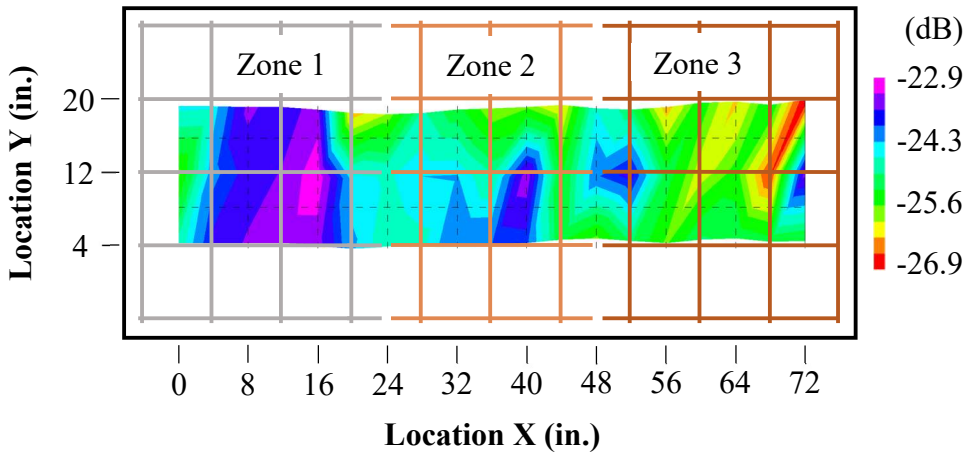

Figure B1: Specimen C1 Top Bar Passes (All) Moist Non-Depth-Corrected GPR Data

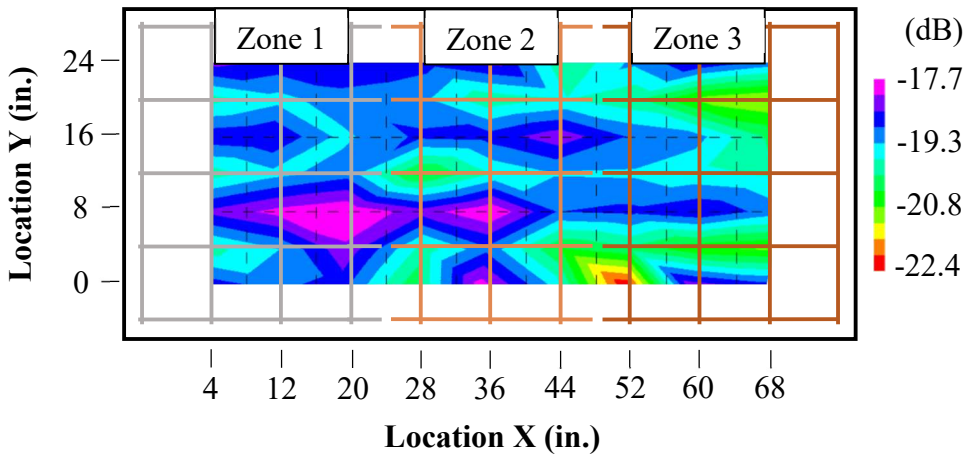

Figure B2 Specimen C1 Bottom Bar Passes (All) Air-Dried Non-Depth-Corrected GPR Data

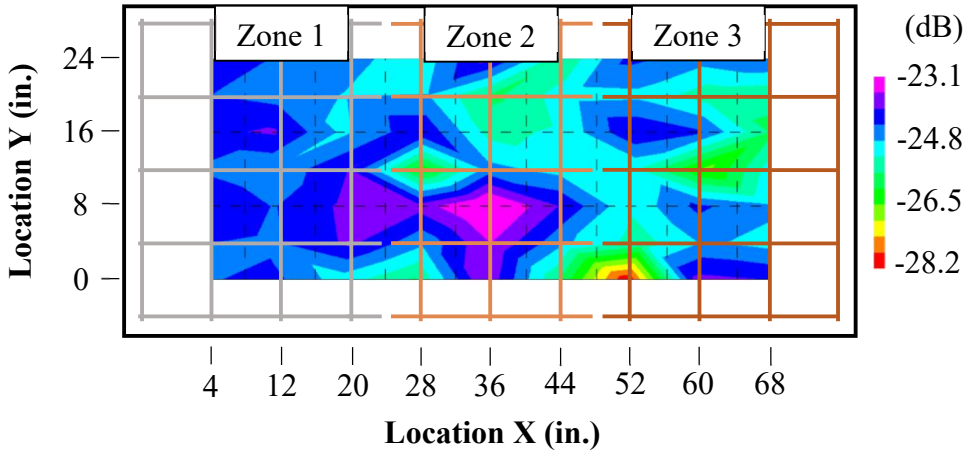

Figure B3: Specimen C1 Bottom Bar Passes (All) Moist Non-Depth-Corrected GPR Data

B2. Non-Depth-Corrected GPR Contour Plots for Test Specimen C2

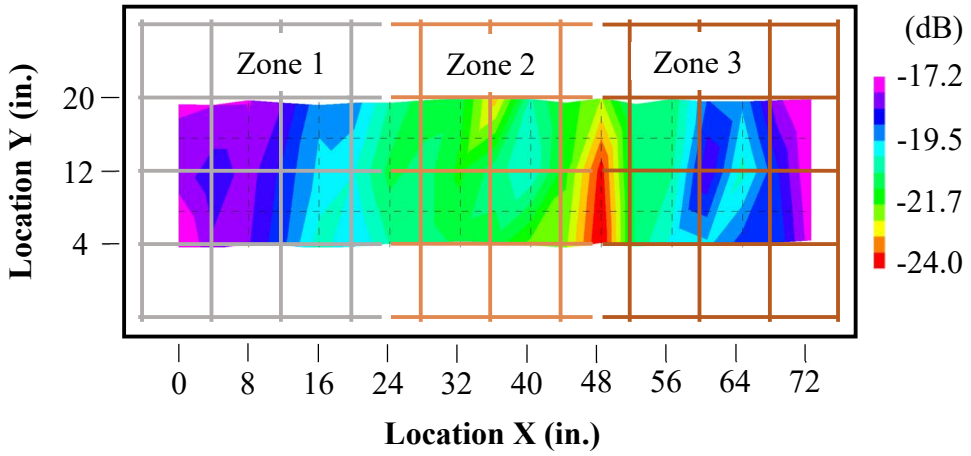

Figure B4 Specimen C2 Top Bar Passes (All) Moist Non-Depth-Corrected GPR Data

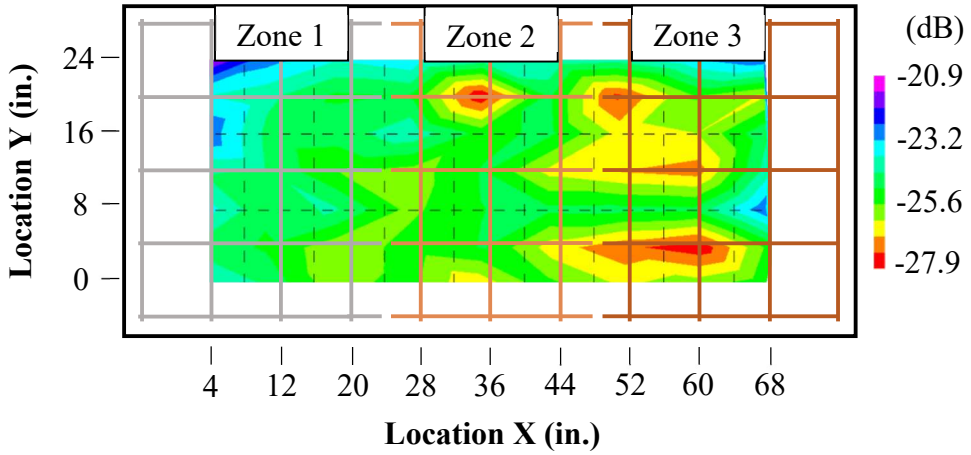

Figure B5 Specimen C2 Bottom Bar Passes (All) Air-Dried Non-Depth-Corrected GPR Data

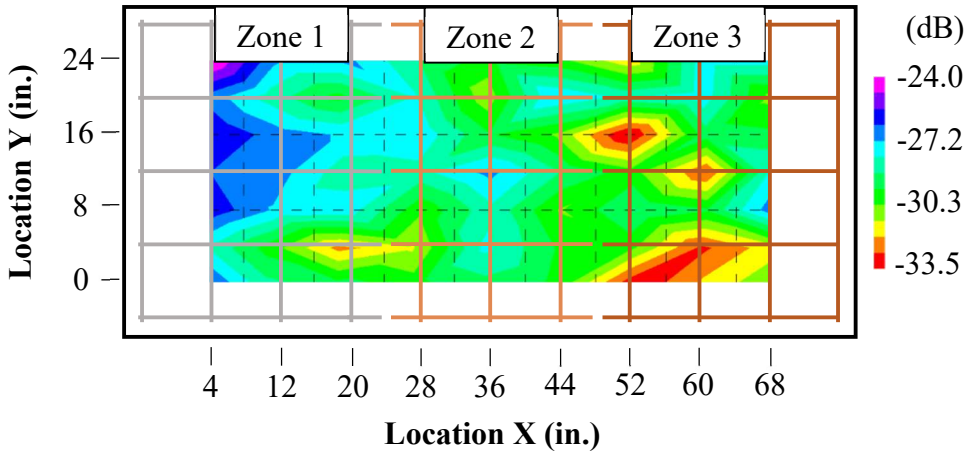

Figure B6 Specimen C2 Bottom Bar Passes (All) Moist Non-Depth-Corrected GPR Data

B.3 Non-Depth-Corrected GPR Contour Plots for Specimen CR1

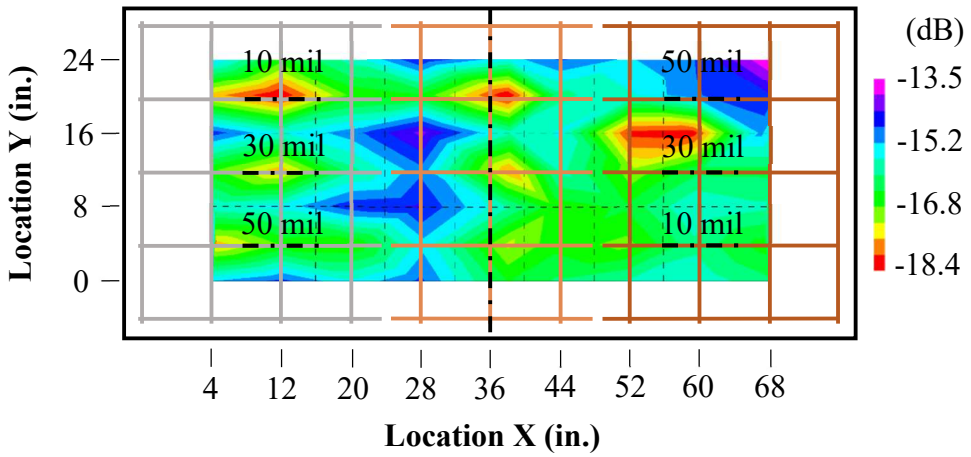

Figure B7 Specimen CR1 Bottom Bar Passes (All) Air-Dried Non-Depth-Corrected GPR Data

B.4 Non-Depth-Corrected GPR Contour Plots for Test Specimen DL1

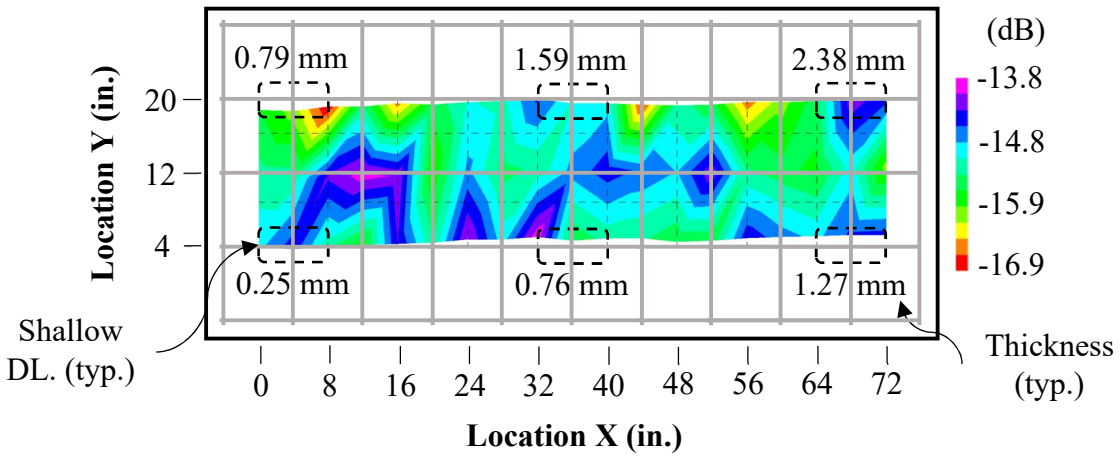

Figure B8: Specimen DL1 Top Bar Passes (All) Moist Non-Depth-Corrected GPR Data

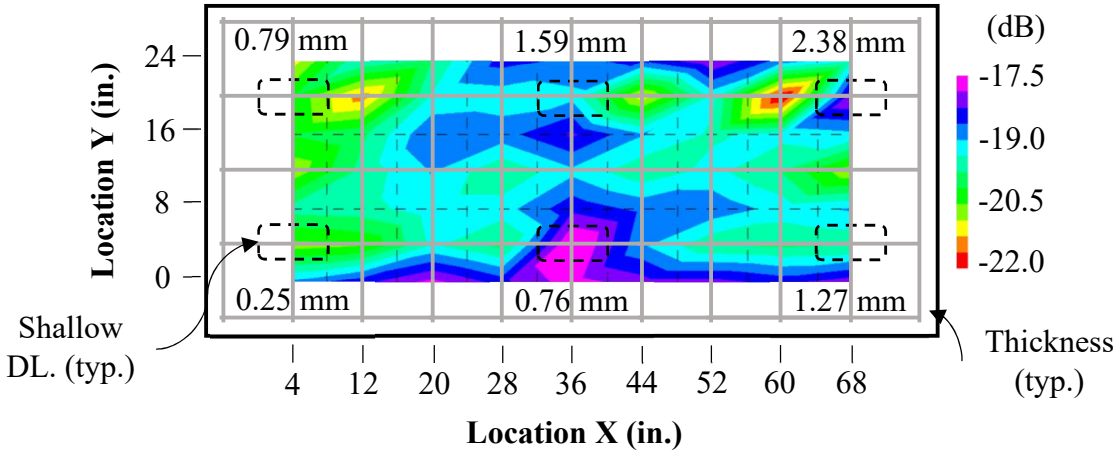

Figure B9 Specimen DL1 Bottom Bar Passes (All) Air-Dried Non-Depth-Corrected GPR Data

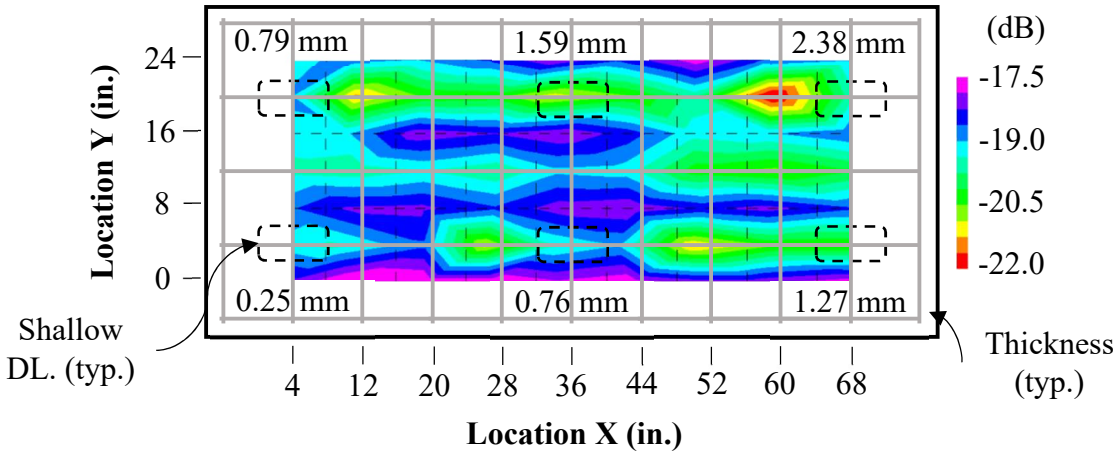

Figure B10: Specimen DL1 Bottom Bar Passes (All) Moist Non-Depth-Corrected GPR Data

B.5 Non-Depth-Corrected GPR Contour Plots for Test Specimen DL2

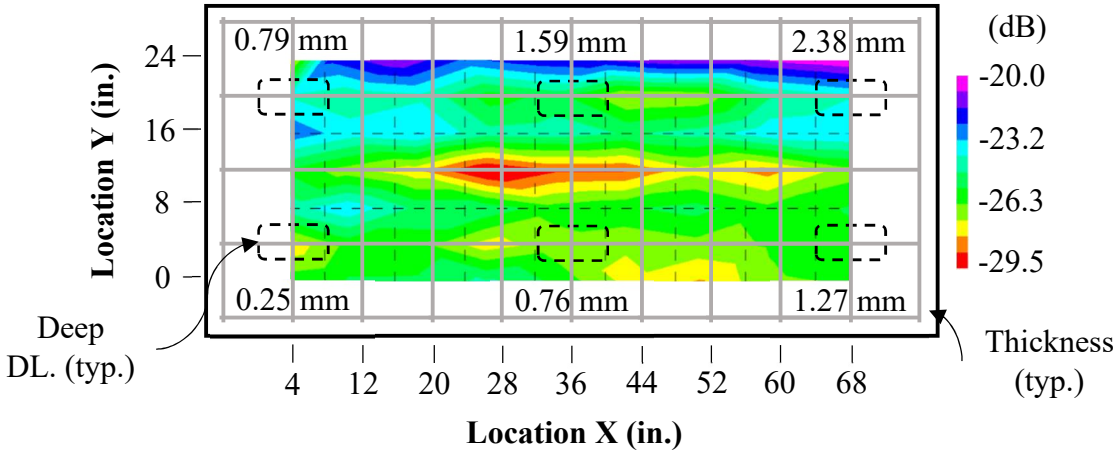

Figure B11: Specimen DL2 Bottom Bar Passes (All) Air-Dried Non-Depth-Corrected GPR Data

B.6 Non-Depth-Corrected GPR Contour Plots for Test Specimen DL3

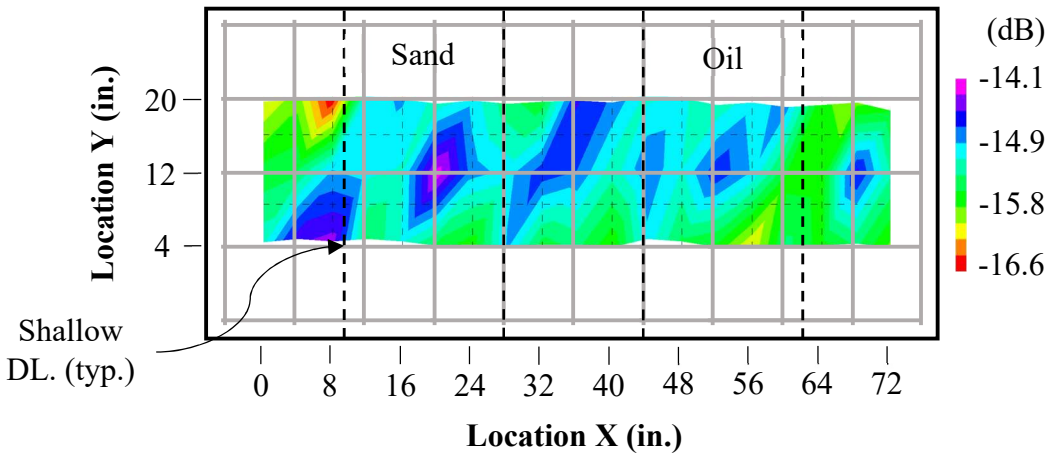

Figure B12: Specimen DL3 Top Bar Passes (All) Moist Non-Depth-Corrected GPR Data

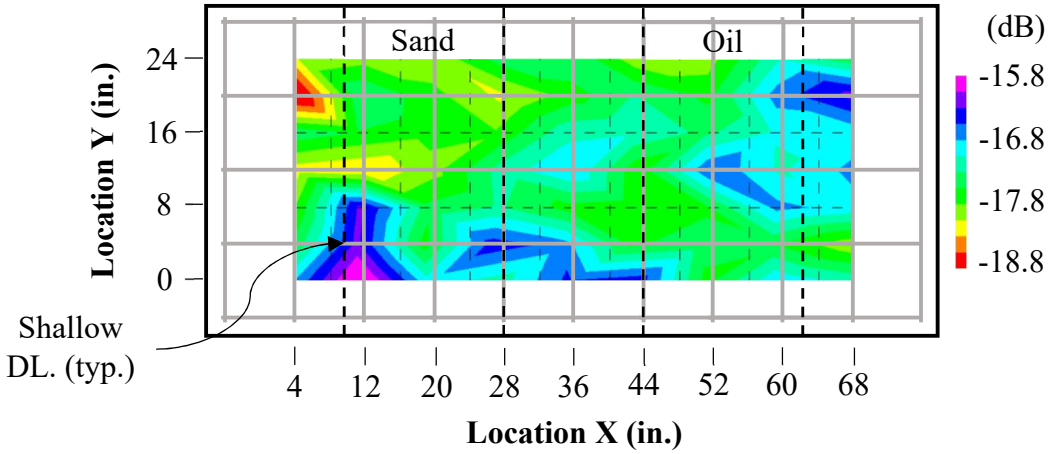

Figure B13: Specimen DL3 Bottom Bar Passes (All) Air-Dried Non-Depth-Corrected GPR Data

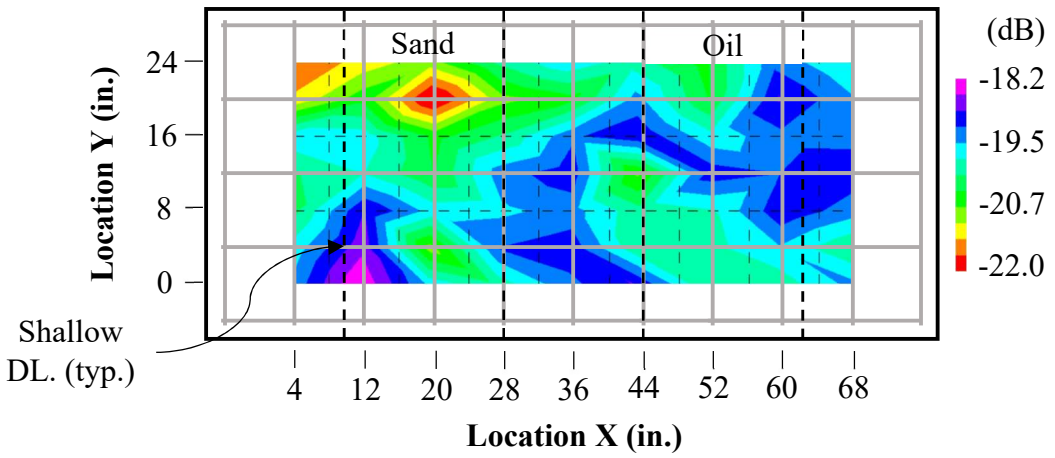

Figure B14: Specimen DL3 Bottom Bar Passes (All) Moist Non-Depth-Corrected GPR Data

B.7 Non-Depth-Corrected GPR Contour Plots for Test Specimen DL4

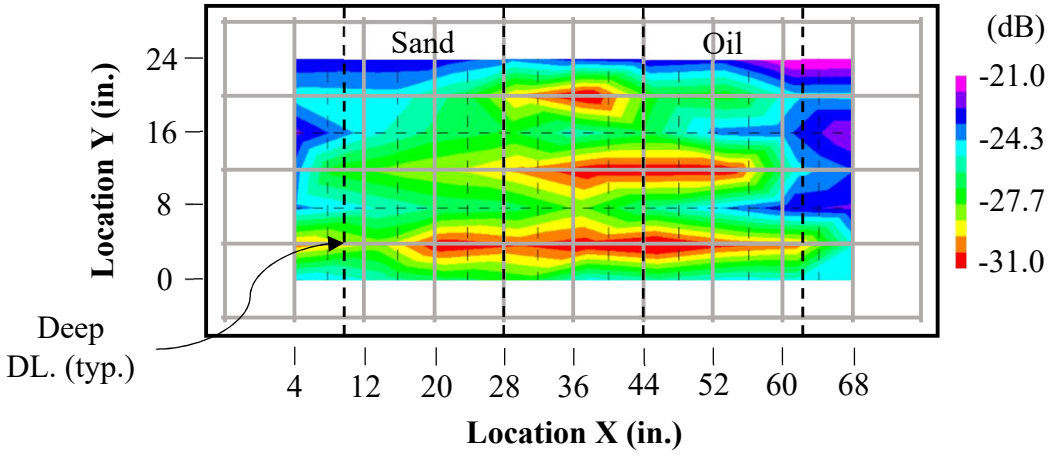

Figure B15: Specimen DL4 Bottom Bar Passes (All) Air-Dried Non-Depth-Corrected GPR Data

B.8 Non-Depth-Corrected GPR Contour Plots for Test Specimen DL5

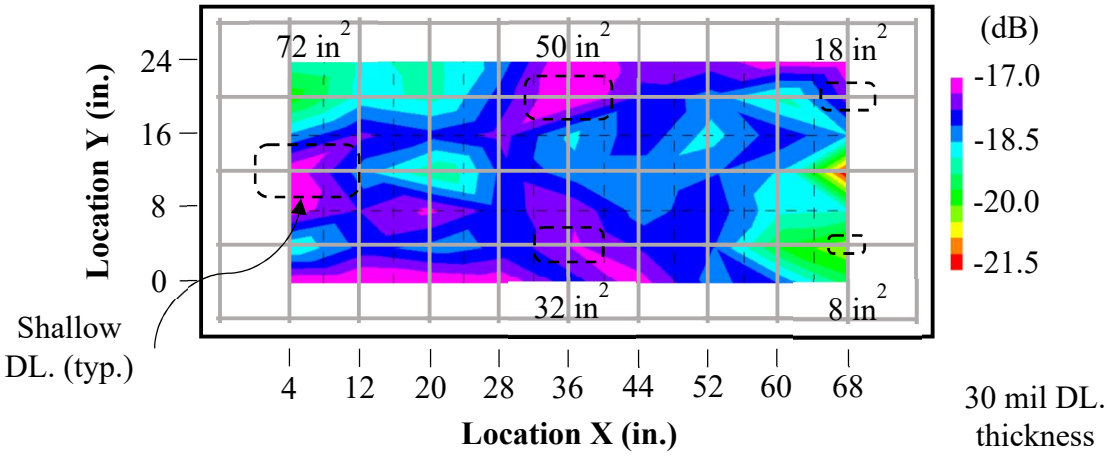

Figure B16: Specimen DL5 Bottom Bar Passes (All) Air-Dried Non-Depth-Corrected GPR Data

B.9 Non-Depth-Corrected GPR Contour Plots for Test Specimen DL6

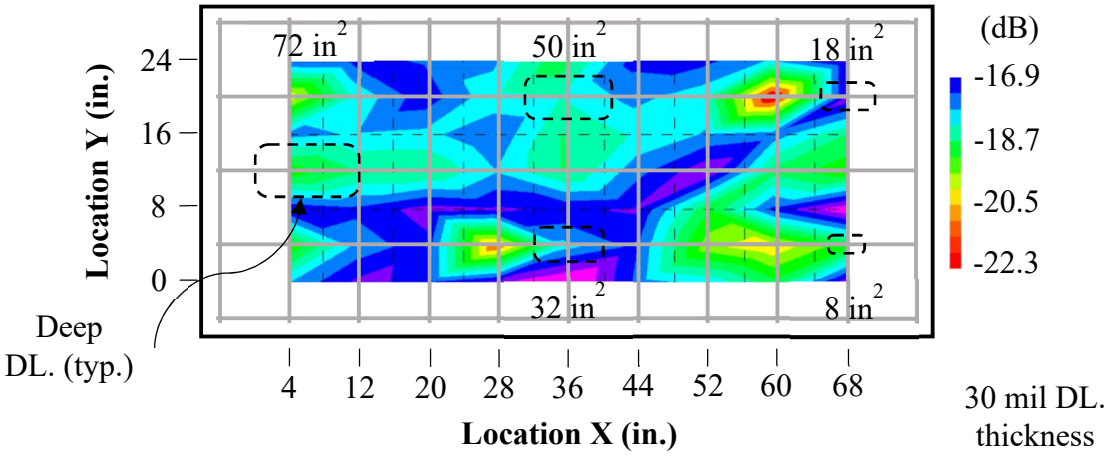

Figure B17: Specimen DL6 Bottom Bar Passes (All) Air-Dried Non-Depth-Corrected GPR Data

B.10 Non-Depth-Corrected GPR Contour Plots for Test Specimen DL7

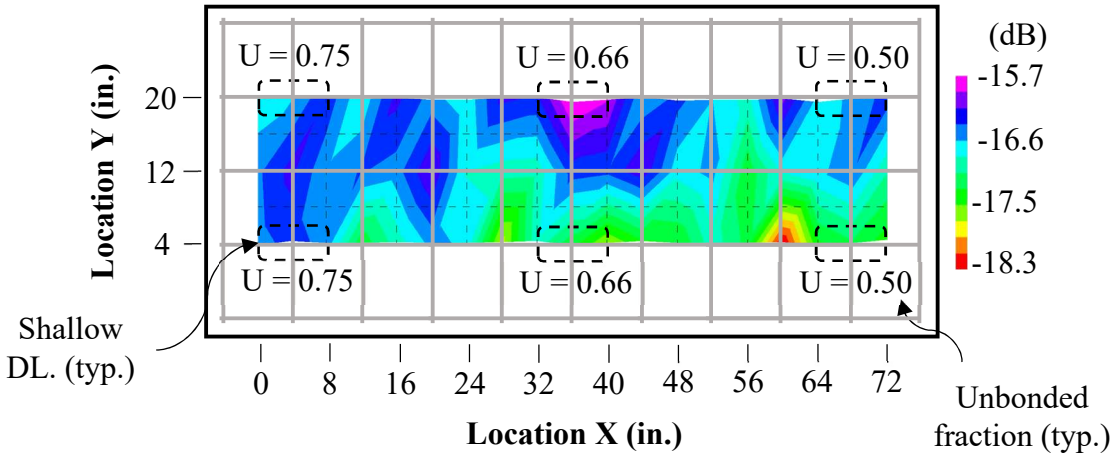

Figure B18: Specimen DL7 Top Bar Passes (All) Moist Non-Depth-Corrected GPR Data

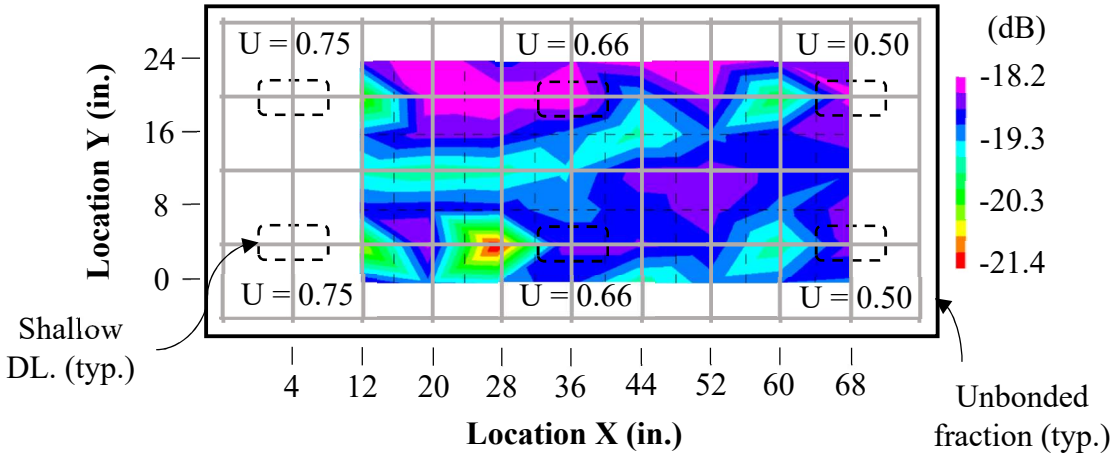

Figure B19: Specimen DL7 Bottom Bar Passes (All) Air-Dried Non-Depth-Corrected GPR Data

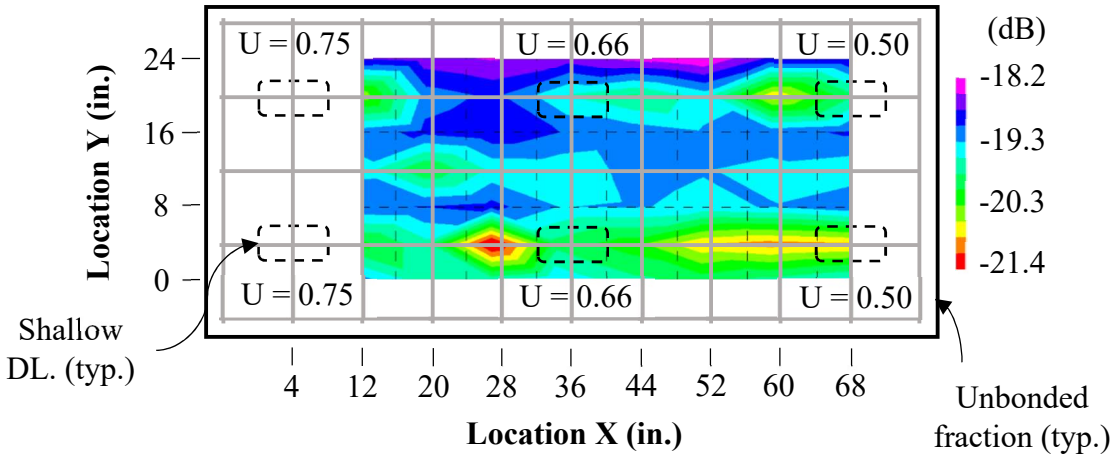

Figure B20: Specimen DL7 Bottom Bar Passes (All) Moist Non-Depth-Corrected GPR Data

B.11 Non-Depth-Corrected GPR Contour Plots for Test Specimen DL8

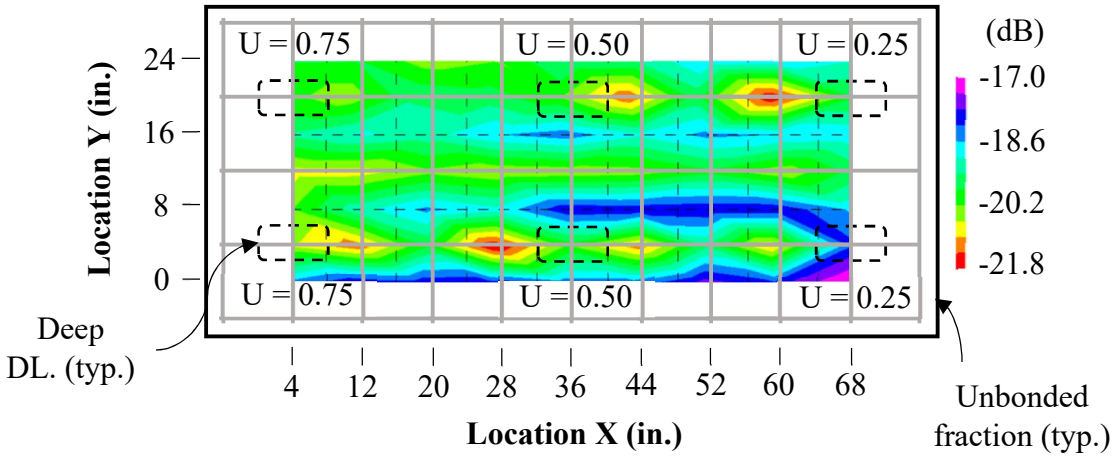

Figure B21: Specimen DL8 Bottom Bar Passes (All) Air-Dried Non-Depth-Corrected GPR Data

B.12 Non-Depth-Corrected GPR Contour Plots for Test Specimen CTRL

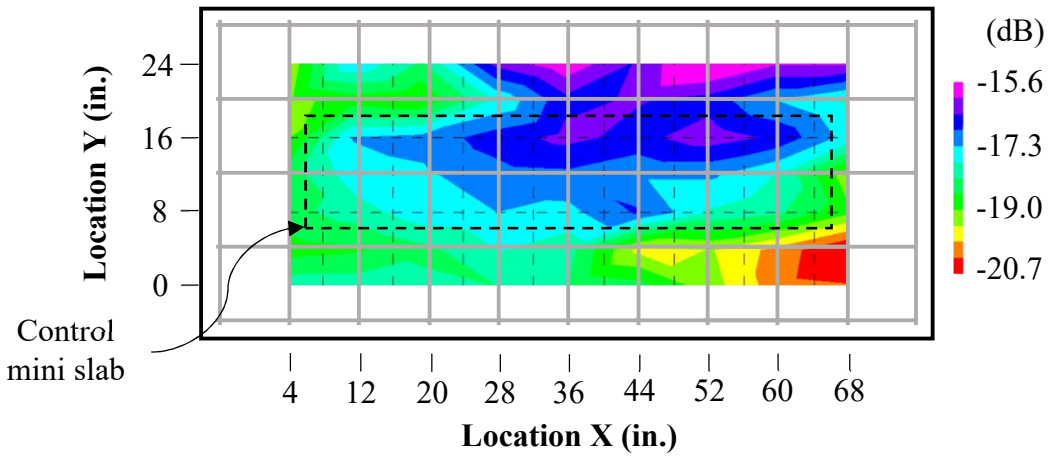

Figure B22: Specimen CTRL Bottom Bar Passes (All) Air-Dried Non-Depth-Corrected GPR Data

B.13 Non-Depth-Corrected GPR Contour Plots for Test Specimen DE2

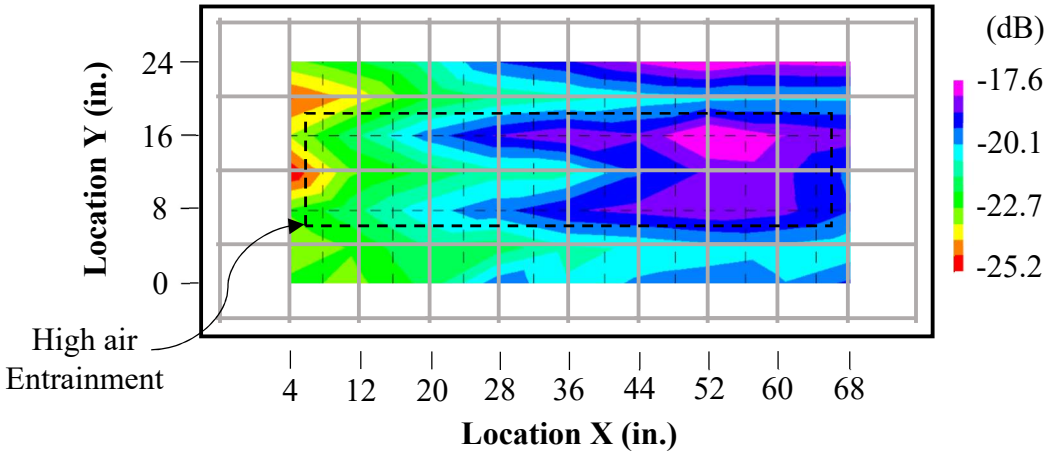

Specimen DE2 Bottom Bar Passes (All) Air-Dried Non-Depth-Corrected GPR Data

B.14 Non-Depth-Corrected GPR Contour Plots for Test Specimen DE3

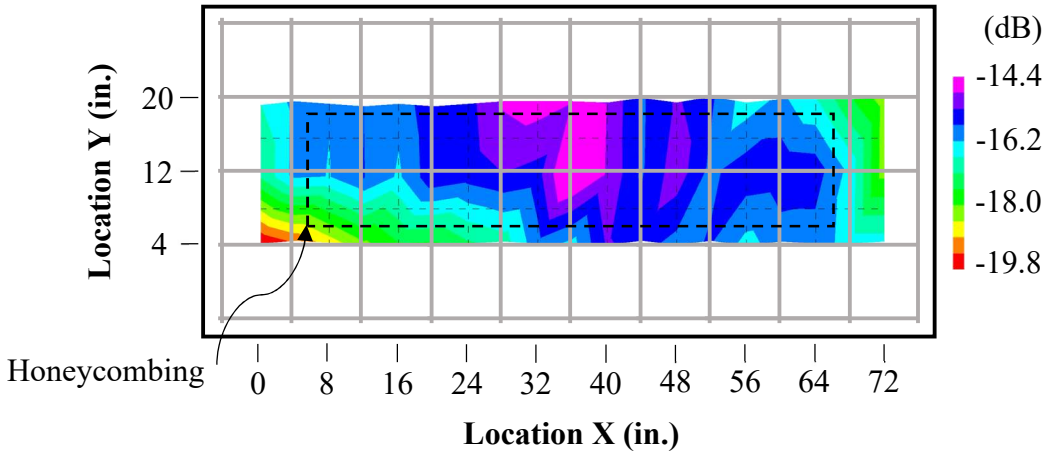

Figure B23: Specimen DE3 Top Bar Passes (All) Moist Non-Depth-Corrected GPR Data

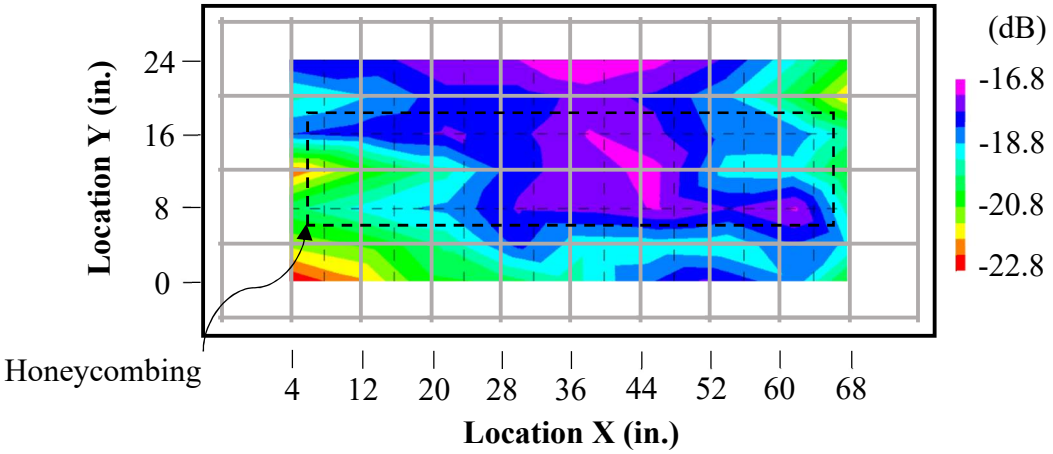

Figure B24: Specimen DE3 Bottom Bar Passes (All) Air-Dried Non-Depth-Corrected GPR Data

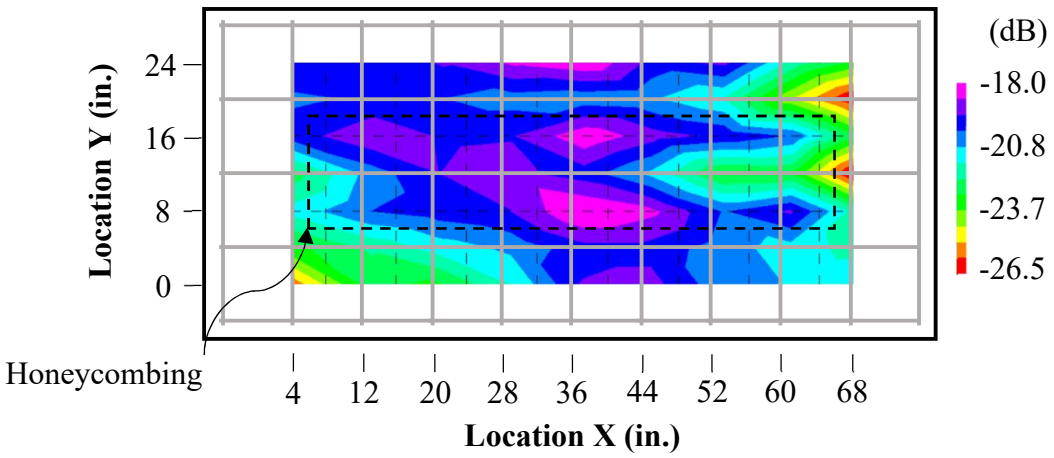

Figure B25: Specimen DE3 Bottom Bar Passes (All) Moist Non-Depth-Corrected GPR Data

B.15 Non-Depth-Corrected GPR Contour Plots for Test Specimen DE4

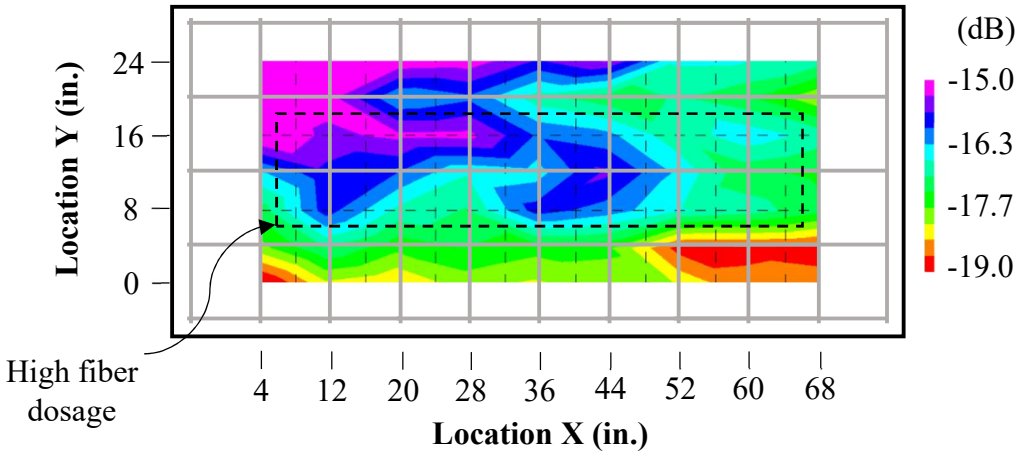

Figure B26: Specimen DE4 Bottom Bar Passes (All) Air-Dried Non-Depth-Corrected GPR Data

B.16 Non-Depth-Corrected GPR Contour Plots for Test Specimen DE5

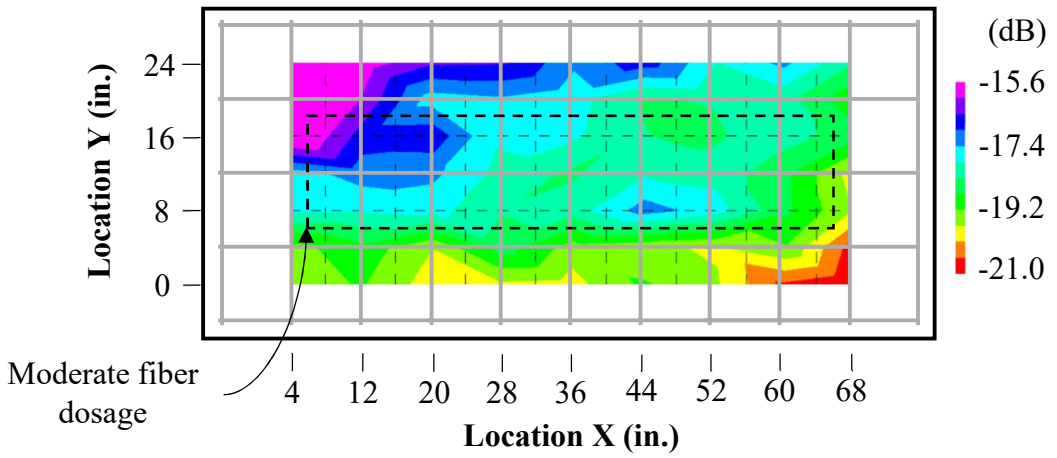

Figure B27: Specimen DE5 Bottom Bar Passes (All) Air-Dried Non-Depth-Corrected GPR Data

B.17 Non-Depth-Corrected GPR Contour Plots for Test Specimen PC1

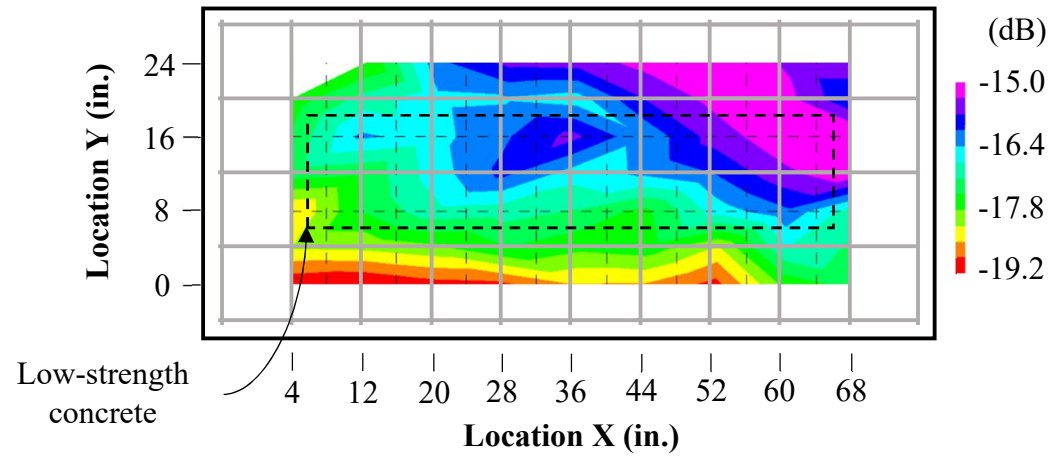

Figure B28: Specimen PC1 Bottom Bar Passes (All) Air-Dried Non-Depth-Corrected GPR Data

B.18 Non-Depth-Corrected GPR Contour Plots for Test Specimen PC2

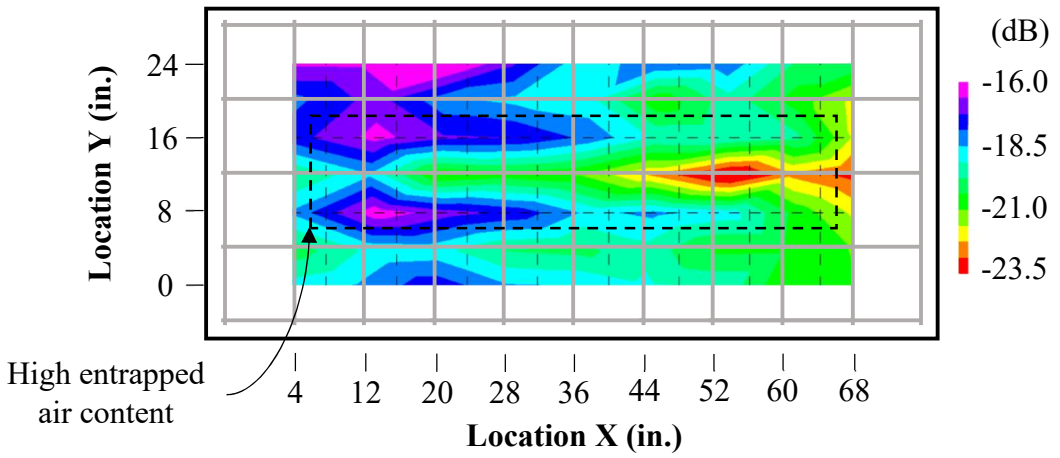

Figure B29: Specimen PC2 Bottom Bar Passes (All) Air-Dried Non-Depth-Corrected GPR Data

B.19 Non-Depth-Corrected GPR Contour Plots for Test Specimen V1

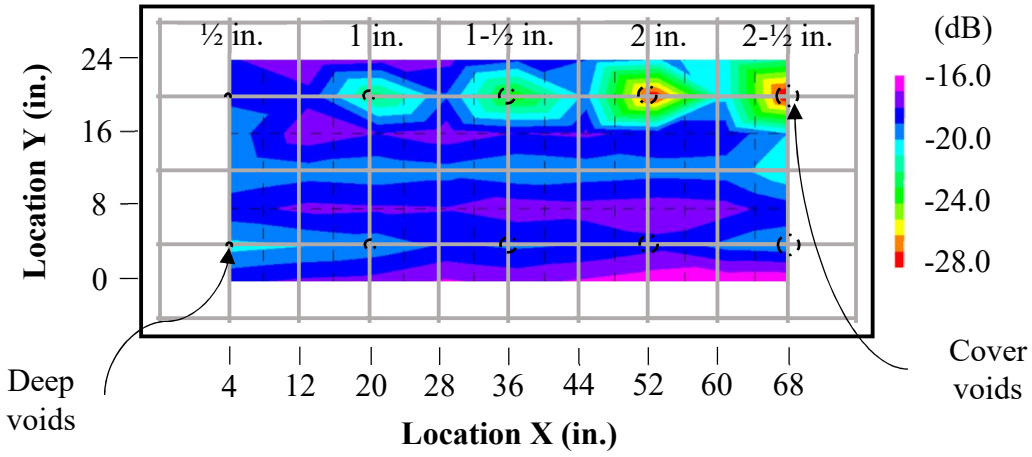

Figure B30: Specimen V1 Bottom Bar Passes (All) Air-Dried Non-Depth-Corrected GPR Data

B.20 Non-Depth-Corrected GPR Contour Plots for Test Specimen V2

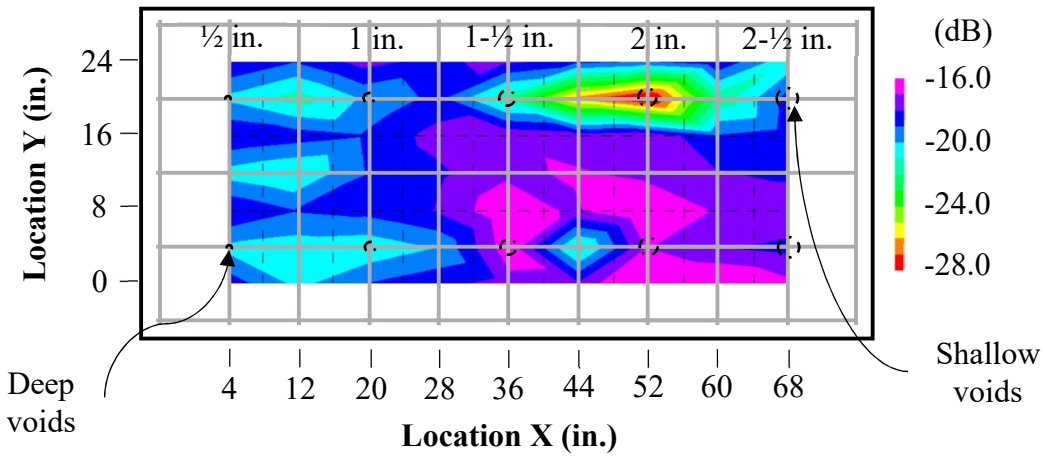

Figure B31: Specimen V2 Bottom Bar Passes (All) Air-Dried Non-Depth-Corrected GPR Data

Appendix C: Additional Air-Dried Depth-Corrected GPR Data Contour Plots for Laboratory Specimens

Appendix C presents those contour plots of air-dried, depth-corrected GPR data of the twenty laboratory specimens not shown in Chapter 4.

C1. Depth-Corrected GPR Data Contour Plot for Specimen DL2

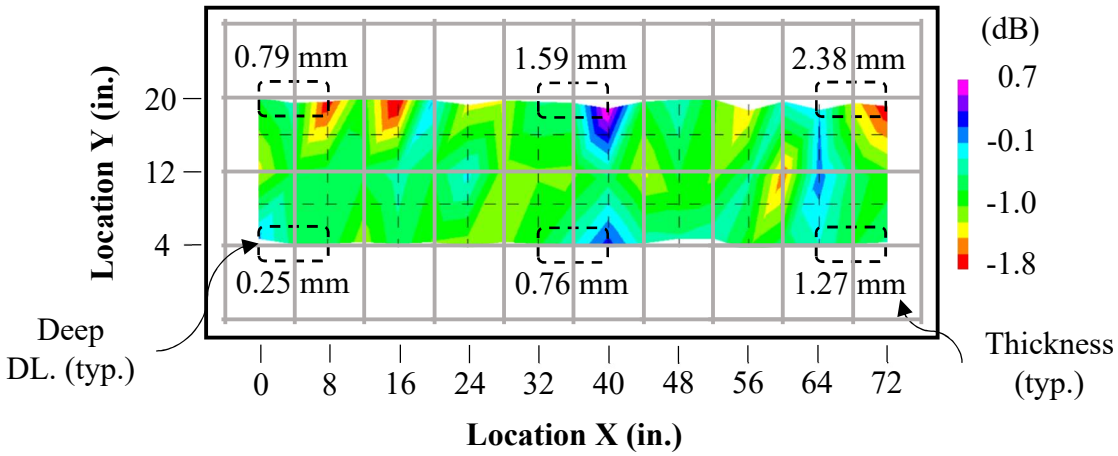

Figure C1: Specimen DL2 Top Bar Passes (All) Air-Dried Depth-Corrected GPR Data

C2. Depth-Corrected GPR Data Contour Plot for Specimen DL3

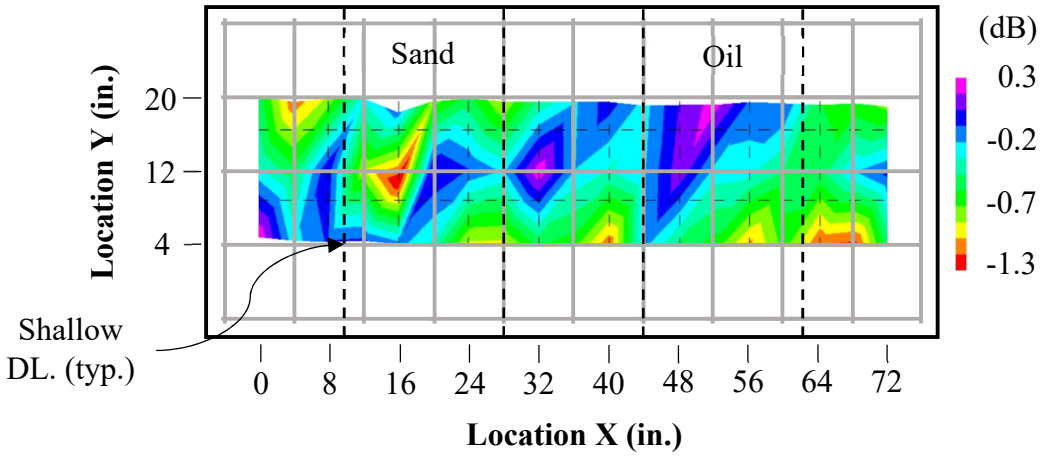

Figure C2 : Specimen DL3 Top Bar Passes (All) Air-Dried Depth-Corrected GPR Data

C3. Depth-Corrected GPR Data Contour Plot for Specimen DL4

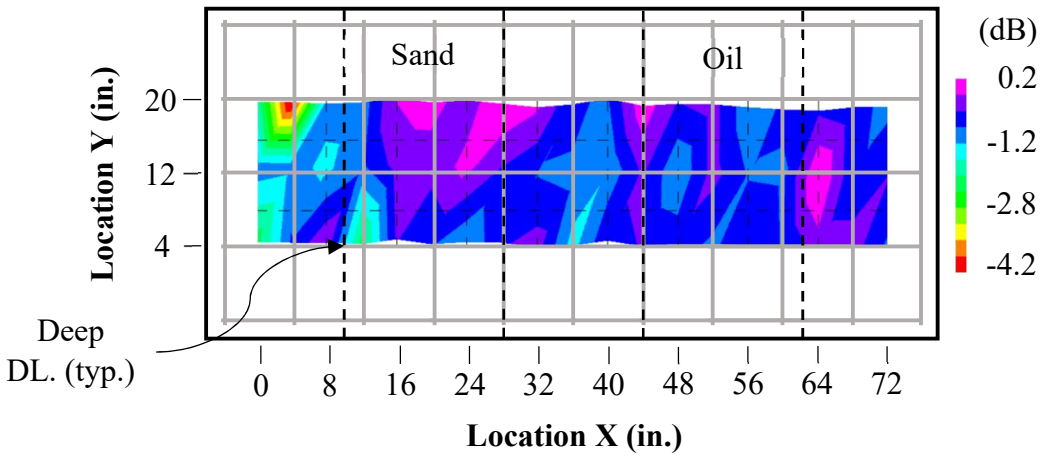

Figure C3: Specimen DL4 Top Bar Passes (All) Air-Dried Depth-Corrected GPR Data

C4. Depth-Corrected GPR Data Contour Plot for Specimen DL5

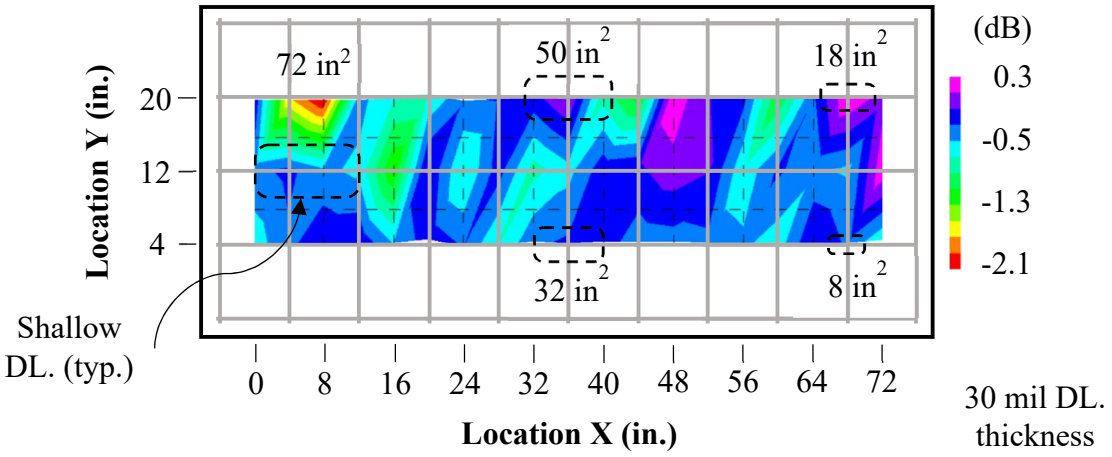

Figure C4: Specimen DL5 Top Bar Passes (All) Air-Dried Depth-Corrected GPR Data

C5. Depth-Corrected GPR Data Contour Plot for Specimen DL6

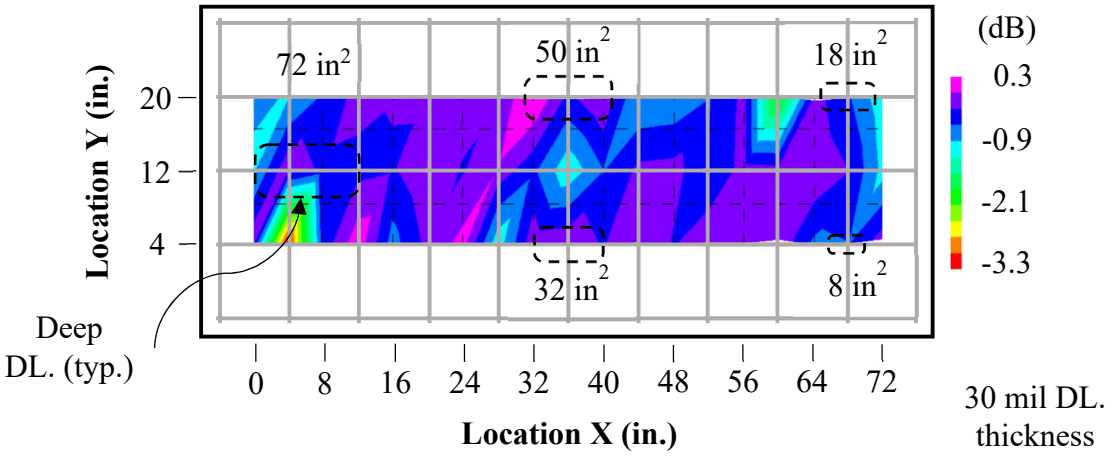

Figure C5: Specimen DL6 Top Bar Passes (All) Air-Dried Depth-Corrected GPR Data

C6. Depth-Corrected GPR Data Contour Plot for Specimen DL7

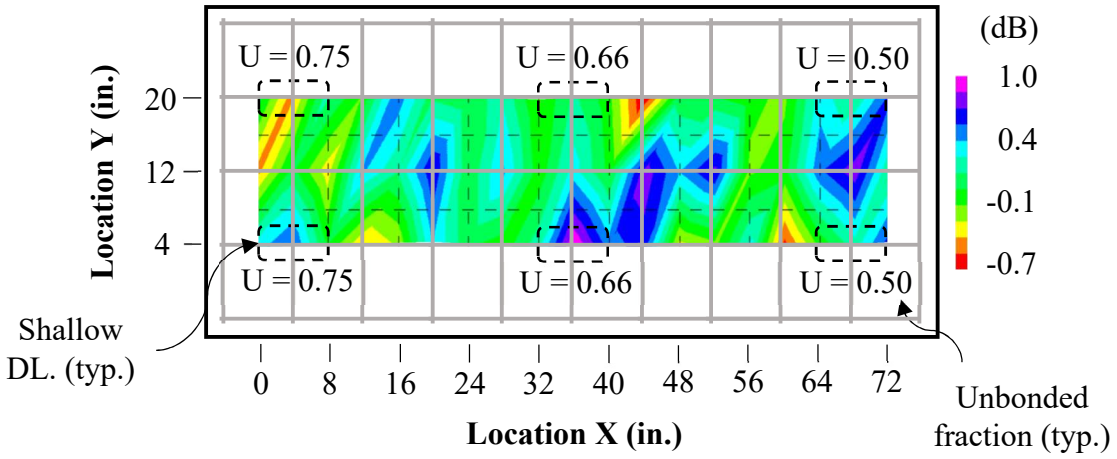

Figure C6: Specimen DL7 Top Bar Passes (All) Air-Dried Depth-Corrected GPR Data

C7. Depth-Corrected GPR Data Contour Plot for Specimen DL8

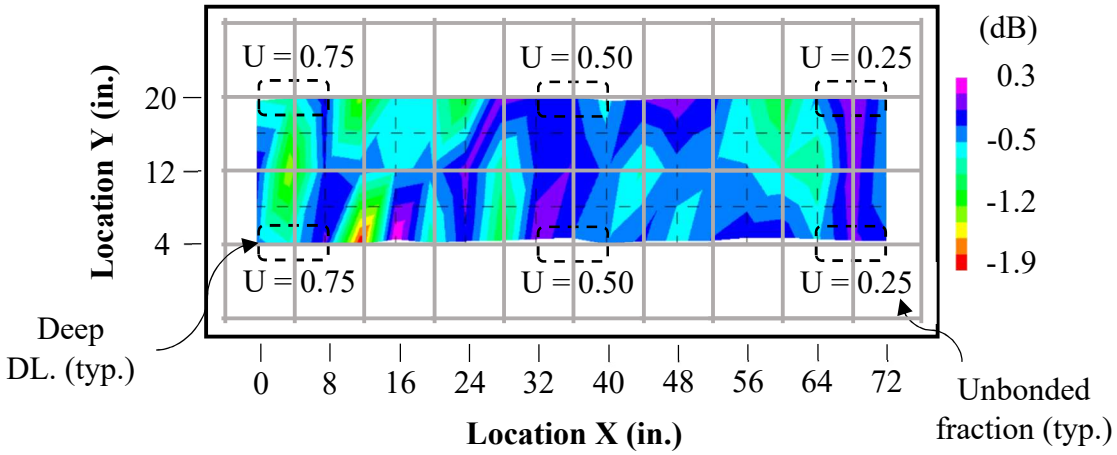

Figure C7: Specimen DL8 Top Bar Passes (All) Air-Dried Depth-Corrected GPR Data

C8. Depth-Corrected GPR Data Contour Plot for Specimen CTRL

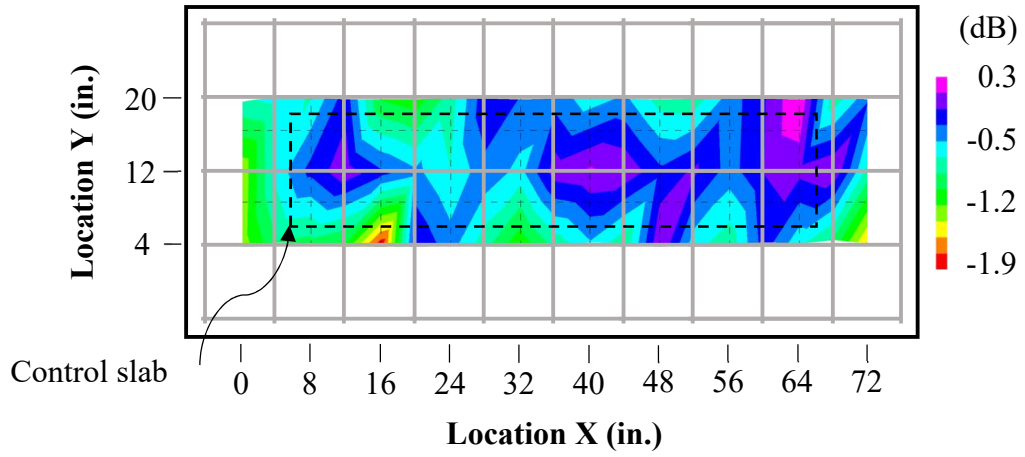

Figure C8: Specimen CTRL Top Bar Passes (All) Air-Dried Depth Corrected GPR Data

C9. Depth-Corrected GPR Data Contour Plot for Specimen DE2

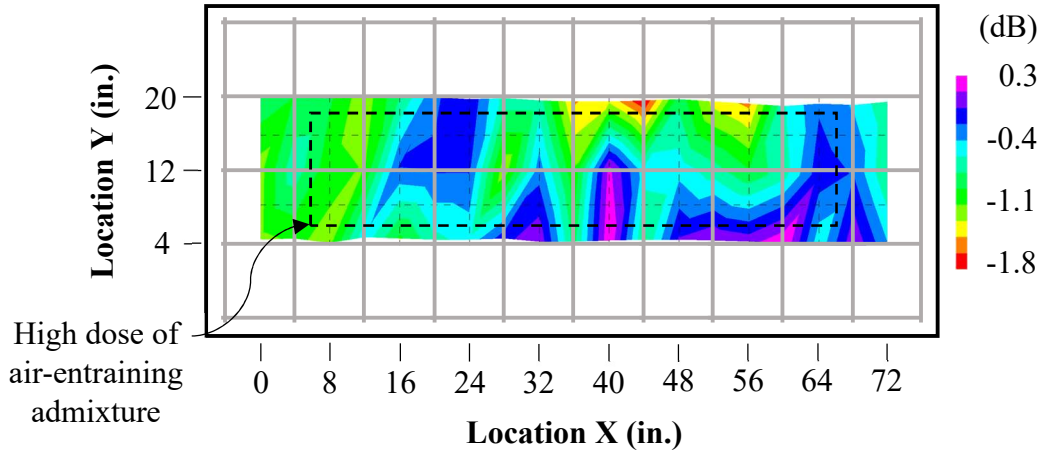

Figure C9: Specimen DE2 Top Bar Passes (All) Air-Dried Depth Corrected GPR Data

C10. Depth-Corrected GPR Data Contour Plot for Specimen DE3

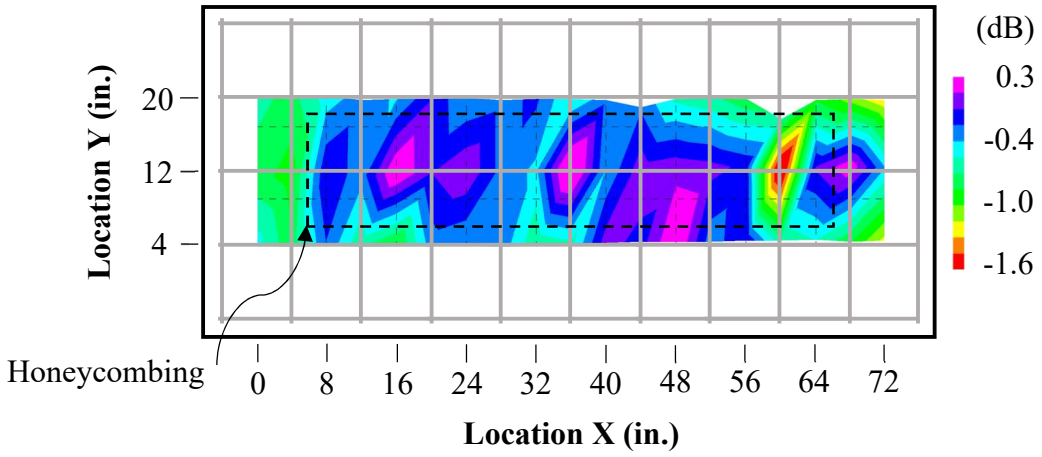

Figure C10: Specimen DE3 Top Bar Passes (All) Air-Dried Depth Corrected GPR Data

C11. Depth-Corrected GPR Data Contour Plot for Specimen DE4

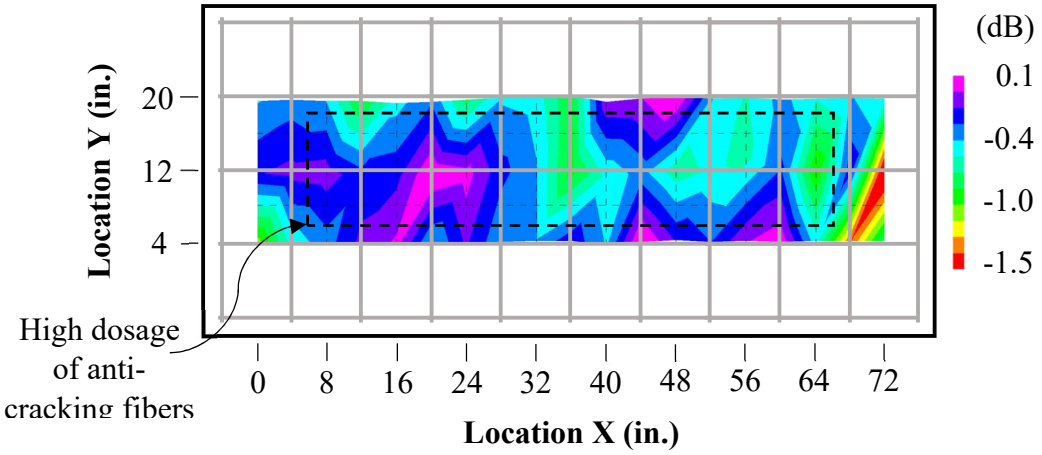

Figure C11: Specimen DE4 Top Bar Passes (All) Air-Dried Depth Corrected GPR Data

C12. Depth-Corrected GPR Data Contour Plot for Specimen DE5

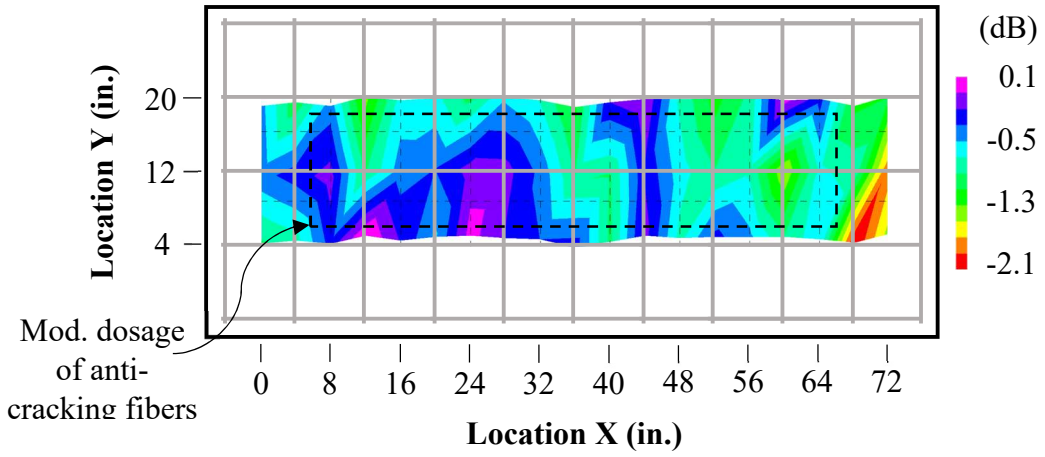

Figure C12: Specimen DE5 Top Bar Passes (All) Air-Dried Depth Corrected GPR Data

C13. Depth-Corrected GPR Data Contour Plot for Specimen PC1

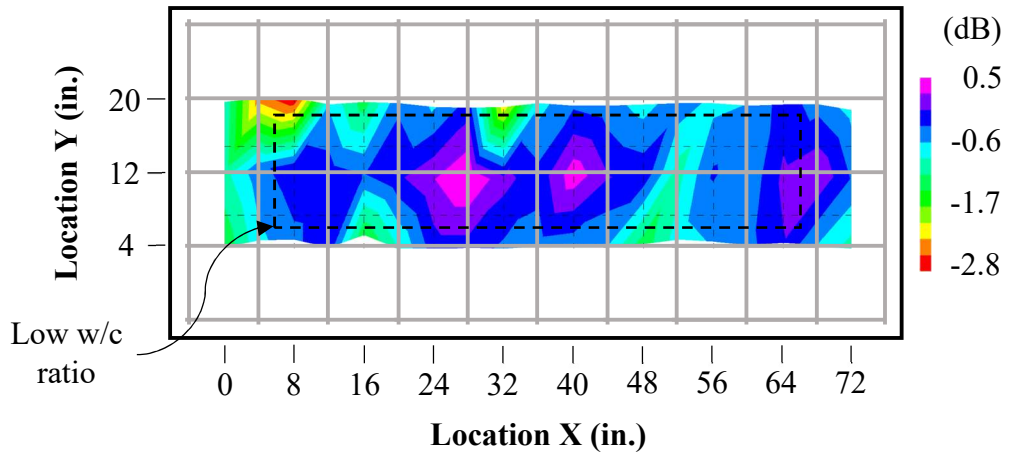

Figure C13: Specimen PC1 Top Bar Passes (All) Air-Dried Depth Corrected GPR Data

C14. Depth-Corrected GPR Data Contour Plot for Specimen PC2

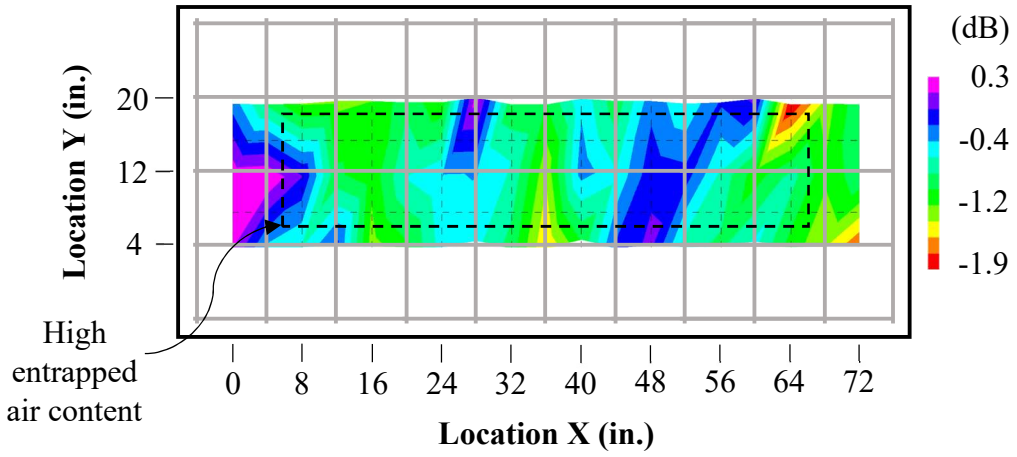

Figure C14: Specimen PC2 Top Bar Passes (All) Air-Dried Depth Corrected GPR Data

C15. Depth-Corrected GPR Data Contour Plot for Specimen V1

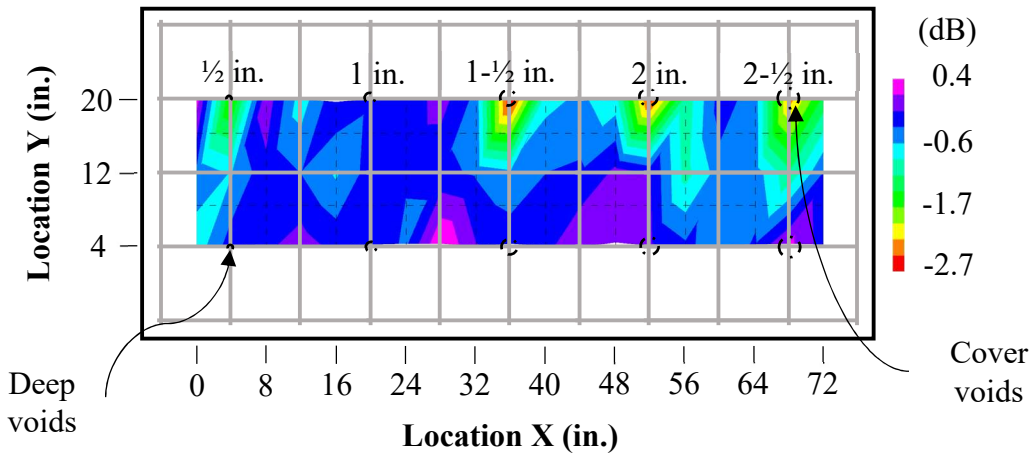

Figure C15: Specimen V1 Top Bar Passes (All) Air-Dried Depth Corrected GPR Data

C16. Depth-Corrected GPR Data Contour Plot for Specimen V2

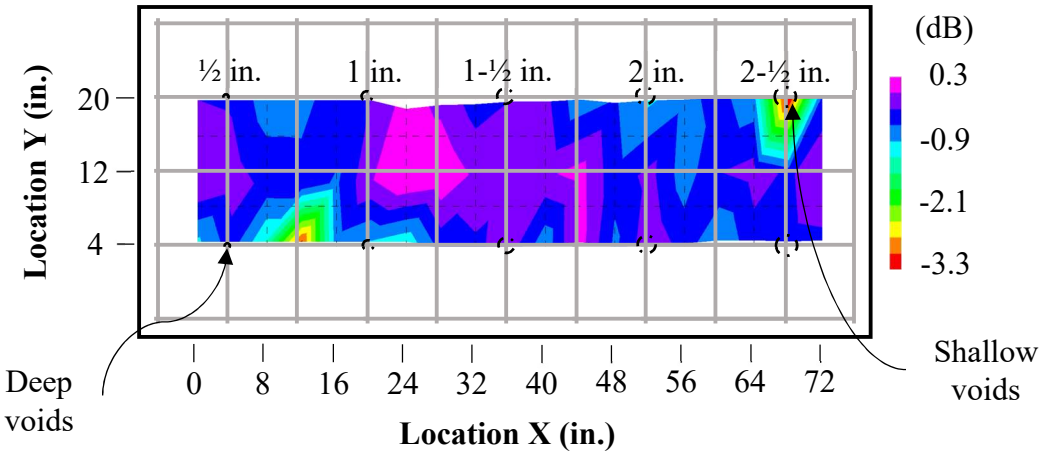

Figure C16: Specimen V2 Top Bar Passes (All) Air-Dried Depth Corrected GPR Data

Appendix D: Impact Echo Post-Processing Algorithm for Bridge Deck Condition Assessment

It has been noted in impact-echo literature that interpretation of impact-echo data requires much experience and training to develop pattern recognition skills (Sansalone 1997). Thus, while an experienced impact-echo operator may be able to successfully analyze data for an accurate condition assessment of a bridge deck, a novice to the method lacking experience and pattern recognition skills may struggle to correctly interpret impact-echo data.

Inspired by this learning curve to implementing impact echo in nondestructive evaluations, the post-processing algorithm presented in this appendix was created by the author and Dr. Anton K. Schindler of Auburn University to assist novice impact-echo operators in successfully interpreting bridge deck data. In turn, novice operators could develop pattern recognition skills while also accurately predicting the condition of bridge decks. This appendix is intended for future use, either in part or total, as part of a standalone publication.

Impact-echo measurements corresponding to the bottom of a bridge deck — i.e. the deck thickness frequency — are normally distributed. This can easily be observed by plotting the cumulative distribution function of thickness frequencies on normal probability paper or on a standard linear (xy) graph by transforming the cumulative probabilities to standard normal random variables. A dataset containing 72 observations of the deck thickness frequency for a reinforced concrete slab is shown in Figure D1. Within that

dataset, multiple instances of the same frequency were recorded due to measurement resolution of the impact-echo system. Nonetheless, a linear trendline fits the dataset quite well with a Pearson correlation coefficient of 0.91, indicating that the data are normally distributed.

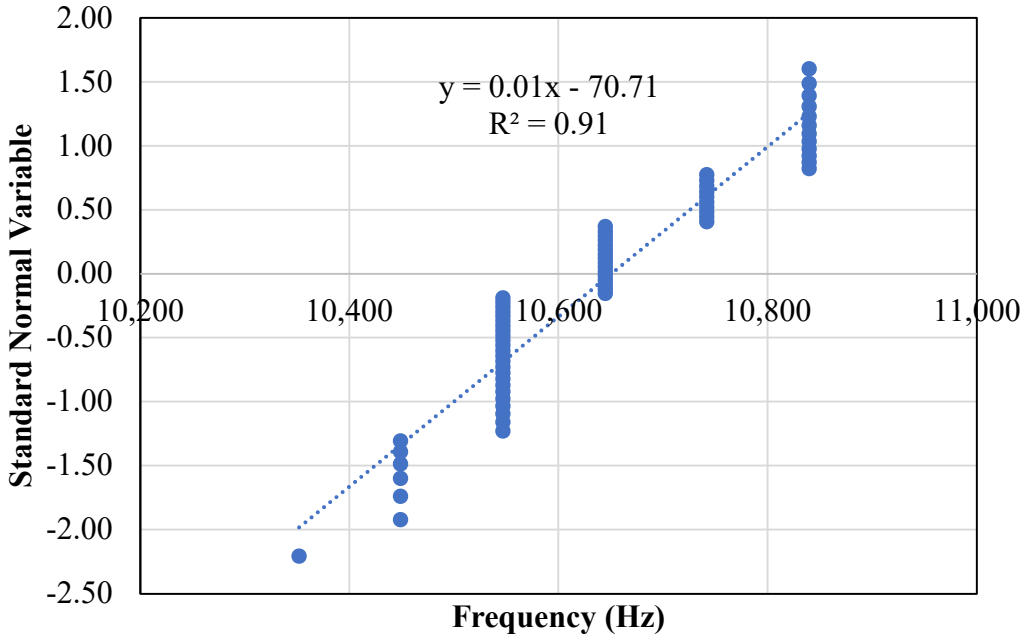

Figure D1: Normal Distribution of Slab Thickness Frequencies

As it has been remarked in literature (Sansalone 1997) that defect detection with impact-echo is facilitated through extensive training and pattern recognition, it stands to reason that frequencies corresponding to bridge deck defects would likely fall outside the normal distribution of sound deck thickness frequencies. Thus, by identifying the portion of an impact-echo dataset corresponding to normally distributed deck thickness frequencies, the remaining frequencies can be flagged as highly likely to have been measured over deck defects. Should one assume that impact-echo deck thickness

frequencies exhibit no skewness, only the corresponding mean and standard error of the frequencies would be needed to define the distribution.

An intuitive theoretical base for estimating the mean deck thickness frequency comes from the following equation reported by Sansalone (1997):

$$T = \frac{\beta C_p}{2 f_p} \tag{D1}$$

where

T = the depth to the reflecting interface, units of length;

β = factor for the cross-sectional geometry of the tested element, 0.96 for a slab;

C_p = the velocity of the P wave in concrete, units of length per time; and

f_p = the frequency of the first transient mode, units of frequency.

If the compression wave velocity is accurately determined and the expected thickness of the deck is known, Equation 1 can be rearranged to solve for the theoretical deck thickness frequency which could serve as an estimated mean for the normal distribution. The compression wave velocity should be determined with maximum accuracy in accordance with ASTM C1383 (2015) as well as the deck thickness from direct measurement, other NDT evaluations, or other ground truth data.

With an estimate of the mean deck thickness frequency determined, an estimation of the corresponding standard error allows for definition of the normal distribution. Through limited experimental testing of laboratory-constructed reinforced concrete slabs,

the author has observed that typical standard errors of the deck thickness frequency range between roughly 130 to 230 Hz, corresponding to coefficients of variation between about 1 and 4.5%. Such a low range in coefficients of variation is indicative of the excellent repeatability of impact-echo measurements. Perhaps a standard coefficient of variation (e.g. 2.5%) could be assumed for a given deck and used in conjunction with the estimated mean deck thickness frequency to compute the standard error. Nonetheless, the ability to estimate the standard error directly from frequency data rather than assume it based on an assumed coefficient of variation may comply better with the range of variation potentially existing among deck thickness frequency data among different bridge decks.

While considering candidate approaches to assessing the deck thickness frequency spread directly from measured data, it was noticed that flexural plate-bending frequencies measured over shallow delaminations cause stark discontinuities in the shape of the cumulative probability distribution when plotted on normal probability paper. To demonstrate this notion, both the deck thickness and flexural plate-bending frequencies corresponding to the defective slab partially portrayed in Figure D1 is presented in Figure D2. Comparing the cumulative probability distributions from Figures D1 and D2, it is noticed that, with the inclusion of the flexural plate-bending frequencies, the Pearson correlation coefficient dropped from 0.91 to 0.53, indicating a strong disruption in the normally-distributed behavior characteristic of the deck thickness frequencies. Further, the addition of the flexural plate-bending frequencies changes the shape of the distribution from a straight line to two straight line segments respectively termed Segment A and Segment B, for discussion purposes. From left to right, the termination of Segment A coincides with the beginning of Segment B, a location that will be referred to as the

breakpoint. The breakpoint appears to mark the termination of flexural plate-bending frequencies and the beginning of deck thickness frequencies. Thus, the breakpoint can be used as an estimate of the smallest frequency within the normal distribution of bridge deck thickness frequencies.

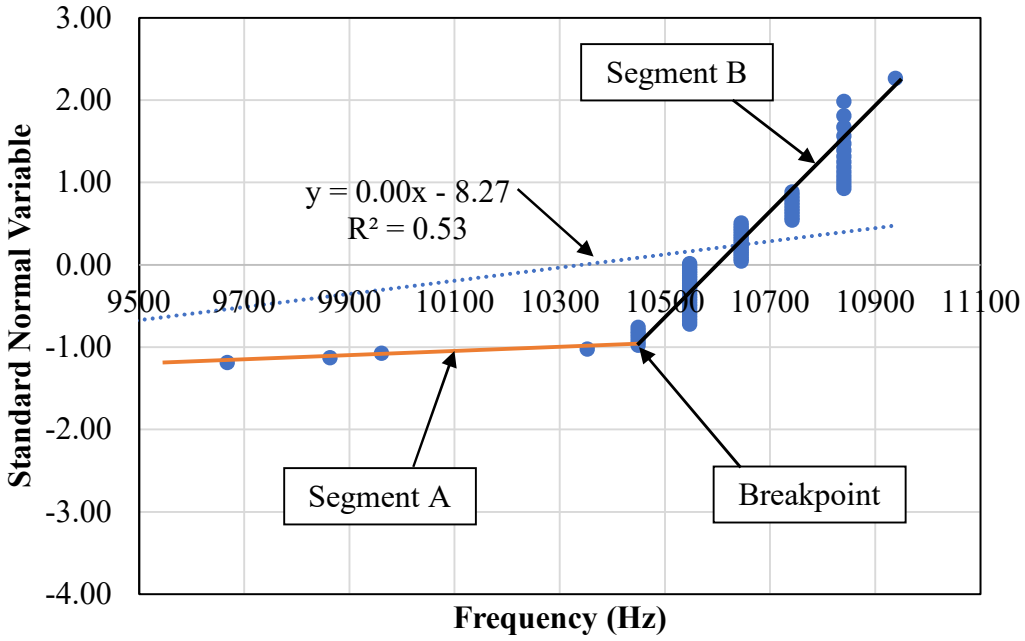

Figure D2: Deck Thickness and Flexural Plate-Bending Frequencies from a Delamination Slab

With the breakpoint known, the distance between the minimum and mean of normally-distributed deck thickness frequencies can be computed. If it is assumed that there is no skewness in the normal distribution, this distance can be added to the theoretical deck thickness frequency (the assumed mean) to determine the maximum deck thickness frequency. With the minimum and maximum bounds of the deck thickness frequencies known, the frequencies outside those bounds can be classified as corresponding to deck defects.

All that remains is to determine a reliable method for detecting the breakpoint. Segmented linear regression analysis aims to detect the point in which two piecewise linear segments meet, making it a seemingly appropriate method for locating the breakpoint between flexural plate-bending and deck thickness frequencies. For this study, a segmented linear regression algorithm developed by Muggeo (2017) was used to detect this breakpoint in impact-echo data. That algorithm uses an initial guess for the breakpoint and iteratively updates it using maximum likelihood estimation until the solution for the breakpoint converges.

It is disadvantageous to require a novice impact-echo operator to make an initial breakpoint guess, as a bad guess may result in the algorithm converging upon the wrong breakpoint. Thus, an initial guess of two standard errors below the deck thickness frequency mean would correspond to the 5^{th} percentile of normally-distributed frequencies, a statistical benchmark hypothesized to likely not be influenced by outliers. The standard error could be estimated using the theoretical mean determined from rearrangement of Equation D1 and an assumed coefficient of variation of 2%, based on laboratory impact-echo testing of normalweight concrete with a specified compressive strength of 4,000 psi.

With a general method in place for determining the breakpoint, the proposed impact-echo post-processing algorithm for determining the condition of a bridge deck is given in the following list. Note that certain special cases for determining an accurate breakpoint not previously discussed are addressed within Step 3.

Impact-Echo Post-Processing Algorithm

Step 1: Calculate the theoretical deck thickness frequency based on the compression wave velocity (determined in accordance with ASTM C1383, 2015) and deck thickness determined through ground truthing.

Step 2: Plot the cumulative probability distribution of the measured impact-echo frequencies on a standard linear (X and Y) graph, transforming cumulative probabilities into corresponding standard normal variables, in accordance with guidance given by Nowak and Collins (2013).

Step 3: Determine the breakpoint.

- **a.** Calculate Pearson's correlation coefficient. If that coefficient is greater than or equal to 0.95, use the average of the three smallest frequencies as the breakpoint. Otherwise, proceed to Step 3(b).
- **b.** Use segmented linear regression as described by Muggeo (2017) to determine the breakpoint. Let the initial breakpoint be two standard errors below the theoretical frequency calculated in Step 1. A 2% coefficient of variation is recommended to calculate the standard error as in Equation D2. If the algorithm produces a breakpoint smaller than the lowest recorded frequency, use the average of the three lowest recorded frequencies as the breakpoint. Further, if the algorithm produces a breakpoint larger than the theoretical frequency calculated in Step 1, proceed to Step 3(c).

$$s = \frac{V * \mu}{100} \quad \text{(D2)}$$

where

s = the sample standard error of the deck thickness frequencies, Hz;

V = the coefficient of variation, 2%, Hz; and

μ = the sample mean of the deck thickness frequencies in Step (1), Hz.

c. Repeat the segmented linear regression algorithm (Muggeo 2017) with the lowest recorded frequency as the initial breakpoint guess. If the algorithm does not accept this datapoint as a guess, continue increasing the guess until it is accepted. If the same breakpoint from Step 3(b) is produced, then use the average of the three lowest frequencies as the breakpoint. Else, use the breakpoint produced from this step.

Step 4: Compute the distance between the theoretical deck thickness frequency from Step 1 and the breakpoint determined from Step 3.

Step 5: Add the distance from Step 4 to the theoretical deck thickness frequency from Step 1.

Step 6: Use the breakpoint determined from Step 3 and the frequency computed in Step 5 as the minimum and maximum expected deck thickness frequencies respectively. Any measured frequencies within the range of frequencies defined by the foregoing two frequencies are predicted to correspond with sound deck. All other measured frequencies are predicted to correspond with deck defects.

Ground truthing is recommended to be performed at the two frequencies computed in Step 6 of the algorithm to verify their validity as the bounds of bridge deck thickness frequencies.

Results of some preliminary testing and validation of the proposed post-processing algorithm are provided hereinafter. Dominant impact-echo frequencies and the corresponding deck condition predicted from the algorithm are shown for laboratory specimens with (1) simulated corrosion-induced delaminations, and (2) shallow delaminations.

Case Study 1: Laboratory Specimen with Corrosion-Induced Delaminations

A 3 ft by 7 ft by 7.25 in. reinforced concrete specimen was constructed to have three distinct zones of differing condition. Reinforcement in Zone 1 was passive and exhibited no delaminations. Moreover, reinforcement in Zones 2 and 3 were active; however, only Zone 3 was damaged from significant delaminations. The dominant frequencies measured during testing of the specimen are shown on the spatial contour plot presented in Figure 3. The dominant frequency excited during testing was relatively uniform between Zones 1 and 2, as neither of those zones contained significant delaminations. However, numerous low-frequencies were recorded in Zone 3, corresponding to flexural-plate bending behavior above shallow delaminations. Thus, considering delaminated areas as defective, Zones 1 and 2 were classified as sound while Zone 3 was defective.

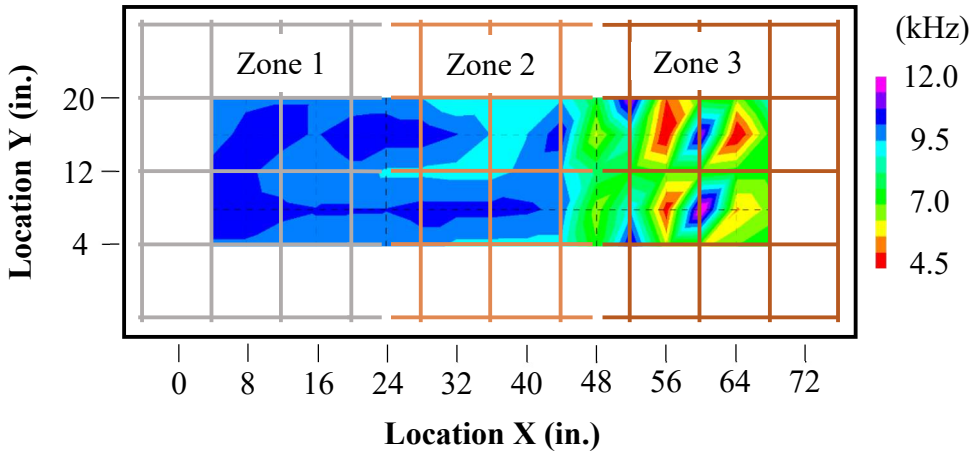

Figure D3: Spatial Contour Plot of Dominant Impact-Echo Frequencies for Specimen with Three Distinct Conditions

For this specimen, the compression wave velocity and thickness were determined to be 13,171 ft/s and 7.25 in. respectively. Thus, the theoretical deck thickness frequency was calculated to be 10,464 Hz. The proposed algorithm resulted in minimum and maximum deck thickness frequencies of 9,277 Hz and 11,701 Hz, respectively. Using these two thresholds to predict sound (shown in a green hue) and delaminated (shown in a red hue) locations on the specimen, the predicted specimen condition was determined and plotted as shown in Figure D4.

From that contour plot, it is observed that the algorithm does a good job in correctly prediction the specimen condition. The entirety of Zone 1 and the majority of Zone 2 were correctly identified as being sound. Furthermore, most of Zone 3 was correctly classified as being delaminated. While there are a few locations in Zone 3 potentially delaminated that are predicted to be sound and a small portion of Zone 2 classified as delaminated, on the whole the correlation between the true condition of the specimen and that predicted by the algorithm is strong.

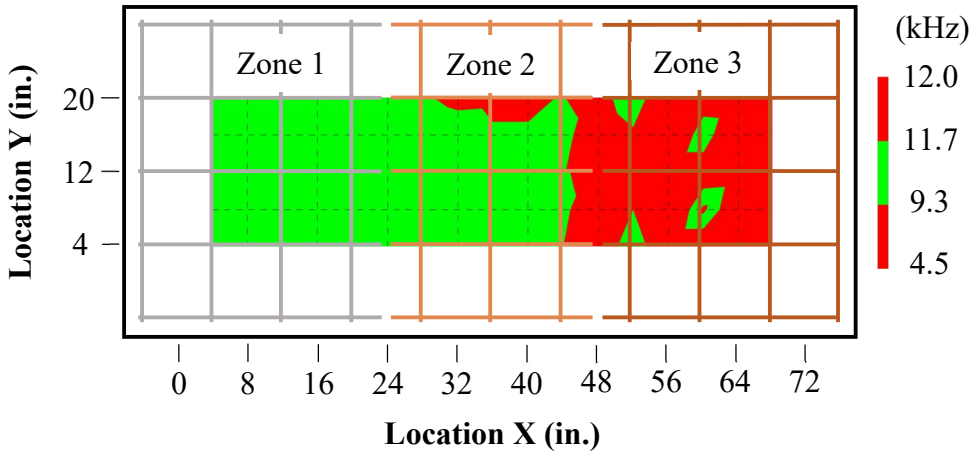

Figure D4: Algorithm-Predicted Condition of Specimen with Corrosion-Induced Delaminations

Case Study 2: Laboratory Specimen with Shallow Delaminations

A 3 ft by 7 ft by 7.25 in. reinforced concrete specimen was constructed to have six unbonded, shallow delaminations with thicknesses ranging from 0.25 to 2.38 mm. The dominant frequencies measured during testing of the specimen are shown on the spatial contour plot presented in Figure D5. As can be observed from that plot, low frequencies (shown in red, yellow, and green hues) indicative of flexural plate-bending behavior were measured over all six shallow delaminations. Moreover, the frequencies (shown in purple hues) measured over the sound portions of the specimen were much higher and generally uniform, indicating compression wave reflection off the bottom of the specimen.

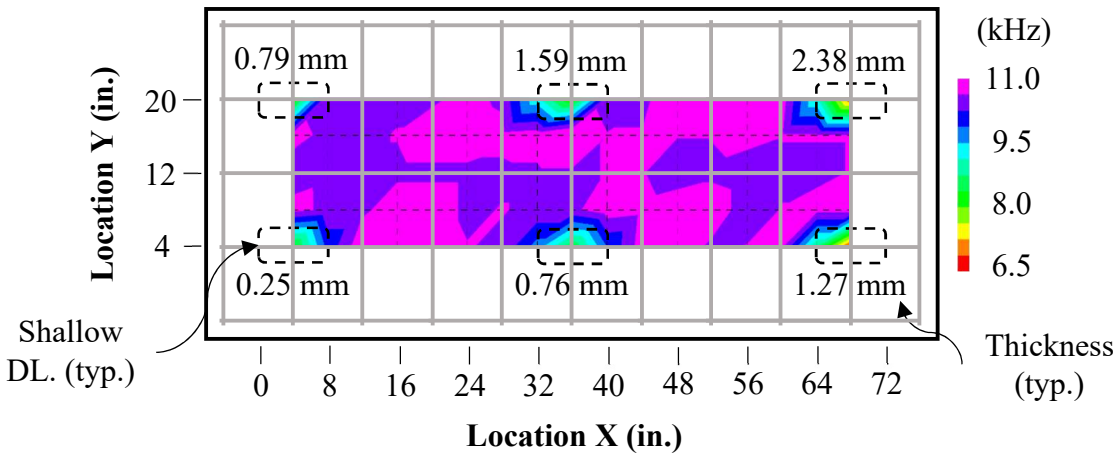

Figure D5: Spatial Contour Plot of Dominant Impact-Echo Frequencies for Specimen with Shallow Delaminations (DL)

For this specimen, the compression wave velocity and thickness were determined to be 13,980 ft/s and 7.25 in. respectively. Thus, the theoretical deck thickness frequency was calculated to be 11,107 Hz. The proposed algorithm resulted in minimum and maximum deck thickness frequencies of 10,422 Hz and 11,792 Hz respectively. Using these two thresholds to predict sound (shown in a green hue) locations and delaminations (shown in a red hue) the predicted specimen condition was determined as shown in Figure D6. From that spatial contour plot, it can be clearly observed that the algorithm was successful in locating all six delaminations. Moreover, most sound portions of the deck were correctly identified by the algorithm.

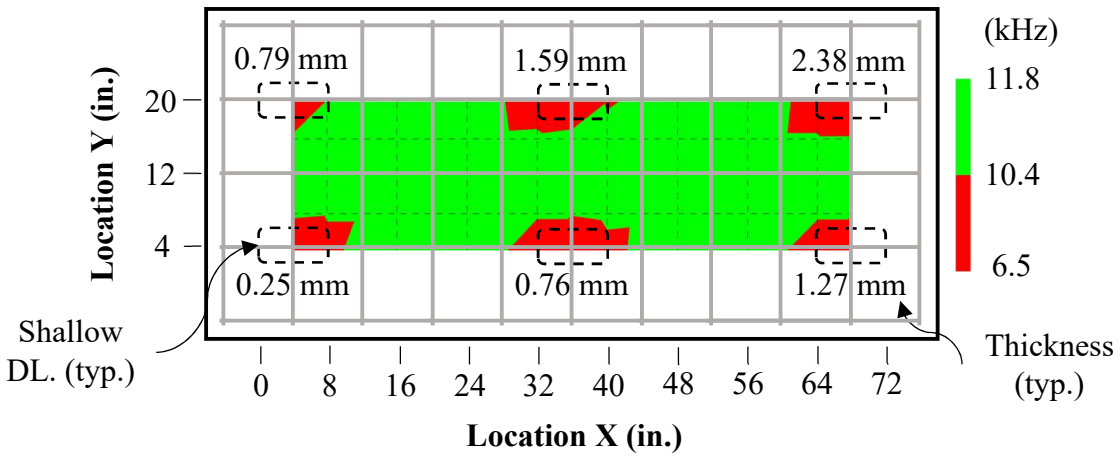

Figure D6: Algorithm-Predicted Condition of Specimen with Shallow Delaminations

The work presented in this appendix proposed a post-processing algorithm to assist novice impact-echo operators in correctly assessing the condition of bridge decks without overlays. Implementation of the algorithm in two case studies of two laboratory specimens respectively, defective with corrosion-induced delaminations and shallow, unbonded delaminations demonstrated that the algorithm can allow for accurate assessment of the condition of a bridge deck. Future work in developing this algorithm will aim to apply it on larger datasets from bridge decks containing multiple types of defects.